Trans-iron Elements in Evolved Stars

Dissertation

der Mathematisch-Naturwissenschaftlichen Fakultät
der Eberhard Karls Universität Tübingen
zur Erlangung des Grades eines
Doktors der Naturwissenschaften
(Dr. rer. nat.)

vorgelegt von
Lisa Löbling
aus Herrenberg

Tübingen
2020

Gedruckt mit Genehmigung der Mathematisch-Naturwissenschaftlichen Fakultät
der Eberhard Karls Universität Tübingen.

Tag der mündlichen Qualifikation: 25.05.2020

Dekan:	Prof. Dr. Wolfgang Rosenstiel
1. Berichterstatter:	Prof. Dr. Klaus Werner
2. Berichterstatter:	Prof. Dr. Dr. Stephan Geier

Contents

List of Abbreviations

(V)LTP	(very) late thermal pulse, comprises LTP and VLTP
AFTP	AGB final thermal pulse
AGB	asymptotic giant branch
AGB	asymptotischer Riesenast
CE	common-envelope
CS	central star
CSPN	central star of the planetary nebula
DA-type WD	WD with H-dominated atmosphere
DAO-type WD	WD with H-dominated atmosphere showing prominent lines of H I and He II
DB-type WD	WD with He-dominated atmosphere showing prominent lines of He I
DO-type WD	WD with He-dominated atmosphere showing prominent lines of He II
EHB	extended horizontal branch
FTP	final thermal pulse
HRD	Hertzsprung-Russell diagram
IGE	iron-group element, i.e. calcium to nickel (atomic number $20 \leq Z \leq 28$)
LTE	local thermodynamic equilibrium
LTP	late thermal pulse
MLT	mixing length theory

NLTE	non-local thermodynamic equilibrium
ODF	opacity-distribution function
OS	opacity-sampling
PhD	Doctor of Philosophy
PN	planetary nebula
r-process	rapid neutron-capture process
RLOF	Roche-lobe overflow
s-process	slow neutron-capture process
S/N	signal-to-noise ratio
sdB	subluminous B-type stars
sdO	subluminous O-type stars
TDU	third dredge-up
TE	thermodynamic equilibrium
TEE	Transeisenelement, see TIE
TIE	trans-iron element, i.e. copper and beyond (atomic number $Z > 28$)
TMAP	Tübingen Model-Atmosphere Package (`https://uni-tuebingen.de/de/41621`)
TOSS	Tübingen Oscillator Strength Service (`http://dc.g-vo.org/TOSS`)
TP	thermal pulse
UV	ultraviolet
UVES	Ultraviolet and Visual Echelle Spectrograph
VLT	Very Large Telescope
VLTP	very late thermal pulse
WD	white dwarf
ZSPN	Zentralstern des planetarischen Nebels

Zusammenfassung

In dieser Arbeit werden Spektralanalysen verschiedener Sterntypen vorgestellt, deren Fokus auf den Häufigkeiten von Transeisenelementen (TEE) liegt. Das übergeordnete Ziel ist es, die Nukleosynthese schwerer Elemente durch Neutroneneinfang auf dem asymptotischen Riesenast (AGB) zu untersuchen. Diese Analysen können helfen, ein besseres Verständnis von Prozessen wie Konvektion, Diffusion, Sternwind und Massenverlust zu erlangen, die für die Entstehung des beobachteten Häufigkeitsmusters verantwortlich sind. Die erste Arbeit (Löbling et al. 2019a) präsentiert die Analyse des Barium-Zentralsterns des planetarischen Nebels (ZSPN) Hen 2−39. Im Zentrum des Nebels befindet sich ein Doppelsternsystem, bestehend aus einem Unterriesen vom Spektraltyp K und dem heißen, ionisierenden post-AGB-Stern. Wir bestätigten die Kohlenstoff- und Barium-Anreicherung des Unterriesen und bestimmten die Häufigkeiten beziehungsweise Obergrenzen für die Häufigkeiten von insgesamt 39 Elementen. Aus dem Vergleich des beobachteten Häufigkeitsmusters im Begleiter mit theoretischen Berechnungen für die Nukleosynthese schließen wir, dass Massentransfer mit einem hohen Akkretionsbruchteil von ca. 15 % der vom Primärstern verlorenen Masse erforderlich ist, weshalb Wind-Roche-Lobe-Overflow als wahrscheinlichster Massentransfermechanismus in diesem System anzusehen ist.
Die beiden anderen Arbeiten präsentieren Spektralanalysen von heißen post-AGB-Sternen mittels NLTE-Sternenatmosphärenmodellen. In Löbling et al. (2019c) wurden die spektroskopischen Zwillinge, die ZSPN von Abell 43 und NGC 7094, analysiert. Neben der Effektivtemperatur und der Oberflächenschwerebeschleunigung wurden genaue Häufigkeiten für eine Vielzahl von Elementen, darunter TEE, bestimmt. Außer für Sauerstoff, sind die beobachteten Häufigkeiten in Übereinstimmung mit theoretischen Werten aus Sternentwicklungsrechnungen für ein Szenario mit einem finalen thermischen Puls beim Verlassen des AGB, der das Wasserstoffdefizit verursacht hat. Die oberen Grenzwerte für die TEE-Häufigkeiten sind geringer als die extrem hohen Werte, die in Atmosphären von heißen wasserstoffarmen Weißen Zwergen gemessen werden und bestätigen daher, dass die Diffusion der für die Anreicherung verantwortliche Prozess ist. Für die beiden ZSPN wird dies durch einen starken Sternwind verhindert.
Um die Hypothese zu überprüfen, dass für die TEE-Anreicherung der Atmosphären von wasserstoffarmen post-AGB-Sternen eine Entwicklung mit einem finalen thermischen Puls und der resultierenden Durchmischung von Hülle und Zwischenschalenmaterial nötig ist, analysierten wir den heißen ZSPN Abell 35 (Löbling et al. 2019b). In diesem Fall waren wir erfolgreich und fanden eine starke Anreicherung, die nicht erwartet wurde. Der Stern ist

wasserstoffreich und von geringer Masse, was eine großflächige Vermischung über einen finalen thermischen Puls ebenso wie durch einen sogenannten „third dredge-up“ ausschließt. Der wissenschaftliche Fortschritt, der sich aus diesem Ergebnis ergibt, besteht darin, dass wir in Frage stellen müssen, ob eine Durchmischung von Hülle und Zwischenschalenregion für die eigentümlichen Elementhäufigkeiten und die starke TEE-Anreicherung in wasserstoffarmen Weißen Zwergen notwendig ist oder ob lediglich Diffusion die ursprünglich vorhandenen TEE anreichert.

Summary

In this work, we performed spectral analyses of different types of stars focusing on the abundances of trans-iron elements (TIEs). The overarching aim is to constrain neutron-capture nucleosynthesis via the slow (s) process on the asymptotic giant branch (AGB) as well as processes like mixing, diffusion, stellar wind, and mass loss that are responsible for the formation of the observed abundance pattern.
The first paper (Löbling et al. 2019a) presents our analysis of the barium (Ba) central star of the planetary nebula (CSPN) Hen 2−39. The nucleus consists of a binary containing a K-type subgiant and the hot ionizing post-AGB star. We confirmed the carbon (C) and Ba enrichment of the subgiant companion and determined abundances and abundance limits for 39 elements in total. From the comparison of the observed abundance pattern in the secondary with theoretical predictions for nucleosynthesis calculations, we find that mass transfer with a high fraction of accretion of $\approx 15\,\%$ of the mass that was ejected by the primary is required. Hence, wind-Roche-lobe overflow (RLOF) is considered the most likely mass transfer mechanism in this system.
The other two works present spectral analyses of hot post-AGB stars by means of non-local thermodynamic equilibrium (NLTE) stellar atmosphere models. In Löbling et al. (2019c), we aimed to revise the effective temperature and surface gravity as well as to determine abundances for a multitude of elements including TIEs in the spectroscopic twins, the CSPNe Abell 43 and NGC 7094. The observed abundances, besides of oxygen (O), are in agreement with theoretical calculations for an AGB final thermal pulse (AFTP) evolution that causes the hydrogen (H)-deficiency. The upper abundance limits for TIEs lie below the strong enrichment found in hot H-deficient white dwarfs (WDs) and confirms that diffusion is the process responsible for the enrichment. For the two CSPNe, this is prevented by a strong stellar wind.
To test the hypothesis of s-process enrichment of the surfaces of H-deficient stars through final-flash mixing, we analyzed the hot H-rich CSPN Abell 35 (Löbling et al. 2019b). In this case, we were successful and found a strong enrichment to an amount that was unexpected. The star is H-rich and of extremely low mass which rules out large-scale mixing via a final thermal pulse (FTP) or third dredge-up (TDU). The scientific progress drawn from this result is, that we need to question the explanation that final flash mixing is really necessary for this peculiar surface abundance pattern or whether it is just diffusion starting from initial material.

Preface

A multitude of chemical elements is of central importance for life in the way we know it on Earth. Thus, the question for the origin of chemical elements is a basic and fundamental one. Today, the periodic table, first introduced by Dimitri Mendeleev and Lothar Meyer (Mendeleev 1869; Meyer 1870), comprises 118 (Oganessian et al. 2006) elements and is still expanding.

In 1814, Joseph von Fraunhofer discovered and cataloged about 600 black lines in the dispersed sunlight but had no explanation for them (Fig. 1, Fraunhofer 1817). They had already been discovered by Wollaston (1802) who interpreted them as black space in between the colors. Spectroscopic analyses to identify elements due to their individual line transitions were pioneered by Robert Bunsen and Gustav Kirchhoff around 1860 in Heidelberg (Kirchhoff & Bunsen 1861). Based on their laboratory experiments, they could identify the black lines that Fraunhofer labeled with the letter D to coincide with the line emitted by sodium salt in a flame. This showed, that the elements present on Earth should also be the building blocks of the Sun, although the origin of these was still unclear.

Inspired from Albert Einstein's theory that mass and energy are equivalent (Einstein 1916), Sir Arthur Stanley Eddington proposed that the Sun produces energy by converting mass, although he could only speculate about the exact process he already figured out the correct one, the fusion of four hydrogen (H) atoms to helium (He) (Eddington 1920). At that time, it was not yet discovered, that the Sun mainly consists of H but a composition similar to Earth was assumed. It needed further work to prove this. The quantum theory of atoms and their spectra of Niels Bohr and Arnold Sommerfeld (Bohr 1913; Sommerfeld 1916) enabled Magh Nad Saha, Alfred Fowler and Edward Milne to interpret stellar spectra by means of atomic physics so that temperature determines the thermal excitation of atoms and, thus, the line strength in the spectrum of the stellar atmosphere (Saha 1921; Fowler & Milne 1923). Using this, Cecilia Payne and later Albrecht Unsöld were able to prove the high H content of stars (Payne 1925; Unsöld 1928).

First, the connection between energy production of stars and the formation of elements was eluded. Alpher et al. (1948) argued, that all known elements came to existence right after the big bang as consequence of a build-up process in a neutron dense environment. Neutrons could decay into protons and electrons and accumulate to heavier elements. This formation mechanism is correct only for H and He, because the accumulation process fails beyond He due to the lack of stable isotopes with five and eight nucleons. The whole process of big bang nucleosynthesis stopped after about 20 minutes, when the Universe became too

Fig. 1: German stamp to celebrate the 200$^{\text{th}}$ birthday of Joseph von Fraunhofer. It shows the spectral energy distribution of the Sun as well as the spectrum including the black lines discovered by Fraunhofer. (`https://upload.wikimedia.org/wikipedia/commons/a/a4/DBP_1987_1313_Joseph_von_Fraunhofer\%2C_Sonnenspektrum.jpg`).

cool and sparse for nuclei to form (Coc & Vangioni 2017). Fred Hoyle postulated, that only H was primordial (Hoyle 1946). Together with Margaret and Geoffrey Burbidge and William Fowler, they made a compelling case for stellar nucleosynthesis. They showed, that stars act as nuclear furnaces and can also fuse elements beyond He for energy production and bridge the unstable five and eight nucleon cores when producing carbon (C) out of He. Furthermore, they found explosions and stellar winds as mechanisms to return the elements to the Universe (Burbidge et al. 1957). A sign, that nucleosynthesis in fact happens in stars, was the detection of technetium (Tc), the lightest element with only unstable isotopes, at the surface of a red-giant star (Merrill 1952). With a half-life of 210 000 yrs[1], ^{99}Tc is too short lived to be primordial. Burbidge et al. (1957) figured out eight processes to be responsible for the formation of stable isotopes beyond H. Beside the reactions for H and He fusion, they, e.g., described the α-process that has now been supplanted by the C, oxygen (O), neon (Ne), and silicon (Si) fusion that happen in massive stars at the end of their nuclear lifetime. All fusion reactions cannot produce elements heavier than iron (Fe), the element with the highest binding energy per nucleon. Furthermore, they found that two different neutron capture processes are operating, the slow (s) and rapid (r) process. Since then, much progress has been made in identifying the astrophysical sites for the production of heavy elements. Exploding white dwarfs (WDs) were found to produce Fe and are now thought to be the main contributor to the formation of iron-group elements (IGEs, calcium to nickel) in the Universe (Leibundgut 2000). Heavy s-process elements are accepted to be formed and expelled to the Universe by low- and intermediate mass stars in the late, asymptotic-giant-branch (AGB) phase of their evolution (Busso et al. 1999). Just recently, neutron star mergers were found to be a major site for the r-process with clear evidence (Kasen et al. 2017). The combination of all nucleosynthesis sites is responsible for the chemical evolution of galaxies. Figure 2 illustrates which element is formed by which process or type of star.

[1]Los Alamos National Laboratory Periodic Table (`http://periodic.lanl.gov`).

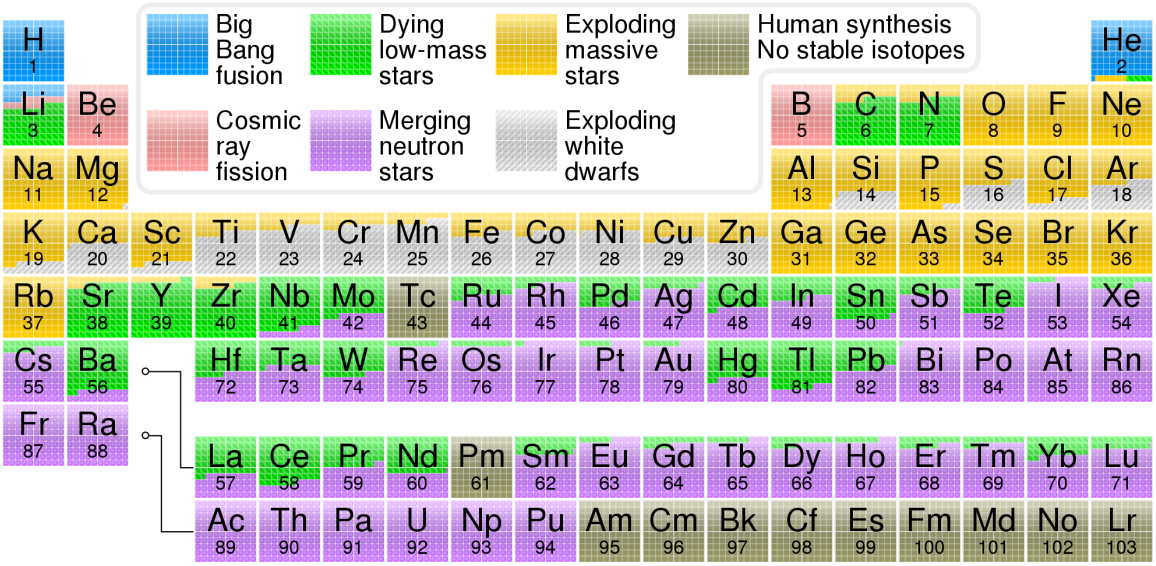

Fig. 2: Periodic table illustrating the origin of the chemical elements in color code. Based on data from Jennifer Johnson (`http://www.astronomy.ohio-state.edu/~jaj/nucleo/`). Graphic from `https://de.wikipedia.org/wiki/Datei:Nucleosynthesis_periodic_table.svg`.

Although qualitatively the production sites and processes for the elements are known, the quantitative predictions from sophisticated nucleosynthesis models about the interior processes, production rates, and element yields are affected by uncertainties. In the case of s-process nucleosynthesis in AGB stars, these concern, e.g., ^{13}C-pocket sizes, mass loss, convective mixing, reaction rates, and neutron poison (Karakas & Lattanzio 2014b).

The aim of this thesis is to perform spectral analyses of hot WDs, i.e., stars that went through the phase of s-process nucleosynthesis, or, in the case of Hen 2−39, of the companion that experienced a period of mass transfer. A precise knowledge of their atmospheric parameters and abundances helps to constrain the physics in their interiors, the yields of the s-process, as well as their evolution history.

In the first Chapter, I give an introduction to stellar evolution and numerical modeling of stellar atmospheres. Chapter 2 connects the topic and motivation for this thesis to recent research. I present the publications written during this PhD project in Chapter 3 and summarize the results in Chapter 4. Chapter 5 gives an outlook to future work.

1 Introduction

1.1 Final stages in the evolution of stars with low and intermediate mass

A vast majority of all stars are formed with an initial mass between 0.07 and 8 $M_\odot$ and will end their lives as WDs. For the Galaxy, it is believed, that stars in that mass range make up 97 % of the whole stellar population (Fontaine et al. 2001). Those with an initial mass between 0.8 and about 8 $M_\odot$ are massive enough to evolve through the AGB when H and He fusion continue in shells around the core made of C and O, the ashes of He burning. Thermal instabilities of the He-burning shell generate pulse-driven convection zones that mix not only the He-rich region in between the He- and H-burning shells but dredge up core material. After the thermal pulse (TP), the outer envelope convection zone can reach into the intershell region and, thus, mix traces of processed material to the envelope as well as H to the upper intershell. This process is called third dredge-up (TDU). It results in the presence of C and protons in the intershell region. Via the interim product nitrogen (N), ^{13}C is produced (^{12}C(p,γ)^{13}N($e^-\ \bar{\nu}_e$)^{13}C) that forms a ^{13}C pocket underneath the H-burning shell (Fig. 1.1). ^{13}C burning acts as a neutron source and provides neutron densities of at most $10^7\,\mathrm{cm}^{-3}$ (Busso et al. 1999). This is the regime of the s-process, which means that unstable isotopes decay before capturing another neutron. Since the interpulse period lasts for a couple of 10^4 yrs, the neutron exposure is nevertheless high enough to enrich s-process elements by a factor of $10^3 - 5 \times 10^4$ compared to the initial abundance within the ^{13}C pocket (Busso et al. 1999).

The surface gravity of the AGB star is very low and although the effective temperature is low as well, the thermal velocity of the particles at the surface is almost sufficient to escape. Due to radiation pressure, a large fraction of the envelope material becomes expelled to the interstellar environment. When the envelope mass decreases to $10^{-2}\,M_\odot$ (Werner & Herwig 2006), the star descends from the AGB. Due to the mass loss, deeper and deeper layers become the surface of the star and, thus, the temperature increases while the bolometric luminosity stays almost constant. When the temperature is high enough, the ultraviolet (UV) radiation of the post-AGB star ionizes the previously ejected material that becomes visible as a planetary nebula (PN). At the point when all nuclear fusion ceases, the stellar remnant enters the WD cooling track and cools towards lower temperatures and higher surface gravities. This canonical picture describes the evolution for the majority of post-AGB

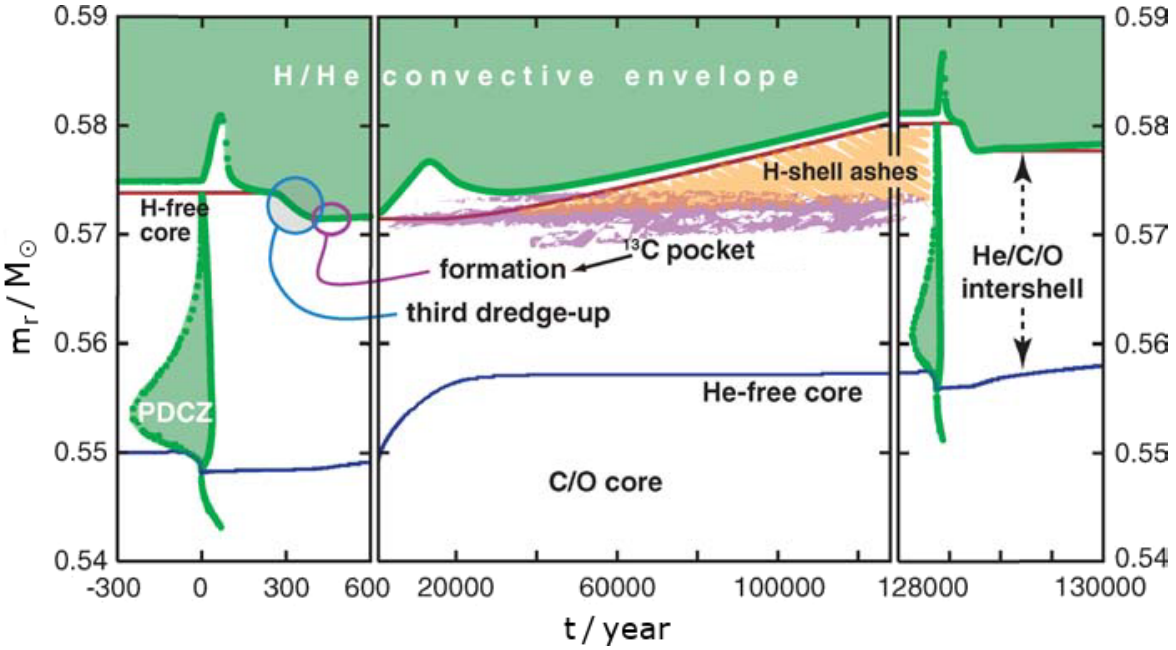

Fig. 1.1: Evolution of the internal structure of an AGB star between two TPs. Convective regions are illustrated in green, the radiative intershell region is not colored. The region of the ^{13}C pocket is indicated in violet. Figure taken from Herwig (2005) and modified.

stars. They retain a H-rich envelope throughout their entire evolution and fade as H-rich WDs of spectral type DA.

1.2 Hydrogen-deficient post-AGB stars

About one fifth of all post-AGB stars turns H-deficient in their evolution (Herwig et al. 1999). Already Heap (1975) reported that the spectra of some central stars of planetary nebulae (CSPNe) are dominated by highly ionized C, O and He lines, some of them even in emission, while no evidence for H was found in the spectrum. These stars belong to the group of PG 1159-type stars. This spectral class is named after the prototype PG 1195−035, that was discovered in the Palomar-Green survey (Wesemael et al. 1985; Green et al. 1986). The atmospheres of these stars show typical compositions of He = [0.30, 0.85], C = [0.15, 0.60], and O = [0.02, 0.20] (Werner & Herwig 2006).
PG 1159 stars are believed to originate from a so-called "born-again scenario", a final flash of the He-burning shell after the descent from the AGB causing the star to expand again and evolve back to the AGB in an extra loop of its evolutionary track in the Hertzsprung-Russell diagram (HRD) (Fig. 1.3). This behavior was first predicted and explored in simulations (Fujimoto 1977; Schönberner 1979) and then invoked to explain the evolutionary path of H-deficient post-AGB stars and WDs. The final flash of the He-burning shell completely alters the canonical evolution described above. A description of the evolution of H-deficient stars can, e.g., be found in Herwig (2005) and Werner & Herwig (2006). The result of such a final thermal pulse (FTP) is a pulse-driven convection zone that mixes the entire envelope

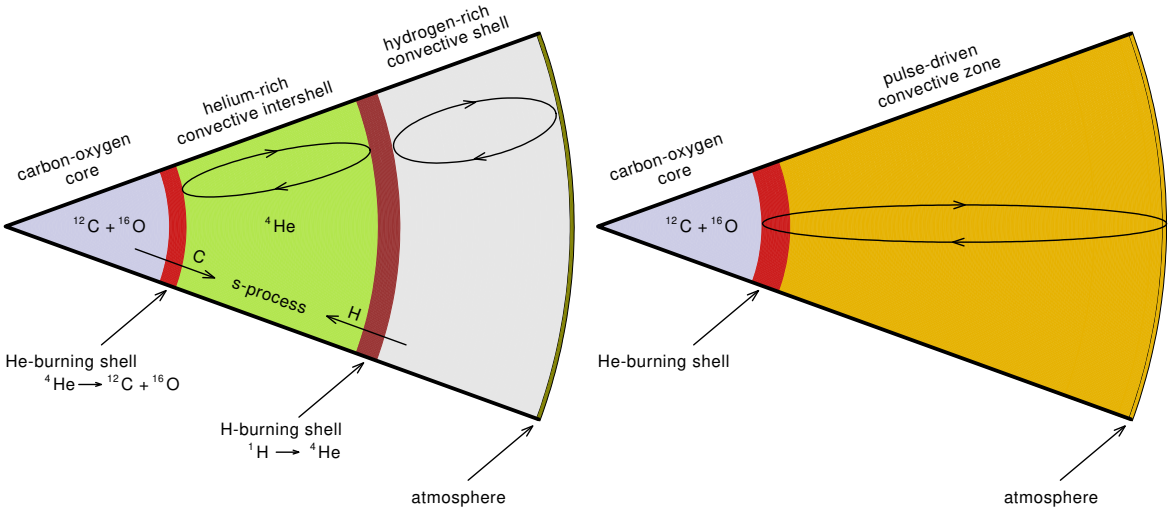

Fig. 1.2: Internal structure of an AGB star during a TP (left) with a convection zone established in the intershell region and during a FTP scenario when a flash induced convection zone mixes the envelope with the intershell region (right). Figure taken from Löbling et al. (2019c).

with the intershell region (Fig. 1.2). The outcome is a H-deficient surface, because the former H-rich envelope becomes diluted in the He-rich intershell material. While the atmospheres of H-rich post-AGB stars can contain traces of nucleosynthesis products that were mixed up by TDU, H-deficient post-AGB star atmospheres basically consist of intershell material.

The surface composition and H content crucially depend on the mass of the envelope compared to the intershell region at the time of the FTP. If it happens right at the descent from the AGB, it is called AGB final thermal pulse (AFTP). During that phase, the envelope and intershell region are of comparable mass $\approx 10^{-2}\,M_{\odot}$ and, thus, the outcome is a so-called hybrid-PG 1159 star with about 20 % H (by mass) in its atmosphere. This scenario does not lead to a "born-again" evolution, whereas a FTP that happens during the bluewards evolution of the post-AGB star at constant luminosity lets the star expand and return to the AGB again. Due to this so-called late thermal pulse (LTP), the star takes an extra loop in the HRD (Fig. 1.3). At the onset of the pulse, the envelope mass has decreased to $\approx 10^{-4}\,M_{\odot}$ and, thus, an LTP results in a post-AGB star with a H content of about 1 % (by mass), which is below the detection limit for spectral analyses. At about the time, when the envelope mass decreased to $\lesssim 10^{-4}\,M_{\odot}$, all nuclear fusion ceases and the star enters the WD cooling sequence. Still then, an FTP is possible. In this case, the surface H is mixed down to the He-burning shell due to the missing entropy border of the H-burning shell that is already "off". Such a very late thermal pulse (VLTP) results in a H-free star. This scenario makes the star return to the AGB twice. First, within a quick evolution of a few years due to the energy production of the H-ingestion and a second time due to the He-shell burning within about 100 yrs, the typical timescale for a TP.

During the post-AGB evolution when the effective temperature is still high, i.e., during the evolution as CSPNe and at the immediate (pre-)WD stage, their atmospheres are still "contaminated" with the mixed up nucleosynthesis products. As CSPNe, the mass loss rate

is still high, so that the atmosphere material is ejected and replaced with material from deeper layers within a few years or less (Unglaub & Bues 2000). Hence, the atmospheric composition reflects the abundance ratios that were established in the FTP mixing. When the star evolves, mass loss and stellar wind decrease. At this stage, the drift velocity due to mass loss and the diffusion velocity due to an interplay of radiative and gravitational accelerations become similar in their amount and the surface composition can be altered. The phenomenon of radiative levitation is efficient for heavy metals due to a multitude of electronic line transitions in the UV regime. With ongoing evolution to lower temperatures and higher surface gravities, another process, namely gravitational settling, takes over. Due to decreased radiative acceleration, heavy elements cannot be sustained in the atmosphere any longer, sink to the stellar interior and become undetectable in spectroscopic analysis. This process takes over at the so-called wind limit (Unglaub & Bues 2000).
Since these compact stellar remnants have surface gravities that are about 10 000 times higher compared to main sequence stars, their atmospheres are made of the lightest element that is present. H-deficient post-AGB stars originating from a VLTP will, thus, turn into DO-type WDs that show no lines of H but of He II. When they cool, they eventually become DB-type WDs with spectra dominated by He I lines. PG 1159-type stars with a remaining fraction of H, regardless whether it is detectable or not, will evolve into H dominated DA WDs possibly via the transition state of a DAO-type WD that is H dominated but also shows lines of He II (Unglaub & Bues 2000).

1.3 Mass transfer

The fraction of stars, that come with a companion is high. For Solar like stars within 67 pc, it is about 50% (Tokovinin 2014). Depending on their separation, the stars will interact during their evolution. Binary interaction is in fact a mechanism, that explains several astrophysical phenomena. Just recently, the merger of two neutron stars was confirmed to explain short γ-ray bursts (Abbott et al. 2017). These so-called kilonova events are found to be the main site to form heavy elements in the r-process (Chornock et al. 2017). Binary systems with at least one WD are the progenitor systems for Type Ia supernovae, a main production site for IGEs and standard candles to measure distances in the Universe (Leibundgut 2000). Peculiar types of stars like O(He) stars are found to be the result of a binary WD merger (Reindl et al. 2014). Binaries are necessary to form systems like cataclysmic variables and super soft X-ray sources that can experience nova eruptions (Knigge 2011). Finally, interacting binaries also explain the formation of chemically peculiar stars like barium (Ba) stars (Sect. 1.4).
All these phenomena arise, when mass and angular momentum are transferred between the components. There are two main processes of mass transfer. Either one star looses mass via stellar wind or material can become gravitationally unbound from the star, when it expands. The latter can be explained with the Roche model (Kopal 1959). In a system of two point masses, the gravitational equipotential line around the masses that touches in the Lagrangian point L_1 on the connecting line of the two masses, defines the Roche lobes around the stars, the maximum region within which the material is gravitationally bound to one of the components (Fig. 1.4). If both stars are located well inside their Roche lobes, the system is called detached. When a star expands in its evolution, it can eventually fill its Roche lobe and transfer mass to the companion in a process called Roche-lobe overflow (RLOF). Such

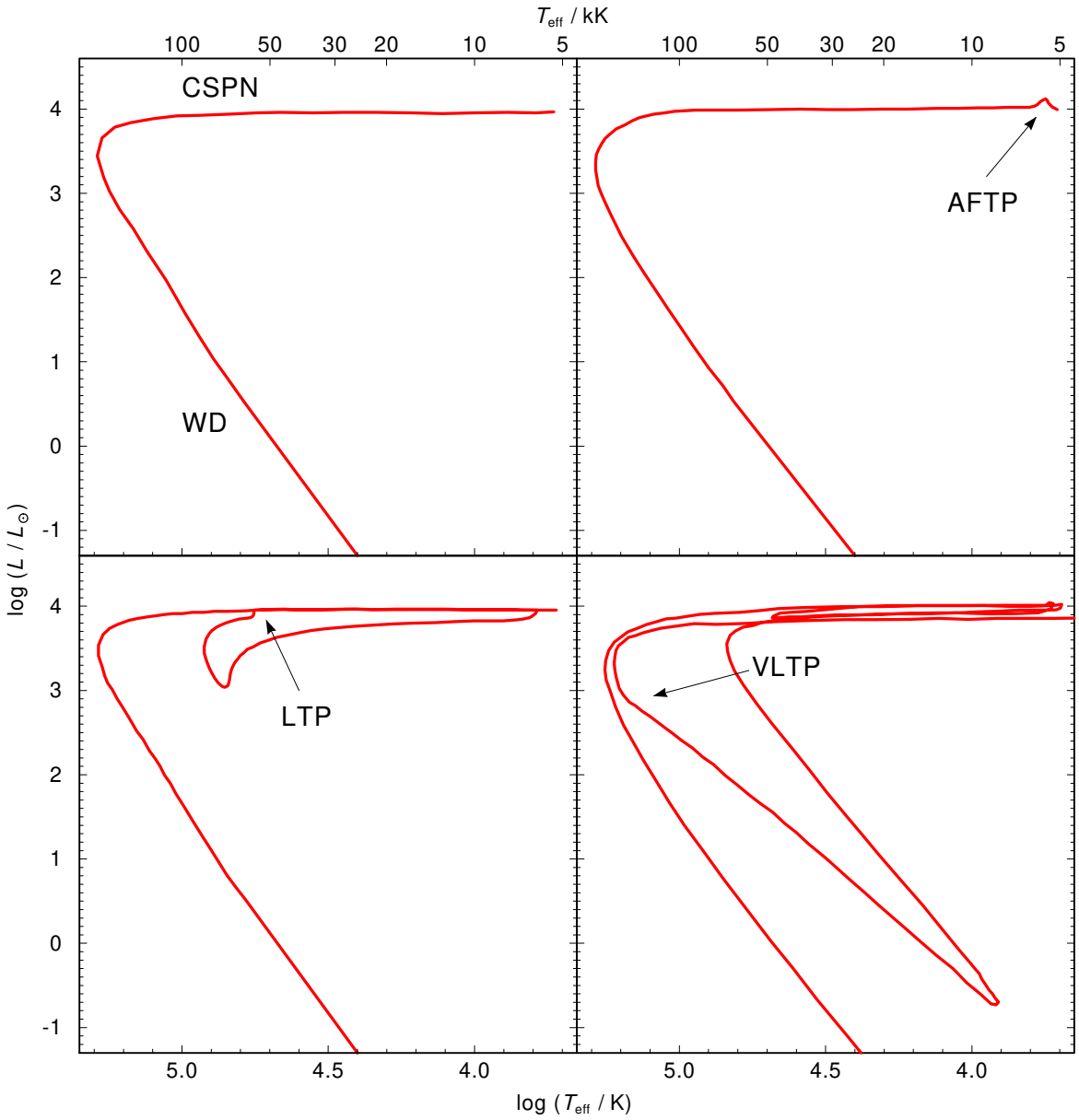

Fig. 1.3: Evolutionary tracks for stars with a final mass of $0.6\,M_\odot$ for different scenarios of post-AGB evolution. Top left: no FTP, top right: AFTP, bottom left: LTP, bottom right: VLTP. The onset of the FTP is indicated with arrows. The tracks for no FTP, AFTP, and LTP are taken from Herwig (2001), the one for VLTP from Althaus et al. (2009).

systems are called semi detached. The time scale for RLOF depends on the mass ratio and separation of the binary as well as the reaction of the donor star on the mass loss (Eggleton 2006). In general, the Roche-lobe radius and the separation decrease, when the donor is more massive than the accretor. For the opposite mass ratio, the separation and Roche-lobe radius increase. Furthermore, stars with radiative layers shrink when losing mass, while stars

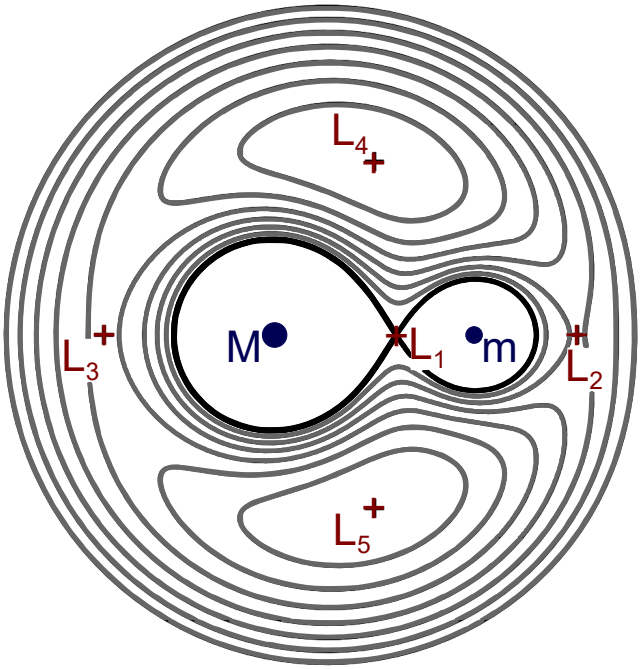

Fig. 1.4: Gravitational equipotential lines (gray) including the Roche lobes (black) in a binary system with the mass ratio $M/m = 3$. The locations of the Lagrangian points are indicated. Figure from `https://commons.wikimedia.org/wiki/File:Roche_potential_contours_q\%3D3_-_equally_spaced.svg` and modified.

with outer convection zones tend to expand (Eggleton 2006). Thus, this can lead to runaway mass loss. Due to the mass transferred, the accretor gets out of equilibrium and may also expand and fill its Roche lobe forming a contact binary (Kippenhahn & Meyer-Hofmeister 1977). This can result in a short common-envelope (CE) phase on the timescale of days, in which the separation decreases significantly due to friction (Taam 1994). This mass-transfer mechanism is not conservative, because most CE material is ejected from the system instead of being accreted.

The wind accretion acts at larger separations and is important for systems in which one component experiences significant mass loss via stellar wind. One example are AGB stars, since they loose a large fraction of their mass before becoming a WD. Mass transfer via wind is, compared to CE evolution, more effective, i.e., the accretion rate of the companion makes up a significant fraction ($2 - 40\,\%$) of the mass loss rate of the AGB star (Chen et al. 2017). If the separation is small, it may occur, that the wind acceleration region is close to the Roche-lobe radius, so that the ejected material fills the Roche lobe and is transferred to the companion through the Lagrangian point L_1 (e.g., Han et al. 1995; Nagae et al. 2004; Mohamed & Podsiadlowski 2007; Abate et al. 2013). This mechanism is known as wind-RLOF. For larger separations, the companion accretes wind material via canonical Bondi-Hoyle (Bondi & Hoyle 1944) accretion. Simulations show, that the percentage of the

accretion rate to the mass-loss rate is much higher for wind-RLOF compared to Bondi-Hoyle accretion (Chen et al. 2017).

1.4 Abell 35-like objects and barium CSPNe

As explained above, a significant fraction of all stars is not single but has at least one companion. This should be true also for evolved stars. Of about 60 confirmed binary CSPNe (Jones & Boffin 2017), only a handfull is known to host a red-giant companion that is enriched in s-process nucleosynthesis products, namely Abell 35, LoTr 5, WeBo 1, Hen 2−39, and Abell 70 (Thevenin & Jasniewicz 1997; Bond et al. 2003; Miszalski et al. 2012, 2013; Tyndall et al. 2013; Aller et al. 2018). The s-process enrichment is determined by a high Ba abundances and, thus, these binary systems are known as Ba CSPNe.
One object of this class, Abell 35, is also the prototype of another subclass, of binary CSPNe with a rapidly rotating late-type subgiant or giant (Bond et al. 1993). The initial group of Abell 35-like objects comprised also LoTr 1 and LoTr 5 besides the prototype. However, LoTr 1 does not show any sign of s-process element enrichment and, thus, not all Abell 35-like CSPNe necessarily also need to be Ba CSPNe.
Ba CSPNe are considered to be precursors of Ba stars, a peculiar class of unevolved stars, i.e., before the AGB phase, that show an enhancement of s-process elements in their atmospheres. They were first discovered by Bidelman & Keenan (1951) and they are believed to form via mass transfer from a companion during the AGB phase. Processed material is mixed to the surface by TDU and can then be transferred via mechanisms like (wind-)RLOF (Sect. 1.3). Based on that, every Ba star should come in a binary with a post-AGB companion. For Ba CSPNe, this is true and clear, since it needs a very hot source to ionize the nebula with its UV radiation and the temperature of the Ba star itself is too low. At the same time, the hot source is very compact so that the (sub-)giant companion can dominate the flux at optical wavelengths. Also the larger group of Ba stars supports the canonical formation channel via mass transfer, since all known Ba stars are found to have a WD companion (McClure et al. 1980; McClure 1983; Jorissen & Mayor 1988; McClure & Woodsworth 1990; Jorissen et al. 1998).

1.5 Stellar atmosphere modeling

All source of information we have to analyze stars and to derive their properties is the light they emit, their electromagnetic spectrum. An observed stellar spectrum stems from the photosphere or atmosphere, where photons are scattered, absorbed and re-emitted. Fundamental parameters like its effective temperature, its surface gravity, its radial and rotational velocity, and the chemical composition of its photosphere can directly be derived from the stellar spectrum. Using these parameters, also the mass, radius, and distance can be determined in a secondary step. To perform these analyses, it is necessary to compare the observed to a synthetic spectrum.

1.5.1 Theory of radiation transfer and atmosphere modeling

The input for the spectrum calculation is an atmosphere model describing the temperature and density stratification. To calculate static stellar atmosphere models, it is necessary to solve the radiation-transfer equation together with the hydrostatic, radiative, and statistical equilibrium. A detailed description of the physics of radiation transport and the theory of stellar atmosphere modeling is given by Mihalas (1978) and Hubeny & Mihalas (2014).
The radiation-transfer equation describes how the specific intensity I_ν changes when traveling through an element of the atmosphere of length ds (Fig. 1.5). The amount dI_ν removed from the radiation field is proportional to the intensity I_ν itself and the length ds

$$dI_\nu = -\kappa(\nu) I_\nu ds \quad . \tag{1.1}$$

The proportional constant $\kappa(\nu)$ is the frequency dependent absorption coefficient or opacity. It is the sum of the products of the atomic cross sections and the number densities of all levels. For a level l of element i, the absorption coefficient is given by

$$\kappa_{i,l}(\nu) = \sum_{u>l} \sigma_{i,lu}(\nu) \cdot n_{i,l}$$

with the cross sections σ_{lu} for all transitions to upper levels u, also including the ionization, i.e., the bound-free cross section. The total absorption coefficient is the given by

$$\kappa(\nu) = \sum_{i}^{\#\text{elements}} \sum_{l}^{\#\text{levels}} \kappa_{i,l}(\nu) \quad .$$

In addition, there are free-free and electron scattering opacities. The unit of the opacity is cm^{-1} and, thus, the inverse of the absorption coefficient is a measure for the mean free path of a photon of frequency ν. The change dI_ν introduced by emission along the path ds is just proportional to the length ds

$$dI_\nu = \eta_\nu ds \tag{1.2}$$

with the emissivity η_ν. In total, the radiation-transfer equation is given by the sum of absorption (1.1) and emission (1.2)

$$dI_\nu = -\kappa(\nu) I_\nu ds + \eta_\nu ds = (\eta_\nu - \kappa(\nu) I_\nu)\, ds \quad . \tag{1.3}$$

Assuming radiative equilibrium means that all energy transport happens via radiation while convection and heat conduction are neglected and that the amount of absorbed and emitted energy are in equilibrium at every depth. Furthermore, no energy is lost or produced in the atmosphere. When introducing the local source function $S_\nu = \eta_\nu / \kappa(\nu)$, the radiative equilibrium can be written as

$$\int_0^\infty (\kappa(\nu) I_\nu - \eta_\nu)\, d\nu = \int_0^\infty \kappa(\nu)\, (I_\nu - S_\nu)\, d\nu = 0 \quad .$$

Hydrostatic equilibrium means, that only forces due to a pressure gradient as well as gravitational forces are taken into account. In spherical symmetry, this is given by

$$\frac{dP}{dr} = g\rho(r)$$

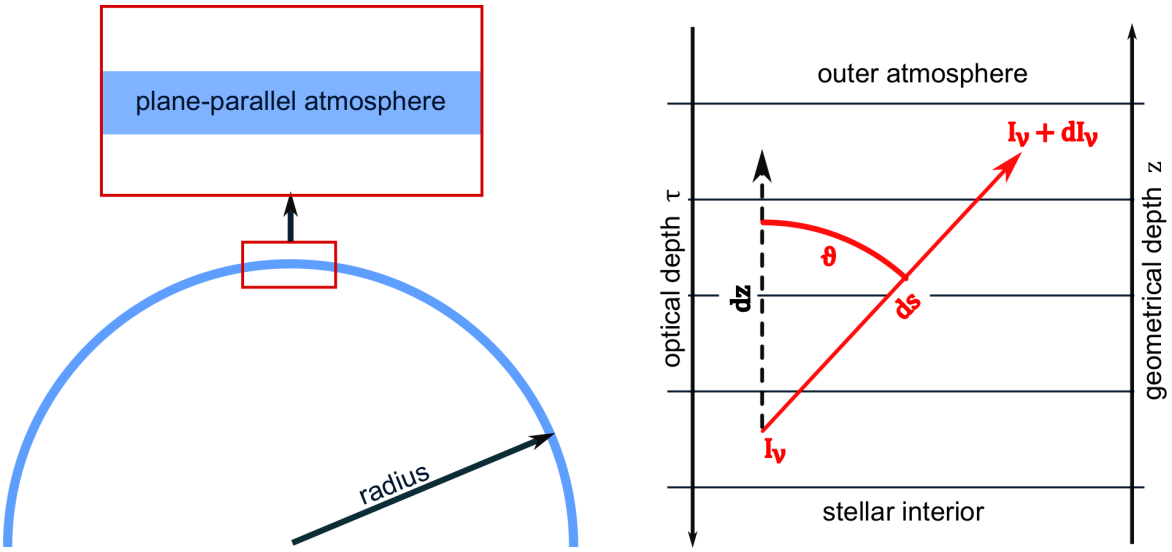

Fig. 1.5: Left: Schematic sketch to illustrate the thin stellar atmosphere compared to the stellar radius. Right: Specific intensity in plane-parallel geometry.

with the local gravity g and the density $\rho(r)$. Unter this assumption, dynamical processes due to stellar wind, pulsations or magnetic fields are neglected.
Statistical equilibrium means, that the population numbers n_i of every electron energy level i are constant over time $dn_i/dt = 0$. For solving the equations, some further assumptions can be made. One is chemical homogeneity such that the elemental composition is the same in every depth of the atmosphere instead of assuming a vertically stratified composition. With the assumption of spherical symmetry, the problem is reduced to one dimension, since the properties only depend on the radial depth coordinate. Unless for giants, the stellar atmosphere is a thin layer compared to the stellar radius. Thus, it is justified to neglect the spherical shape and just assume a plane-parallel geometry (Fig. 1.5). The radiation-transfer equation (1.3) can be transformed using $dz = \cos\vartheta\, ds$ and the substitution $\cos\vartheta = \mu$

$$\mu \frac{dI_\nu}{dz} = (\eta_\nu - \kappa(\nu) I_\nu) \quad , \quad \mu \in (-1, 1] \tag{1.4}$$

The geometrical depth z can be replaced by the optical depth

$$d\tau(\nu) = -\kappa(\nu) dz \quad \Leftrightarrow \quad \tau(\nu, z) = \int_{z'=0}^{z} \kappa(\nu) dz'$$

A difference of $\Delta\tau(\nu) = 1$ corresponds to the length of the photon mean free path. Using $\tau(\nu)$, (1.4) transforms to

$$\mu \frac{dI_\nu}{d\tau} = \frac{1}{\kappa(\nu)} (\eta_\nu - \kappa(\nu) I_\nu) = S_\nu - I_\nu \quad . \tag{1.5}$$

In general, due to energy loss by radiation into the Universe, a stellar atmosphere is not in the state of thermodynamic equilibrium (TE). For stars with high gravity and low temperature,

the photon mean free path is short. For those objects, collisions are the dominating process driving electronic transitions. In this case, it is valid to assume a local thermodynamic equilibrium (LTE) for every depth of the atmosphere, so that the velocity distribution is Maxwellian and the local source function is given by the Planck function for the local equilibrium temperature $S_\nu = B_\nu(T)$. In LTE, the computation of occupation numbers simplifies and is only depending on the local temperature T and electron density n_e. The ratio of the occupation numbers n_{up} and n_{low} of two levels of the same ion is given by the Boltzmann equation (Boltzmann 1866)

$$\frac{n_{\mathrm{up}}}{n_{\mathrm{low}}} = \frac{g_{\mathrm{up}}}{g_{\mathrm{low}}} \exp\left(-\frac{E_{\mathrm{up}} - E_{\mathrm{low}}}{k_B T}\right)$$

with the statistical weights g and energies E of the levels and the Boltzmann constant k_B. The ratio of occupation numbers of levels within neighboring ionization stages and, thus, the whole local ionization equilibrium can be determined using the Saha equation (Saha 1921)

$$\frac{n_{\mathrm{up}}}{n_{\mathrm{low}}} = \frac{2}{n_e}\left(\frac{2\pi m_e k_B T}{h^2}\right)^{3/2} \frac{g_{\mathrm{up}}}{g_{\mathrm{low}}} \exp\left(-\frac{E_{\mathrm{up}} - E_{\mathrm{low}}}{k_B T}\right)$$

with the electron mass m_e and the Planck constant h.
The simplification to LTE is not valid for very hot stars, i.e., of spectral type A and earlier. Here radiation driven transitions are important and the photon field is not in equilibrium with a local temperature but stems from different layers and depths of the atmosphere. In this non-local thermodynamic equilibrium (NLTE) case, the occupation numbers also depend on the radiation field while this itself depends on the occupation numbers which results in a coupled, non linear radiation-transfer equation. The regimes, where LTE is valid and where NLTE is strongly needed are illustrated by Rauch (2012). The occupation number n_i of level i is determined by populating and depopulating rates for which holds in statistical equilibrium ($dn_i/dt = 0$)

$$\sum_{j \neq i} n_j P_{ji} = n_i \sum_{j \neq i} P_{ij}$$

with the rate coefficients P_{ij}. These consist of radiative terms R_{ij} as well as of collisional terms C_{ij}. The first are of the form

$$R_{ij} = 4\pi \int_0^\infty \frac{\sigma_{ij}(\nu)}{h\nu} J_\nu d\nu$$

with the mean intensity

$$J_\nu = \frac{1}{4\pi} \int_{4\pi} I_\nu d\omega$$

and the transition cross section $\sigma_{ij}(\nu)$ that, for bound-bound transitions, depends on the oscillator strength. The collisional terms C_{ij} are, in general, of the form $C_{ij} = n_e q_{ij}(T)$ with $q_{ij}(T) \sim T^{-1/2}$. Thus, collisional and radiative rates depend differently on the temperature. While the radiative rates ($R_{ij} \sim T^k$ with $k > 1$) increase with temperature, the collisional rates decrease ($C_{ij} \sim \sqrt{T}^{-1}$).

1.5.2 Numerical implementation in the ATLAS code

The ATLAS stellar atmosphere code was first presented by Kurucz (1970). It is written in FORTRAN and calculates chemically homogeneous LTE atmosphere models in hydrostatic equilibrium (Nesvacil et al. 2003). The standard code assumes plane-parallel geometry though also a version in spherical geometry exists (Lester & Neilson 2008). The code treats convection based on the mixing length theory (MLT, Böhm-Vitense 1958). The mixing length is the distance that a parcel of gas can travel upwards before desintegrating. It is the product of the pressure-scale height and a mixing parameter. The latest versions of the code, ATLAS9 and ALTAS12 differ in the handling of opacity. While ATLAS9 uses the method of opacity-distribution functions (ODFs), ATLAS12 employs the opacity-sampling (OS) method (Castelli 2005). Both methods are described by Carbon (1984). The treatment of the frequency dependent opacity in the atmosphere calculation is a crucial point because several integrals over all frequencies need to be calculated. In the OS method, a sufficiently large number of frequency points ν_i is selected for which the absorption coefficient $\kappa(\nu_i)$ is determined by the sum of all line, ionization and scattering opacities. Thus, ATLAS12 is more flexible and can be used to calculate models for any input abundances and microturbulent velocity. While ATLAS9 models rely on pre-calculated ODFs for given abundances and microturbulent velocities, they are less flexible but offer the advantage that the model calculation itself is faster by orders of magnitude once the ODFs are available. For the ODF method, the whole frequency range is divided into subsections over which the source function, in the case of LTE the Planck function, does not vary significantly, so that the frequency integral over radiation dependent properties can be assumed to be independent on the frequency order (Kurucz 2014). Thus, the absorption coefficient can be sorted with increasing opacity over the interval. This opacity distribution function can then be approximated at a certain number of points (the standard is $10 - 12$) for which the radiation field is evaluated. Compared to the OS method, the radiation-transfer equation is solved for about a factor of 1000 less points. The final model is determined in an iterative process (Kurucz 1970). A guessed temperature structure is taken as start model for which pressure, occupation numbers, and opacity are evaluated. With these, the radiation field and total flux are determined. The emergent flux does, in general, not fulfill the assumption of constant flux throughout the atmosphere, so that the temperature structure is corrected and the scheme is repeated until the flux is constant and the temperature correction is sufficiently small.

1.5.3 Numerical implementation in the TMAP code

The Tübingen Model Atmosphere Package (TMAP) is a FORTRAN code for the computation of static, chemically homogeneous NLTE model atmospheres in plane-parallel geometry. It has been developed since the 1980s (Werner 1986, 1989; Werner et al. 2003; Rauch & Deetjen 2003). The program solves the radiation-transfer equation together with the constraint equations for statistical, hydrostatic, and radiative equilibrium for a set of depth points and frequency points. For this program, the frequency grid is chosen to sample the cross sections for the transitions of all ions that are taken into account. The system is coupled over all frequency points due to the statistical and radiative equilibrium constraints and over all depths due to the radiation-transfer equation. The TMAP code is based on the approach of introducing an approximate lambda operator Λ^*_ν so that the radiation-transfer equation (1.5)

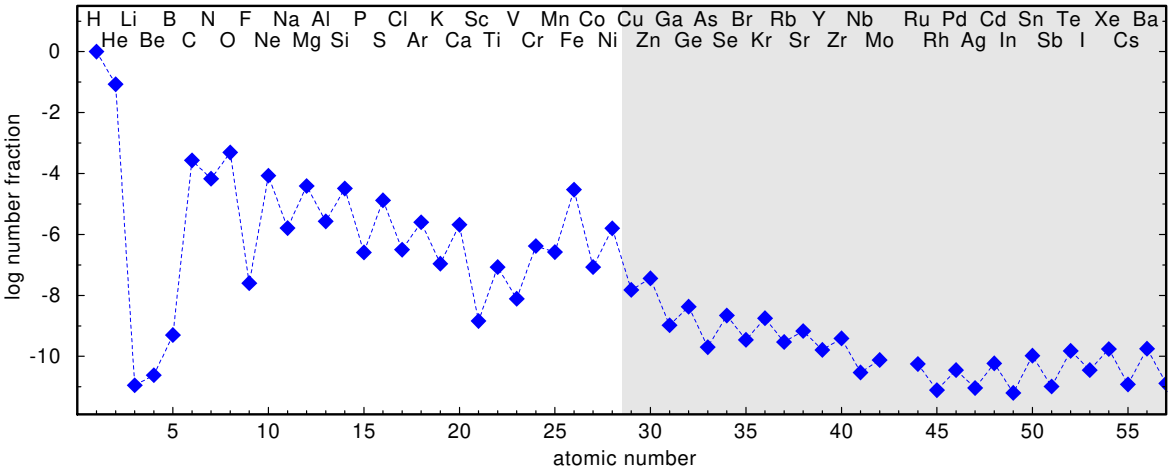

Fig. 1.6: Solar abundances for H to Ba by number relative to H ($\log(n(\mathrm{X})/n(\mathrm{H}))$, Asplund et al. 2009; Scott et al. 2015a,b; Grevesse et al. 2015). The region of TIEs is highlighted with gray background.

can be written as

$$J_\nu^{(i)} = \Lambda_\nu^* S_\nu^{(i)} + (\Lambda_\nu - \Lambda_\nu^*) S_\nu^{(i-1)}$$

for the iteration step i with the exact lambda operator Λ_ν. The second term can be seen as correction $\Delta J_\nu^{(i)}$ that needs to be added when applying the approximate lambda operator instead of the exact one to the source function. This iteration scheme is continued until the source function $S_\nu^{(i)}$ and $S_\nu^{(i-1)}$ agree within the chosen accuracy.

1.6 Trans-iron elements

The cosmic abundance of elements beyond the iron group (atomic number $Z > 28$, trans-iron elements, TIEs) is relatively low. In the Sun, none of them has a number fraction (relative to H) above 5×10^{-8} (Fig. 1.6). Some of the tabulated solar abundances cannot be determined from spectroscopy but are interpolated from theoretical s-process production rates (krypton (Kr), xenon (Xe)) or derived from meteorite abundances (e.g., arsenic (As), selenium (Se), bromine (Br), cadmium (Cd), tellurium (Te), iodine (I), Asplund et al. 2009; Scott et al. 2015a,b; Grevesse et al. 2015).

First detections of neutral of singly ionized TIEs in giants and chemically peculiar stars were possible already by the mid of the last century (Bidelman & Keenan 1951; Merrill 1952; Merrill & Lowen 1953, 1954; Merrill & Greenstein 1956; Bidelman 1962). The first detection of lines of higher ionized TIEs in hot subluminous B- and O-type stars (sdB, sdO) was reported by O'Toole (2004). They employed compilations of measured energy levels and transition wavelengths for resonance lines of TIEs and their measured or calculated transition probabilities (Morton 2000, 2003). Using this database, O'Toole & Heber (2006) measured abundances for gallium (Ga), germanium (Ge), tin (Sn), and lead (Pb) in sdB and sdO stars and found an enrichment of up to a factor of 1000 compared to solar values.

The likely explanation for this is diffusion, i.e., the equilibrium of gravitational settling and radiative levitation together with mass loss (Unglaub & Bues 2001). At the same time, the first successful detection of Ge in a hot H-rich (DA-type) WD (Vennes et al. 2005) with solar abundance was reported and Chayer et al. (2005) detected Ge, As, Se, Sn, Te, and I in three H-deficient, He-rich (DO-type) WDs. The enrichment of $3 - 1000$ times solar in the DO-type WDs, was discussed to be either due to effective diffusion or, on the other hand the signature of AGB nucleosynthesis. These abundance measurements were based on either pure LTE calculations or NLTE atmosphere models with a subsequent LTE line formation calculation for the TIEs. The first detection of Kr and Xe in a WD, namely the hot DO-type WD RE 0503−289, was reported by Werner et al. (2012). For the first time, they included TIEs in a full NLTE calculation and measured the abundances based on these models. With its temperature and surface gravity ($T_{\rm eff} = 70$ kK, $\log(\,g\,/\,{\rm cm/s^2}\,) = 7.5$, Rauch et al. 2016b), it is clearly in the regime where NLTE atmosphere models are strongly recommended (Sect. 1.5.1). The difficulty is, that for the calculation of reliable NLTE occupation numbers the precise knowledge of not only the energy levels but also of the transition probabilities for all lines are needed (Sect. 1.5.1). Employing quantum mechanically calculated transition probabilities, Rauch et al. (2012, 2013, 2014a,b, 2015b,a, 2016a,b, 2017a,b, 2020) could perform NLTE abundance measurements for 17 TIEs, namely copper (Cu), zinc (Zn), Ga, Ge, Se, As, Br, Kr, strontium (Sr), zirconium (Zr), molybdenum (Mo), indium (In), Sn, Te, I, Xe, and Ba in RE 0503−289. The oscillator strengths were calculated using a relativistic Hartree-Fock approach (Cowan 1981, see work cited above for details about the calculations for the different elements and their ionization stages) and are available via the Tübingen Oscillator Strength Service (TOSS). All TIEs in RE 0503−289 show supersolar abundances up to a factor of 100 000. Rauch et al. (2016a) found, that it is radiative levitation that strongly enhances these elements in hot DO-type WDs.

1.6.1 Handling of trans-iron elements in the TMAP code

As explained above, it is necessary to have as complete as possible atomic data for the NLTE abundance analysis. On the other hand, although modern NLTE codes can handle several hundreds and even more than 2000 NLTE levels, this is not enough to include classical model atoms for IGEs or TIEs due to the complexity of their atomic structure and the large number of energy levels and transitions (up to millions per ionization stage). Furthermore, a large number of levels and transitions slows down the computation. To include IGEs and TIEs in the model calculation, TMAP uses a statistical method. The large number of atomic energy levels is combined into superlevels (Rauch & Deetjen 2003). The individual transitions are merged into superlines by a weighted sum over all individual cross sections.

2 Work in context

2.1 Spectral analysis of the barium central star of the planetary nebula Hen 2−39

The CSPN Hen 2−39 belongs to the class of Ba CSPNe (Sect. 1.4) since Miszalski et al. (2013) found the subgiant companion to be enriched with Ba. The wavelength range and resolution of the spectra did not allow them to investigate abundances of further s-process elements. The aim of this work was to analyze recent optical spectra of the K-type companion obtained with the Ultraviolet and Visual Echelle Spectrograph (UVES) at the Very Large Telescope (VLT) to detect signatures of further s-process key elements and determine their abundances. While the abundance determination for TIEs in hot stars is hampered by a lack of atomic data for levels and transitions that need to be included in NLTE atmosphere calculations, the atomic data for resonance lines of low ionization stages has already been used since the mid of the last century for TIE line identifications in cool stars (Sect. 1.6). When assuming that the TIEs are present in the companion's atmosphere due to transfer of processed material from the AGB star, this can be used to constrain the yields of the s-process on the AGB, instead of a direct measurement of TIE abundances in the hot CSPN. The most promising element for this analysis is Tc, the lightest element with no stable isotope. The detection of Tc in the atmosphere of a red giant (Merrill 1952) was direct evidence that it is synthesized in these stars and that TDU happens and brings it to the stellar surface. The half-life of ^{99}Tc of 210 000 yrs is shorter than the stellar lifetime of red giants. Thus, Tc that is found in these stars needs to be synthesized in them and cannot be due to initial metallicity. The detection of Tc in the companion would be direct proof for prior mass transfer since the companion cannot have initial Tc or synthesize it. The TIE abundances in the companion of the hot central star (CS) can furthermore be utilized to constrain another important but still poorly understood process, namely mass transfer (Sect. 1.3). By comparing the amount of TIEs in the envelope of the companion with the predictions for the amount of ejected mass of TIEs from evolution calculations, it becomes possible to evaluate whether the enrichment can really be due to transferred, ejected AGB material. If a AGB star ejects a sufficient amount of TIE material to pollute the companion and one assumes that no other process alters the abundances of the companion, it allows to constrain how much of the ejected mass needs to be accreted. This is, together with the period and separation, a characteristic parameter to identify different mass-transfer mechanisms like Bondi-Hoyle accretion, RLOF, or CE phase.

2.2 Spectral analysis of the hybrid PG 1159-type central stars of the planetary nebulae Abell 43 and NGC 7094

WD 1751+106 and WD 2134+125 (McCook & Sion 1999), the CSs of Abell 43 and NGC 7094, belong to the class of hybrid PG 1159 stars. Since they are H-deficient but still show detectable amounts of H in their atmospheres (Ziegler et al. 2012), they are believed to stem from an AFTP (Sect. 1.2). Not only the nebulae appear similar in shape, with their spherical filamentary structure they belong to the so-called Galactic soccer balls (Rauch 1999), but also the CSs are found to be spectroscopic twins. They have the same effective temperature and gravity and also the abundances, not only for H, are similar. Both have already been subject of several spectral analyses (Dreizler et al. 1995; Napiwotzki 1999). The subsolar Fe abundances (Miksa et al. 2002) were understood as probable signature of s-process nucleosynthesis, indicating that the Fe content has been reduced and synthesized to heavier elements. The availability of newly calculated oscillator strengths for several TIEs offers the possibility to check this hypothesis by determining s-process abundances. This is one of several aims of this work. The mentioned atomic data had been used for the successful abundances analysis of the hot DO-type WD RE 0503−289 (Sect. 1.6). In contrast to the diffusion shaped abundance pattern of RE 0503−289, CSPNe are located before the wind limit (Sect. 1.1, Unglaub & Bues 2000) and, thus, should have a chemically homogeneous wind and reflect the abundance yields of AGB nucleosynthesis. A further aim of this work was to determine the abundances for s-process elements in the two stars, to strengthen the explanation for the extreme enrichment of DO WDs through diffusion by lower abundances in CSPNe. The s-process abundances in CSPNe should also offer the possibility to compare to the predictions from numerical nucleosynthesis calculations and, thus, to constrain parameters for still poorly understood aspects like the ^{13}C-pocket sizes, mass loss, convective mixing, reaction rates, and neutron density (Karakas & Lattanzio 2014a). The evolution of hybrid PG 1159 stars had not been subject of a detailed simulation using stellar evolutionary codes. Previous works needed to employ either evolutionary tracks for H- or He-dominant post-AGB stars to determine masses. One goal of this work is to calculate stellar evolution tracks to derive a mass and compare numerical evolution timescales to those obtained from nebular properties. This allows to derive a stellar mass and, based on this, a spectroscopic distance. The precise parallax distances of the Gaia satellite provide an independent measurement to validate the spectroscopic method.

2.3 First discovery of trans-iron elements in a DAO-type white dwarf

BD−22°3467, the CS of the ionized nebula Abell 35, had already been subject of a detailed spectral analysis of Ziegler et al. (2012). They determined $T_{\rm eff} = 80\,$kK and $\log g = 7.2$ and also abundances for elements up to nickel (Ni) but could not disentangle the mystery of its evolution history. Abell 35 was discovered and classified by Abell (1955, 1966). The CS was found to be a binary with a visible nucleus classified as G8 III−IV (Jacoby 1981). The hot CS is not visible in the optical wavelength range but the ionized nebula is evidence, that

a very hot source needs to exist in its center. Grewing & Bianchi (1988) identified it as DAO-type WD, that dominates the flux in the UV range ($\lambda < 2800\,\text{Å}$). In a first analysis of both components, Herald & Bianchi (2002) found $T_{\text{eff}} = 80\,\text{kK}$ and $\log g = 7.7$ for the hot and $T_{\text{eff}} = 5\,\text{kK}$ and $\log g = 3.5$ for the cool star. Frew & Parker (2010) analyzed the nebula and found that Abell 35 only mimics a PN and they classified the nebula as "bow shock nebula in a photoionized Strömgren sphere". This does not necessarily need to be material ejected during AGB and post-AGB evolution. With this result, the first doubts about the post-AGB nature of the object came up. The fast proper motion (Gaia Collaboration et al. 2018) strengthens this even more, because the fast star should have left its ejected nebula within a shorter time than the post-AGB age of hot WDs. Eventually, the low surface gravity of Ziegler et al. (2012) corresponds to a very low mass that would allow a direct evolution from the extended horizontal branch (EHB) to the WD cooling track without prior AGB evolution. One result, that clearly contradicts the theory that BD−22°3467 is a post-EHB object is the fact, that the companion was found to be enriched with Ba and, therefore, Abell 35 belongs to the small group of PNe hosting a binary with a s-process polluted companion (Sect. 1.4). This pollution cannot easily be explained if not via mass transfer from an AGB star. The aim of this work was to reinspect the UV spectrum of BD−22°3467, to employ the recent atomic data for TIEs (Sect. 1.6) to determine their abundances in BD−22°3467, and to derive constraints for the evolution history.

3 Publications

In this chapter, all publications that I lead and to which I contributed are presented. Those, marked with *, are reproduced within this work with permission from Astronomy & Astrophysics, ESO and Monthly Notices from the Royal Astronomical Society, RAS. For those, where I am not the leading author, my contribution is summarized.

3.1 Refereed journals

- **Rauch et al. (2017a)**
  Rauch, T., Gamrath, S., Quinet, P., Löbling, L., Hoyer, D., Werner, K., Kruk, J. W., & Demleitner, M. (2017) "Stellar laboratories VIII. New Zr IV−VII, Xe IV−V, and Xe VII oscillator strengths and the Al, Zr, and Xe abundances in the hot white dwarfs G191−B2B and RE 0503−289", A&A, 599, A142,
  Contribution: Compilation of atomic data for aluminum to construct a new model atom to be used with the TMAP code

- **Löbling (2018)**
  "Sliding along the Eddington Limit–Heavy-Weight Central Stars of Planetary Nebulae", Galaxies, 6, 65

- **Bischoff-Kim et al. (2019)**
  Bischoff-Kim, A., Provencal, J. L., Bradley, P. A., Montgomery, M. H., Shipman, H. L., Harrold, S. T., Howard, B., Strickland, W., Chandler, D., Campbell, D., Arredondo, A., Linn, R., Russell, D. P., Doyle, D., Brickhouse, A., Peters, D., Kim, S.-L., Jiang, X. J., Mao, Y.-N., Kusakin, A. V., Sergeev, A. V., Andreev, M., Velichko, S., Janulis, R., Pakstiene, E., Aliçavuş, F., Horoz, N., Zola, S., Ogłoza, W., Koziel-Wierzbowska, D., Kundera, T., Jableka, D., Debski, B., Baran, A., Meingast, S., Nagel, T., Löbling, L., Heinitz, C., Hoyer, D., Bognár, Z., Castanheira, B. G. & Erdem, A. (2019) "GD 358: Three Decades of Observations for the In-depth Asteroseismology of a DBV Star", ApJ, 871, 13
  Contribution: Five nights of observations with the 80 cm telescope of the Institute for Astronomy and Astrophysics, Tübingen

- **Löbling et al. (2019a)***
  Löbling, L., Boffin, H. M. J., & Jones, D. (2019) "Spectral analysis of the barium central star of the planetary nebula Hen 2−39", A&A, 624, A1

- **Löbling et al. (2019c)***
  Löbling, L., Rauch, T., Miller Bertolami, M. M., Todt, H., Friederich, F., Ziegler, M., Werner, K., & Kruk, J. W. (2019) "Spectral analysis of the hybrid PG 1159-type central stars of the planetary nebulae Abell 43 and NGC 7094", MNRAS, 489, 1054

- **Löbling et al. (2019b)***
  Löbling, L., Maney, M. A., Rauch, T., Gamrath, S., Quinet, P., Werner, K., & Kruk, J. W. (2019) "First discovery of trans-iron elements in a DAO-type white dwarf (BD−22°3467)", MNRAS, 492, 528

- **Löbling (2020)**
  "NLTE Spectral analysis of the intermediate helium-rich sdB star CPD−20°1123", submitted to MNRAS

3.2 Unrefereed journals

- **Löbling (2017)**
  "The Tübingen Model-Atom Database: A Revised Aluminum Model Atom and its Application for the Spectral Analysis of White Dwarfs", ASPC, 509, 235

A&A 624, A1 (2019)
https://doi.org/10.1051/0004-6361/201834466

Astronomy & Astrophysics

Spectral analysis of the barium central star of the planetary nebula Hen 2–39⋆

L. Löbling[1,2], H. M. J. Boffin[1], and D. Jones[3,4]

[1] European Southern Observatory, Karl-Schwarzschild-Str. 2, 85748 Garching bei München, Germany
[2] Institute for Astronomy and Astrophysics, Kepler Center for Astro and Particle Physics, Eberhard Karls University, Sand 1, 72076 Tübingen, Germany
e-mail: loebling@astro.uni-tuebingen.de
[3] Instituto de Astrofísica de Canarias, 38205 La Laguna, Tenerife, Spain
[4] Departamento de Astrofísica, Universidad de La Laguna, 38206 La Laguna, Tenerife, Spain

Received 19 October 2018 / Accepted 4 February 2019

ABSTRACT

Context. Barium stars are peculiar red giants characterized by an overabundance of the elements synthesized in the slow neutron-capture nucleosynthesis (s-process elements) along with an enrichment in carbon. These stars are discovered in binaries with white dwarf companions. The more recently formed of these stars are still surrounded by a planetary nebula.
Aims. Precise abundance determinations of the various s-process elements, of further key elements that act as indicators for effectiveness of nucleosynthesis on the asymptotic giant branch and, especially, of the lightest, short-lived radionuclide technetium will establish constraints for the formation of s-process elements in asymptotic giant branch stars as well as mass transfer through, for example, stellar wind, Roche-lobe overflow, and common-envelope evolution.
Methods. We performed a detailed spectral analysis of the K-type subgiant central star of the planetary nebula Hen 2−39 based on high-resolution optical spectra obtained with the Ultraviolet and Visual Echelle Spectrograph at the Very Large Telescope using local thermodynamic equilibrium model atmospheres.
Results. We confirm the effective temperature of $T_{\rm eff}$ = (4350 ± 150) K for the central star of the planetary nebula Hen 2−39. It has a photospheric carbon enrichment of [C/H] = 0.36 ± 0.08 and a barium overabundance of [Ba/Fe] = 1.8 ± 0.5. We find a deficiency for most of the iron-group elements (calcium to iron) and establish an upper abundance limit for technetium ($\log \epsilon_{\rm Tc} < 2.5$).
Conclusions. The quality of the available optical spectra is not sufficient to measure abundances of all s-process elements accurately. Despite large uncertainties on the abundances as well as on the model yields, the derived abundances are most consistent with a progenitor mass in the range 1.75–3.00 $M_\odot$ and a metallicity of [Fe/H] = −0.3 ± 1.0. This result leads to the conclusion that the formation of such systems requires a relatively large mass transfer that is most easily obtained via wind-Roche lobe overflow.

Key words. planetary nebulae: individual: Hen 2–39 – stars: abundances – stars: evolution – stars: AGB and post-AGB – stars: chemically peculiar – binaries: general

1. Introduction

So far, only a small number of planetary nebulae (PNe) have been identified to host a binary with a giant or subgiant component dominating the optical wavelength range and showing peculiar surface element abundances that indicate late stage stellar evolution nuclear synthesis. These stars exhibit signatures of slow neutron-capture nucleosynthesis (s-process) in their spectra and in some cases an enrichment in carbon (C).

For the object of this work, the central star (CS) of the PN Hen 2−39 (PN G283.8−04.2, Wray 16−64; Henize 1967; Acker et al. 1992; Wray 1966), Miszalski et al. (2013a) determined an overabundance for the s-process element barium (Ba) of [Ba/Fe][1] = 1.5 ± 0.25 and an enrichment of [C/H] = 0.42 ± 0.02 in a spectral analysis based on mid-resolution spectra obtained with the Southern African Telescope (SALT; Buckley et al. 2006) with the Robert Stobie Spectrograph (RSS; Burgh et al. 2003; Kobulnicky et al. 2003). These findings confirm the membership of the K-type nucleus of Hen 2−39 in the small group of Ba central stars of planetary nebulae (CSPNe) along with LoTr 5, WeBo 1, and Abell 70 (Thevenin & Jasniewicz 1997; Bond et al. 2003; Miszalski et al. 2012; Tyndall et al. 2013; Aller et al. 2018).

Ba CSPNe are prime examples of progenitors of Ba stars that were described by Bidelman & Keenan (1951). Because of their evolutionary status, namely still being on the main sequence or a red giant, these stars did not yet experience AGB nucleosynthesis and, thus, cannot have synthesized heavy elements. McClure et al. (1980) discovered the binary nature of Ba stars and proposed that mass transfer was key to explain these sources. Boffin & Jorissen (1988) performed detailed simulations of wind mass transfer to explain the pollution of the Ba star from an evolved companion with the products of asymptotic giant branch (AGB) nucleosynthesis that are dredged up to the stellar surface (Herwig 2005; Werner & Herwig 2006). More recently, other mechanisms were proposed in which the material is transferred to the still unevolved companion (Boffin 2015) via Roche-lobe overflow (RLOF; e.g. Han et al. 1995) or wind-RLOF (e.g. Nagae et al. 2004; Mohamed & Podsiadlowski 2007; Abate et al. 2013).

⋆ Based on data products from observations made with ESO Telescopes at the La Silla Paranal Observatory under program ID 093.D-0332(A).

[1] [A/B] = $\log(n_{\rm A}/n_{\rm B}) - \log(n_{\rm A,\odot}/n_{\rm B,\odot})$ with the number fractions n for element A and B.

This scenario is strongly supported by the fact that, so far, all Ba stars are found in binaries with white dwarf (WD) companions (McClure et al. 1980; McClure 1983; Jorissen & Mayor 1988; McClure & Woodsworth 1990; Jorissen et al. 1998), which is also definitely clear for the Ba CSPNe since the Ba star is not hot enough to ionize the ambient ejected material that is visible as the surrounding PN. Although the (pre-)WD companion must be there without any doubt, it can be difficult to detect against the bright companion even in the UV. Recently, more and more WD companions of Ba stars (Gray et al. 2011) and pre-WD companions of Ba CSPNe have been detected (e.g. Abell 70; Miszalski et al. 2012), which doubtlessly confirms the formation scenario. The still poorly understood mechanism of mass transfer in these systems is subject of ongoing research. The challenge is to determine their orbital parameters, such as eccentricity and period and to reproduce these with theoretical binary evolution models (Saladino et al. 2018; De Marco 2009).

These stars are expected to show orbital periods of several hundred days, which are typical values for Ba stars (Jorissen et al. 1998). However, there is the CSPN binary in the Necklace Nebula (PN G054.6−03.4; Corradi et al. 2011) standing out toward shorter periods. Miszalski et al. (2013b) found a period of 1.16 d for the post-CE system from the analysis of the C-dwarf secondary. On the other side of the period range, current analyses also indicate that there are systems with values up to several years and with larger eccentricities (Jones et al. 2017).

Ba CSPNe are ideal to study AGB nucleosynthesis. They provide a snapshot of an evolutionary stage with ideal conditions for analyzing not only the polluted cool (sub)giant star but also the ejected material of the nebula around the polluting post-AGB star (e.g. Madonna et al. 2017, 2018). The short duration of the PN phase ($\approx 10^4$ yr) guarantees that the mass transfer happened recently and that the companion has not yet had time to adjust. Also, in some cases, the polluted star is still unevolved and did not experience the first dredge-up (DU) that would affect the surface element composition including the nucleosynthesis outcomes from the polluting post-AGB star.

By comparing the results of our comprehensive spectral analysis to theoretical AGB nucleosynthesis models (Karakas & Lugaro 2016; Karakas et al. 2018), new insights into Ba stars and PNe are gained. It is worth mentioning the s-process mechanisms including atomic reaction rates, the source of neutrons and neutron exposure, internal stellar structures, and mixing processes occurring in a thermal-pulsing AGB star. This allows us to constrain the progenitor mass of the post-AGB star and the number of thermal pulses (TPs) on the AGB. Including binary evolution models (Saladino et al. 2018; De Marco 2009), these objects offer the opportunity to study the CE process and (wind-) RLOF, which are still far from being understood (Miszalski et al. 2013b; Jones & Boffin 2017), and in addition the fraction of mass transferred (Boffin & Jorissen 1988) and, following from this, the dilution factor in the Ba star itself and, thus, the mixing processes at work in (sub)giant stars (Husti et al. 2009). In particular, Ba CSPNe such as Hen 2−39 offer the possibility to detect technetium (Tc), which is the lightest element with no stable isotopes, in their atmospheres. This element was first detected by Merrill (1952) in the atmospheres of red giants, which proved that it is synthesized in evolved stars, since the half-life of ^{99}Tc of 210 000 yr[2] is much shorter than the previous giant evolutionary phase. It is thus only observed in AGB stars currently undergoing thermal pulses (TPs; Van Eck & Jorissen 1999; Lebzelter & Hron 2003) and, hence, the determination of the Tc surface abundance of the Ba CSPN indicates the mass-transfer link between the binary components in the PN and establishes a definite indicator for the existence of the third dredge-up (TDU). Assuming a typical post-AGB age of some 10^3−10^4 yr (Miller Bertolami 2016) for the primary component and taking into account that the dynamical process of mass transfer is short compared to this number (Iben & Livio 1993; Chen et al. 2017), a large fraction of the transferred Tc should still be present in the stellar atmosphere.

We describe the observations, stellar atmosphere models, and analysis techniques in Sects. 2 and 3, respectively. The spectral analysis follows in Sects. 4 and 5. The results are discussed in Sect. 6. We summarize and conclude in Sect. 7.

2. Observations

The spectral analysis of Hen 2−39 is based on spectra in the optical wavelength range obtained with the Ultraviolet and Visual Echelle Spectrograph (UVES; Dekker et al. 2000) at the Very Large Telescope (VLT) at the Paranal Observatory of the European Southern Observatory under ESO program 093.D−0332(A). The data products created from this data were retrieved from the ESO Science Archive Facility. The observation log, including the signal-to-noise ratio (S/N), of the spectra used in this paper is shown in Table A.1. All spectra were taken with a resolving power of R = 42 000−44 000.

We used the spectral analysis code ISpec (Blanco-Cuaresma et al. 2014) to determine the radial velocities for each single observation via cross-correlation with a model template spectrum created using the fundamental parameters $T_{\rm eff}$, $\log g$, C abundance, and metallicity determined by Miszalski et al. (2013a). The heliocentric corrected radial velocities for the 18 observations are given in Table 1. To improve the S/N, all observations were shifted to the rest-frame velocity and subsequently co-added. To simulate the resolution of the instrument, all synthetic spectra shown in this work were convolved with Gaussians (full width half maximum ($FWHM$) = 0.12 Å).

3. Model atmospheres, atomic data, and analysis techniques

We used the stellar synthesis code SPECTRUM[3] (Gray & Corbally 1994, version 2.76) to calculate synthetic spectra for the analysis of the observed high-resolution spectra with the ATLAS9 model atmosphere grids[4] (Kurucz 1991; Castelli & Kurucz 2003) as input. These one-dimensional models are based upon the solar abundances from Grevesse & Sauval (1998) and are calculated under the presumption of plane-parallel geometry and local thermodynamic equilibrium (LTE), which is valid for stars in this temperature and gravity regime (Hubeny et al. 2003). For the wavelength values and oscillator strengths of the lines selected in our analysis, we used the values provided within the distribution of SPECTRUM. Data for Tc I were retrieved from the Atomic Spectra Database[5] of the National Institute of Standards and Technology (NIST). For Tc II, we used the data provided by Palmeri et al. (2007). We calculated an extensive grid of synthetic spectra spanning from $T_{\rm eff}$ = 3500 to 6000 K

[2] Los Alamos National Laboratory Periodic Table http://periodic.lanl.gov

[3] http://www.appstate.edu/~grayro/spectrum/spectrum.html

[4] http://kurucz.harvard.edu/grids.html

[5] https://www.nist.gov/pml/atomic-spectra-database

Table 1. Observation time and heliocentric radial velocities for the 18 observations of the Ba CSPN of Hen 2−39.

MJD	$v_{\rm rad}$
56 750.117	44.79 ± 1.06
56 750.135	44.76 ± 1.01
56 750.154	46.61 ± 1.00
56 750.172	45.64 ± 1.09
56 751.032	46.05 ± 0.93
56 751.050	46.47 ± 0.92
56 751.070	46.34 ± 1.07
56 751.088	46.29 ± 1.03
56 751.109	45.35 ± 1.05
56 751.127	45.17 ± 1.05
56 760.108	45.43 ± 0.94
56 760.126	45.56 ± 1.06
56 762.018	45.79 ± 1.09
56 762.035	45.21 ± 1.00
56 762.053	45.64 ± 1.06
56 762.070	45.91 ± 1.08
56 762.088	45.96 ± 1.10
56 762.106	46.24 ± 1.09

($\Delta T_{\rm eff} = 250$ K between 4000 and 5000 K and $\Delta T_{\rm eff} = 500$ K otherwise) and from $\log g\,({\rm cm^{-1}\,s^{-2}}) = 0.0$ to 4.0 ($\Delta \log g = 0.5$) with a metallicity of [M/H] = −0.3 around the literature values of $T_{\rm eff} = 4250 \pm 150$ K and $\log g = 2.0 \pm 0.5$ (Miszalski et al. 2013a). For the determination of abundances, we relied on the model with $T_{\rm eff} = 4250$ K and $\log g = 2.5$ and varied the abundance of one single element over a range of at least 2.5 dex with a step of 0.5 dex. The exceptions to this are C, for which we varied the abundance in steps of 0.05 dex over a range of 0.25 dex, and N with a range of 1.5 dex and steps of 0.3 dex. Since the spectrum is crowded with absorption lines that are broadened by rotation, we could not measure equivalent widths to determine the fundamental parameters. We performed the analysis of the different parameters by selecting wavelength regions that show a strong influence of these particular species. The final values were then derived using a χ^2-method applied to the synthetic spectra grid for the selected regions.

4. Stellar parameters

4.1. Rotation

To determine $v_{\rm rot} \sin i = 38 \pm 5\,{\rm km\,s^{-1}}$, we used a fit of a synthetic spectrum calculated with the literature values given by Miszalski et al. (2013a) and convolved with rotational profiles for values from $v_{\rm rot} \sin i = 0$ to $50\,{\rm km\,s^{-1}}$ to two regions spanning from 6440 to 6515 Å and from 7030 to 7070 Å dominated by strong C_2 molecular absorption bands (Fig. 1).

4.2. Effective temperature and surface gravity

The many rotationally broadened lines in the observation also hamper the determination of equivalent widths. Thus, we used a set of diagnostic lines of Fe I, Fe II, Ti I, Ti II, Sc I, Sc II, and Mg I and performed a χ^2-fit for selected wavelength regions. The set is composed of the lines that Tabernero et al. (2018) used for a similar spectral analysis. Furthermore, we included some Fe I and Fe II lines that are used by the Brussels Automatic Code for

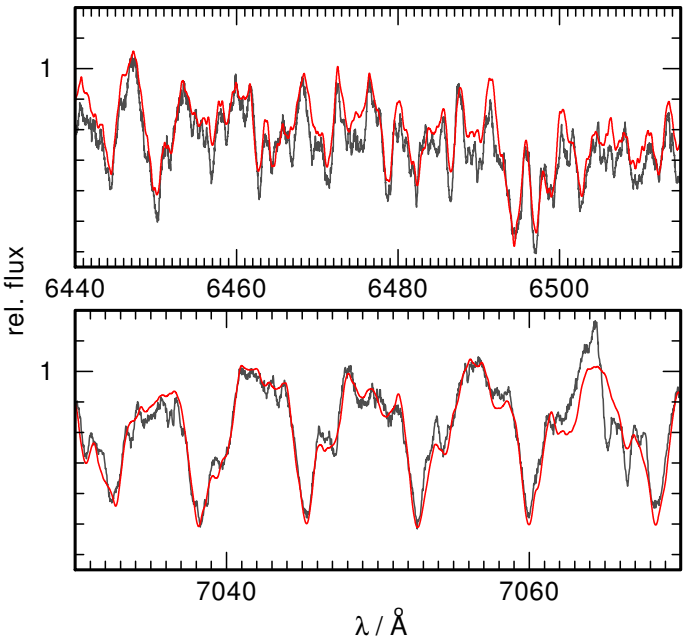

Fig. 1. Synthetic spectra (red) convolved with a rotational profile of $v_{\rm rot} = 38\,{\rm km\,s^{-1}}$ around strong C_2 and CN molecular absorption bands compared with observations (gray).

Characterizing High accuracy Spectra (BACCHUS[6]; Masseron et al. 2016). Finally, we added lines for Fe I, Fe II, Ti I, Ti II, Sc I, and Sc II for which we obtained the largest theoretical equivalent widths in the calculation of the synthetic spectra and that did not saturate. The resulting collection of wavelength regions used for the analysis and the list of diagnostic lines is shown in Table A.2. They cover a wide range of different excitation potentials and oscillator strengths. After a first determination of $T_{\rm eff}$ and $\log g$, we found a degeneracy in $\log g$ due to the fact that the strength of the computed lines in the regime around the literature values varies very little as a function of $\log g$ for a fixed value of $T_{\rm eff}$. A spectroscopic determination of $\log g$ is hampered by uncertain values for the distance and brightness (Sect. 6.3). Thus, we adopt a value of $\log g = 2.5 \pm 0.5$ that is typical for Ba giants of that type (e.g. de Castro et al. 2016). This approach seems to be reasonable because a change of $\Delta \log g = 0.5$ only marginally affects the derived abundances compared to the significant statistical errors. We derive $T_{\rm eff} = (4350 \pm 150)$ K. Figures A.1 and A.2 illustrate the spectroscopic determination of these parameters by showing the difference due to a variation of $T_{\rm eff}$ and $\log g$.

5. Element abundances

We used model atmospheres with $T_{\rm eff} = 4250$ K and $\log g = 2.5$ from the grid and performed line-profile fits for the following elements to determine their abundances. The results are given in Table 2. In our analysis, we assumed the atomic data to be correct and did not propagate uncertainties on atomic data. The continuum placement uncertainty is also assumed to be small as the continuum placement is shifted during the fitting procedure. To estimate the impact of a varied $T_{\rm eff}$ and $\log g$ on the determined abundances, we redid part of our analysis with models with varied $T_{\rm eff}$ between 4000 and 4500 K at $\log g$ varied between 2.0 and 3.0. We also varied the microturbulence

[6] http://www.astro.ulb.ac.be/pmwiki/Spectro/Bacchus

Table 2. Element abundances determined for Hen 2−39 in $\log\epsilon = 12 + \log(n_X/n_H)$, $[X/H] = \log(n_X/n_H) - \log(n_{X,\odot}/n_{H,\odot})$, and $[X/Fe] = \log(n_X/n_{Fe}) - \log(n_{X,\odot}/n_{Fe,\odot})$ with the number fraction n_X for element X.

Element	$\log\epsilon$	[X/H]	[X/Fe]	Error
C	8.9	0.36	0.71	0.08
N	8.3	0.3	0.7	0.8
Na	6.0	−0.3	0.1	0.7
Al	5.8	−0.7	−0.3	1.0
S	8.1	0.8	1.2	1.2
K	4.8	−0.3	0.1	1.0
Ca	5.9	−0.4	−0.1	1.0
Sc	<2.4	<−0.7	<−0.4	
Ti	4.0	−0.9	−0.6	1.4
V	3.1	−0.9	−0.6	1.0
Cr	5.1	−0.5	−0.2	1.3
Mn	5.1	−0.3	0.0	1.0
Fe	7.1	−0.3		1.0
Co	5.1	0.2	0.5	1.0
Ni	6.5	0.2	0.6	1.3
Cu	5.0	0.8	1.2	1.5
Zn	<5.8	<1.2	<1.6	
Rb	3.7	1.1	1.4	1.3
Sr	3.6	0.6	1.0	1.5
Y	2.3	0.0	0.4	1.5
Zr	2.4	−0.2	0.2	1.5
Nb	<2.0	<0.7	<1.0	
Mo	2.9	1.0	1.4	1.3
Tc	<2.5			
Ru	<3.5	<1.7	<2.1	
Ba	3.6	1.4	1.8	0.5
La	2.3	1.1	1.5	1.6
Ce	<3.5	<2.0	<2.3	
Pr	<3.0	<2.4	<2.7	
Nd	1.9	0.4	0.8	1.5
Sm	<1.7	<0.8	<1.1	
Eu	<1.1	<0.6	<1.0	
Gd	<2.6	<1.5	<1.8	
Tb	<0.8	<0.5	<0.8	
Dy	<4.5	<3.4	<3.8	
Er	<2.4	<1.6	<1.9	
Hf	<1.8	<1.0	<1.4	
W	1.4	0.7	1.1	1.5
Os	<2.9	<1.5	<1.8	

velocity by $\pm 2.0\,\mathrm{km\,s^{-1}}$, which was kept fixed at $2.0\,\mathrm{km\,s^{-1}}$ in the initial analysis. By far, the impact of a change in temperature is the largest. Compared to this error, the variation in $\log g$ and microturbulence velocity become negligible. Furthermore, we investigated the influence of the metallicity of the model atmosphere grid that was chosen for the analysis on the determined abundances and repeated part of the analysis with different input model metallicities between −0.5 and 0. Raising (lowering) the metallicity by a certain amount results in a Fe abundance that is lower (higher) by roughly 1.3-fold that amount. Consistency is reached for the grid with [M/H] = −0.3 that gives a Fe abundance of [Fe/H] = 0.3 ± 1.0. In our analysis, we find a C enrichment but cannot determine the O abundance and, thus, use the solar value. The resulting C/O ratio is larger than one. To test whether it is justified to use an O-rich model atmosphere grid (model 1) with solar abundances, we employed the ATLAS9

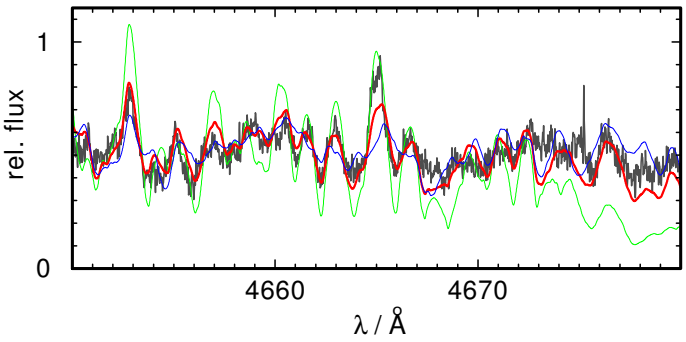

Fig. 2. Observation (gray) of Hen 2−39 compared to model spectra with $T_{\rm eff} = 4250$ K and $\log g = 2.5$ for a selected region of strong C_2 absorption for [C/H] = 0.46, 0.36, 0.26 (green, red, and blue, respectively).

code and calculated a test model with a C abundance increased to the value found in our analysis (model 2). Furthermore, we calculated a second test model with the increased C abundance and an O abundance reduced by one dex (model 3). We redid the abundance analysis for C and Ba and found the same abundance for C from model 1 and 2. For the model with increased C and decreased O abundance, we get a C abundance that is 0.03 dex higher. Compared to model 1, the Ba abundance for model 2 is higher by 0.04 dex and by 0.2 dex for model 3. The difference between the O-rich model 1 and the C-rich model 2 is shown in Fig. A.3. The effect of the model atmosphere on the abundances is in a range that justifies relying on the available model atmosphere grid. Thus, we did not compute a C-rich grid. However, this adds another uncertainty to the abundances. We obtain large errors arising from the crowdedness of the observed spectrum that we estimate by detailed line profile fits and evaluation based on the χ-by-eye method. In many cases, this is the main contributor to the total error. It ranges between 0.05 dex for C and about 0.4 dex for the light metals up to about 1 dex for the iron group and trans-iron elements. To take the uncertainties in $T_{\rm eff}$ and $\log g$ into account, we did this procedure for the corners of the grid stated above ($T_{\rm eff}$ = 4000 K, $\log g$ = 3.0 and 4500 K, 2.0). The abundance errors arising from this effect range between 0.03 dex for C and about 0.5 dex for the other metals. The total errors given in Table 2 are the maximum differences for the abundances that are possible within the error limits of this grid.

Carbon. We analyzed the C abundance using spectrum synthesis calculations for the region of strong C_2 absorption from 4650 to 4737 Å (Fig. 2). We confirm the C enhancement and our result of [C/H] = 0.36 ± 0.08 agrees within 1σ with the value derived by Miszalski et al. (2013a) from their mid-resolution spectra.

Nitrogen. Using the C abundances, we derived the N abundance from synthetic calculations for the wavelength regions 7030−7070 Å and 7900−8100 Å affected by strong CN absorption bands. Figure 3 shows the best result. We find N to be enriched to the same level as C with [N/H] = 0.3 ± 0.8. We could not identify any line of oxygen in the observed spectrum and, thus, were unable to fix an abundance value for O. In our analysis, we adopt the solar value. To get an idea of the $^{12}C/^{13}C$ ratio, we analyzed the CN absorption band in the region 8100−8200 Å and included the line list for $^{13}C^{14}N$ from Sneden et al.(2014; Fig. 4). From the inspection of the observation, we cannot claim to find a enhancement in ^{13}C resulting in

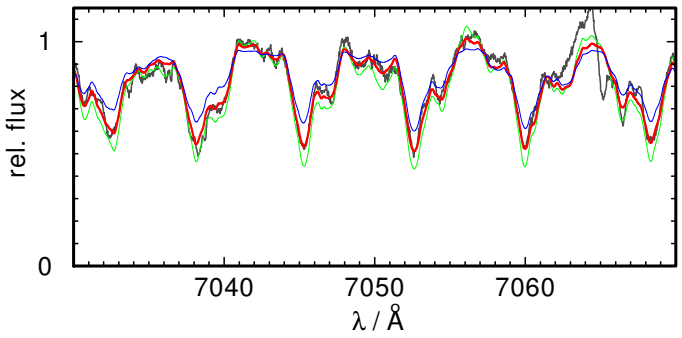

Fig. 3. Like Fig. 2, for strong CN absorption for [N/H] = 1.1, 0.3, −0.5 (green, red, and blue, respectively).

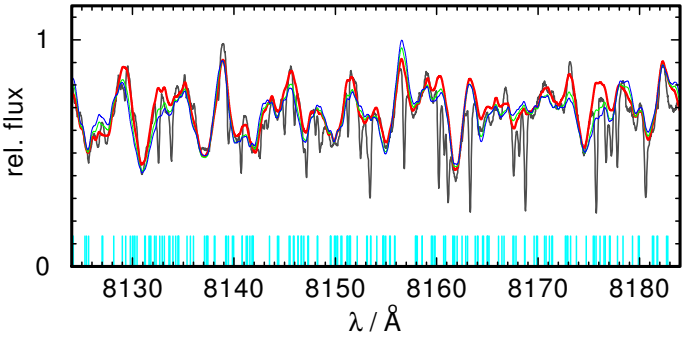

Fig. 4. Like Fig. 2, for strong CN absorption for $^{12}C/^{13}C$ = 90, 10, 5 (red, green, and blue, respectively). ^{13}CN absorption lines are indicated at the bottom in cyan.

$^{12}C/^{13}C$ lower than the solar value of 90, although this cannot be ruled out.

Light metals: sodium to potassium. For the following elements, we used the most prominent absorption features in the synthetic spectra, which show the largest impact of a change of the abundance (Table A.3). The Na doublet Na II $\lambda\lambda$ 5890.8, 5896.5 Å (Fig. A.4) is used to find a Na abundance of [Na/Fe] = 0.1 ± 0.7, which resembles well with the sample of Ba stars analyzed by de Castro et al. (2016, Fig. 6). From a fit to the regions affected by absorption due to Al we derive [Al/Fe] = −0.3 ± 1.0. Ba stars typically show a slight enhancement in Al, which is also present in the sample of de Castro et al. (2016). For S we derive [S/Fe] = 1.2 ± 1.2 and for K we found [K/Fe] = 0.1 ± 1.0.

Iron-peak elements: calcium to copper. Selected absorption features due to neutral Ca to Cu are shown in Figs. A.5 and A.6. We performed a fit for a set of Fe I and Fe II absorption lines and found this star to be metal-poor with [Fe/H] = −0.3 ± 1.0. For all iron-peak elements prior to Fe, we found solar values or slight underabundances, namely [Ca/Fe] = −0.1 ± 1.0, [Ti/Fe] = −0.6 ± 1.4, [V/Fe] = −0.6 ± 1.0, [Cr/Fe] = −0.2 ± 1.3, and [Mn/Fe] = 0.0 ± 1.0. For Sc, we determined an upper limit of [Sc/Fe] = −0.4. These low values for the α elements Ca and Ti do not correspond with the trend in the sample of de Castro et al. (2016) who found an enrichment of these elements compared to Fe with decreasing metallicity. The values close to solar for the other elements, however, are in good agreement with the sample showing a clustering of the abundances around [X/Fe] = 0.0. For the elements of this group subsequent to Fe, we determined overabundances compared to Fe of [Co/Fe] = 0.5 ± 1.0, [Ni/Fe] = 0.6 ± 1.3, and [Cu/Fe] = 1.2 ± 1.5.

Trans-iron elements: zinc to osmium. Selected wavelength regions that are among those showing the largest impact of a change in abundance for the elements of this group are shown in Figs. A.7–A.9. Since we found only few significant absorption features for the majority of these elements, the statistical errors of the determined values are large (often >1 dex) and in many cases only upper abundance limits could be established. We obtained [Zn/Fe] < 1.6 and [Rb/Fe] = 1.4 ± 1.3. For the elements around the first peak of the s-process, we found [Sr/Fe] = 1.0 ± 1.5, [Y/Fe] = 0.4 ± 1.5, and [Zr/Fe] = 0.2 ± 1.5. Despite the large uncertainties, we find a good agreement with the Sr abundances of the sample of Karinkuzhi et al. (2018, Fig. 6). The Sr abundances for most of the Ba stars of Merle et al. (2016) are slightly lower but some reach up to 1 dex as well. Also the Y abundance of Hen 2−39 agrees well with the sample of Merle et al. (2016), whereas the majority of Ba giants of Karinkuzhi et al. (2018) and de Castro et al. (2016) crowd around higher values of Y. The [Zr/Fe] abundances of Karinkuzhi et al. (2018) are significantly higher (all >1 dex), whereas some of the Ba stars of Merle et al. (2016) agree with low values of [Zr/Fe]. Also the sample of de Castro et al. (2016) clusters around [Zr/Fe] ≈ 1 but also shows stars with comparatively low values like that for Hen 2−39. For the elements subsequent to this peak, we determined [Nb/Fe] < 1.0, [Mo/Fe] = 1.4 ± 1.3, and [Ru/Fe] < 2.1.

One key element of this analysis is the radioactive Tc. The strongest absorption features that appear in the synthetic spectra are Tc I $\lambda\lambda$ 4031.6, 4095.7, 4238.2, 4262.3, 4297.1 Å. Unfortunately, these lines could not be clearly identified in the observed spectrum but it could be used to establish an upper abundance limit of $\log \epsilon_{Tc} < 2.5$[7].

For the determination of the Ba abundance, we used Ba II $\lambda\lambda$ 4554.0, 4931.1, 5853.7, 6141.7, 6496.9 Å. The first two are very strong and sensitive to small variations of the abundance (Fig. A.8). This helped to constrain [Ba/Fe] = 1.8 ± 0.5, which agrees within the error limits with the previous value of Miszalski et al. (2013a). The values determined by Karinkuzhi et al. (2018) for this element range from 0.81 ≤ [Ba/Fe] ≤ 2.67. Also the sample of Merle et al. (2016) shows a scatter between almost solar and 2.5. Our strong enrichment found for Hen 2-39, thus, is not exceptional (Fig. 6).

La II absorption lines yield [La/Fe] = 1.5 ± 1.6. For the other elements of the second peak of the s-process we found [Ce/Fe] < 2.3, [Pr/Fe] < 2.7, and [Nd/Fe] = 0.8 ± 1.5. The upper limit for Ce lies above the value range of 1.02 ≤ [Ce/Fe] ≤ 1.76 determined by Karinkuzhi et al. (2018) and also above that of Merle et al. (2016) ranging from solar to 1.5 dex. The Ba stars of de Castro et al. (2016) cluster around an enrichment of 1.0 dex and none of these stars reach values above 2.5 dex. Our upper limit for Pr lies above the value range of 1.18 ≤ [Pr/Fe] ≤ 2.55 of Merle et al. (2016). However, our value for the Nd abundance is below their range of values. The star with the lowest Nd abundance shows [Nd/Fe] = 1.18, whereas the sample of de Castro et al. (2016) clustering around [Nd/Fe] ≈ 1.0 perfectly agrees with our value within the error limits.

For the further rare-earth elements Sm, Eu, Gd, Tb, Dy, and Er, we could only establish upper abundance limits (Table 2). These elements are not analyzed by Merle et al. (2016) and de Castro et al. (2016). Karinkuzhi et al. (2018) found ranges

[7] $\log \epsilon = 12 + \log(n_X/n_H)$.

of 1.02 ≤ [Sm/Fe] ≤ 2.17, 0.96 ≤ [Eu/Fe] ≤ 1.43, and 1.60 ≤ [Dy/Fe] ≤ 2.51. Our upper limits of [Sm/Fe] < 1.1, and [Eu/Fe] < 1.0 lie within these ranges; [Dy/Fe] < 3.8 is significantly higher. Furthermore, we could determine the abundances of Hf, W, and Os to be [Hf/Fe] < 1.4, [W/Fe] = 1.1 ± 1.5, and [Os/Fe] < 1.8.

6. Discussion

6.1. Element abundances

We compared our results with the yields from nucleosynthesis calculations of Karakas & Lugaro (2016) for a metallicity of $Z = 0.007$, in line with the low metallicity of $Z = 0.006$ that we determined from $Z = 10^{[Fe/H]}Z_\odot$ with [Fe/H] = −0.3 and $Z_\odot = 0.0134$ (Asplund et al. 2009). From these models and those of Karakas et al. (2018), it becomes obvious that AGB nucleosynthesis does not affect the abundances of the iron peak elements and, thus, it seems reasonable to assume the same low metallicity for both components of the binary.

The fact that we cannot see a ^{13}C enhancement agrees very well with the theoretical calculations predicting even an enhancement of the initial solar ^{12}C/^{13}C-ratio for models with initial masses $1.5\,M_\odot \leq M_{ini} \leq 4.0\,M_\odot$ where our estimated initial mass (Sect. 6.2) lies within.

The finding that the iron-peak elements prior to Fe show underabundances and those subsequent to Fe are enhanced leads to the speculation that this pattern may be caused by neutron capture on the former elements as seed species and the formation of elements heavier than Fe. Figure 5 also shows an enrichment due to AGB nucleosynthesis for the elements subsequent to Fe.

The observed N enhancement of [N/Fe] = 0.7 ± 0.8 (Fig. 5) is in line with the enhancement found for the Ba stars of Karinkuzhi et al. (2018, Fig. 6). A high [N/C] ratio as found for this object is discussed in the literature (e.g. Smiljanic et al. 2006; Merle et al. 2016). These authors argue that CN processing in Ba stars could result in higher N abundances. According to Smiljanic et al. (2006), an increased [N/C] ratio can be caused by mixing events such as the first DU or by a more complex mixing process due to rotation for intermediate mass stars. This would be an indicator for hydrogen burning via the CNO-cycle in the stellar core. With the assumed mass for the primary star (Sect. 6.2), this should be the dominating fusion process in this star. The fast rotation of the Ba-CSPN is most likely due to transfer of angular momentum from the primary and therefore does not imply that this star was rotating exceptionally fast initially so as to affect its [N/C] abundance ratio.

For Tc, we could not identify the presence of any line without doubt and, thus, cannot constrain the abundance further than $\log \epsilon_{Tc} < 2.5$. Therefore, we cannot claim this star to have Tc in its atmosphere, which would directly lead to the necessity of prior mass transfer. The models of Karakas & Lugaro (2016) predicted a final surface abundance between $\log \epsilon_{Tc} = 1.11$ and 1.24 for the models with initial masses between 2.1 and 2.5 $M_\odot$, which lies well below the upper limit for Hen 2−39. Another diagnostic element reflecting recent s-process nucleosynthesis is Nb. According to Neyskens et al. (2015), this mono-isotopic species is synthesized by the decay of the radioactive ^{93}Zr produced by s-process nucleosynthesis. Compared to ^{99}Tc, this species has a longer half-life time of 1.53 Myr. Following our estimate made for Tc (Sect. 1), we do not expect an significant enrichment in Nb, since the primary's post-AGB age should be much shorter than the ^{93}Zr half-life and, thus, a large fraction of this species should still be present. Thus, the Nb/Zr would not represent the ^{93}Zr/Zr ratio at the end of the AGB and cannot be employed as proof for prior mass transfer. Furthermore, the Zr abundance can be determined only within a very large error range and for Nb, we find an upper limit only.

The detection of Tc is not hampered by the resolution of the spectrograph. The limiting factor is the S/N. We estimate the needed S/N that would be necessary to clearly distinguish between a model without Tc and one with $\log \epsilon_{Tc} = 1.2$. From Fig. 7, it becomes clear, that the current S/N is not sufficient to determine a Tc abundance of that level. Currently, the single spectra have a S/N of 3 at that wavelength region. This is increased by co-adding all the spectra, but still a S/N increased by a factor of 3 would be necessary. According to the UVES exposure time calculator (ETC), the needed S/N would require about a six fold longer exposure. For the future Extremely Large Telescope (ELT) the estimate is more promising. By using the E-ELT Spectroscopic ETC, we find that the required S/N is reached with an exposure of about half that of a single observation used in this analysis. For stars with a lower rotational velocity, the detection would become easier (Fig. 7). Unfortunately, all Ba CSPNe that are known up to now seem to rotate fast (shortest period of 4.7 d for Abell 70 and WeBo 1 and longest period of 5.9 d for LoTr 5; Bond et al. 2003; Miszalski et al. 2012; Aller et al. 2018), most likely because of the transfer of angular momentum by accretion of matter from the companion.

6.2. Mass transfer

By comparing our determined enrichment in s-process elements to the yields from evolutionary models for different initial masses of Karakas et al. (2018), we try to confirm that this can be the result of realistic mass transfer. For a primary that is currently in the stage of a CSPN, the secondary should have a mass that is lower by about 5% to be currently in the evolutionary stage of a red giant (assuming a mass dependent relation for the main-sequence lifetime $t \sim M^{-2.5}$). According to Joss et al. (1987), these stars should have a radiative core of about 0.3 $M_\odot$ and a convective envelope of a mass $M_{env} = M_{ini} - 0.3\,M_\odot$ within which the accreted mass becomes diluted. We want to determine a realistic mass range for the primary by comparing the total mass for the different elements that is ejected during the AGB evolution with the mass that the secondary would have needed to accrete to become that enriched. The mass of element X that needs to be accreted is given by $M_{need} = M_{env}(mf_{X,final} - mf_{X,initial})$ with a final mass fraction $mf_{X,final}$ according to our analysis results and an initial mass fraction $mf_{X,initial}$ according to the low metallicity. In Fig. 8, we show the needed mass compared to the total ejected mass for C, N, and the elements heavier than Fe that show a significant production due to AGB nucleosynthesis. Since most of the abundances could not be constrained within small error limits, we focus on the C and Ba abundances. For all models of Fig. 8 and some additional models, we calculated the percentage of the total ejecta that would need to be accreted to produce the observed enrichment (Table 3). It is obvious that only the models for an initial mass between 1.5 and 4.0 $M_\odot$ can explain the enrichment due to a realistic mass transfer. For the models with the lowest initial masses as well as for those with the highest masses, the ratio of the yield of Ba to that of C is smaller, i.e., these models produce a smaller amount of Ba compared to C. The fraction of accreted mass of C and Ba should be equal. Thus, a 1.75–3.00 $M_\odot$ progenitor seems to be most consistent with the abundance determinations. For this analysis, we used the models with the largest ^{13}C-pocket that are available

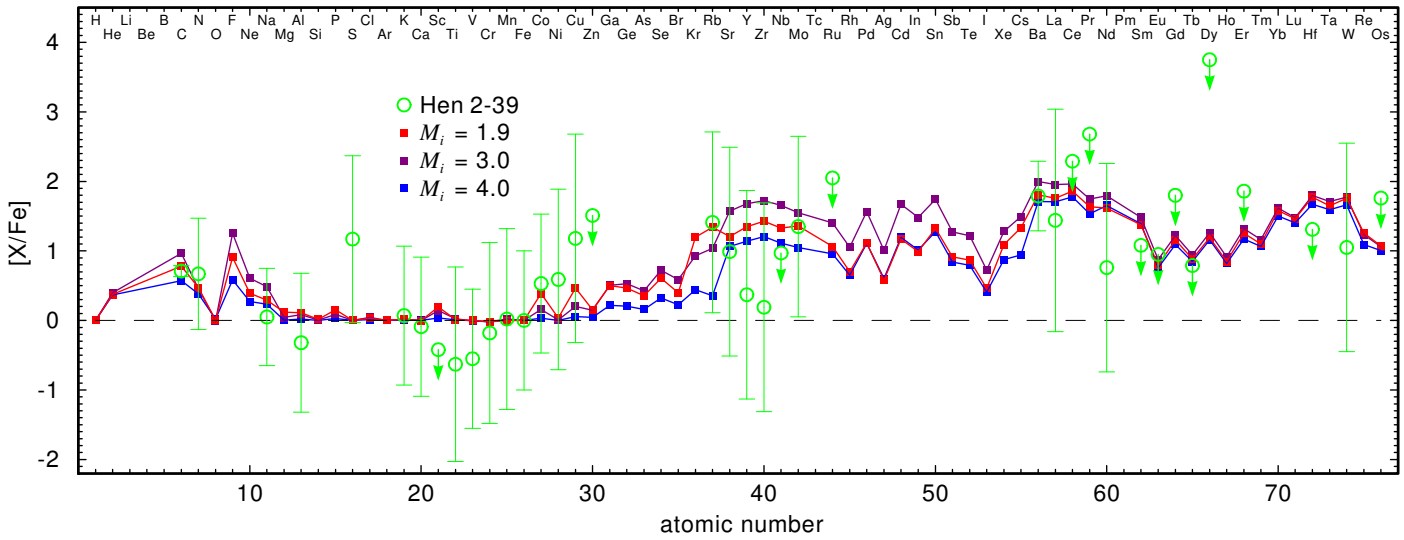

Fig. 5. Atmospheric element abundances of Hen 2−39 compared to the final yields of a selection of evolutionary models from Karakas & Lugaro (2016) with a metallicity of $Z = 0.007$. The initial masses are indicated in the upper panel. Arrows indicate upper limits.

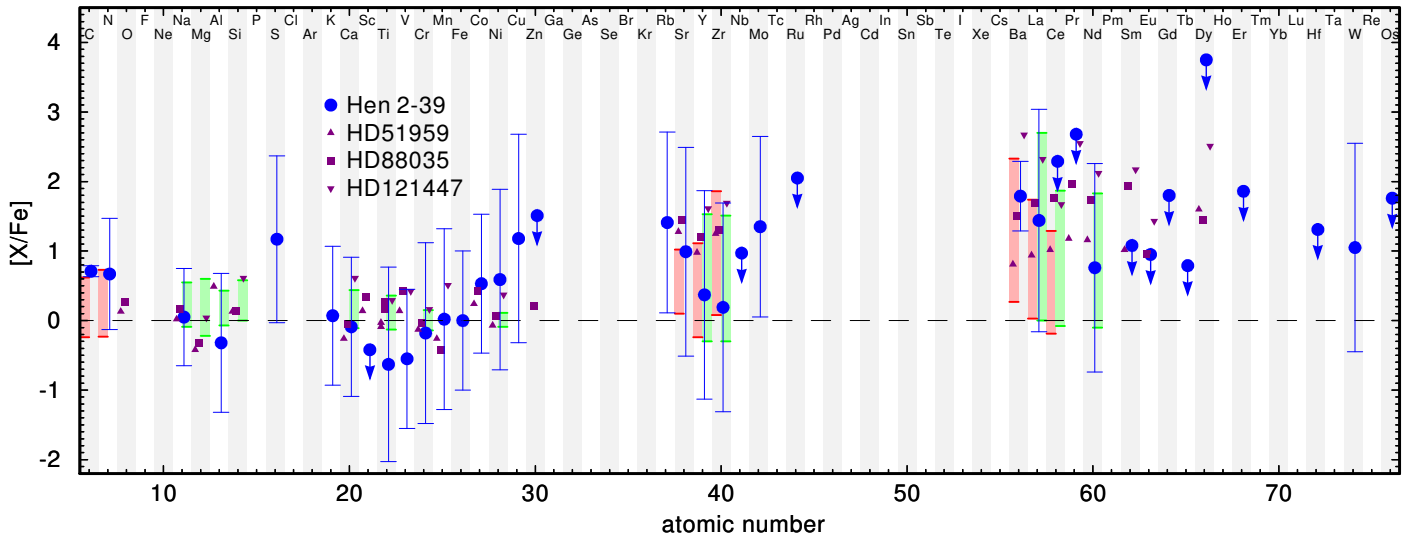

Fig. 6. Atmospheric element abundances of Hen 2−39 (blue) compared to the values for the three Ba stars HD515959, HD88035, and HD121447 analyzed by Karinkuzhi et al. (2018, purple) and the ranges that Merle et al. (2016, red) and de Castro et al. (2016, green) found for their sets of Ba-stars. Arrows indicate upper limits.

from Karakas & Lugaro (2016). The larger the pocket size, the lower the yield of C and the higher that of Ba, i.e., the ratio of the yield of Ba to that of C is larger. Even for the models with the largest ^{13}C-pocket, the percentage of the total ejecta that would need to be accreted is higher considering the Ba abundance compared to the C abundance. This ratio becomes worse for smaller pocket sizes. In addition to the choice of the ^{13}C-pocket, yields of the evolutionary models are affected by uncertainties due to mass loss, convective mixing, reaction rates, and neutron poisons (Karakas & Lattanzio 2014). These effects are not evaluated by Karakas & Lugaro (2016) and we take the tabulated yields without considering an error range. However, the progentitor mass estimate is affected by large uncertainties on the abundances and on the model yields and, thus, should be treated with caution.

This result leads to the conclusion that even such a high enrichment can reasonably be explained with realistic mass-transfer mechanisms such as wind-RLOF (Chen et al. 2017). In this scenario only a small fraction of mass becomes unbound from the binary and the percentage of accreted mass ranges between 20 and 40%. Simulations indicate that a binary with a wide separation, where mass transfer would act via the Bondi-Hoyle mechanism, can be ruled out since the percentage of accreted mass decreases to only 2–3% (Theuns et al. 1996). CE evolution would imply a short orbital period (≤ a few days), which is not the case for this binary and, thus, this scenario is also ruled out.

6.3. Spectroscopic distance

For Hen 2−39, several different distances are published. The nebular analysis of Miszalski et al. (2013a) yields 5.7 kpc. Frew et al. (2016) found $7.6^{+1.5}_{-1.3}$ kpc based on the companion spectral type. The CSPN of Hen 2−39 is in the *Gaia* data release (DR2, ID: 5256396485463285504, Gaia Collaboration 2018).

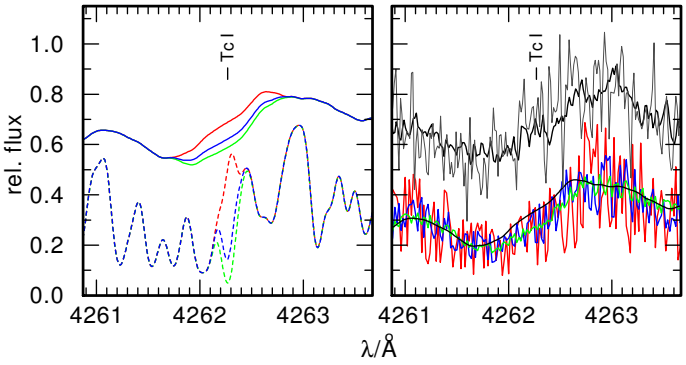

Fig. 7. *Left panel*: comparison between models with $\log \epsilon_{\rm Tc} = 0.0, 1.2, 2.5$ (red, blue, green) for models broadened with a rotational profile ($v_{\rm rot} = 36\,{\rm km\,s^{-1}}$, solid lines with 0.35 offset) and without rotation (dashed). *Right panel*: comparison between a rotationally broadened model without Tc (black) and models with $\log \epsilon_{\rm Tc} = 1.2$ with different levels of artificial noise (S/N of the single observation: red, S/N of co-added spectrum: blue, required S/N: green). For comparison, the observation is shown with an offset of 0.35 (single spectrum: gray, co-added spectra: black).

Table 3. Percentage of the total ejecta that would need to be accreted to produce the observed enrichment of Hen 2−39 for evolutionary models of Karakas & Lugaro (2016) with $Z = 0.007$ for different initial masses.

$M_{\rm ini}/M_\odot$	C	Ba
1.00	156	2215
1.50	49	94
1.75	25	36
1.90	26	32
2.10	14	17
2.25	15	18
2.50	12	15
2.75	9	15
3.00	10	15
3.50	12	24
4.00	18	27
5.00	89	1311

The parallax of 0.0564 ± 0.0340 mas is affected by a large error corresponding to relative errors of 60.3%. The object is also contained in the catalog of distances of Bailer-Jones et al. (2018) derived from the DR2 data. They found $9.071^{+2.939}_{-1.962}$ kpc. With our result for the companion mass, we would like to get a clue for the distance for the binary in Hen 2–39. Using the assumed giant $\log g = 2.5$, the derived mass of about 2.2 $M_\odot$ for the Ba star, and the determined $T_{\rm eff}$, we get

$$M_{\rm bol} = M_{\rm bol,\odot} + 2.5\,(\log g - \log g_\odot) - 2.5 \log\left(\frac{M}{M_\odot}\right) - 10 \log\left(\frac{T_{\rm eff}}{T_{\rm eff\odot}}\right) = 0.262.$$

The solar values are taken from the *Sun Facts Sheet* from the NASA Goddard Space Flight Center[8] and we use $M_{\rm bol,\odot} = 4.74$ mag for the Sun derived from the standardized absolute bolometric magnitude scale defined by the international astronomical union (Mamajek et al. 2015). The error of $M_{\rm bol}$ is dominated by the uncertainty of $\log g$. Assuming an uncertainty of $\Delta \log g = 0.5$ and $\Delta M = 0.5\,M_\odot$, we get $\Delta M_{\rm bol} = 1.316$. Nevertheless, we can derive the absolute visual magnitude $M_{\rm V} = M_{\rm bol} - {\rm BC}(V) = 0.852 \pm 1.525$. The bolometric correction of ${\rm BC}(V) = -0.590 \pm 0.209$ is calculated using the approach of Alonso et al. (1999) including the preliminary values for $T_{\rm eff}$ and the Fe abundance.

We can now estimate the distance via the distance modulus but the known V magnitude shows a much larger uncertainty than the more recent infrared magnitudes (Table 4). By comparing the calculated flux normalized on the K magnitude of Cutri et al. (2003) with the B and V magnitudes of Tylenda et al. (1991) and those for the I, J, and K bands from Epchtein et al. (1999), it becomes obvious that our model agrees very well with the brightness values in all filters (Fig. 9). Thus, we decided to rely on the precise I magnitude for the distance estimation. Using the color relation for $(V - I)$ from Alonso et al. (1999) for the given $T_{\rm eff}$, we find $(V - I) = 1.543^{+0.124}_{-0.110}$ mag. This leads to an absolute M_I brightness of $M_I = -0.691^{+1.635}_{-1.649}$ mag.

Miszalski et al. (2013a) determined an extinction of $E_{\rm B-V} = 0.37$ mag. With the Galactic extinction law with $R_V = 3.1$ and the relation from Cardelli et al. (1989), we derive the total absorption for the I band of $A_I = 0.5\,A_V = 0.5 \times 3.1\,E_{\rm B-V} = 0.565$ mag. Now, we find $d = 10^{-(M_I - I + A_I - 5)/5} = 9.15^{+10.65}_{-4.90}$ kpc. The large error is again an effect of the assumed uncertainty in $\log g$ but, nevertheless, the value agrees with all other distance values within these limits. Furthermore, this value is very close to that derived from the *Gaia* parallax measurement. With a precise distance measurement, we could get a second handle on the mass of the Ba star. The mass could then be derived by comparing its properties to evolutionary tracks for different masses and compared with our value derived using the abundance yields of evolutionary models.

With its Galactic latitude of −4.239° (Gaia Collaboration 2018), the star is located $0.676^{+0.789}_{-0.362}$ kpc below the Galactic plane, which means that it is just below the edge of the Galactic thin disk (Rix & Bovy 2013) and, thus, should belong to the thick disk. This assignation is in agreement with the observed low metallicity since simulations for the Galactic metallicity distribution predict negative metallicity gradients for low scale heights and may change the sign at about a scale height of 1.5 kpc. Ivezić et al. (2012) also found thick disk stars to be more metal poor (median [Fe/H] = −0.6) compared to thin disk stars (median [Fe/H] = −0.2), where Hen 2−39 lies just in the middle. Furthermore, we can use $M_{\rm bol}$ to estimate the luminosity $L/L_\odot = 10^{(M_{\rm bol,\odot} - M_{\rm bol})/2.5} = 61.83^{+145.95}_{-43.43}$ and the radius

$$\frac{R}{R_\odot} = \sqrt{\frac{L}{L_\odot}\frac{T_{\rm eff\odot}^4}{T_{\rm eff}^4}} = 13.84^{+13.38}_{-6.78}.$$

Using the rotational velocity from Sect. 4.1 and the radius the star should have a rotational period of 18.4 d for a high inclination of $i = 90°$. Miszalski et al. (2013a) detected a photometrically variability of the star with a period of 5.46 d. Assuming this value for the rotation, we can find an inclination of $i = 17.22^{\circ\,+18.30}_{\ -8.53}$. The parameters are summarized in Table 5. We speculate that the rotational axis of the giant is perpendicular to the binary orbital plane. The low inclination is then in good agreement with the ring-like appearance of the nebula (Miszalski et al. 2013a), which indicates a nearly pole-on view and therefore a binary orbital plane almost in the plane of the sky (Hillwig et al. 2016).

[8] https://nssdc.gsfc.nasa.gov/planetary/factsheet/sunfact.html, Version 29-06-2018.

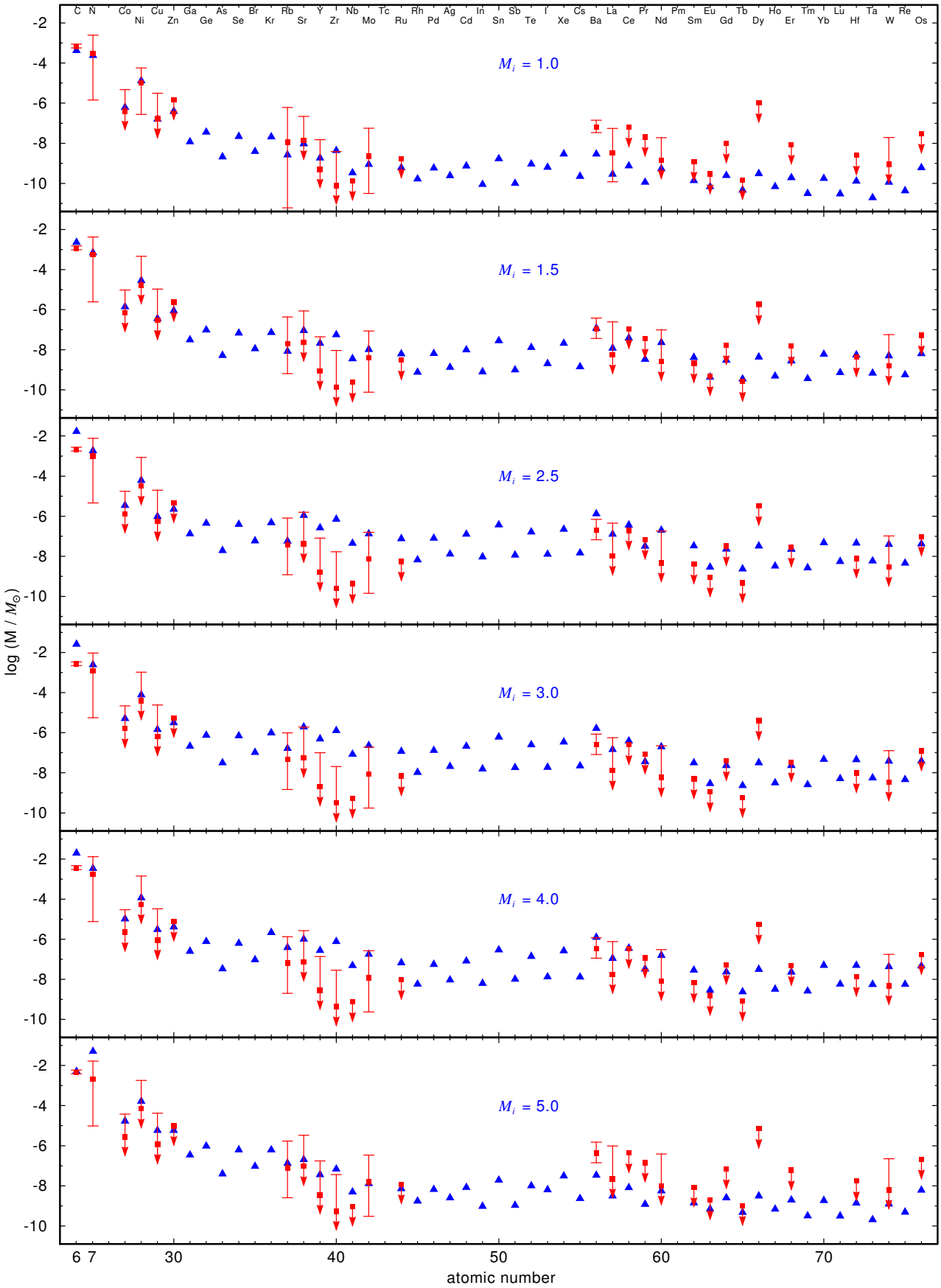

Fig. 8. Total amount of mass ejected during AGB evolution of different elements for evolutionary models from Karakas & Lugaro (2016) for $Z = 0.007$ with initial masses of 1.0–5.0 $M_\odot$ (blue, initial mass indicated in the panel) compared to the need of accreted mass to reproduce the determined abundance values of the secondary via mass transfer (red).

Table 4. Brightnesses in different filters for the Ba CSPN of Hen 2–39.

Filter	Magnitude	Reference
B	17.9 ± 0.5	Tylenda et al. (1991)
V	16.5 ± 0.5	Tylenda et al. (1991)
I	14.68 ± 0.03	Epchtein et al. (1999)
J	13.474 ± 0.033	Cutri et al. (2003)
H	12.614 ± 0.033	Cutri et al. (2003)
K	12.338 ± 0.030	Cutri et al. (2003)

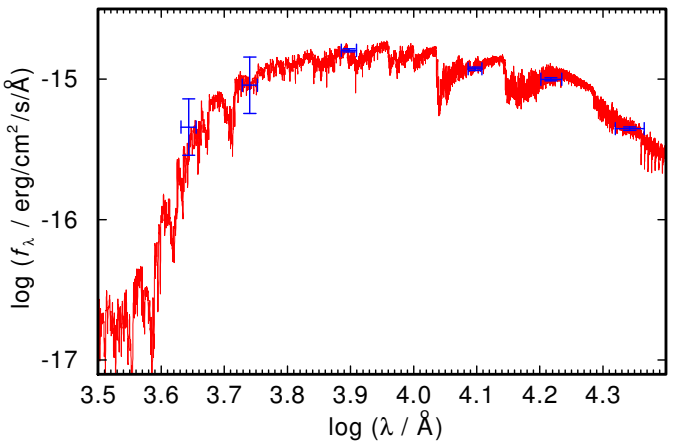

Fig. 9. Synthetic spectrum of our best model of Hen 2−39 normalized to the H magnitude of Cutri et al. (2003) and convolved with a Gaussian with $FWHM$ = 5 Å for clarity, including interstellar reddening with E_{B-V} = 0.37 (red) compared with the observed magnitudes (Table 4).

Table 5. Properties of the CSPN of Hen 2−39.

$T_{\rm eff}$	(4350 ± 150) K
Distance[a]	5.7 kpc
Distance[b]	$\left(9.071^{+2.939}_{-1.962}\right)$ kpc
Distance	$\left(9.15^{+10.65}_{-4.90}\right)$ kpc
BC(V)	(−0.590 ± 0.209) mag
$M_{\rm bol}$	0.262 ± 1.316
$(V-I)_0$	$1.543^{+0.124}_{-0.110}$
$E(B-V)$[a]	−0.37
$L/L_\odot$	$61.83^{+145.95}_{-43.43}$
$M/M_\odot$	2.2 ± 0.5
$\log g$	2.5 ± 0.5
$R/R_\odot$	$13.84^{+13.38}_{-6.78}$
Rotation period[a]	5.46 d
$v_{\rm rot} \sin i$	38 ± 5 km s^{-1}
i	$\left(17.22^{+18.30}_{-8.53}\right)^\circ$

References. [(a)]Miszalski et al. (2013a) [(b)]Bailer-Jones et al. (2018).

7. Summary and conclusions

We presented and discussed the spectral analysis of UVES spectra of the Ba CSPN of Hen 2−39. Within the error limits, we confirm the result of Miszalski et al. (2013a) that the observed nucleus of Hen 2−39 has a cool atmosphere of $T_{\rm eff}$ = (4350 ± 150) K. Furthermore, we confirm the C and Ba enrichment but can significantly improve the abundances of [C/H] = 0.36 ± 0.08 and [Ba/Fe] = 1.8 ± 0.50 due to the high resolution of the analyzed spectra. We determined abundances or upper abundance limits for 26 trans-iron elements for the first time. For Tc, the lightest element with no stable isotope, we find an upper abundance limit of $\log \epsilon_{\rm Tc} < 2.5$. This does not confirm the presence of Tc in the atmosphere of the star proving prior mass transfer. The limiting factor is not the resolution of the spectrum. For a clear detection of Tc, an exposure time about six times longer than that of all the spectra combined would be required to obtain the necessary S/N ratio. We can find a low metallicity of [Fe/H] = −0.3 ± 1.0 for the Ba giant. The determined abundance pattern requires mass transfer from a companion with an extremely high enrichment of AGB nucleosynthesis products. The comparison with nucleosynthesis models of Karakas & Lugaro (2016) indicates an initial mass of 1.75–3.00 $M_\odot$ for the primary. The percentage of ejected mass that needs to be accreted indicates that the preferred mass transfer mechanism is wind-RLOF. A wide binary involving Bondi-Hoyle accretion can be ruled out as can a CE evolution. For this star, the distance is rather uncertain. Thus, it cannot be used for a spectroscopic determination of the mass by interpolation from evolutionary tracks. A precise spectroscopic determination of the distance is hampered by the fact that $\log g$ cannot be constrained within narrow error limits from the analysis of the spectra. It is highly desirable to get a more precise distance measurement. This would also help to get a second value for the mass of the Ba CSPN to compare with that derived from the comparison with AGB models. With this second measurement, it would be possible to refine the primary mass estimate and place stronger constraints on the mass transfer. Our result for the height above the Galactic plane places this system among the thick disk population, in good agreement with the subsolar metallicity derived by our analysis.

Acknowledgements. We thank the anonymous referee for their constructive review of the manuscript. We thank Brent Miszalski and Thomas Rauch for their helpful comments and suggestions. L.L. is supported by the German Research Foundation (DFG, grant WE 1312/49-1) and by the Studentship Programme of the European Southern Observatory. D.J. gratefully acknowledges the Spanish Ministry of Economy and Competitiveness (MINECO) under the grant AYA2017-83383-P. This research has made use of NASA's Astrophysics Data System and the SIMBAD database, operated at CDS, Strasbourg, France. This work has made use of data from the European Space Agency (ESA) mission *Gaia* (`https://www.cosmos.esa.int/gaia`), processed by the *Gaia* Data Processing and Analysis Consortium (DPAC, `https://www.cosmos.esa.int/web/gaia/dpac/consortium`). Funding for the DPAC has been provided by national institutions, in particular the institutions participating in the *Gaia* Multilateral Agreement.

References

Abate, C., Pols, O. R., Izzard, R. G., Mohamed, S. S., & de Mink, S. E. 2013, A&A, 552, A26
Acker, A., Marcout, J., Ochsenbein, F., et al. 1992, The Strasbourg-ESO Catalogue of Galactic Planetary Nebulae. Parts I, II (Garching: European Southern Observatory)
Aller, A., Lillo-Box, J., Vučković, M., et al. 2018, MNRAS, 476, 1140
Alonso, A., Arribas, S., & Martínez-Roger, C. 1999, A&AS, 140, 261
Asplund, M., Grevesse, N., Sauval, A. J., & Scott, P. 2009, ARA&A, 47, 481
Bailer-Jones, C. A. L., Rybizki, J., Fouesneau, M., Mantelet, G., & Andrae, R. 2018, AJ, 156, 58
Bidelman, W. P., & Keenan, P. C. 1951, ApJ, 114, 473
Blanco-Cuaresma, S., Soubiran, C., Heiter, U., & Jofré, P. 2014, A&A, 569, A111
Boffin, H. M. J. 2015, Ecology of Blue Straggler Stars (Berlin, Heidelberg: Springer-Verlag)
Boffin, H. M. J., & Jorissen, A. 1988, A&A, 205, 155
Bond, H. E., Pollacco, D. L., & Webbink, R. F. 2003, AJ, 125, 260
Buckley, D. A. H., Swart, G. P., & Meiring, J. G. 2006, Proc. SPIE, 6267, 62670Z

Burgh, E. B., Nordsieck, K. H., Kobulnicky, H. A., et al. 2003, in Instrument Design and Performance for Optical/Infrared Ground-based Telescopes, eds. M. Iye, & A. F. M. Moorwood, Proc. SPIE, 4841, 1463
Cardelli, J. A., Clayton, G. C., & Mathis, J. S. 1989, ApJ, 345, 245
Castelli, F., & Kurucz, R. L. 2003, in Modelling of Stellar Atmospheres, eds. N. Piskunov, W. W. Weiss, & D. F. Gray, IAU Symp., 210, A20
Chen, Z., Frank, A., Blackman, E. G., Nordhaus, J., & Carroll-Nellenback, J. 2017, MNRAS, 468, 4465
Corradi, R. L. M., Sabin, L., Miszalski, B., et al. 2011, MNRAS, 410, 1349
Cutri, R. M., Skrutskie, M. F., van Dyk, S., et al. 2003, VizieR Online Data Catalog: II/246
de Castro, D. B., Pereira, C. B., Roig, F., et al. 2016, MNRAS, 459, 4299
De Marco O. 2009, PASP, 121, 316
Dekker, H., D'Odorico, S., Kaufer, A., Delabre, B., & Kotzlowski, H. 2000, in Optical and IR Telescope Instrumentation and Detectors, eds. M. Iye, & A. F. Moorwood, Proc. SPIE, 4008, 534
Epchtein, N., Deul, E., Derriere, S., et al. 1999, VizieR Online Data Catalog: II/240
Frew, D. J., Parker, Q. A., & Bojičić, I. S. 2016, MNRAS, 455, 1459
Gaia Collaboration 2018, VizieR Online Data Catalog: I/345
Gray, R. O., & Corbally, C. J. 1994, AJ, 107, 742
Gray, R. O., McGahee, C. E., Griffin, R. E. M., & Corbally, C. J. 2011, AJ, 141, 160
Grevesse, N., & Sauval, A. J. 1998, Space Sci. Rev., 85, 161
Han, Z., Eggleton, P. P., Podsiadlowski, P., & Tout, C. A. 1995, MNRAS, 277, 1443
Henize, K. G. 1967, ApJS, 14, 125
Herwig, F. 2005, ARA&A, 43, 435
Hillwig, T. C., Jones, D., De Marco, O., et al. 2016, ApJ, 832, 125
Hubeny, I., Mihalas, D., & Werner, K., eds. 2003, in Stellar Atmosphere Modeling, ASP Conf. Ser., 288, 17
Husti, L., Gallino, R., Bisterzo, S., Straniero, O., & Cristallo, S. 2009, PASA, 26, 176
Iben, Jr. I., & Livio, M. 1993, PASP, 105, 1373
Ivezić, Ž., Beers, T. C., & Jurić, M. 2012, ARA&A, 50, 251
Jones, D., & Boffin, H. M. J. 2017, Nat. Astron., 1, 0117
Jones, D., Van Winckel, H., Aller, A., Exter, K., & De Marco, O. 2017, A&A, 600, L9
Jorissen, A., & Mayor, M. 1988, A&A, 198, 187
Jorissen, A., Van Eck, S., Mayor, M., & Udry, S. 1998, A&A, 332, 877
Joss, P. C., Rappaport, S., & Lewis, W. 1987, ApJ, 319, 180
Karakas, A. I., & Lattanzio, J. C. 2014, PASA, 31, e030
Karakas, A. I., & Lugaro, M. 2016, ApJ, 825, 26
Karakas, A. I., Lugaro, M., Carlos, M., et al. 2018, MNRAS, 477, 421
Karinkuzhi, D., Goswami, A., Sridhar, N., Masseron, T., & Purandardas, M. 2018, MNRAS, 476, 3086
Kobulnicky, H. A., Nordsieck, K. H., Burgh, E. B., et al. 2003, in Instrument Design and Performance for Optical/Infrared Ground-based, eds. M. Iye & A. F. M. Moorwood Telescopes, Proc. SPIE, 4841, 1634
Kurucz, R. L. 1991, in Stellar Atmospheres: Beyond Classical Models, eds. L. Crivellari, I. Hubeny, & D. G. Hummer (Berlin: Springer Science & Business Media), NATO ASIC Proc., 341, 441
Lebzelter, T., & Hron, J. 2003, A&A, 411, 533
Madonna, S., García-Rojas, J., Sterling, N. C., et al. 2017, MNRAS, 471, 1341
Madonna, S., Bautista, M. A., Dinerstein, H., et al. 2018, ApJL, 861, L8
Mamajek, E. E., Torres, G., Prsa, A., et al. 2015, ArXiv e-prints [arXiv:1510.06262]
Masseron, T., Merle, T., & Hawkins, K. 2016, Astrophysics Source Code Library [record ascl:1605.004]
McClure, R. D. 1983, ApJ, 268, 264
McClure, R. D., Fletcher, J. M., & Nemec, J. M. 1980, ApJ, 238, L35
McClure, R. D., & Woodsworth, A. W. 1990, ApJ, 352, 709
Merle, T., Jorissen, A., Van Eck, S., Masseron, T., & Van Winckel, H. 2016, A&A, 586, A151
Merrill, P. W. 1952, ApJ, 116, 21
Miller Bertolami, M. M. 2016, A&A, 588, A25
Miszalski, B., Boffin, H. M. J., Frew, D. J., et al. 2012, MNRAS, 419, 39
Miszalski, B., Boffin, H. M. J., Jones, D., et al. 2013a, MNRAS, 436, 3068
Miszalski, B., Boffin, H. M. J., & Corradi, R. L. M. 2013b, MNRAS, 428, L39
Mohamed, S., & Podsiadlowski, P. 2007, in 15th European Workshop on White Dwarfs, eds. R. Napiwotzki & M. R. Burleigh, ASP Conf. Ser., 372, 397
Nagae, T., Oka, K., Matsuda, T., et al. 2004, A&A, 419, 335
Neyskens, P., van Eck, S., Jorissen, A., et al. 2015, Nature, 517, 174
Palmeri, P., Quinet, P., Biémont, É., et al. 2007, MNRAS, 374, 63
Rix, H.-W., & Bovy, J. 2013, A&ARv, 21, 61
Saladino, M. I., Pols, O. R., van der Helm, E., Pelupessy, I., & Portegies Zwart, S. 2018, A&A, 618, A50
Smiljanic, R., Barbuy, B., de Medeiros, J. R., & Maeder, A. 2006, Rev. Mex. Astron. Astrofis. Conf. Ser., 26, 45
Sneden, C., Lucatello, S., Ram, R. S., Brooke, J. S. A., & Bernath, P. 2014, ApJS, 214, 26
Tabernero, H. M., Dorda, R., Negueruela, I., & González-Fernández, C. 2018, MNRAS, 476, 3106
Theuns, T., Boffin, H. M. J., & Jorissen, A. 1996, MNRAS, 280, 1264
Thevenin, F., & Jasniewicz, G. 1997, A&A, 320, 913
Tylenda, R., Acker, A., Stenholm, B., Gleizes, F., & Raytchev, B. 1991, A&AS, 89, 77
Tyndall, A. A., Jones, D., Boffin, H. M. J., et al. 2013, MNRAS, 436, 2082
Van Eck, S., & Jorissen, A. 1999, A&A, 345, 127
Werner, K., & Herwig, F. 2006, PASP, 118, 183
Wray, J. D. 1966, Ph.D. Thesis, Northwestern University, IL, USA

Appendix A: Additional figures and tables

Table A.1. Observation log for the UVES observations.

Start time (UT)	λ (Å)	Exp. time (s)	*S/N*
2014-04-03 02:42:47	5654–9465	1500	14.8
2014-04-03 02:42:51	3732–5000	1500	3.7
2014-04-03 03:08:39	5654–9465	1500	14.1
2014-04-03 03:08:39	3732–5000	1500	3.3
2014-04-03 03:36:22	5654–9465	1500	12.6
2014-04-03 03:36:26	3732–5000	1500	3.1
2014-04-03 04:02:13	5654–9465	1500	14.5
2014-04-03 04:02:14	3732–5000	1500	3.7
2014-04-04 00:40:42	5654–9465	1500	13.5
2014-04-04 00:40:46	3732–5000	1500	3.1
2014-04-04 01:06:34	5654–9465	1500	13.1
2014-04-04 01:06:34	3732–5000	1500	2.9
2014-04-04 01:34:52	5654–9465	1500	14.8
2014-04-04 01:34:59	3732–5000	1500	3.7
2014-04-04 02:00:47	3732–5000	1500	3.5
2014-04-04 02:00:47	5654–9465	1500	14.8
2014-04-04 02:32:05	5654–9465	1500	14.5
2014-04-04 02:32:11	3732–5000	1500	3.2
2014-04-04 02:57:59	3732–5000	1500	3.3
2014-04-04 02:58:00	5654–9465	1500	14.1
2014-04-13 02:30:36	5654–9465	1450	12.9
2014-04-13 02:30:40	3732–5000	1450	2.9
2014-04-13 02:55:38	3732–5000	1450	3.2
2014-04-13 02:55:39	5654–9465	1450	13.7
2014-04-15 00:20:10	5654–9465	1450	14.3
2014-04-15 00:20:14	3732–5000	1450	3.0
2014-04-15 00:45:11	5654–9465	1450	11.3
2014-04-15 00:45:12	3732–5000	1450	2.4
2014-04-15 01:10:37	5654–9465	1450	12.9
2014-04-15 01:10:41	3732–5000	1450	2.7
2014-04-15 01:35:39	3732–5000	1450	2.9
2014-04-15 01:35:39	5654–9465	1450	13.4
2014-04-15 02:01:20	5654–9465	1500	13.1
2014-04-15 02:01:24	3732–5000	1500	2.8
2014-04-15 02:27:11	5654–9465	1500	13.1
2014-04-15 02:27:12	3732–5000	1500	2.6

Table A.2. Diagnostic lines used for the determination of stellar parameters.

λ interval (Å)	$\lambda_{\rm line}$ (Å)	Ion	$E_{\rm low}$ (cm^{-1})	$E_{\rm up}$ (cm^{-1})	log gf
4020.400 ± 1.30	4020.400	Sc I	0	24 866	−0.130
4023.690 ± 1.30	4023.690	Sc I	168	25 014	0.210
4045.820 ± 1.30	4045.820	Fe I	11 976	36 686	0.280
4054.544 ± 1.30	4054.544	Sc I	0	24 657	−0.750
4063.605 ± 1.30	4063.605	Fe I	12 561	37 163	0.072
4071.740 ± 1.30	4071.740	Fe I	12 969	37 521	−0.022
4082.390 ± 1.30	4082.390	Sc I	168	24 657	−0.444
4233.170 ± 1.30	4233.170	Fe II	20 831	44 447	−1.995
4271.760 ± 1.30	4271.760	Fe I	11 976	35 379	−0.164
4305.820 ± 1.40	4305.720	Sc II	4803	28 021	−1.200
	4305.910	Ti I	6843	30 060	0.300
4307.900 ± 1.30	4307.900	Fe I	12 561	35 768	−0.300
4314.080 ± 1.30	4314.080	Sc II	4988	28 161	−0.220
4320.750 ± 1.30	4320.750	Sc II	4883	28 021	−0.100
4325.010 ± 1.30	4325.010	Sc II	4803	27 918	−0.250
4325.760 ± 1.30	4325.760	Fe I	12 969	36 079	−0.300
4351.769 ± 1.30	4351.769	Fe II	21 812	44 785	−2.100
4374.472 ± 1.30	4374.472	Sc II	4988	27 841	−0.640
4383.550 ± 1.30	4383.550	Fe I	11 976	34 782	0.200
4395.040 ± 1.30	4395.040	Ti II	8744	31 491	−0.660
4400.398 ± 1.30	4400.398	Sc II	4883	27 602	−0.480
4404.761 ± 1.30	4404.761	Fe I	12 561	35 257	−0.142
4415.560 ± 1.30	4415.560	Sc II	4803	27 444	−0.510
4443.812 ± 1.30	4443.812	Ti II	8710	31 207	−0.690
4468.500 ± 1.30	4468.500	Ti II	9118	31 491	−0.270
4501.273 ± 1.30	4501.273	Ti II	8998	31 207	−0.684
4522.634 ± 1.30	4522.634	Fe II	22 939	45 044	−2.119
4534.400 ± 2.50	4533.239	Ti I	6843	28 896	0.563
	4533.969	Ti II	9976	32 025	−0.612
	4534.778	Ti I	6743	28 788	0.376
	4535.570	Ti I	6661	28 703	0.172
4549.550 ± 1.45	4549.474	Fe II	22 810	44 785	−1.957
	4549.617	Ti II	12 775	34 748	−0.110
4555.893 ± 1.30	4555.893	Fe II	22 810	44 754	−2.281
4563.761 ± 1.30	4563.761	Ti II	9851	31 757	−0.795
4571.968 ± 1.30	4571.968	Ti II	12 677	34 543	−0.209
4629.339 ± 1.30	4629.339	Fe II	22 637	44 233	−2.379
4670.407 ± 1.30	4670.407	Sc II	10 945	32 350	−0.518
4920.000 ± 5.00	4915.233	Ti I	15 220	35 560	−0.945
	4918.954	Fe I	33 507	53 831	−0.672
	4918.993	Fe I	23 111	43 435	−0.365
	4919.867	Ti I	17 424	37 744	−0.260
	4920.502	Fe I	22 846	43 163	0.058
	4921.769	Ti I	17 540	37 852	−0.005
	4922.827	Sc I	16 023	36 331	−0.418
	4923.927	Fe II	23 318	43 621	−1.319
4981.732 ± 1.30	4981.732	Ti I	6843	26 911	0.586
5701.545 ± 1.00	5701.545	Fe I	20 641	38 175	−1.565
5705.464 ± 1.00	5705.466	Fe I	34 692	52 214	−1.581
5732.000 ± 1.30	5731.762	Fe I	34 329	51 771	−1.174
	5732.275	Fe I	40 257	57 698	−1.191
5747.954 ± 1.00	5747.954	Fe I	37 163	54 555	−0.599
5861.108 ± 1.00	5861.107	Fe I	34 547	51 604	−2.761
5934.654 ± 1.00	5934.653	Fe I	31 686	48 532	−1.192
5952.800 ± 1.00	5952.716	Fe I	32 134	48 928	−2.513
	5952.889	Fe I	34 040	50 833	−3.725
6151.617 ± 1.00	6151.617	Fe I	17 550	33 802	−3.582
6165.360 ± 1.00	6165.361	Fe I	33 413	49 628	−1.667

Notes. If no interval is given, the line belongs to the previous interval.

Table A.2. continued.

λ interval (Å)	λ_{line} (Å)	Ion	E_{low} (cm^{-1})	E_{up} (cm^{-1})	log gf
6170.500 ± 1.00	6170.504	Fe I	38 678	54 880	−0.654
	6171.006	Fe I	38 175	54 376	−1.788
6173.334 ± 1.00	6173.341	Fe I	17 927	34 122	−3.081
	6173.642	Fe I	35 856	52 050	−3.413
6191.500 ± 1.00	6191.558	Fe I	19 621	35 768	−1.287
6210.658 ± 1.30	6210.658	Sc I	0	16 097	−1.090
6265.132 ± 1.00	6265.141	Fe I	17 550	33 507	−2.834
6305.657 ± 1.30	6305.657	Sc I	168	16 023	−0.950
6318.000 ± 1.00	6318.018	Fe I	19 788	35 612	−2.338
6336.823 ± 1.00	6336.830	Fe I	29 733	45 509	−1.260
6408.000 ± 1.00	6407.643	Fe I	32 874	48 476	−3.620
	6408.026	Fe I	29 733	45 334	−1.230
	6408.332	Fe I	35 379	50 980	−3.563
6475.624 ± 1.00	6475.632	Fe I	20 641	36 079	−3.070
6481.870 ± 1.00	6481.878	Fe I	18 378	33 802	−3.080
6807.000 ± 1.00	6806.622	Fe I	44 023	58 710	−1.744
	6806.843	Fe I	21 999	36 686	−3.210
	6807.288	Fe I	42 533	57 219	−2.735
6810.262 ± 1.00	6810.262	Fe I	37 158	51 837	−1.120
8434.957 ± 1.30	8434.957	Ti I	6843	18 695	−0.886
8514.400 ± 1.90	8514.072	Fe I	17 727	29 469	−2.229
	8515.109	Fe I	24 339	36 079	−2.073
8518.300 ± 1.50	8518.028	Ti I	17 215	28 952	−1.250
	8518.352	Ti I	15 157	26 893	−1.089
8582.350 ± 1.35	8582.258	Fe I	24 119	35 768	−2.133
8611.800 ± 0.90	8611.803	Fe I	22 947	34 556	−1.900
8679.000 ± 2.10	8678.997	Fe I	48 516	60 035	−3.806
	8679.632	Fe I	40 052	51 570	−1.512
8682.900 ± 1.30	8682.979	Ti I	8492	20 006	−1.941
8688.950 ± 1.65	8688.624	Fe I	17 550	29 056	−1.212
8692.000 ± 1.00	8692.331	Ti I	8437	19 938	−2.295
8711.500 ± 3.00	8710.174	Mg I	47 841	59 319	−1.550
	8710.392	Fe I	39 626	51 103	−0.555
	8712.676	Mg I	47 844	59 319	−1.670
	8713.188	Fe I	23 784	35 257	−3.148
8730.750 ± 0.95	8730.497	Ti I	27 026	38 477	−2.024
8735.250 ± 1.75	8734.712	Ti I	8492	19 938	−2.384
	8736.020	Mg I	47 957	59 401	−0.690
8742.250 ± 0.75	8742.446	Si I	47 352	58 787	−0.630
8757.200 ± 1.60	8757.187	Fe I	22 947	34 363	−2.026
8792.850 ± 1.35	8793.342	Fe I	37 163	48 532	−0.196
8806.000 ± 2.70	8806.756	Mg I	35 051	46 403	−0.137
	8808.170	Fe I	40 405	51 754	−1.109
8824.360 ± 1.15	8824.220	Fe I	17 727	29 056	−1.540
8838.750 ± 1.25	8838.428	Fe I	23 052	34 363	−1.980

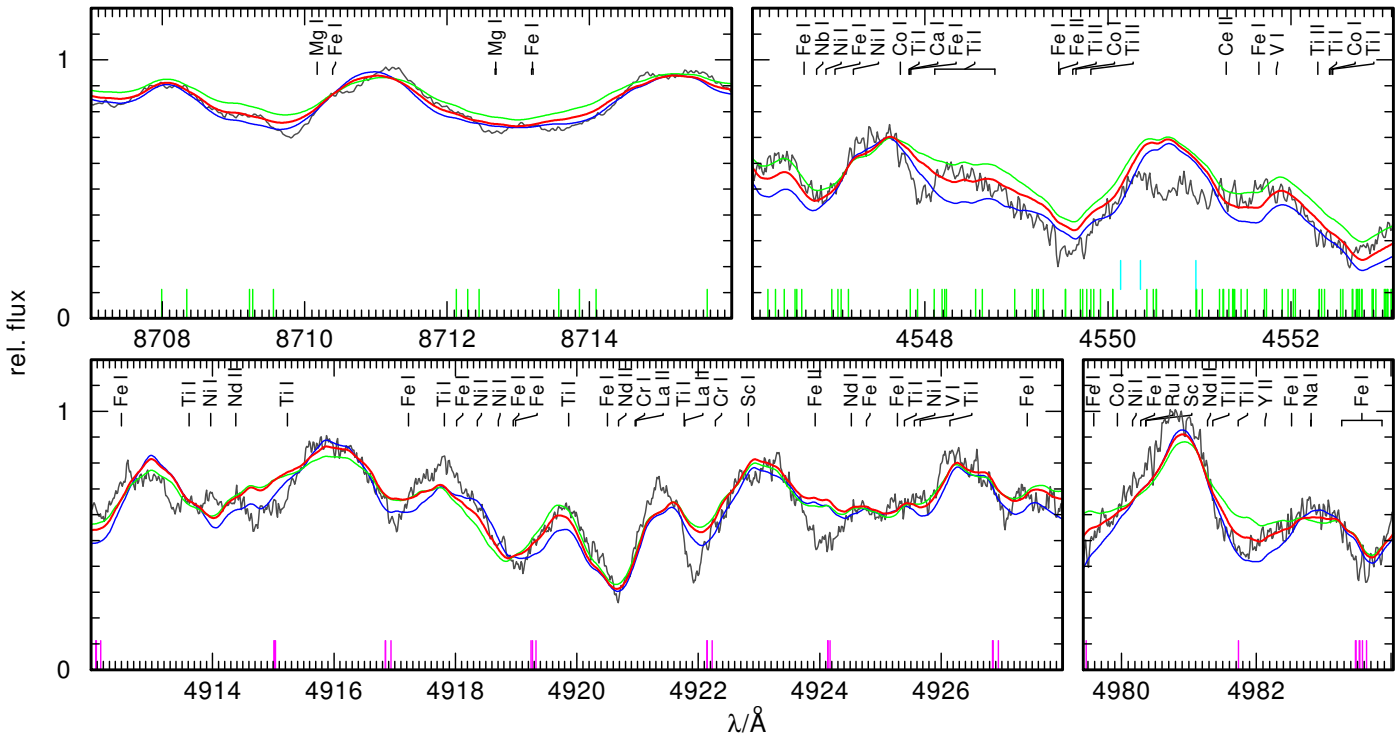

Fig. A.1. Observation (gray) of Hen 2–39 compared to model spectra with $T_{\rm eff}$ = 4000, 4250, 4500 K (blue, red, green) for selected regions that were used for the determination of $T_{\rm eff}$. CN, C_2, and CH absorption lines are indicated at the bottom in green, purple, and cyan, respectively. All absorption lines that appear with an equivalent width ≥ 20 mÅ in the calculated spectrum are indicated.

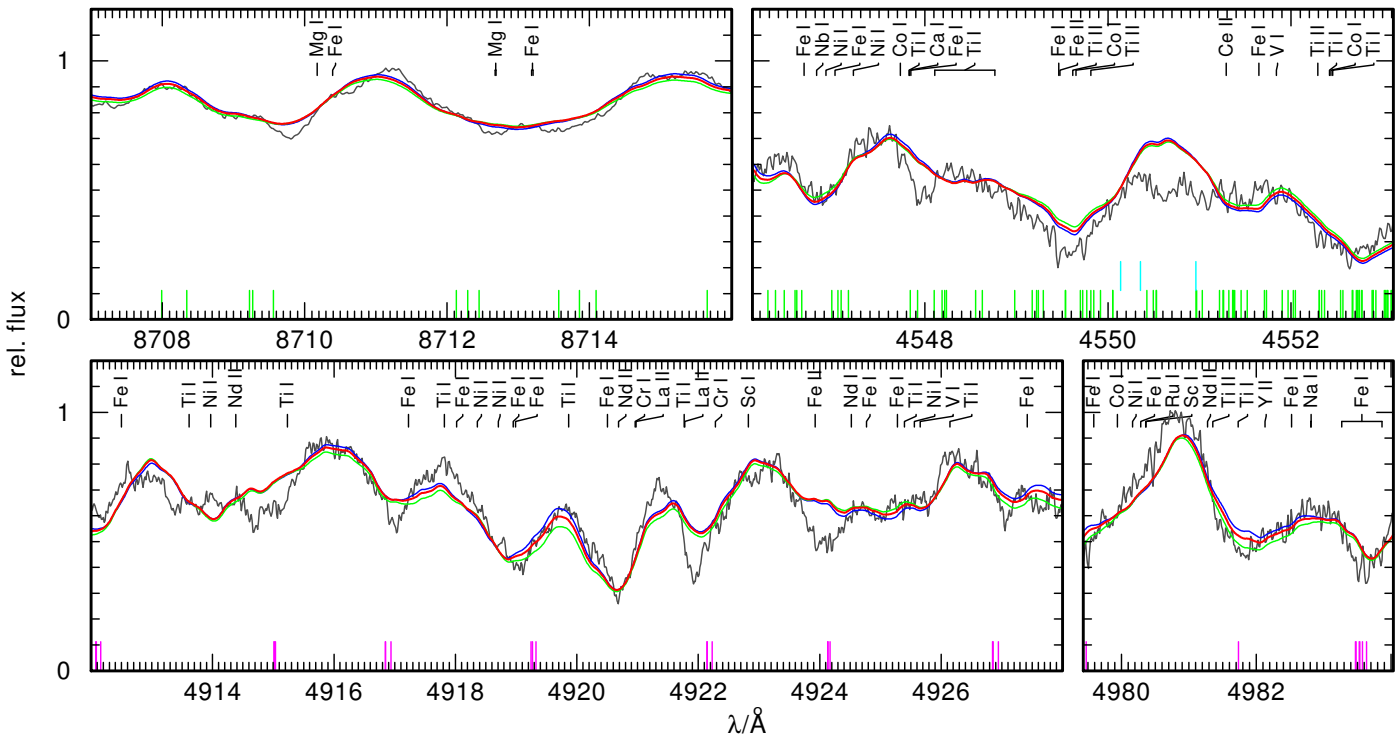

Fig. A.2. Like Fig. A.1, for log g = 2.0, 2.5, 3.0 (blue, red, green).

Table A.3. Diagnostic lines used for our determination of element abundances.

$\lambda_{\rm line}$ (Å)	Ion	$E_{\rm low}$ (cm^{-1})	$E_{\rm up}$ (cm^{-1})	log gf
5889.951	Na I	0	16 973	0.101
5895.924	Na I	0	16 956	−0.197
6696.185	Al I	32 435	47 365	−1.576
6698.670	Al I	25 438	40 272	−1.960
6698.673	Al I	25 348	40 272	−1.647
6905.646	Al I	32 435	46 912	−1.287
7083.969	Al I	32 435	46 548	−1.111
7361.568	Al I	32 435	46 016	−0.903
7835.309	Al I	32 435	45 195	−0.649
7836.134	Al I	32 437	45 195	−0.494
7836.134	Al I	32 437	45 195	−1.795
8773.896	Al I	32 437	43 831	−0.161
8773.898	Al I	32 437	43 831	−1.462
7725.046	S I	9239	22 180	−6.000
7698.974	K I	0	12 985	−0.170
5857.451	Ca I	23 652	40 720	0.257
6161.297	Ca I	20 349	36 575	−1.293
6162.173	Ca I	15 316	31 539	−0.167
6169.042	Ca I	20 349	36 555	−0.804
6169.563	Ca I	20 371	36 575	−0.527
6343.308	Ca I	35 819	51 579	0.845
6361.786	Ca I	35 897	51 611	0.954
6449.810	Ca I	20 335	35 835	−0.550
6455.600	Ca I	20 349	35 835	−1.350
6462.570	Ca I	20 349	35 819	0.310
6471.668	Ca I	20 371	35 819	−0.680
6493.788	Ca I	20 335	35 730	0.140
6499.654	Ca I	20 349	35 730	−0.650
8498.023	Ca II	13 650	25 414	−1.312
8542.091	Ca II	13 711	25 414	−0.362
8662.141	Ca II	13 650	25 192	−0.623
4729.200	Sc I	11 520	32 659	−0.502
4729.236	Sc I	11 558	32 697	−0.385
4734.105	Sc I	11 520	32 637	−0.110
4753.161	Sc I	0	21 033	−1.658
4779.348	Sc I	168	21 086	−1.613
4791.511	Sc I	168	21 033	−2.075
5700.164	Sc I	11 558	29 096	0.290
5717.307	Sc I	11 610	29 096	−0.505
5724.107	Sc I	11 558	29 023	−0.627
6305.657	Sc I	168	16 023	−0.950
6378.807	Sc I	0	15 673	−2.632
6413.324	Sc I	168	15 757	−2.677
4314.080	Sc II	4988	28 161	−0.220
4431.370	Sc II	4883	27 444	−1.830
6279.740	Sc II	12 102	28 021	−1.265
6309.920	Sc II	12 074	27 918	−1.630
4455.320	Ti I	11 640	34 079	0.480
4518.023	Ti I	6661	28 788	−0.252
4522.796	Ti I	6599	28 703	−0.265
4533.239	Ti I	6843	28 896	0.563
4534.778	Ti I	6743	28 788	0.376
4535.570	Ti I	6661	28 703	0.172
4535.916	Ti I	6599	28 639	−0.026
4536.043	Ti I	6557	28 596	−0.129
4548.765	Ti I	6661	28 639	−0.274
4552.456	Ti I	6743	28 703	−0.262
4656.468	Ti I	0	21 469	−1.344
4681.908	Ti I	387	21 740	−1.129

Table A.3. continued.

$\lambda_{\rm line}$ (Å)	Ion	$E_{\rm low}$ (cm^{-1})	$E_{\rm up}$ (cm^{-1})	log gf
4981.732	Ti I	6843	26 911	0.586
6258.713	Ti I	11 777	27 750	−0.090
8382.530	Ti I	6599	18 525	−1.632
8426.506	Ti I	6661	18 525	−1.253
4025.140	Ti II	4898	29 734	−1.960
4394.060	Ti II	9851	32 603	−1.669
4395.040	Ti II	8744	31 491	−0.660
4417.720	Ti II	9396	32 026	−1.240
4468.500	Ti II	9118	31 491	−0.270
4549.617	Ti II	12 775	34 748	−0.110
4563.761	Ti II	9851	31 757	−0.795
4352.870	V I	553	23 520	−0.800
4379.240	V I	2425	25 254	0.600
4384.706	V I	553	23 353	−1.905
4384.720	V I	2311	25 112	0.000
4395.230	V I	2153	24 899	0.320
4406.072	V I	8579	31 268	−1.000
4406.640	V I	2425	25 112	−0.280
4407.637	V I	2311	24 993	−0.840
4408.200	V I	2220	24 899	−0.100
4408.508	V I	2112	24 789	−0.610
4408.512	V I	2153	24 830	−0.130
4408.520	V I	2112	24 789	−0.820
4419.940	V I	2220	24 839	−1.480
4420.120	V I	2153	24 771	−2.252
4459.760	V I	2311	24 728	−0.570
4460.290	V I	2425	24 839	−0.240
5698.520	V I	8579	26 122	−0.036
5727.048	V I	8716	26 172	0.088
5737.059	V I	8579	26 004	−0.675
6135.361	V I	8476	24 771	−0.750
6150.157	V I	2425	18 680	−1.277
6243.105	V I	2425	18 438	−0.878
6274.649	V I	2153	18 086	−1.657
6531.440	V I	9825	25 131	−1.320
6531.466	V I	23 935	39 241	−2.931
4274.800	Cr I	0	23 386	−0.231
4274.891	Cr I	24 200	47 586	−2.233
4289.720	Cr I	0	23 305	−0.360
4527.332	Cr I	20 524	42 606	−0.906
4535.695	Cr I	20 524	42 565	−0.570
4600.741	Cr I	8095	29 825	−1.305
4600.775	Cr I	23 934	45 663	−2.354
4652.152	Cr I	8095	29 585	−1.026
4708.018	Cr I	25 549	46 783	0.110
4718.426	Cr I	25 771	46 959	0.097
4829.314	Cr I	20 524	41 225	−1.630
4829.372	Cr I	20 524	41 225	−0.787
5783.886	Cr I	26 796	44 081	−0.177
5787.965	Cr I	26 796	44 069	0.033
5791.006	Cr I	26 788	44 051	0.324
6924.179	Cr I	27 820	42 258	−0.135
7462.378	Cr I	23 499	36 896	−0.040
8947.180	Cr I	25 039	36 212	−0.724
4554.988	Cr II	32 837	54 784	−1.249
4235.295	Mn I	23 297	46 901	−0.030
4458.260	Mn I	24 788	47 212	−0.042
4761.512	Mn I	23 819	44 815	−0.138
4762.367	Mn I	23 297	44 289	0.426

Table A.3. continued.

λ_{line} (Å)	Ion	E_{low} (cm^{-1})	E_{up} (cm^{-1})	log gf
4765.846	Mn I	23 720	44 696	−0.077
4766.418	Mn I	23 549	44 523	0.098
4823.524	Mn I	18 705	39 431	0.144
6013.513	Mn I	24 779	41 404	−0.397
4045.820	Fe I	11 976	36 686	0.280
4063.605	Fe I	12 561	37 163	0.072
4063.627	Fe I	33 096	57 698	−0.691
4071.740	Fe I	12 969	37 521	−0.022
4271.760	Fe I	11 976	35 379	−0.164
4325.739	Fe I	0	23 111	−4.815
4325.760	Fe I	12 969	36 079	−0.300
4383.550	Fe I	11 976	34 782	0.200
4404.761	Fe I	12 561	35 257	−0.142
5701.545	Fe I	20 641	38 175	−1.565
4233.113	Fe II	54 871	78 487	−3.448
4233.137	Fe II	74 498	98 115	−2.864
4233.170	Fe II	20 831	44 447	−1.995
4555.893	Fe II	22 810	44 754	−2.281
4813.449	Co I	23 153	43 922	−2.121
4813.467	Co I	25 938	46 707	0.050
6450.247	Co I	13 796	29 295	−1.698
6814.942	Co I	15 774	30 444	−1.700
7052.868	Co I	15 774	29 949	−1.440
4519.979	Ni I	13 521	35 639	−2.570
4715.757	Ni I	28 578	49 778	−0.331
4786.531	Ni I	27 580	48 467	−0.244
4831.169	Ni I	29 084	49 778	−0.291
4918.362	Ni I	30 980	51 306	−0.109
4984.112	Ni I	30 619	50 678	0.226
5892.868	Ni I	16 017	32 982	−2.141
6314.653	Ni I	15 610	31 442	−2.402
6482.810	Ni I	15 610	31 031	−2.630
6914.559	Ni I	15 734	30 192	−2.270
7409.346	Ni I	30 619	44 112	−0.237
7414.500	Ni I	16 017	29 501	−2.570
5700.237	Cu I	13 245	30 784	−2.312
5782.127	Cu I	13 245	30 535	−1.720
4810.528	Zn I	32 890	53 672	−0.137
7800.259	Rb I	0	12 817	0.137
7947.597	Rb I	0	12 579	−0.167
4741.918	Sr I	14 318	35 400	−0.320
4872.488	Sr I	14 504	35 022	−0.200
6504.000	Sr I	18 067	33 442	0.260
7070.070	Sr I	14 899	29 039	−0.180
4235.934	Y I	530	24 131	−0.490
4839.855	Y I	11 532	32 188	0.480
6191.718	Y I	0	16 146	−0.970
6222.578	Y I	0	16 066	−1.700
6435.004	Y I	530	16 066	−0.820
4235.730	Y II	1045	24 647	−1.425
4982.129	Y II	8328	28 394	−1.290
7881.881	Y II	14 833	27 517	−0.570
4236.550	Zr I	0	23 604	−1.000
4772.323	Zr I	5023	25 972	0.040
4784.913	Zr I	5540	26 434	−0.490
5879.782	Zr I	1241	18 244	−1.670
6127.475	Zr I	1241	17 556	−1.060
6134.585	Zr I	0	16 296	−1.280

Table A.3. continued.

$\lambda_{\rm line}$ (Å)	Ion	$E_{\rm low}$ (cm^{-1})	$E_{\rm up}$ (cm^{-1})	log gf
6143.252	Zr I	570	16 844	−1.100
6990.869	Zr I	5023	19 324	−1.220
7102.954	Zr I	5249	19 324	−0.840
8070.115	Zr I	5889	18 277	−0.790
4443.000	Zr II	11 984	34 485	−0.160
4205.303	Nb I	392	24 165	−0.850
4523.397	Nb I	1143	23 244	−0.800
4546.818	Nb I	1587	23 574	−0.750
4573.075	Nb I	2154	24 015	−0.560
4663.818	Nb I	1587	23 023	−0.740
5751.408	Mo I	11 454	28 837	−1.014
5791.839	Mo I	11 454	28 715	−1.046
5858.266	Mo I	11 858	28 924	−0.996
6619.134	Mo I	10 768	25 872	−1.252
4031.626	Tc I	2573	27 370	0.39
4095.668	Tc I	3251	27 660	−0.01
4238.191	Tc I	0	23 588	−0.39
4262.270	Tc I	0	23 455	−0.18
4297.058	Tc I	0	23 265	−0.03
4206.015	Ru I	8084	31 853	−0.480
4385.385	Ru I	7483	30 280	−0.610
4385.645	Ru I	9058	31 853	−0.490
4410.025	Ru I	9184	31 853	−0.380
4460.027	Ru I	8771	31 186	−0.530
4554.517	Ru I	6545	28 495	0.130
4554.029	Ba II	0	21 952	0.170
4934.076	Ba II	0	20 262	−0.150
5853.668	Ba II	4874	21 952	−1.000
6141.713	Ba II	5675	21 952	−0.076
6496.930	Ba II	4874	20 262	0.130
4354.400	La II	7340	30 305	−0.210
4354.412	La II	7395	30 353	−0.500
4526.111	La II	6227	28 315	−0.770
4574.860	La II	1394	23 247	−1.140
4662.498	La II	0	21 442	−1.240
4970.386	La II	2592	22 705	−1.190
5797.565	La II	1971	19 214	−1.410
5805.773	La II	1016	18 236	−1.610
6390.477	La II	2592	18 236	−1.450
4324.785	Ce II	7713	30 829	−0.514
4324.790	Ce II	7662	30 785	−0.050
4386.827	Ce II	1874	24 663	−0.582
4408.851	Ce II	7234	29 909	−0.965
4408.870	Ce II	7179	29 860	0.120
4408.894	Ce II	10 314	32 989	−0.857
4418.780	Ce II	6968	29 592	0.310
4427.916	Ce II	4323	26 900	−0.460
4427.920	Ce II	4275	26 859	−0.610
4427.916	Ce II	4323	26 900	−0.460
4427.920	Ce II	4275	26 859	−0.610
4428.438	Ce II	4266	26 841	−0.657
4444.700	Ce II	8532	31 024	0.110
4483.893	Ce II	6968	29 263	0.010
4483.900	Ce II	6937	29 239	−0.050
4572.278	Ce II	5514	27 378	0.001
4429.254	Pr II	2998	25 569	−0.010
4205.600	Nd II	5086	28 857	0.070
4232.380	Nd II	513	24 134	−1.020
4351.290	Nd II	1470	24 445	−1.210

Table A.3. continued.

$\lambda_{\rm line}$ (Å)	Ion	$E_{\rm low}$ (cm^{-1})	$E_{\rm up}$ (cm^{-1})	log gf
4358.161	Nd II	2585	25 524	−0.280
4358.170	Nd II	4512	27 449	−0.060
4358.161	Nd II	2585	25 524	−0.280
4358.170	Nd II	4512	27 449	−0.060
4385.660	Nd II	1650	24 445	−0.550
4391.100	Nd II	2585	25 352	−0.240
4414.440	Nd II	513	23 160	−0.840
4446.390	Nd II	1650	24 134	−0.500
4680.737	Nd II	513	21 872	−1.260
4706.543	Nd II	0	21 241	−0.880
4715.586	Nd II	1650	22 850	−1.070
4820.339	Nd II	1650	22 390	−1.240
4229.713	Sm II	327	23 962	−1.224
4390.855	Sm II	1489	24 257	−0.804
4420.524	Sm II	2689	25 304	−0.695
4433.890	Sm II	3499	26 046	−0.572
4676.902	Sm II	327	21 702	−1.407
4522.581	Eu II	1669	23 774	−0.678
6645.064	Eu II	11 128	26 173	0.204
7426.569	Eu II	10 313	23 774	−0.149
4053.640	Gd I	999	25 661	0.297
4191.075	Gd II	3444	27 298	−0.653
4394.720	Gd II	6533	29 288	−0.060
4394.720	Gd II	6605	29 353	−1.783
4752.526	Tb II	0	21 036	−0.816
4186.819	Dy I	0	23 878	0.693
4077.966	Dy II	828	25 343	−0.058
4409.383	Dy II	0	22 673	−1.420
4301.596	Er II	0	23 241	−1.487
4419.608	Er II	13 572	36 192	0.386
7131.816	Hf I	0	14 018	−1.690
7237.112	Hf I	4568	18 382	−0.840
4294.605	W I	2951	26 230	−0.735
4659.853	W I	0	21 454	−1.900
4260.848	Os I	0	23 463	−1.440
4420.468	Os I	0	22 616	−1.530
4793.993	Os I	4159	25 013	−1.990

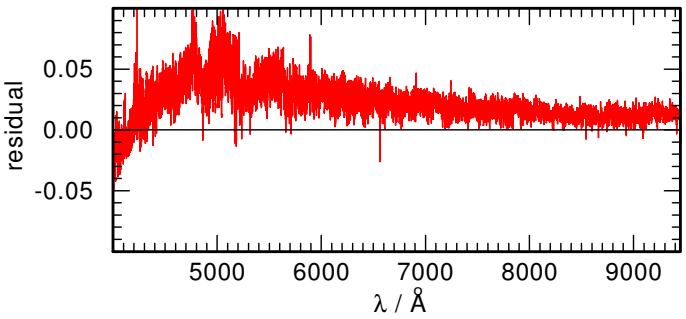

Fig. A.3. Difference between the newly computed C-rich test model (model 2) and the O-rich model from the available grid (model 1) for $T_{\rm eff}$ = 4250 K and log g = 2.5.

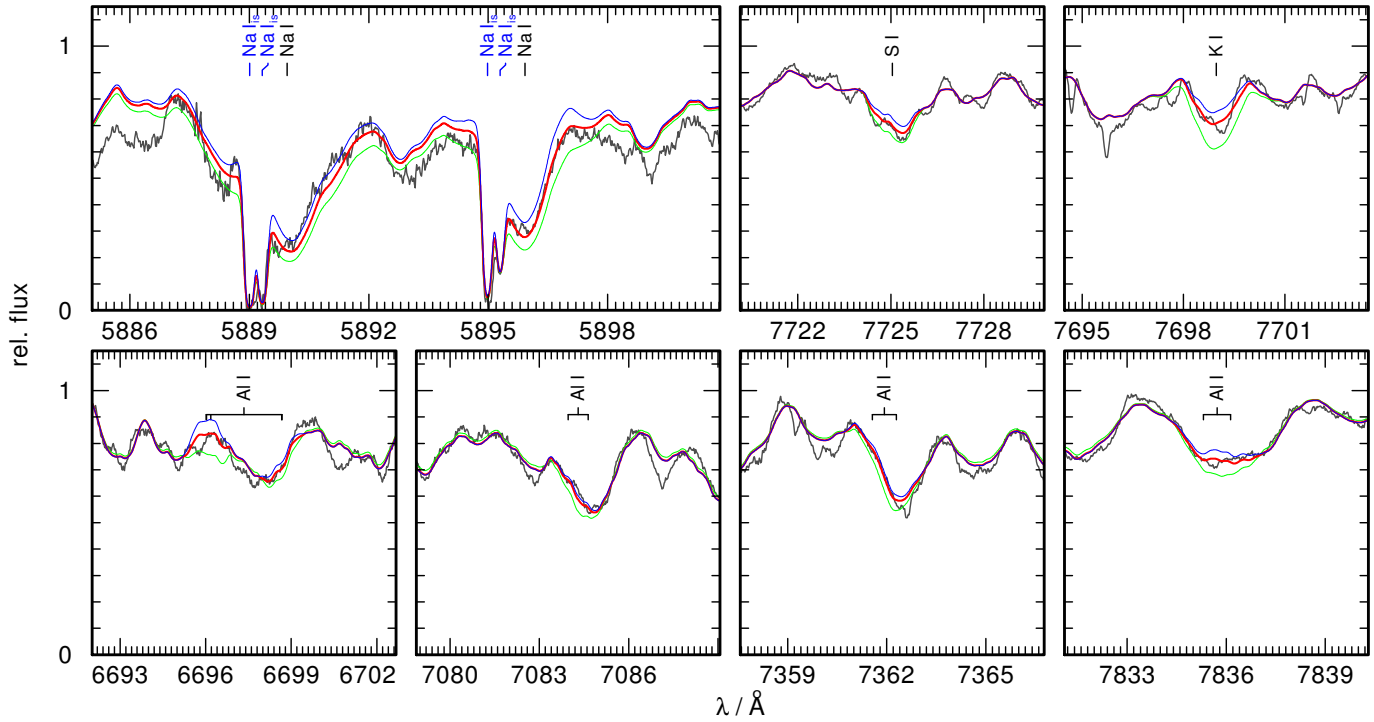

Fig. A.4. Observation (gray) of Hen 2−39 compared to model spectra for selected regions around absorption lines of Na I for [Na/Fe] = 0.35, 0.05, −0.25 (green, red, and blue, respectively), S I for [S/Fe] = 2.17, 1.17, 0.17, Al I for [Al/Fe] = 0.68, −0.32, −1.32, and K I for [K/Fe] = 1.07, 0.07, −0.93. Interstellar absorption lines are indicated with blue marks.

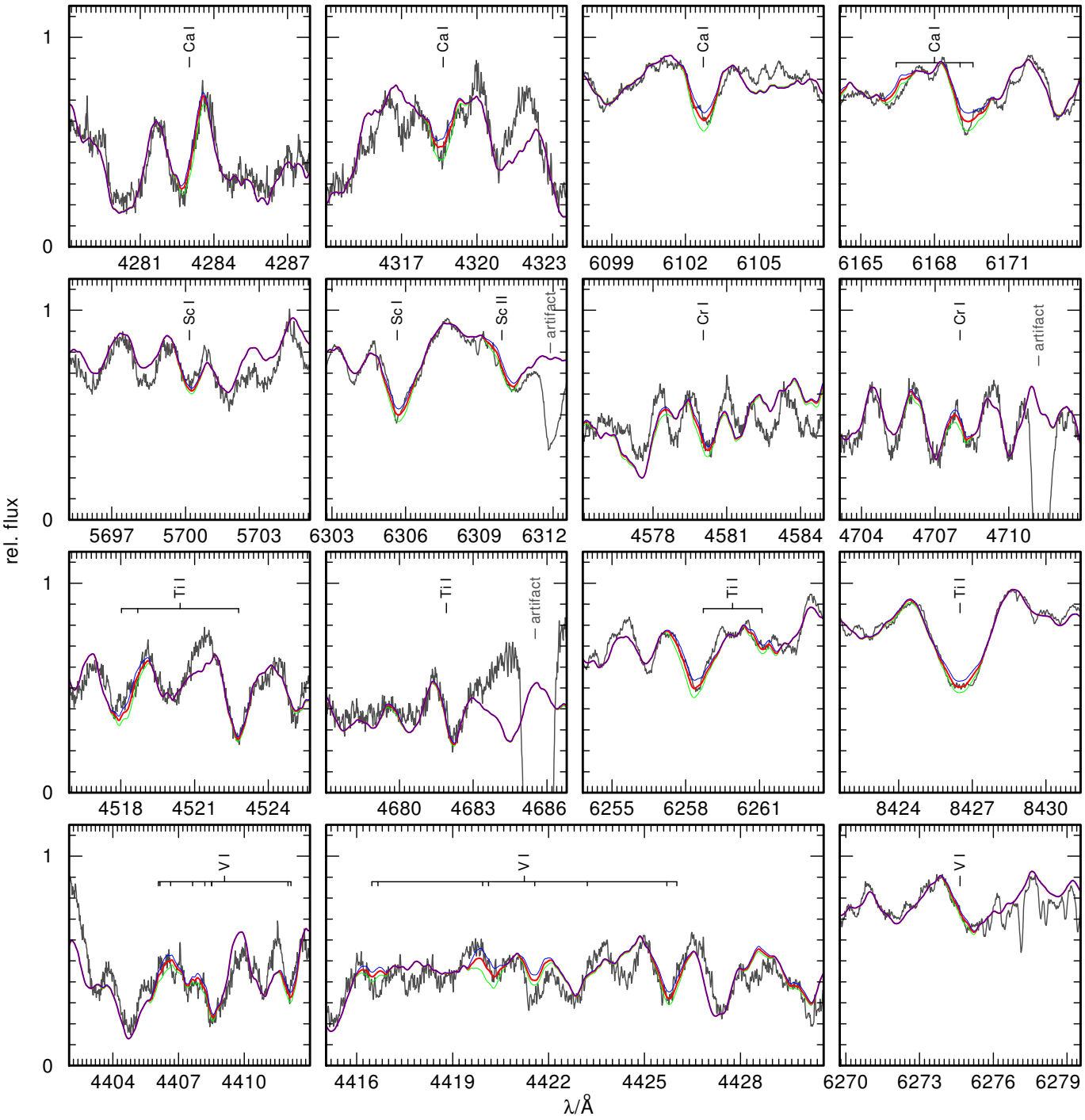

Fig. A.5. Observation (gray) of Hen 2−39 compared to model spectra for selected regions around absorption lines of Ca I for [Ca/Fe] = 0.41, −0.09, −0.59 (green, red, and blue, respectively), Sc I for [Sc/Fe] = 0.08, −0.42, −0.92, Cr I for [Cr/Fe] = 0.32, −0.18, −0.68, Ti I for [Ti/Fe] = −0.13, −0.63, −1.13, and V I for [V/Fe] = −0.05, −0.55, −1.05. Artifacts arising from the overcorrection of nebula lines are indicated.

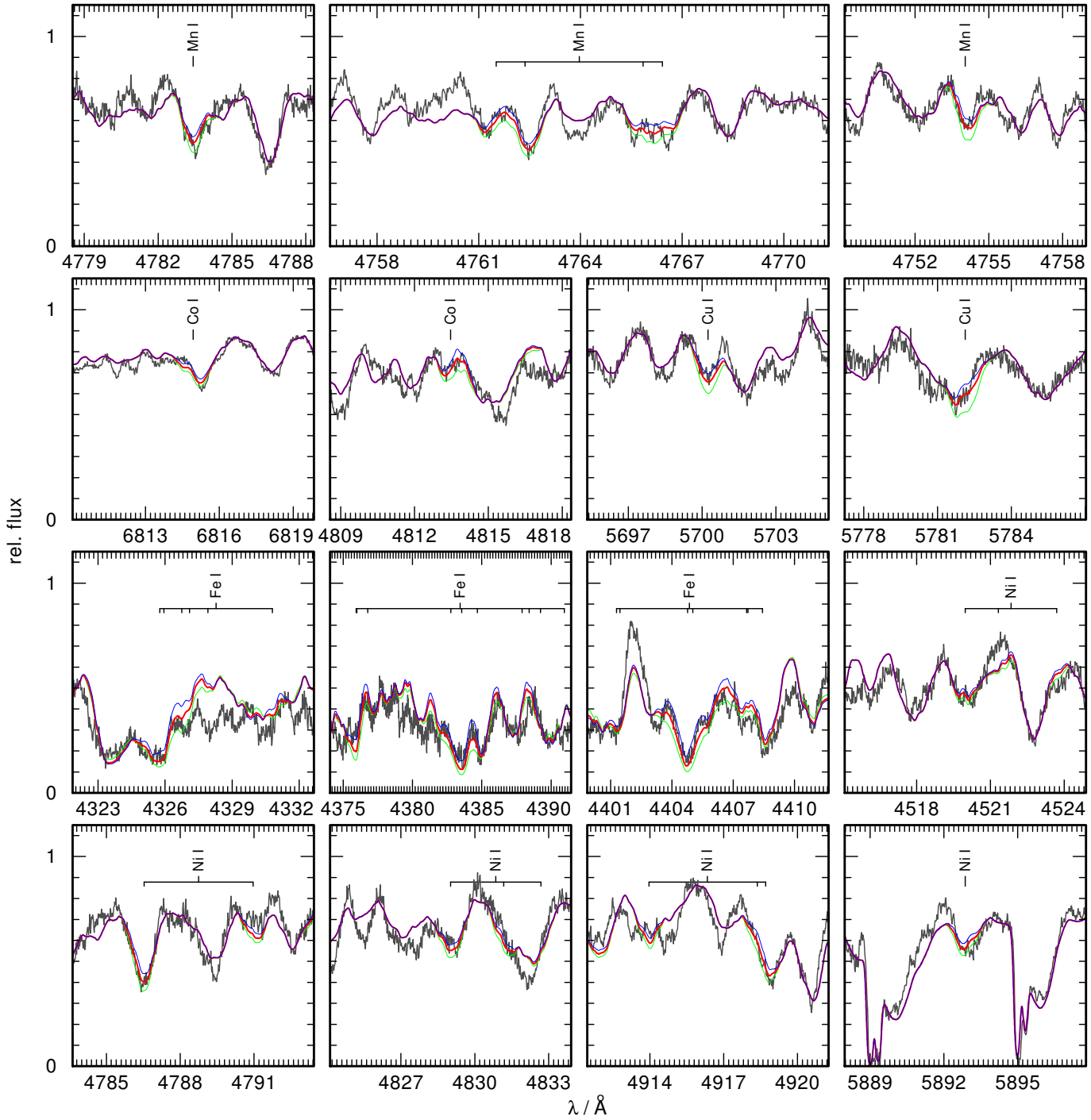

Fig. A.6. Observation (gray) of Hen 2−39 compared to model spectra for selected regions around absorption lines of Mn I for [Mn/Fe] = 0.52, 0.02, −0.48 (green, red, and blue, respectively), Co I for [Co/Fe] = 1.03, 0.53, 0.03, Cu I for [Cu/Fe] = 2.18, 1.18, 0.18, Fe I for [Fe/H] = 0.15, −0.35, −0.85, and Ni I for [Ni/Fe] = 1.09, 0.59, 0.09. Interstellar absorption lines are indicated with blue marks.

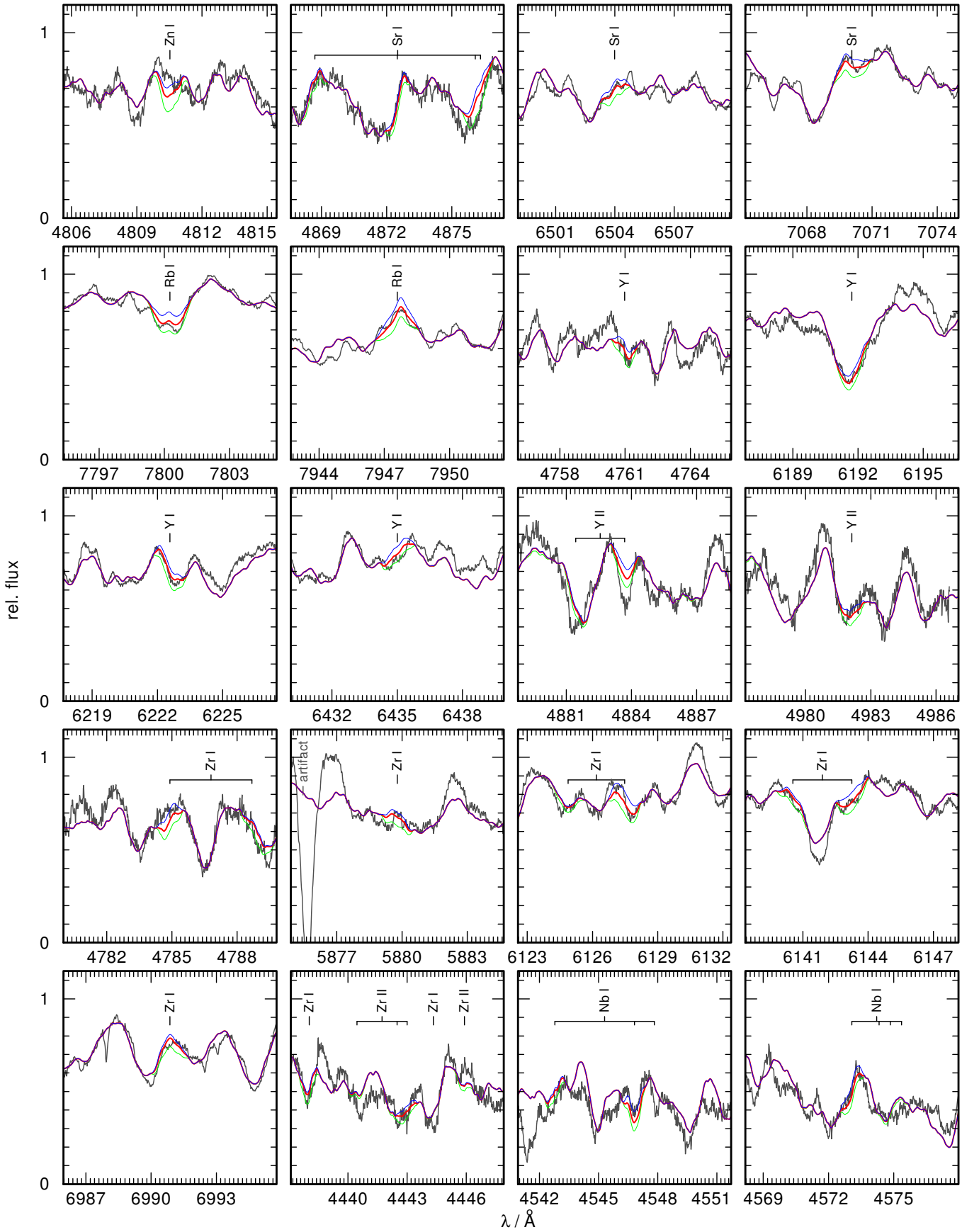

Fig. A.7. Observation (gray) of Hen 2−39 compared to model spectra for selected regions around absorption lines of Zn I for [Zn/Fe] = 2.51, 1.51, 0.51 (green, red, and blue, respectively), Sr I for [Sr/Fe] = 1.99, 0.99, −0.01, Rb I for [Rb/Fe] = 2.41, 1.41, 0.41, Y I and Y II for [Y/Fe] = 1.37, 0.37, −0.63, Zr I and Zr II for [Zr/Fe] = 1.19, 0.19 − 0.81, and Nb I for [Nb/Fe] = 1.97, 0.97, −0.03. Artifacts arising from the overcorrection of nebula lines are indicated.

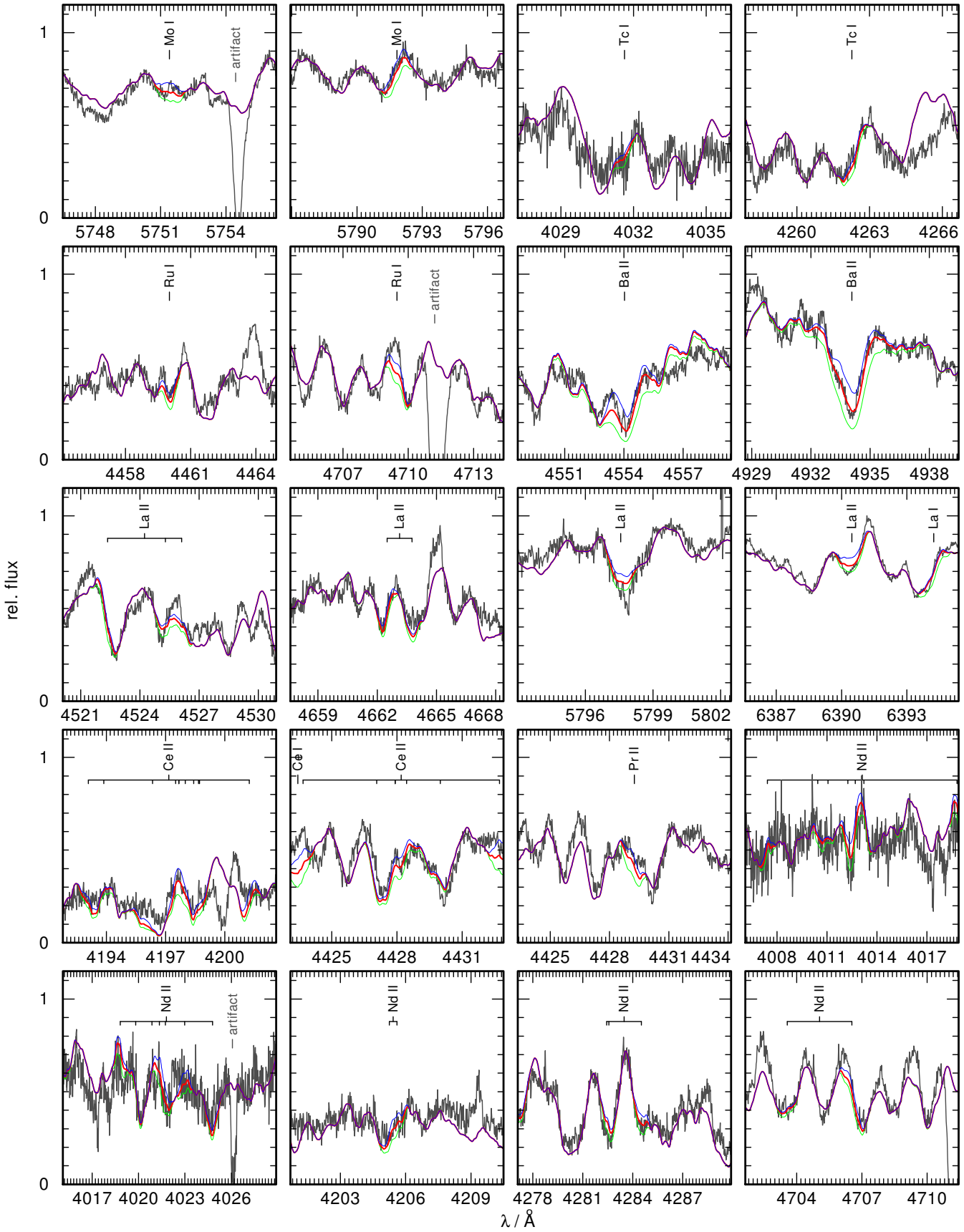

Fig. A.8. Observation (gray) of Hen 2−39 compared to model spectra for selected regions around absorption lines of Mo I for [Mo/Fe] = 2.35, 1.35, 0.35 (green, red, and blue, respectively), Tc I for $\log \epsilon_{\mathrm{Tc}}$ = 3.5, 2.5, 1.5, Ru I for [Ru/Fe] = 3.05, 2.05, 1.05, Ba II [Ba/Fe] = 2.29, 1.79, 1.27, La II for [La/Fe] = 2.44, 1.44, 0.44, Ce I and Ce II for [Ce/Fe] = 3.29, 2.29, 1.29, Pr II for [Pr/Fe] = 3.68, 2.68, 1.68, and Nd I for [Nd/Fe] = 1.76, 0.76, −0.24. Artifacts arising from the overcorrection of nebula lines are indicated.

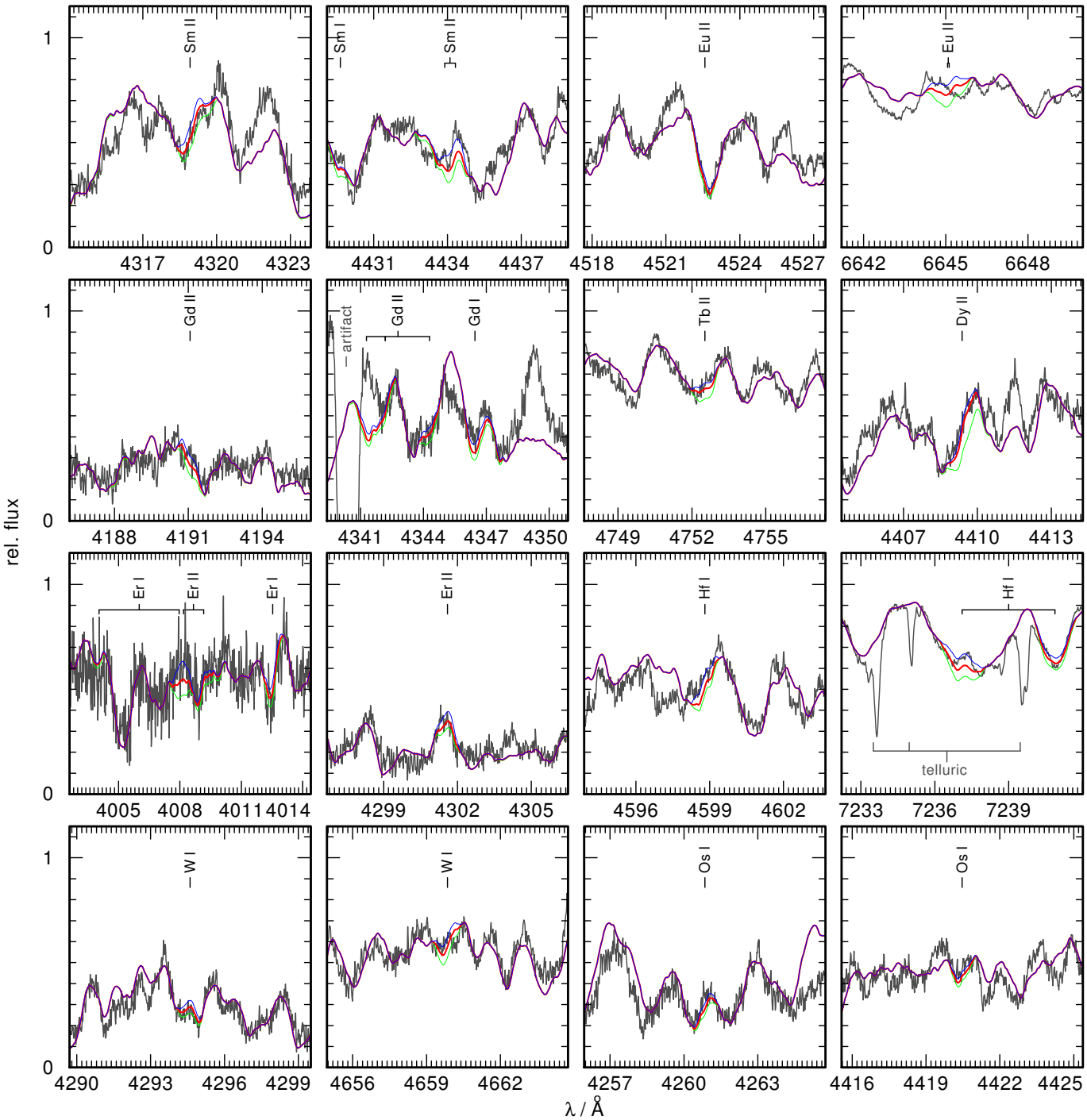

Fig. A.9. Observation (gray) of Hen 2−39 compared to model spectra for selected regions around absorption lines of Sm I and Sm II for [Sm/Fe] = 2.08, 1.08, 0.08 (green, red, and blue, respectively), Eu II for [Eu/Fe] = 1.95, 0.95, −0.05, Gd I and Gd II [Gd/Fe] = 2.80, 1.80, 0.80, Tb II for [Tb/Fe] = 1.79, 0.79, −0.21, Dy II for [Dy/Fe] = 4.75, 3.75, 2.75, Er I and Er II [Er/Fe] = 2.86, 1.86, 0.86, Hf I for [Hf/Fe] = 2.31, 1.31, 0.31, W I for [W/Fe] = 2.05, 1.05, 0.05, and Os I for [Os/Fe] = 2.76, 1.76, 0.76. Artifacts arising from the overcorrection of nebula lines are indicated.

Monthly Notices
of the
ROYAL ASTRONOMICAL SOCIETY

MNRAS **489,** 1054–1071 (2019)
Advance Access publication 2019 July 25

doi:10.1093/mnras/stz1994

Spectral analysis of the hybrid PG 1159-type central stars of the planetary nebulae Abell 43 and NGC 7094

L. Löbling [1]★ T. Rauch [1] M. M. Miller Bertolami,[2,3] H. Todt,[4] F. Friederich,[1] M. Ziegler,[1] K. Werner [1] and J. W. Kruk[5]

[1]*Institute for Astronomy and Astrophysics, Kepler Center for Astro and Particle Physics, Eberhard Karls University, Sand 1, D-72076 Tübingen, Germany*
[2]*Instituto de Astrofísica La Plata, CONICET-UNLP, Paseo del Bosque s/n, (B1900FWA) La Plata, Argentina*
[3]*Facultad de Ciencias Astronómicas y Geofísicas, UNLP, Paseo del Bosque s/n, (B1900FWA) La Plata, Argentina*
[4]*Institute of Physics and Astronomy, University of Potsdam, Karl-Liebknecht-Str. 24/25, D-14476 Potsdam, Germany*
[5]*NASA Goddard Space Flight Center, Greenbelt, MD 20771, USA*

Accepted 2019 July 16. Received 2019 June 18; in original form 2019 April 30

ABSTRACT

Stellar post asymptotic giant branch (post-AGB) evolution can be completely altered by a final thermal pulse (FTP) which may occur when the star is still leaving the AGB (AFTP), at the departure from the AGB at still constant luminosity (late TP, LTP) or after the entry to the white-dwarf cooling sequence (very late TP, VLTP). Then convection mixes the He-rich material with the H-rich envelope. According to stellar evolution models the result is a star with a surface composition of H $\approx$ 20 per cent by mass (AFTP), $\approx$1 per cent (LTP), or (almost) no H (VLTP). Since FTP stars exhibit intershell material at their surface, spectral analyses establish constraints for AGB nucleosynthesis and stellar evolution. We performed a spectral analysis of the so-called hybrid PG 1159-type central stars (CS) of the planetary nebulae Abell 43 and NGC 7094 by means of non-local thermodynamical equilibrium models. We confirm the previously determined effective temperatures of $T_{\rm eff} = 115\,000 \pm 5\,000$ K and determine surface gravities of $\log(g\,/\,({\rm cm\,s^{-2}})) = 5.6 \pm 0.1$ for both. From a comparison with AFTP evolutionary tracks, we derive stellar masses of $0.57^{+0.07}_{-0.04}$ M$_\odot$ and determine the abundances of H, He, and metals up to Xe. Both CS are likely AFTP stars with a surface H mass fraction of 0.25 ± 0.03 and 0.15 ± 0.03, respectively, and an Fe deficiency indicating subsolar initial metallicities. The light metals show typical PG 1159-type abundances and the elemental composition is in good agreement with predictions from AFTP evolutionary models. However, the expansion ages do not agree with evolution time-scales expected from the AFTP scenario and alternatives should be explored.

Key words: stars: abundances – stars: AGB and post-AGB – stars: atmospheres – stars: evolution – stars: individual: WD 1751 + 106 – stars: individual: WD 2134 + 125.

1 INTRODUCTION

Asymptotic giant branch (AGB) stars are important contributors to the formation of elements heavier than iron (trans-iron elements, TIEs). Schematically, the internal structure of an AGB star is illustrated in Fig. 1. It is composed of an inner C/O core, the two burning shells with an He, C, and O rich intershell region in between and an H-rich convective envelope on top. These stars experience several thermal pulses (TPs) during which the intershell region becomes convectively unstable and C-rich both due to He burning and to dredge up from the core. Additionally, small amounts of H can be partially mixed into the intershell region during the expansion and cooling of the envelope that follows a TP. The presence of large amounts of ^{12}C mixed with traces of H at high temperatures leads to the formation of ^{13}C that acts as a neutron source for the slow neutron capture process (s-process). The intershell region of AGB stars is the main astrophysical site for the s-process. The stellar post-AGB evolution divides into two major channels of H-rich and H-deficient stars. The latter comprise about a quarter of all post-AGB stars and include He- and C-dominated stars. While the He-dominated, H-deficient stars may be the result of stellar mergers (Reindl et al. 2014b), it is commonly accepted that the C-rich are the outcome of a (very) late He-shell flash (late thermal pulse, LTP, cf. Werner & Herwig 2006). The occurrence of a thermal pulse in a post-AGB star or white dwarf was predicted

★ E-mail: loebling@astro.uni-tuebingen.de

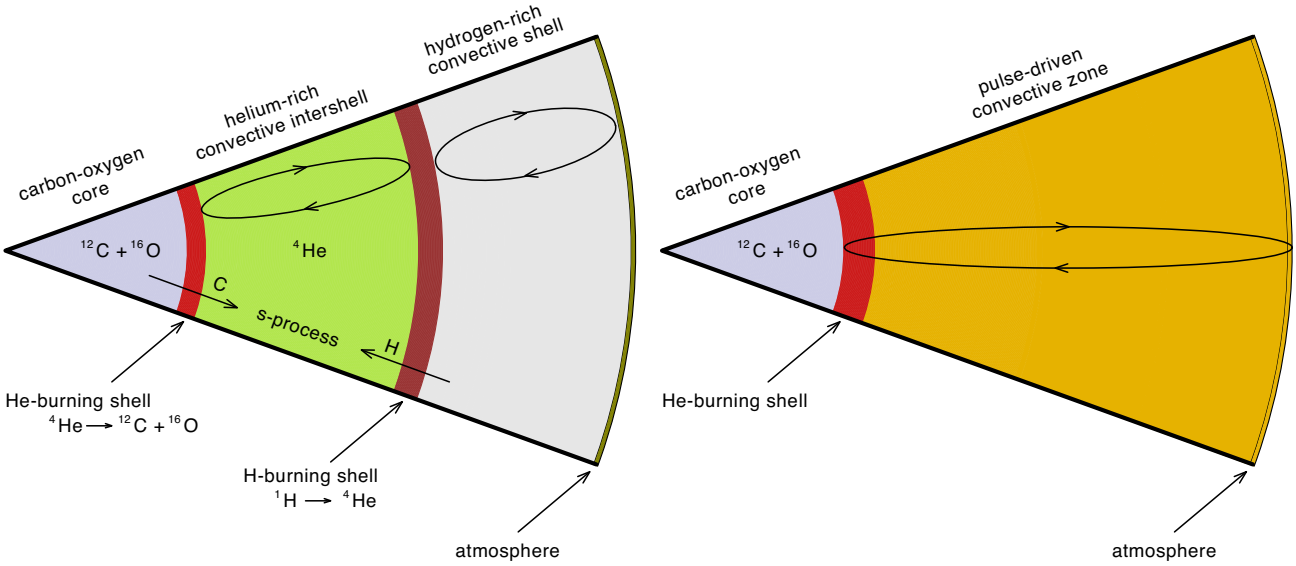

Figure 1. Left: Internal structure (not to scale) of an AGB star during a thermal pulse. Right: Internal structure of a post-AGB star after having experienced a final thermal pulse that caused flash induced mixing of the envelope and the intershell region.

by, e.g. Paczyński (1970), Schönberner (1979), Iben et al. (1983). The particular timing of the final thermal pulse (FTP), determines the amount of remaining photospheric H (cf. Herwig 2001). Still on the AGB (AGB final thermal pulse, AFTP), flash-induced mixing of the H-rich envelope ($\approx 10^{-2}\,M_{\odot}$) with the He-rich intershell layer ($\approx 10^{-2}\,M_{\odot}$) reduces the H abundance to about 10–20 per cent but H I lines remain detectable. After the departure from the AGB, the H-rich envelope is less massive ($10^{-4}\,M_{\odot}$). If the nuclear burning is still 'on', i.e. the star evolves at constant luminosity, the mixing due to a late thermal pulse (LTP) reduces H below the detection limit (about 10 per cent by mass at the relatively high surface gravity). After the star has entered the white-dwarf cooling sequence and the nuclear burning is 'off', a very late thermal pulse (VLTP) will produce convective mixing of the entire H-rich envelope (no entropy barrier due to the H-burning shell) down to the bottom of the He-burning shell where H is burned. In that case, the star will become H free at that time. The internal structure of such a post-AGB star that underwent a FTP scenario is illustrated in Fig. 1.

The spectroscopic class of PG 1159 stars (effective temperatures of $75\,000\,\mathrm{K} \lesssim T_{\rm eff} \lesssim 250\,000\,\mathrm{K}$ and surface gravities of $5.5 \lesssim \log(g\,/\,(\mathrm{cm\,s^{-2}})) \lesssim 8.0$) belongs to the H-deficient, C-rich evolutionary channel (e.g. Werner & Herwig 2006), with the sequence AGB → [WC]-type Wolf-Rayet stars → PG 1159 stars → DO-type white dwarfs (WDs). In the AFTP and LTP scenarios with any remaining H, the stars will turn into DA-type WDs. In PG 1159 star photospheres, He, C, and O are dominant with mass fractions of He = [0.30,0.92], C = [0.08,0.60], and O = [0.02,0.20] (Werner, Rauch & Kruk 2016).

Napiwotzki & Schönberner (1991) discovered the spectroscopic sub-class of so-called hybrid PG 1159 stars. They found that WD 1822 + 008 (McCook & Sion 1999), the central star (CS) of the planetary nebula (PN) Sh 2 − 68 exhibits strong Balmer lines in its spectrum. The hybrid PG 1159 stars are thought to be AFTP stars. Presently, only five of them are known, namely the CSPNe of Abell 43, NGC 7094, Sh 2 − 68, HS 2324 + 3944, and SDSS 152116.00 + 251437.46 (Werner & Herwig 2006; Werner, Rauch & Kepler 2014).

Abell 43 (PN G036.0 + 17.6) was discovered by Abell (1955, object No. 31) and classified as PN (Abell 1966, No. 43). NGC 7094 (PN G066.7 − 28.2) was discovered in 1885 by Swift (1885). Kohoutek (1963) identified it as a PN (K 1 − 19). Narrow-band imaging of Abell 43 and NGC 7094 (Rauch 1999) revealed apparent sizes (in west-east and north-south direction) of $1'28'' \times 1'20''$ and $1'45'' \times 1'46''$, respectively.

Abell 43 and NGC 7094 belong to the group of so-called 'Galactic Soccerballs' (Rauch 1999) because they exhibit filamentary structures that remind of the seams of a traditional leather soccer ball. These structures may be explained by instabilities in the dense, moving nebular shell (Vishniac 1983). While Abell 43 is almost perfectly round and most likely expanded into a void in the ISM, NGC 7094 shows some deformation that may be a hint for ISM interaction.

Another recently discovered member of this group is the PN Kn 61 (SDSS J192138.93 + 381857.2, Kronberger et al. 2012; De Marco et al. 2015). García-Díaz et al. (2014) compared medium-resolution optical spectra of the CSPN Kn 61 with spectra published by Werner et al. (2014) and found a particularly close resemblance of the CSPN Kn 61 to SDSS 075415.12 + 085232.18, an H-deficient PG 1159-type star with $T_{\rm eff} = 120\,000 \pm 10\,000\,\mathrm{K}$, $\log g = 7.0 \pm 0.3$, and a mass ratio C/He = 1. Other members and candidates to become a Galactic Soccerball nebula are known, e.g. the PN NGC 1501 (PN G144.5 + 06.5). An investigation on the three-dimensional ionization structure by Ragazzoni et al. (2001) had shown that it might resemble a Soccerball nebula in a couple of thousands of years. The CSPN, however, is of spectral type [WC4] (Koesterke & Hamann 1997) and cannot resemble a progenitor star of the CSs of Abell 43 and NGC 7094. In this paper, we analyse the hybrid PG 1159-type CSs of Abell 43 and NGC 7094, that we introduce briefly in the following paragraphs.

A first spectral analysis of the CSs of Abell 43 and NGC 7094, namely WD 1751 + 106 and WD 2134 + 125 (McCook & Sion 1999), respectively, with non-local thermodynamical equilibrium (NLTE) model atmospheres that considered opacities of H, He, and C was presented by Dreizler, Werner & Heber (1995). They analysed medium-resolution optical spectra and found that their

synthetic spectra, calculated with $T_{\rm eff} = 110\,000$ K, $\log g = 5.7$, and a surface-abundance pattern of H/He/C = 42/51/5 (by mass, H is uncertain), reproduced equally good the observations of both stars making them a pair of spectroscopic twins.

Napiwotzki (1999) used medium-resolution optical spectra and an extended H + He-composed NLTE model-atmosphere grid. With a statistical (χ^2) approach, he found $T_{\rm eff} = 116\,900 \pm 5500$ K and $\log g = 5.51 \pm 0.22$ for WD 1751 + 106 and $T_{\rm eff} = 125\,900 \pm 7700$ K and $\log g = 5.45 \pm 0.23$ for WD 2134 + 125. An attempt to measure the Fe abundance of WD 2134 + 125 from far ultraviolet (FUV) observations performed with Far Ultraviolet Spectroscopic Explorer (FUSE) revealed a strong Fe underabundance of 1–2 dex (Miksa et al. 2002). This was not in line with expectations from stellar evolution theory (e.g. Busso, Gallino & Wasserburg 1999). Ziegler et al. (2009) found also an underabundance of Ni of about 1 dex for both stars. The transformation of Fe to Ni seems therefore unlikely to be the reason for the Fe deficiency. They reanalysed $T_{\rm eff}$ and $\log g$ of WD 2134 + 125 and found $T_{\rm eff} = 100\,000 \pm 15\,000$ K and $\log g = 5.5 \pm 0.2$ with an improved abundance ratio of H/He = 17/69 (by mass). Furthermore, the element abundances of the C–Ne, Si, P, and S were determined. Ringat et al. (2011) reanalysed WD 1751 + 106 and found $T_{\rm eff} = 105\,000 \pm 10\,000$ K and $\log g = 5.6 \pm 0.3$. Also the element abundances of C–Ne, Si, P, and S were determined and agree with the values of Friederich (2010). Löbling (2018) found $T_{\rm eff} = 115\,000 \pm 5000$ K for both stars and $\log g = 5.4 \pm 0.1$ and $\log g = 5.5 \pm 0.1$ for WD 2134 + 125 and WD 1751 + 106, respectively. She considered 31 elements in her analysis and determined abundances in individual line-formation calculations. This work is a continuative analysis giving a more extensive description.

For NLTE model-atmosphere calculations, reliable atomic data is mandatory to construct detailed model atoms to represent individual elements. In the last decade, the availability of such atomic data improved, e.g. Kurucz's line lists for iron-group elements (IGEs), namely Ca–Ni, were strongly extended in 2009 (Kurucz 2009, 2011) by about a factor of 10. In addition, transition probabilities and oscillator strengths for many TIEs were calculated recently (Table A3, available online). Therefore, we decided to perform a detailed spectral analysis of the hybrid PG 1159-type CSPNe Abell 43 and NGC 7094, by means of state-of-the-art NLTE model-atmosphere techniques. We describe the available observations and our model atmospheres in Sections 2 and 3, respectively. The spectral analyses follow in Sections 4 and 5. We investigate on the stellar wind of both stars in Section 6 and determine stellar masses, distances, and luminosities in Section 7. We summarize the results and conclude in Section 8.

2 OBSERVATIONS

Our spectral analysis is based on high signal-to-noise ratio (S/N) and high-resolution observations from the far ultraviolet (FUV) to the optical wavelength range. UV spectra were retrieved from the Barbara A. Mikulski Archive for Space Telescopes (MAST). To improve the S/N, multiple observations in the same set-up were co-added. The spectra were partly processed with a low-pass filter (Savitzky & Golay 1964). To simulate the instruments' resolutions, all synthetic spectra shown in this paper are convolved with respective Gaussians. The observation log for all space- and ground-based observations of WD 1751 + 106 and WD 2134 + 125 used for this work is given in Table A2, available online.

Radial and rotational velocity. We measured radial velocity shifts for all observations using prominent lines of He II, C IV, O V and O VI, Si V, and Fe VII and shifted the spectra to rest wavelength.

The observed line profiles are broadened but the quality of the spectra does not unambiguously allow to decide whether it is due to stellar rotation or caused by some wind related macro turbulence. For WD 1751 + 106, we selected O VI λλ 1124.7, 1124.9 Å and S VI λ 1117.8 Å (Fig. 2) to determine a rotational velocity of $v_{\rm rot} \sin i = 18 \pm 5\,{\rm km\,s^{-1}}$. This new determination revises the previous higher value of $v_{\rm rot} \sin i = 42 \pm 13\,{\rm km\,s^{-1}}$ (Rauch et al. 2004). The profiles of these lines also agree with broadening with radial-tangential macro turbulence profiles (Gray 1975) with the same velocity (Fig. 2). For WD 2134 + 125, we used O VI λλ 1122.4, 1122.6, 1124.7, 1124.9 and N V λ 1242.6 Å (Fig. 2) to determine $v_{\rm rot} \sin i = 28 \pm 5\,{\rm km\,s^{-1}}$. This value agrees within the error limits with the value of $46 \pm 16\,{\rm km\,s^{-1}}$ from Rauch et al. (2004). Again, we cannot claim this broadening to be rotation alone because the profiles can also be reproduced with radial-tangential macro turbulence profiles with $v_{\rm macro} = 35 \pm 5\,{\rm km\,s^{-1}}$.

Interstellar reddening. It was measured by a comparison of observed UV fluxes and optical and infrared brightnesses with our synthetic spectra. The latter were normalized to the Two Micron All Sky Survey (2MASS; Skrutskie et al. 2006; Cutri et al. 2003) brightnesses and then, Fitzpatrick's law (Fitzpatrick 1999) was applied to match the observed UV continuum flux level (Fig. A1, available online). We determined $E_{B-V} = 0.265 \pm 0.01$ and $E_{B-V} = 0.135 \pm 0.01$ for WD 1751 + 106 and WD 2134 + 125, respectively.

We determined the interstellar neutral H column density from the comparison of theoretical line profiles of Ly α with the observations (Fig. A9, available online). These are best reproduced at $n_{\rm H\,I} = 1.0 \pm 0.1 \times 10^{21}\,{\rm cm^{-2}}$ and $n_{\rm H\,I} = 6.5 \pm 0.1 \times 10^{20}\,{\rm cm^{-2}}$ for WD 1751 + 106 and WD 2134 + 125, respectively. Our values of $\log (n_{\rm H\,I}/E_{B-V}) = 21.58 \pm 0.02$ and $\log (n_{\rm H\,I}/E_{B-V}) = 21.68 \pm 0.03$, respectively, agree well with the prediction from the Galactic reddening law of Groenewegen & Lamers (1989, $\log (n_{\rm H\,I}/E_{B-V}) = 21.58 \pm 0.1$).

Interstellar line absorption. This absorption in the FUSE observations was modelled with the line-profile fitting procedure OWENS (Hébrard et al. 2002; Lemoine et al. 2002; Hébrard & Moos 2003). It allows to consider several individual clouds in the interstellar medium (ISM) with individual chemical compositions, column densities for each of the included molecules and ions, radial and turbulent velocities, and temperatures. The FUV observations are strongly contaminated by ISM line absorption and, thus, it is necessary to reproduce these lines well to unambiguously identify photospheric lines (cf. Ziegler et al. 2007, 2012). In the FUSE spectra of WD 1751 + 106 and WD 2134 + 125, ISM absorption lines from H_2 ($J = 0 - 5$), HD, C I-III, N I-II, O I, Si II, P II, S III, Ar I, and Fe II were identified and simulated.

3 MODEL ATMOSPHERES AND ATOMIC DATA

To calculate synthetic spectra, we used the Tübingen NLTE Model Atmosphere Package (TMAP[1]; Werner et al. 2003; Werner, Dreizler & Rauch 2012). The models assume plane-parallel geometry, are chemically homogeneous, and in hydrostatic and radiative equilibrium. TMAP considers level dissolution (pressure ionization) following Hummer & Mihalas (1988) and Hubeny, Hummer & Lanz

[1] http://astro.uni-tuebingen.de/ TMAP

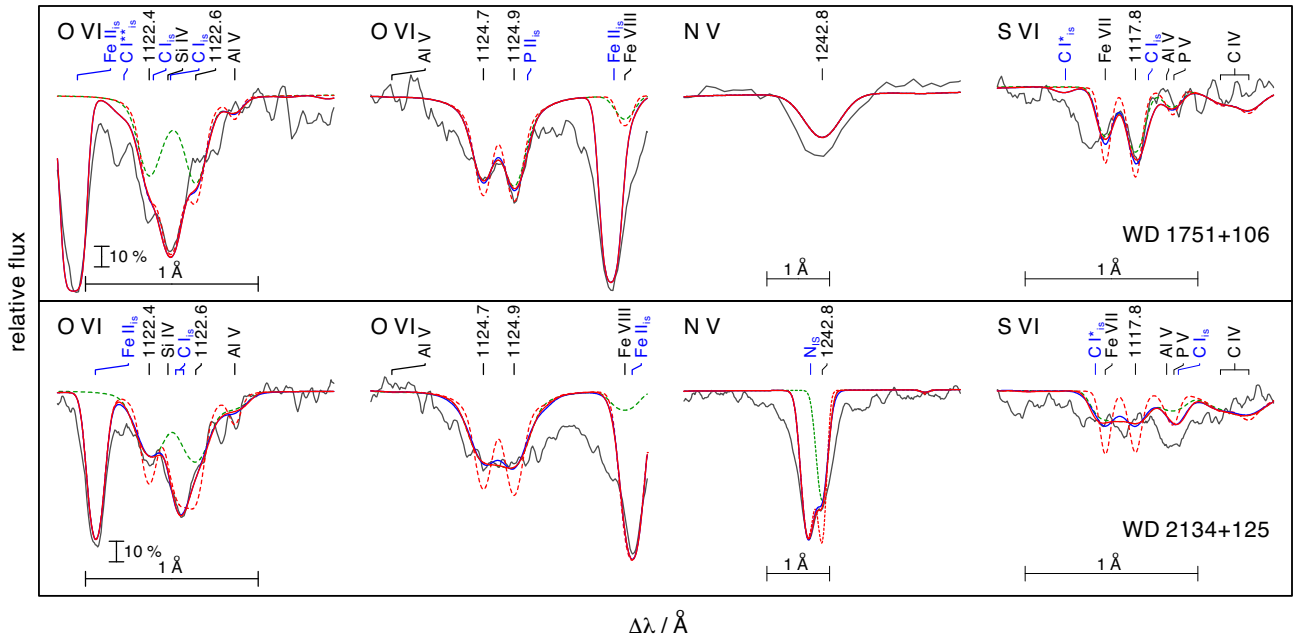

Figure 2. Synthetic spectra (red) convolved with rotational profiles ($v_{\rm rot} = 18\,{\rm km\,s^{-1}}$ for WD 1751 + 106, upper panels and $v_{\rm rot} = 28\,{\rm km\,s^{-1}}$ for WD 2134 + 125, lower panels) and convolved with radial-tangential macro turbulence profiles (blue, $v_{\rm macro} = 18\,{\rm km\,s^{-1}}$ for WD 1751 + 106, upper panels and $v_{\rm macro} = 35\,{\rm km\,s^{-1}}$ for WD 2134 + 125, lower panels) around O VI, N V, and S VI lines (marked with their wavelengths at the top of the panels) calculated from our final models compared with observations (gray). A model without extra broadening (red, dashed) and one without interstellar absorption (green, dashed) are shown. Interstellar absorption lines are indicated by blue marks.

(1994). Stark-broadening tables of Tremblay & Bergeron (2009, extended tables of 2015, private communication) and Schöning & Butler (1989) are used to calculate the theoretical profiles of H I and He II lines, respectively. To represent the elements considered by TMAP, model atoms were retrieved from the Tübingen Model Atom Database (TMAD; Rauch & Deetjen 2003) that has been constructed as part of the Tübingen contribution to the German Astrophysical Virtual Observatory (GAVO[2]). For IGEs and TIEs (atomic weight $Z \geq 29$), we used Kurucz's line lists[3] (Kurucz 2009, 2011) and recently calculated data for Zn, Ga, Ge, Se, Kr, Sr, Zr, Mo, Te, I, Xe, and Ba (Table A3, available online) that is available via the Tübingen Oscillator Strengths Service (TOSS). For the elements with $Z \geq 20$, we created model atoms using a statistical approach that calculates super levels and super lines (Rauch & Deetjen 2003). The statistics of all elements considered in our model-atmosphere calculations are summarized in Table A1, available online.

To simulate prominent P Cygni profiles in the observations, we used the Potsdam Wolf–Rayet (PoWR) code that has been developed for expanding atmospheres and considers mass loss due to a stellar wind (Section 6). These models are used to determine mass-loss rates and terminal wind velocities.

4 EFFECTIVE TEMPERATURE AND SURFACE GRAVITY

Model atmospheres grids ($\Delta T_{\rm eff} = 5000\,{\rm K}$ and $\Delta \log g = 0.1$) were calculated around the literature values of Löbling (2018). These models consider opacities of 31 elements from H to Ba for which the ionization fractions of the considered ions are shown in Fig. A8, available online. The abundances used for the calculation of the atmospheric structure are given in Table A4, available online. The best agreement for the line width and depth increment for the observed He II λλ 4025.6, 4100.1, 4199.8, 4338.7, 4859.3, 5411.5 Å, and H I λλ 4101.7, 4340.5, 4861.3 Å was obtained for surface gravity values of $\log g = 5.6 \pm 0.1$ for WD 1751 + 106 (Fig. A2, available online) and WD 2134 + 125 (Fig. A3, available online). The value for WD 2134 + 125 is also verified by the depth increment of the He II Fowler series (Fig. A4, available online). The lower surface gravity values of Löbling (2018) were based on model atmospheres assuming the abundances found by Friederich (2010). Using new models with a revised He/H ratio and including opacities of more elements, these previous values appear too low. Higher values for $\log g$ have an impact on the final masses which are lower compared to previous values (Section 7). We confirm the temperature determination of $T_{\rm eff} = 115\,000 \pm 5\,000\,{\rm K}$ for both stars by Löbling (2018) by the evaluation of the O V/O VI ionization equilibrium using O V λλ1371.3, 1506.7, 1506.7, 1506.8, 4930.2, 4930.3 Å and O VI λλ 1124.7, 1124.9, 3811.3, 3834.2 Å (Fig. A5, available online). We adopt $T_{\rm eff} = 115\,000\,{\rm K}$ and $\log g = 5.6$ for WD 1751 + 106 and WD 2134 + 125 for our further analysis.

5 METAL ABUNDANCES

In the following paragraphs, we discuss all elements, that were considered in this analysis. To determine the abundances, we varied them in subsequent line formation calculations in steps of 0.2 dex or smaller. The abundances were derived by line-profile fits and evaluation by eye. For illustration, some representative spectral lines are shown in Figs 3–7. These values are affected by typical errors estimated to 0.3 dex by redoing the abundance

[2] http://www.g-vo.org
[3] http://kurucz.harvard.edu/atoms.html

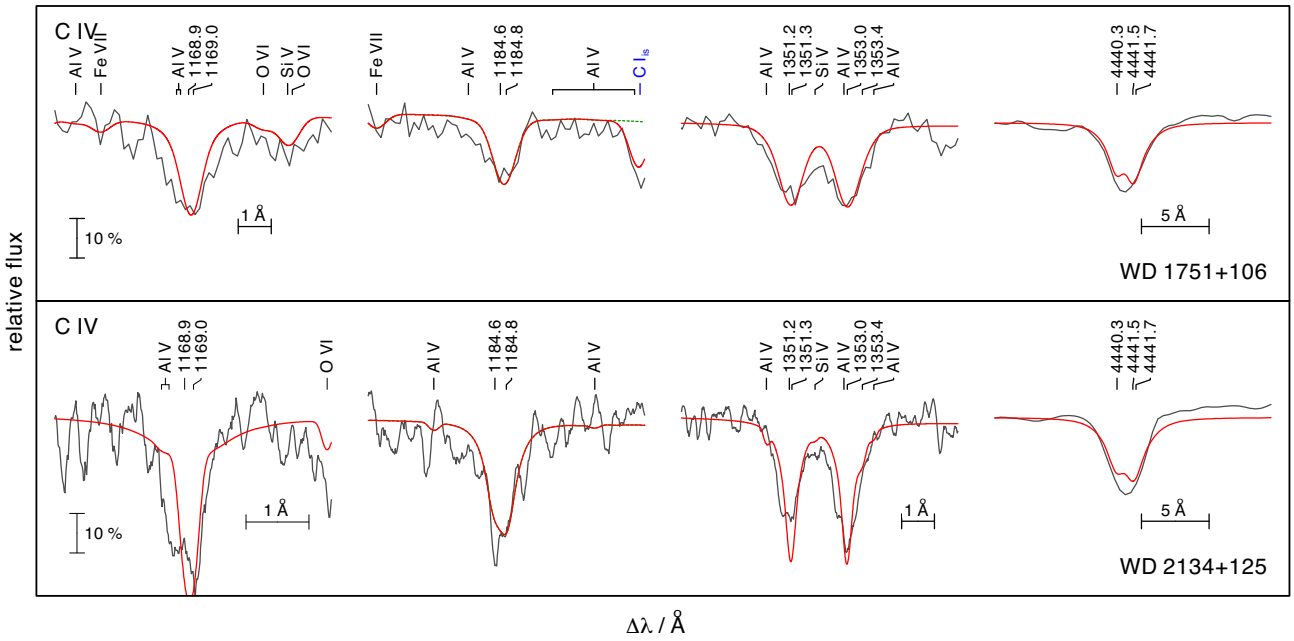

Figure 3. Synthetic spectra (red) around C IV lines calculated from our final model compared with observations (gray).

determination for models at the edges of the error range for $T_{\rm eff}$ and $\log g$ (we used a model with $T_{\rm eff} = 120\,000$ K, $\log g = 5.5$ and one with $T_{\rm eff} = 110\,000$ K and $\log g = 5.7$). If no line identification was possible, we determined upper limits by reducing the abundance until the strongest computed lines become undetectable within the noise of the spectrum. The results are summarized in Table 3. The whole FUSE spectra compared with our final models are shown in Fig. A6, available online, and the GHRS spectrum of WD 1751 + 106 as well as the STIS spectrum of WD 2134 + 125 in Fig. A7, available online. The solar abundances are taken from Asplund et al. (2009), Scott et al. (2015b,a), and Grevesse et al. (2015).

Carbon. Detailed line-profile fits were performed for C IV λλ 1168.9, 1169.0, 1184.6 Å in the FUSE observations, C IV λλ 1351.2, 1351.3, 1353.0 Å in the GHRS or STIS observations, and the C IV lines at 3685–3691 Å, 4440–4442 Å, 4785–4790 Å, 5016–5019 Å, and 6591–6593 Å in the UVES SPY observations (Fig. 3). We achieve [C] = log (abundance/solar abundance) = 2.0 for WD 1751 + 106 and [C] = 2.1 for WD 2134 + 125.

Nitrogen. The photospheric N V λλ 1238.8, 1242.8 Å resonance doublet in the STIS spectrum of WD 2134 + 125 is blended by strong interstellar absorption. Therefore, we used N V λλ 4943.2, 4944.0, 4945.34945.6, 4945.7 Å in addition (Fig. 4) and determined [N] = 0.6 for WD 1751 + 106 and [N] = − 0.3 for WD 2134 + 125.

Oxygen. The determination of the O abundance in WD 2134 + 125 is hampered by the fact that all useful lines in the UV and FUV are either blended with interstellar lines or display strong P Cygni profiles (e.g., O V λ 1371.3 Å and O VI λλ 1031.9, 1037.6 Å). We used O VI λλ 1122.4, 1122.6, 1124.7, 1124.9 Å in the FUSE spectra and O VI λλ 5289.5, 5289.8, 5290.7, 5292.0 Å in the UVES SPY spectra (Fig. 4) to determine [O] = − 0.2 for WD 1751 + 106 and [O] = − 0.1 for WD 2134 + 125. Furthermore, we employed PoWR to calculate wind profiles. Details on the wind models are given in Section 6.

Fluorine. The strong line F VI λ 1139.5 Å shows a P Cygni profile. For an abundance determination with our static models, we analysed F V λλ 1082.3, 1087.8, 1088.4 Å (Fig. 4), which are reproduced best with an abundance of [F] = 1.0 for WD 1751 + 106 and [F] = 1.5 for WD 2134 + 125 (the same value was measured by Werner, Rauch & Kruk 2005). These abundances exceed the values of Ringat et al. (2011) and Ziegler et al. (2009) but agree with the value of [F] = 1.2 (Reiff et al. 2008) for WD 2134 + 125, who employed a wind model for their analysis. We examined the profile of F VI λ 1139.5 Å in our PoWR wind model and verified the newly determined abundances.

Neon. All lines of Ne V with observed wavelengths in the FUSE and STIS wavelength range that are available from the National Institute for Standards and Technology (NIST) Atomic Spectra Database[4] (Kramida et al. 2018) are affected by a wavelength uncertainty of 1.5 Å or blended with interstellar absorption like Ne V λ 946.9 Å. Ne VI λλ 1645.1, 1645.6, 1666.2, 1667.8, 1679.7 Å are visible in the STIS spectrum of WD 2134 + 125 and used for an estimate of the Ne abundance (Fig. 4). Ne VII λ 1319.8 Å is also detectable but blended with Si V λ 1319.6 Å. The optical lines Ne VII λλ 3643.6, 3853.5, 3866.7, 3873.3, 3894.0, 3905.3, 3912.0 Å are very weak. We determine [Ne] = 1.2 for WD 2134 + 125 and pose an upper limit of [Ne] < 1.5 for WD 1751 + 106 owing to the resolution of the GHRS observation and the fact that the strong Ne VI lines are not within the GHRS range. Ne VII λ 973.3 Å exhibits a strong P Cygni profile. The wind profile of this line in the PoWR model confirms the Ne abundance.

Magnesium. No Mg line can be identified in the observations. Based on the computed lines of Mg IV λλ 1346.5, 1346.6, 1382.5, 1385.7, 1387.5 Å (Fig. 5), we find upper limits of [Mg] < 0.5 for WD 2134 + 125 and [Mg] < 0.8 for WD 1751 + 106. The latter

[4] https://physics.nist.gov/PhysRefData/ASD/lines_form.html

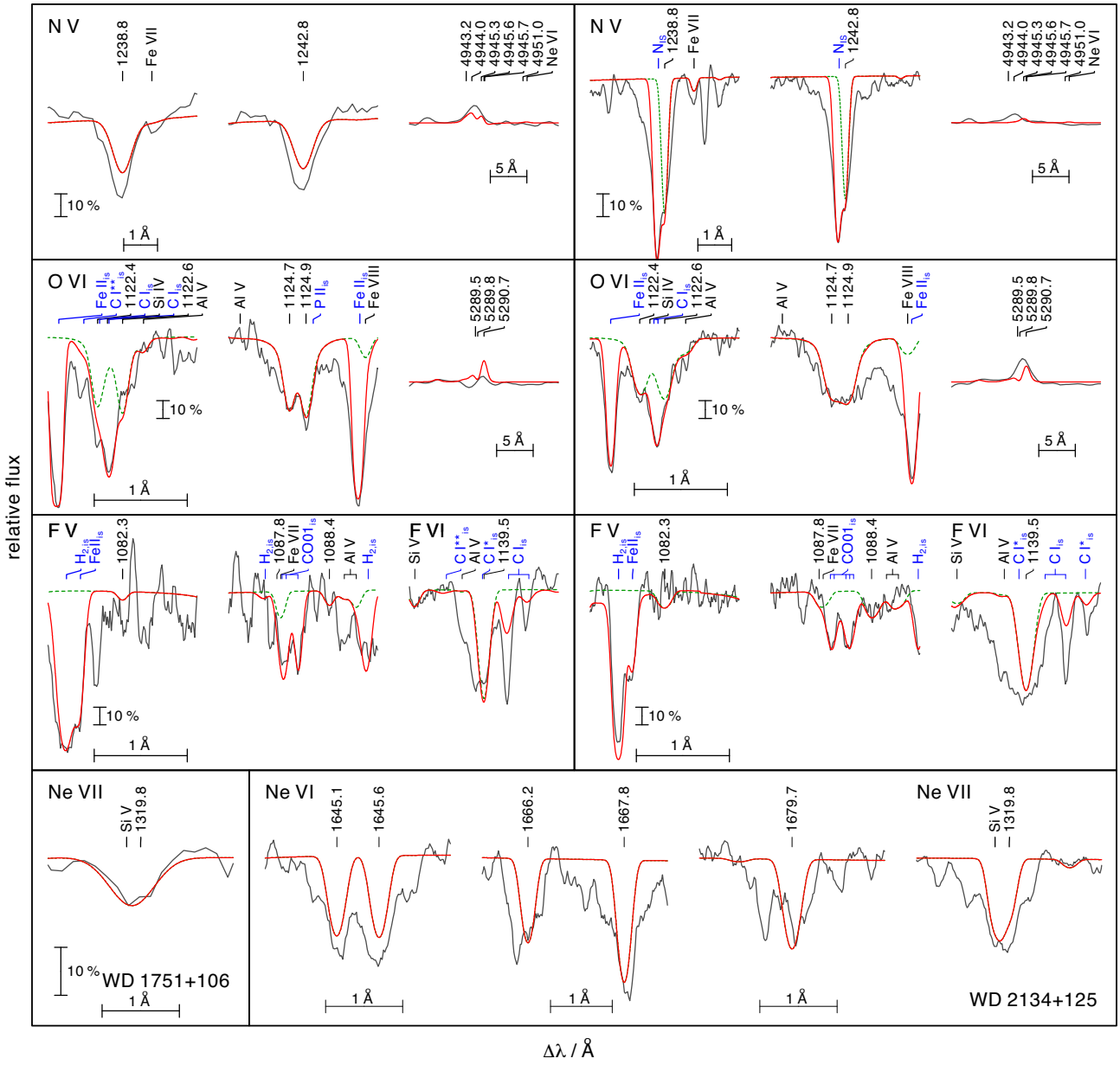

Figure 4. Like Fig. 3, for N V, O VI, F V–VI, and Ne VI–VII.

value is higher due to the lower resolution of the GHRS observation compared to the one obtained with STIS.

Aluminum. Al V λλ 1090.1, 1287.7, 1288.2, 1369.3 Å are the most prominent Al lines in the synthetic spectra (Fig. 5). We determined an abundance of [Al] = 0.6 for WD 2134 + 125 and an upper limit of [Al] < 0.7 for WD 1751 + 106.

Silicon. In the STIS and GHRS observations of both stars, the Si IV λλ 1393.8, 1402.8 Å resonance doublet is blended by interstellar absorption lines. Thus, our abundance determination is based on Si IV λ 1128.3 Å and Si V λλ 1118.8, 1251.4, 1276.0, 1291.4, 1319.6 Å (Fig. 5). These lines indicate [Si] = − 0.6 for WD 1751 + 106. For WD 2134 + 125, we used the same lines as well as Si V λλ 1465.5, 1582.7 Å and measured [Si] = − 0.7.

Phosphorus. We used the strongest P lines, namely P V λλ 1118.0, 1128.0 Å, in the theoretical spectra to establish upper limits of [P] < 0.3 for WD 1751 + 106 and [P] < 0.4 for WD 2134 + 125 (Fig. 5).

Sulfur. The most prominent S lines in the FUSE spectrum of WD 1751 + 106 and WD 2134 + 125, S VI λλ 933.4, 944.5 Å are both blended by interstellar H_2 lines and thus it is uncertain to derive the S abundance. From S VI λλ 1000.4, 1000.5, 1117.8 Å (Fig. 5), we determine [S] = − 0.1 and [S] ≤ − 0.6 for WD 1751+106 and WD 2134 + 125 , respectively.

Chlorine. Cl VII λλ 949.0, 949.1, 996.7, 997.0 Å are present in the synthetic spectra but cannot be identified in the FUSE observations of both stars. Based on these lines, we determined upper limits of [Cl] < 1.1 and [Cl] < 1.0 for WD 1751 + 106 and WD 2134 + 125, respectively.

Argon. The strong Ar VIII λ 1063.6 Å line is blended by interstellar absorption and thus can not be used to derive an abundance value for

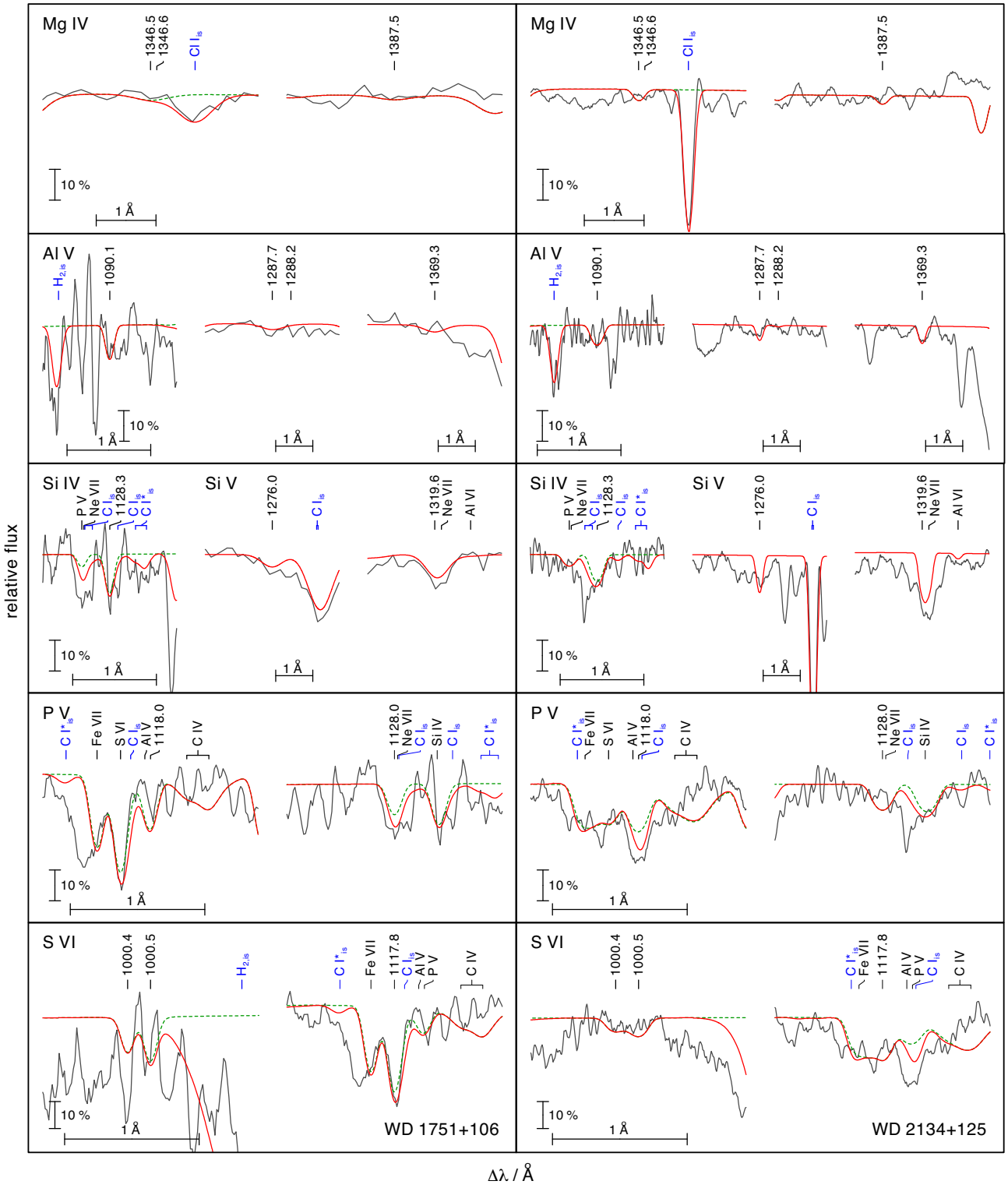

Figure 5. Like Fig. 3, for Mg IV, Al V, Si IV–V, P V, and S VI.

argon. We used Ar VIII λ 1164.1 Å to derive an upper limit of [Ar] < 0.3 for WD 1751 + 106 and [Ar] < -0.3 for WD 2134 + 125 (Fig. 6).

Calcium. The strongest line in the synthetic spectra, namely Ca IX λ 1116.0 Å, is blended with a strong interstellar H_2 absorption feature. For WD 1751 + 106, this line appears in the wing of the H_2 line and is used to derive an upper limit of [Ca] $<$ 0.0.

Chromium. None of the Cr VII lines appearing in the synthetic spectrum has been identified in the observation. We used Cr VII λλ 1170.1, 1186.6, 1187.3 Å to determine upper limits of [Cr] < 2.0 for WD 1751 + 106 and WD 2134 + 125.

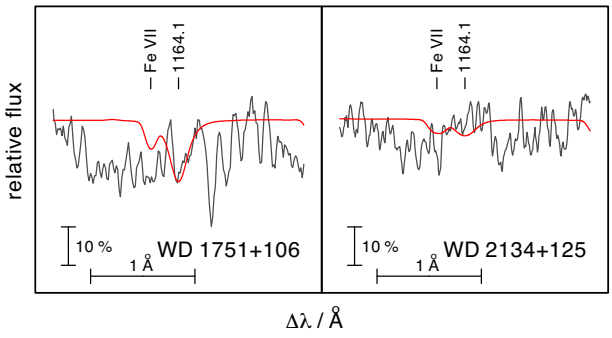

Figure 6. Synthetic spectra around Ar VIII λ 1164.1 Å calculated from our final models compared with the FUSE observations.

Iron. In previous analysis of NGC 7094, Miksa et al. (2002) found subsolar values of at least 1 dex for Fe. For the CS of Abell 43, they found a solar upper limit for Fe. With extended model atoms, Löbling (2018) checked and correct this result and determined [Fe] = −0.4 for WD 1751 + 106 and [Fe] = −0.8 for WD 2134 + 125. These values are supported also by our final model including all opacities of 31 elements (Fig. 7). Previous analyses that assumed a larger deficiency, did not take line broadening due to stellar rotation or macro turbulence into account explaining the lower Fe abundances. A solar Fe abundance can be ruled out since the computed lines of Fe VII appear too strong (Fig. 7)

Nickel. The dominating ionization stages of the IGEs in the expected parameter regime are VII and VIII. Due to the lack of POS lines of Ni in these stages in Kurucz's line list (Kurucz 1991, 2009) for the spectral ranges of FUSE, STIS, and GHRS, no Ni lines could be detected and identified. In their analysis, Ziegler et al. (2009) used Ni VI lines and determined upper Ni abundance limits only. Their subsolar values may again be a result of not taking additional broadening due to rotation or macro turbulence into account. Furthermore, they assumed lower temperatures and higher gravities for both stars. The Ni VI lines are very sensitive to $T_{\rm eff}$ and are significantly stronger for a model with $T_{\rm eff}$ reduced by 10 kK (Fig. 8).

No strong lines in the spectra of both stars were found from the elements Sc, Ti, V, Mn, Ni, and Co. Therefore, these elements were combined to a generic model atom (Rauch & Deetjen 2003). All IGEs were taken into account with solar abundances ratios normalized to the Fe abundance in the final model calculations.

Zinc. The strong lines Zn V λλ 1132.3, 1123.7, 1133.0, 1133.1, 1133.3, 1133.5, 1174.3, 1180.0 Å appear in the synthetic spectra but could not be identified in the observations. Thus, we can only derive an upper limit of [Zn] < 1.0 for both stars.

Gallium. We used the strongest line Ga VI λ 1006.9 Å to determine an upper limit of [Ga] < 2.0 for WD 1751 + 106 and WD 2134 + 125.

Germanium. Ge VI λλ 920.5, 926.8, 988.2 Å are partly blended by interstellar absorption features. The analysis yields an upper limit of [Ge] < 2.0 for both stars.

Krypton. Kr VII λλ 1166.9, 1169.6, 1195.6, 1284.6 Å are present in the models. We used these lines to measure an upper limit of [Kr] < 3.5 for both stars.

Zirconium. By analysing STIS observation of WD 2134 + 125 around the computed lines Zr VII λλ 1233.6, 1235.0, 1376.6 Å, we derived an upper limit of [Zr] < 3.0. Due to the fact that these lines are located in the range of the lower resolution GHRS observation of WD 1751 + 106, we were not able to derive a reasonable value for this star.

Tellurium. We used Te VI λ 1071.4 Å, the strongest computed line in the FUSE range, to ascertain [Te] ≤ 4.0 for WD 1751 + 106 and [Te] ≤ 3.5 for WD 2134 + 125.

Iodine. The strongest computed lines I VI λλ 911.2, 915.4, 919.2 Å are useless for the abundance measurement, since they are blended by interstellar absorption. Based on I VI λλ 1045.4, 1120.3, 1153.3 Å, we derived upper limits of [I] < 4.6 and [I] < 5.0 for WD 1751 + 106 and WD 2134 + 125, respectively.

Xenon. We used the strongest line Xe VII λ 995.5 Å to determine an upper limit of [Xe] < 4.0 for WD 2134 + 125. The quality of the FUSE observation of WD 1751 + 106 around this line does not suffice to determine the Xe abundance.

Selenium, strontium, molybdenum, and barium. Even if we increase the Se, Sr, Mo, and Ba abundances in the synthetic models to thousand times solar, no lines of these elements appear in the computed spectra.

In our final models, all TIEs are taken into account with solar abundance ratios normalized to the determined Fe abundance value. The temperature and density structure and the ionization fractions of all ions considered in the final model for WD 2134 + 125 are shown in Fig. A8, available online.

6 STELLAR WIND AND MASS LOSS

At $T_{\rm eff}$ = 115 000 K and log g = 5.6 the stars have luminosities of almost 4 000 $L_\odot$ (Section 7). They are located close to the Eddington limit and experience mass loss due to a radiation-driven wind (cf. Pauldrach et al. 1988) and, hence, exhibit prominent P Cygni profiles in their UV spectra (Fig. 9). Koesterke & Werner (1998) and Koesterke, Dreizler & Rauch (1998) investigated the wind properties of WD 2134 + 125 by means of NLTE models for spherically expanding atmospheres and determined the mass-loss rate $\dot{M}$ and the terminal wind velocity v_∞ from HST/GHRS and ORFEUS-SPAS II[5] observations, respectively. They found $\log[\dot{M}/(M_\odot {\rm yr}^{-1})] = -7.3$ from C IV λλ 1548.20, 1550.77 Å and $\log[\dot{M}/(M_\odot {\rm yr}^{-1})] = -7.7$ from O VI λλ 1031.91, 1037.61 Å and v_∞ = 3 500 km s^{-1}, which is slightly lower than the former value of v_∞ = 3 900 km s^{-1} of Kaler & Feibelman (1985) based on the analysis of spectra obtained with IUE. Guerrero & De Marco (2013) used lines of O VI and found 3610 km s^{-1} for WD 2134 + 125 and 3000–3600 km s^{-1} from the analysis of O vi and Ne VII lines for WD 1751 + 106.

For the analysis of the wind lines in the UV range we used the PoWR model atmosphere code. This is a state-of-the-art NLTE code that accounts for mass loss, line blanketing, and wind clumping. It can be employed for a wide range of hot stars at arbitrary metallicities (e.g. Oskinova et al. 2011; Hainich et al. 2014, 2015; Reindl et al. 2014a; Shenar et al. 2015; Reindl et al. 2017), since the hydrostatic and wind regimes of the atmosphere are treated consistently (Sander et al. 2015). The NLTE radiative transfer is calculated in the co-moving frame. Any model can be specified by its luminosity L, stellar temperature $T_{\rm eff}$, surface gravity g, and mass-loss rate $\dot{M}$ as main parameters. In the subsonic region, the velocity field is defined such that a hydrostatic density stratification is approached (Sander et al. 2015). In the supersonic region, the

[5]Orbiting and Retrievable Far and Extreme Ultraviolet Spectrometer – Space Pallet Satellite II.

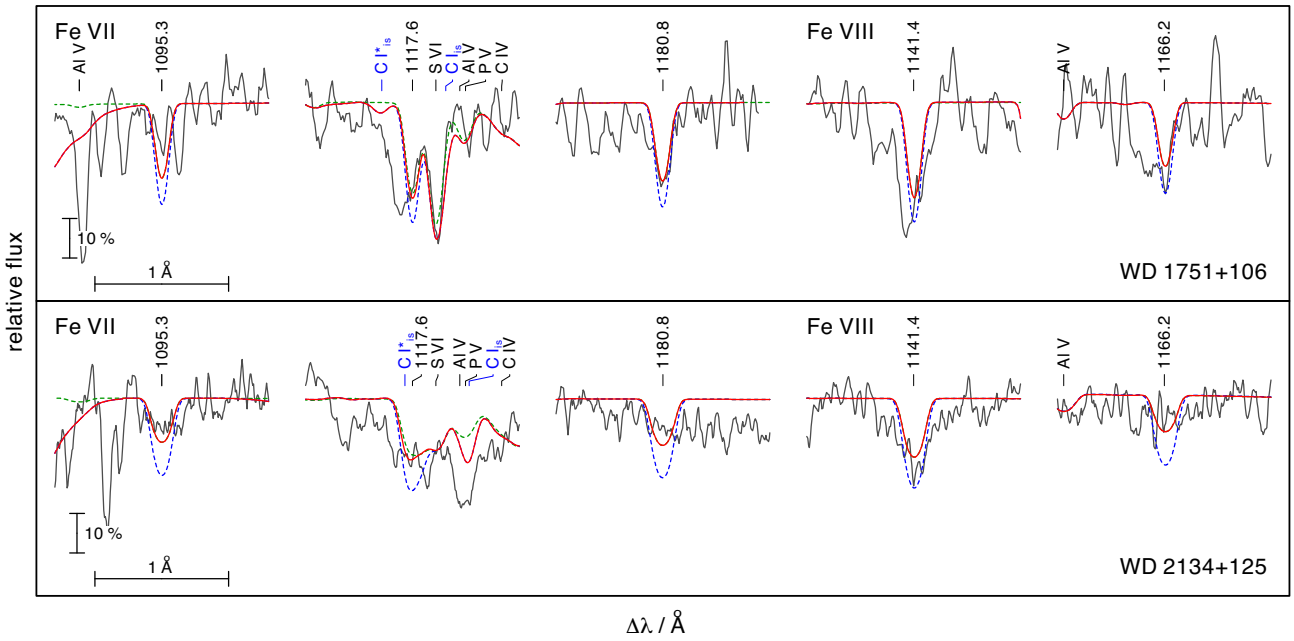

Figure 7. Synthetic spectra around Fe VII and VIII lines calculated from our final models with [Fe] = −0.4 (red, full) and solar (blue, dashed) compared with the FUSE observation.

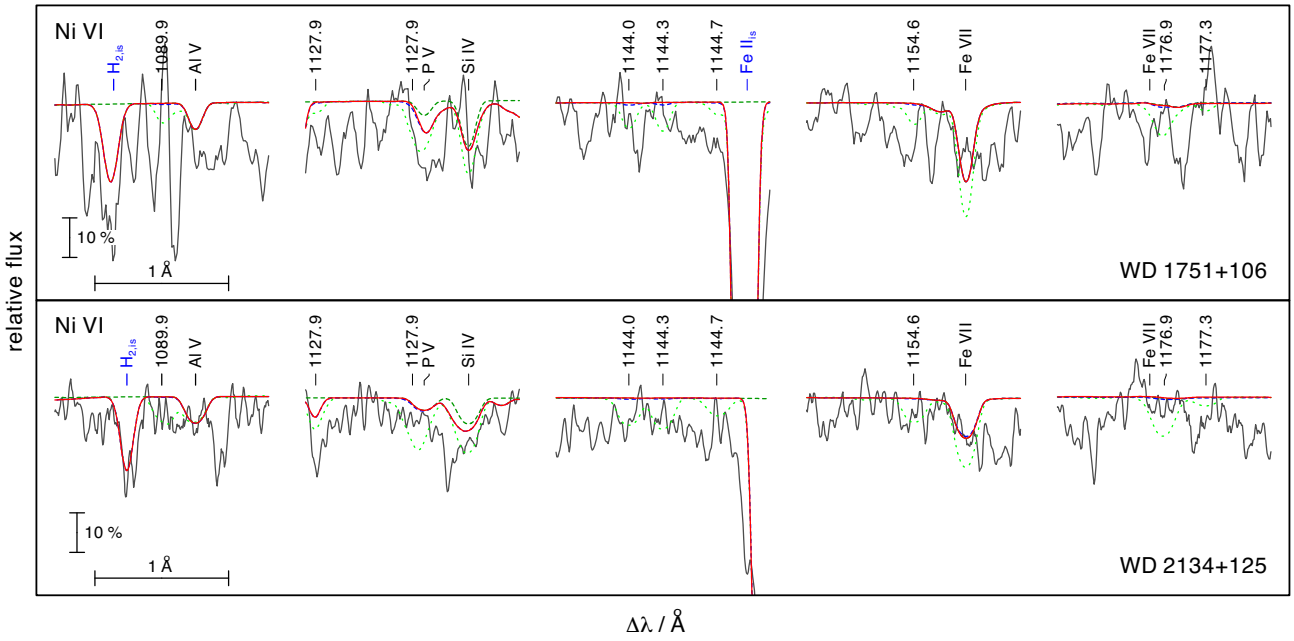

Figure 8. Top panel: Synthetic spectra around Ni VI lines calculated from our final models for WD 1751 + 106 with $T_{\rm eff}$ = 115 kK and [Ni] = − 0.4 (red, full) and 1 dex supersolar (blue, dashed) and $T_{\rm eff}$ = 105 kK and Ni 1 dex supersolar (green, dotted). Bottom: For WD 2134 + 125 with $T_{\rm eff}$ = 115 kK and [Ni] = − 0.8 (red, full) and 1 dex supersolar (blue, dashed) and $T_{\rm eff}$ = 105 kK and Ni 1 dex supersolar (green, dotted).

wind velocity field $v(r)$ is pre-specified assuming the so-called β-law (Castor, Abbott & Klein 1975). Wind clumping is taken into account in first-order approximation (Hamann & Gräfener 2004) with a density contrast $D = \varrho_{\rm cl}/\langle\varrho\rangle$ between the clumps and a smooth wind of same mass-loss rate. As we do not assume an interclump medium, $D = f_V^{-1}$.

We adopted the stellar parameters from the TMAP analysis as given in Table 3. Our calculations include complex model atoms for H, He, C, N, O, F, Ne, Si, P, S, and the iron group elements Sc, Ti, V, Cr, Mn, Fe, Co, Ni.

The only P Cygni line that is not saturated and is sensitive enough to the mass-loss rate is C IV λλ 1548, 1551 Å . For WD 1751 + 106 the quality of the UV observation in this wavelength range is very poor. However, we found that the mass-loss rate must be $\log[\dot{M} / (\mathrm{M}_\odot\,\mathrm{yr}^{-1})] \lesssim -8.1$ to obtain a model that is compatible with the observation. The STIS spectrum of WD 2134 + 125 in this

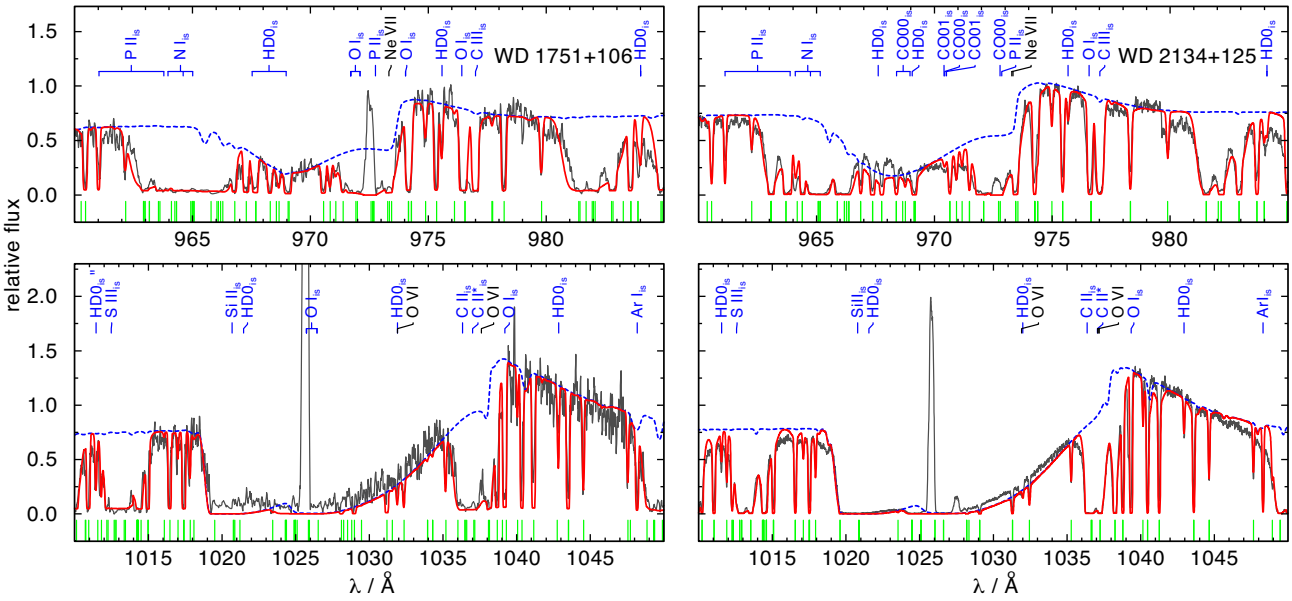

Figure 9. Comparison of synthetic spectra calculated with PoWR (blue line, dotted) compared with the FUSE observation of WD 1751 + 106 (left) and WD 2134 + 125 (right). In red a combined wind + ISM spectrum is shown. The wind models are calculated with a mass-loss rate of $\log[\dot{M} / (\mathrm{M}_\odot\ \mathrm{yr}^{-1})] = -8.1$, and $v_\infty = 3500\,\mathrm{km\,s^{-1}}$ for WD 1751 + 106 and $v_\infty = 3300\,\mathrm{km\,s^{-1}}$ for WD 2134 + 125. Upper panel: around Ne VII λ 973.33 Å, lower: around O VI λλ 1031.91, 1037.61 Å. The green marks at the bottom of each panel indicate wavelengths of strong interstellar H_2 lines.

wavelength range has a much better quality. We obtained the best fit to the complicated line profile of C IV λλ 1548, 1551 Å by models with a mass-loss rate of $\log[\dot{M} / (M_\odot/\mathrm{yr})] \approx -8.1$. In both cases, we assumed a density contrast of $D = 10$, which is typically found for H-deficient CSPNe winds (Todt, Hamann & Gräfener 2008).

The blue edges of the P Cygni profiles of O VI λλ 1032, 1038 Å and C IV λλ 1548, 1551 Å were used to estimate the terminal wind velocity for WD 2134 + 125 of about $v_\infty = 3300 \pm 100\ \mathrm{km\,s^{-1}}$ and a $\beta = 0.6$. Additional broadening due to depth dependent microturbulence with $v_\mathrm{D} = 20\ \mathrm{km\,s^{-1}}$ in the photosphere, estimated from, e.g. the F VI λ1140 line, up to $v_\mathrm{D} = 230\ \mathrm{km\,s^{-1}}$ in the outer wind was taken into account and allows to fit the width of the O VI (Fig. 9) and the C IV resonance lines simultaneously. Similar values have been obtained for WD 1751 + 106, i.e. $v_\infty = 3500 \pm 100\ \mathrm{km\,s^{-1}}$ and $v_\mathrm{D} = 50\ \mathrm{km\,s^{-1}}$ in the photosphere up to $v_\mathrm{D} = 180\ \mathrm{km\,s^{-1}}$ in the outer wind. At these high mass-loss rates, the stellar wind is coupled and the photosphere is chemically homogeneous (Unglaub 2007, 2008).

7 MASS, LUMINOSITY, AND DISTANCE

The determination of the mass of WD 1751 + 106 and WD 2134 + 125 is difficult since their evolutionary history is not unambiguous. If they are AFTP stars no appropriate set of evolutionary tracks is available in the literature to compare with. Lawlor & MacDonald (2006) presented a variety of calculations for the evolution of H-deficient post-AGB stars. The so-called AGB departure type V scenario (departure from the AGB during an He flash) and the type IV scenario appear to be in the transition between AFTP and LTP (Table 1). A different H/He ratio should have an influence on the result (cf. Miller Bertolami & Althaus 2007). To decide which grid of post-AGB tracks should be used, we calculated some AFTP models with LPCODE (Althaus et al. 2003, 2005) (Table 1). This was done by recomputing the end of the AGB evolution of three models presented in Miller Bertolami (2016) and tuning the mass loss at the end of the AGB phase as to enforce an AFTP event. These sequences have (M_ZAMS, Z_ZAMS, M_f) = (1.25M$_\odot$, 0.01, 0.566M$_\odot$), (1.00M$_\odot$, 0.001, 0.550M$_\odot$), (1.50M$_\odot$, 0.001, 0.594M$_\odot$) (Table 1). At the location of the stars in the $\log g - T_\mathrm{eff}$ diagram, the tracks for VLTP and AFTP stars coincide (Fig. 10). Thus, the approach of using VLTP tracks for the determination of the mass is acceptable.

We find $M = 0.57^{+0.07}_{-0.04}\,\mathrm{M}_\odot$ for WD 1751 + 106 and WD 2134 + 125. Using the initial–final mass relation of Cummings et al. (2018), these stars originate from progenitors with initial mass of about 1.0–1.1 M$_\odot$. From the 0.515, 0,530, 0,542, 0,565, 0.584, 0.609, and 0.664 M$_\odot$ tracks (Fig. 10), we determine the luminosity of $\log L / \mathrm{L}_\odot = 3.77^{+0.23}_{-0.24}$ for WD 1751 + 106 and WD 2134 + 125.

The spectroscopic distances are calculated following the flux calibration[6] of Heber et al. (1984),

$$f_\mathrm{V} = 3.58 \times 10^{-9} \times 10^{-0.4 m_{\mathrm{V}_0}}\ \mathrm{erg\,cm^{-2}\,s^{-1}\,Å^{-1}} \quad (1)$$

with $m_{\mathrm{V}_0} = m_\mathrm{V} - 2.175c$, $c = 1.47E_{B-V}$. We take $m_\mathrm{V} = 14.75 \pm 0.13$ (Acker et al. 1992) and $c = 0.390 \pm 0.015$ using our determination of E_{B-V} for WD 1751 + 106 and $m_\mathrm{V} = 13.68 \pm 0.25$ (Acker et al. 1992) and $c = 0.199 \pm 0.015$ for WD 2134 + 125. The distance is derived from

$$d\ /\ pc = 7.11 \times 10^4 \sqrt{H_\nu (M/\mathrm{M}_\odot) \times 10^{(0.4 m_{\mathrm{V}_0} - \log g)}}\,. \quad (2)$$

The Eddington flux at $\lambda_\mathrm{eff} = 5454$ Å of our final model atmospheres including all 31 elements is $H_\nu = (1.89 \pm 0.19) \times 10^{-3}\mathrm{erg\,cm^{-2}\,s^{-1}\,Hz^{-1}}$ for WD 1751 + 106 and $H_\nu = (1.88 \pm 0.20) \times 10^{-3}\mathrm{erg\,cm^{-2}\,s^{-1}\,Hz^{-1}}$ for WD 2134 + 125. We derive

[6] http://astro.uni-tuebingen.de/~rauch/SpectroscopicDistanceDetermination.gif

Table 1. Photospheric abundances of WD 1751 + 106 and WD 2134 + 125 compared with evolutionary models.

$T_{\rm eff}$ (K)	log (g / (cm s^{-2}))	H	He	C	N	O	Ne	Comment
				(Mass fraction)				
115 000	5.6	0.15	0.52	0.31	0.000 3	0.003 3	0.001 9	WD 2134 + 125 , our atmosphere model
115 000	5.6	0.25	0.46	0.27	0.002 6	0.004 4	0.012	WD 1751 + 106 , our atmosphere model
84 000	5.0	0.444	0.539	0.012	0.002	0.002	0.000 8	Lawlor & MacDonald (2006, AGB departure type IV)
140 000	6.0	0.106	0.794	0.085	0.002	0.012	0.003	Lawlor & MacDonald (2006, AGB departure type IV)
87 000	5.0	0.565	0.427	0.005	0.000 9	0.000 9	0.000 4	Lawlor & MacDonald (2006, AGB departure type V)
150 000	6.0	0.164	0.775	0.051	0.001 4	0.005 7	0.002	Lawlor & MacDonald (2006, AGB departure type V)
		0.197	0.450	0.296	0.000 1	0.056	0.000 78	AFTP model $M_{\rm f} = 0.550$, $Z = 0.001$
		0.137	0.390	0.357	0.000 6	0.104	0.008 5	AFTP model $M_{\rm f} = 0.566$, $Z = 0.01$
		0.219	0.445	0.258	0.000 7	0.055	0.021	AFTP model $M_{\rm f} = 0.594$, $Z = 0.001$

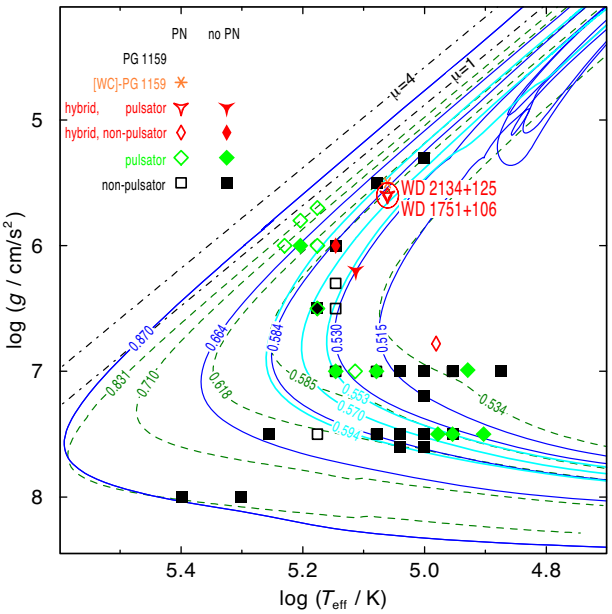

Figure 10. Positions of WD 1751 + 106 (Abell 43) and WD 2134 + 125 (NGC 7094) with their error ellipses and related objects in the log $T_{\rm eff}$ − log g plane compared with evolutionary tracks (labelled with the respective masses in $M_\odot$) of VLTP stars (Miller Bertolami & Althaus 2006, blue full lines), of H-burning post-AGB stars (calculated with initial solar metallicity, Miller Bertolami 2016, green dashed lines), and of AFTP stars (cyan, thick lines).The dash–dotted $\mu = 1$ and 4 lines indicate the Eddington limits for pure H and He atmospheres, respectively.

distances of $d = 2.23^{+0.31}_{-0.33}$ kpc for WD 1751 + 106 and $d = 1.65^{+0.32}_{-0.31}$ kpc for WD 2134 + 125. WD 1751 + 106 is located $0.67^{+0.10}_{-0.10}$ kpc above the Galactic plane and WD 2134 + 125 has a depth below the Galactic plane of $0.78^{+0.15}_{-0.15}$ kpc. Taking into account the angular sizes of the nebulae measured from narrow-band images by Rauch (1999), the nebula shells of Abell 43 and NGC 7094 have radii of $R = 0.48^{+0.07}_{-0.07}$ pc and $R = 0.42^{+0.08}_{-0.08}$ pc, respectively. With the measured expansion velocity of 40 ± 2 km s^{-1} for Abell 43 and 38 ± 2 km s^{-1} for NGC 7094 (Pereyra, Richer & López 2013), the expansion times are $11\,600^{+1\,600}_{-1\,700}$ yr and $10\,900^{+2\,100}_{-2\,000}$ yr, respectively. These dynamical time-scales place a lower limit to the actual age of the PNe since velocity gradients and the acceleration over time are not taken into account (Gesicki & Zijlstra 2000). Dopita et al. (1996) derived typical correction factors of 1.5. Both stars are targets of the Gaia mission and contained in the data made public in the second data release (DR2). Gaia measured parallaxes of 0.″431 ± 0.″061 and 0.″615 ± 0.″059 (Gaia Collaboration 2018) for WD 1751 + 106 (ID 4488953930631143168) and WD 2134 + 125 (ID 1770058865674512896), respectively. This corresponds to relative errors of 14.1 per cent and 9.5 per cent. From these values, Bailer-Jones et al. (2018) derived distances of $2.19^{+0.35}_{-0.27}$ kpc for WD 1751 + 106 and $1.55^{+0.16}_{-0.13}$ kpc for WD 2134 + 125 . These values are in good agreement with our spectroscopic distance determination and validate the mass determination by spectroscopic means using stellar atmosphere models and evolutionary tracks.

8 DISCUSSION

Our aim was to determine the element abundances of WD 1751 + 106 and WD 2134 + 125 beyond He and H. The results are shown in Table 3. By comparing our results to the abundances of other post-AGB stars and evolutionary models, we are able to conclude constraints for nucleosynthesis processes and evolutionary channels. The H-deficient nature of WD 1751 + 106 and WD 2134 + 125 suggests that here, as in other H-deficient stars, we see nuclear processed material on the surface that has formed either during the progenitor AGB phase or the same mixing and burning processes that lead to the H-deficiency in the first place. Fig. 11 illustrates the following sections.

8.1 Comparison to other hybrid PG 1159 stars

The group of known hybrid PG 1159 stars comprises the CS of Sh 2 – 68 and HS 2324 + 3944 (WD 1822 + 008 and WD 2324 + 397, respectively, McCook & Sion 1999) and SDSS 152116.00 + 251437.46 (Werner & Herwig 2006; Werner et al. 2014), besides the two program stars of this work. The known atmospheric parameters for these objects are summarized in Table 2. For WD 1822 + 008, Gianninas et al. (2010) found $T_{\rm eff} = 84\,460$ K and log $g = 7.24$. Its position in the log $T_{\rm eff}$–log g diagram (Fig. 10) suggests that the star is already located close to the beginning of the WD cooling track and is thus further evolved than the two stars of this work. The large distance of 1000 ± 400 pc (Binnendijk 1952) was reduced and better constrained to $399.7^{+11.8}_{-12.5}$ pc (Bailer-Jones et al. 2018) using Gaia data. With its a diameter of 400 arcsec ± 70 arcsec (Fesen, Gull & Heckathorn 1983), the PN has a radius of $0.388^{+0.082}_{-0.078}$ pc. Considering an expansion velocity of 7.5 km s^{-1} (Hippelein & Weinberger 1990), this yields a dynamic time-scale of $50\,600^{+10\,700}_{-10\,200}$ yr, which confirms the suggestion from

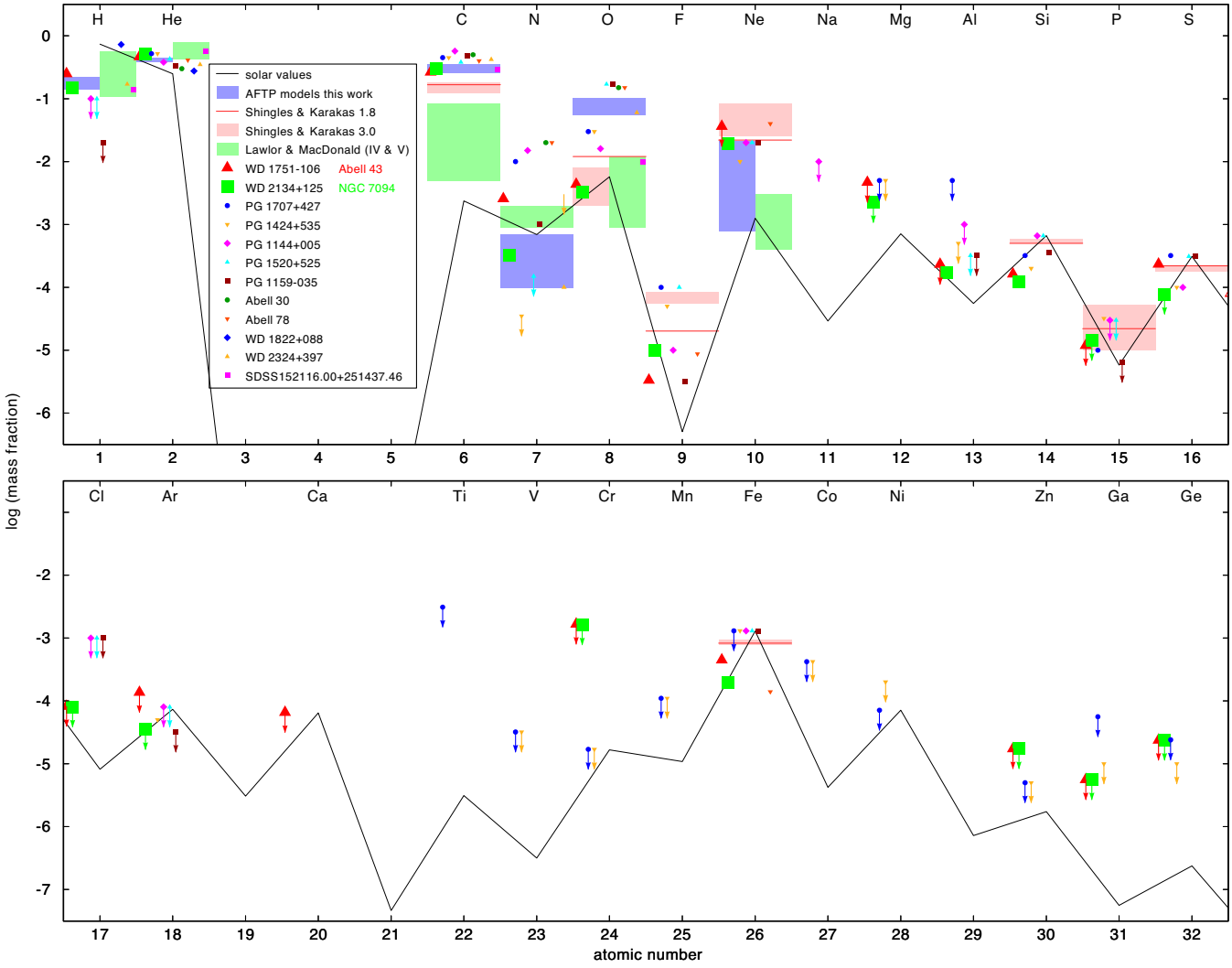

Figure 11. Photospheric abundances for a set of PG 1195 stars and calculated ranges from evolutionary models. For the models of Shingles & Karakas (2013), the initial mass of the star in $M_{\odot}$ is given in the legend box. Upper limits are indicated with arrows. The solid black lines indicates solar abundances.

Table 2. Photospheric abundances of WD 1751 + 106 and WD 2134 + 125 with other hybrid PG 1159 stars and the CSPNe Abell 30 and Abell 78.

Object	$T_{\rm eff}$	log (g / (cm s^{-2}))	H	He	C	N	O	Reference
	(K)		(Mass fraction)					
WD 2134 + 125	115 000	5.6	0.15	0.52	0.31	0.000 3	0.003 2	This work
WD 1751 + 106	115 000	5.6	0.25	0.46	0.27	0.002 6	0.004 4	This work
WD 1822 + 008	84 460	7.24	0.66	0.34				Gianninas et al. (2010)
WD 2324 + 397	130 000	6.2	0.17	0.35	0.42	0.000 1	0.06	Dreizler et al. (1996); Dreizler (1999)
SDSS 152116.00 + 251437.46	140 000	6.0	0.14	0.56	0.29		0.01	Werner et al. (2014)
Abell 30	115 000	5.5		0.41	0.40	0.04	0.15	Leuenhagen, Koesterke & Hamann (1993)
Abell 78	117 000	5.5		0.30	0.50	0.02	0.15	Toalá et al. (2015); Werner & Koesterke (1992)

the location in the log $T_{\rm eff}$–log g diagram and assigns Sh 2 − 68 to the group of oldest and largest PNe. It has a lower element ratio of He/H compared to WD 1751 + 106 and WD 2134 + 125 . This might result from ongoing depletion of heavier elements from the atmosphere due to gravitational settling.

WD 2324 + 397 ($T_{\rm eff}$ = 130 000 ± 10 000 K and log g = 6.2 ± 0.2; Dreizler et al. 1996) and SDSS 152116.00 + 251437.46 ($T_{\rm eff}$ = 140 000 ± 15 000 K and log g = 6.0 ± 0.3; Werner et al. 2014) are members of this group without an ambient PN (Werner et al. 1997). The C abundance is similar to the values determined for our two program stars. Considering the C/H ratio, the value for SDSS 152116.00 + 251437.46 is close to the one of WD 2134 + 125 while the one for WD 2324 + 397 is slightly higher. Both their O/H ratios exceeds the values of our two program stars by a factor of 2 or even more. The N/H ratio of the stars for which it is known is very low. The He/H ratio of WD 2324 + 397 resembles the value of WD 1751 + 106 whereas WD 2134 + 125 has a higher He content similar to SDSS 152116.00 + 251437.46.

Table 3. Parameters of WD 1751 + 106 and WD 2134 + 125 compared with literature values.

	WD 1751 + 106		WD 2134 + 125	
	Literature	This work	Literature	This work
$T_{\rm eff}$ (kK)	115 ± 5 [a]	115 ± 5	115 ± 5 [a]	115 ± 5
$\log(g\,/\,({\rm cm\,s^{-2}}))$	5.5 ± 0.1 [a]	5.6 ± 0.1	5.4 ± 0.1 [a]	5.6 ± 0.1
E_{B-V}	0.265 ± 0.035 [b]	0.265 ± 0.010	0.150 ± 0.040 [c]	0.135 ± 0.010
$n_{\rm H\,I}\,({\rm cm^{-2}})$	$(1.0 \pm 0.2) \times 10^{21}$ [b]	$(1.0 \pm 0.1) \times 10^{21}$	$(7.0 \pm 0.1) \times 10^{20}$ [c]	$(6.5 \pm 0.1) \times 10^{20}$
$v_{\rm rad}$ (km s^{-1})	-42.0 ± 11.5 [d]	-100 ± 10	-101.1 ± 30.8 [d]	-53 ± 10
d (kpc)	2.47 ± 0.30 [e]	$2.23^{+0.31}_{-0.33}$	1.75 ± 0.36 [e]	$1.65^{+0.32}_{-0.31}$
$M\,/\,{\rm M_\odot}$	$0.53^{+0.10}_{-0.02}$ [b]	$0.57^{+0.07}_{-0.04}$	$0.53^{+0.06}_{-0.06}$ [c]	$0.57^{+0.07}_{-0.04}$
$\log(L\,/\,{\rm L_\odot})$	$3.44^{+0.50}_{-0.58}$ [b]	$3.77^{+0.23}_{-0.24}$		$3.77^{+0.23}_{-0.24}$
$R_{\rm PN}$ (pc)	0.51 [f]	$0.48^{+0.07}_{-0.07}$	0.51 [f]	$0.42^{+0.08}_{-0.08}$

Notes: [a]Löbling (2018), [b]Friederich (2010), [c]Ziegler (2008), [d]Durand, Acker & Zijlstra (1998), [e]Frew et al. (2016), [f]Napiwotzki (1999), [g]Ringat et al. (2011), [h]Ziegler et al. (2009).

8.2 Comparison to Abell 30 and Abell 78

Comparing the results of our analysis to the parameters known for the CSs of the PNe Abell 30 and Abell 78 is of special interest, because these objects are located at almost the same position in the $\log T_{\rm eff}$–$\log g$ diagram. Both are [WC]-PG 1159 transition objects with $T_{\rm eff} = 115\,000$ K and $\log g = 5.5$ (Leuenhagen et al. 1993) and $T_{\rm eff} = 117\,000 \pm 5000$ K and $\log g = 5.5$ (Werner & Koesterke 1992; Toalá et al. 2015). Their element mass fractions are also included in Table 2. Obvious are the higher He and lower C, N, and O abundances in our two hybrid PG 1159 stars. This may result from different evolutionary channels. The CSs of Abell 30 and Abell 78 both underwent a born-again scenario (Iben et al. 1983) resulting in a return to the AGB, whereas the hybrid PG 1159 stars experience a final He-shell flash at the departure from the AGB. This AFTP evolution may be the reason for the smaller amount of C, N, and O in the atmosphere in contrast to a (V)LTP scenario. Toalá et al. (2015) found an Fe deficiency of about one dex for Abell 78. This subsolar Fe abundance is in good agreement with the results for WD 1751 + 106 and WD 2134 + 125, although they show a smaller Fe deficiency. The high Ne abundance of 4 per cent by mass of the CS of Abell 78 (Toalá et al. 2015) and the revised N abundance of 1.5 per cent by mass for both CSPNe (Guerrero et al. 2012; Toalá et al. 2015) exceed the values determined for our two hybrid stars and are also an indicator for different evolutionary channels, namely VLTP and AFTP evolution. In common with the CS of Abell 78 is the high abundance of F (25 times solar; Toalá et al. 2015) compared to 9.3 and 29 times solar, for WD 1751 + 106 and WD 2134 + 125 respectively). Their mass-loss rates of $\dot{M}/{\rm M_\odot} = 2.0 \times 10^{-8}\,{\rm yr^{-1}}$ (Guerrero et al. 2012) and $\dot{M}/{\rm M_\odot} = 1.6 \times 10^{-8}\,{\rm yr^{-1}}$ (Toalá et al. 2015) are about a factor 2 higher than the ones determined for WD 1751 + 106 and WD 2134 + 125 (Section 6). The PNe Abell 30 and Abell 78 look very similar in shape but appear different to the 'Galactic Soccerballs'.

8.3 Comparison to PG 1159 stars, hot post-AGB stars, and nucleosynthesis models

Karakas & Lugaro (2016) presented a grid of evolutionary models for different initial masses and metallicities. For stars with initial masses $M \leq 3\,{\rm M_\odot}$, they predict an enhanced production of C, N, F, Ne, and Na compared to solar values and normalized to the value for Fe. This prediction for the surface abundances of post-AGB stars is in line with our abundance determinations (Fig. 12). Another set of evolutionary models for initial masses of $1.8 - 6\,{\rm M_\odot}$ was calculated by Shingles & Karakas (2013) to investigate the resulting element yields of the species He, C, O, F, Ne, Si, P, S, and Fe depending on uncertainties in nucleosynthesis processes. They present the intershell abundances of their stellar models that should represent the surface abundances of PG 1159 stars. As described in (Section 1), the surface abundances of hybrid PG 1159 stars should reflect a mixture of the abundances of the former H-rich envelope and the intershell.

The C abundances of our two program stars resemble the values of other PG 1159 stars like for example the prototype star PG 1159 − 035 (Jahn et al. 2007), the hot PG 1159 stars PG 1520 + 525 and PG 1144 + 005 (Werner et al. 2016) and the 'cooler' PG 1707 + 427 and PG 1424 + 535 (Werner, Rauch & Kruk 2015).

The subsolar O abundances of the two stars analysed in this work are significantly lower than the supersolar values of the stars mentioned above. However, the O abundance of the hybrid PG 1159 stars lie within the predicted range of Shingles & Karakas (2013) (O mass fraction between 0.2 and 1.2 per cent) and Lawlor & MacDonald (2006) in comparison to the PG 1159 stars. The large range in O abundances may be caused by different effectiveness of convective boundary mixing of the pulse-driven convection zone into the C/O core in the thermal pulses on the AGB.

An N enrichment is predicted for PG 1159 stars that experienced a VLTP scenario due to a large production of ^{14}N in an H-ingestion flash (HIF; cf. Werner & Herwig 2006). WD 1751 + 106 and WD 2134 + 125 experienced an AFTP without HIF what corresponds to their comparatively low N abundance. The value for WD 2134 + 125 lies within the range that is predicted by AFTP models whereas the value for WD 1751 + 106 is higher.

The set of PG 1159 stars shows a large range of F abundances from low mass fractions of 3.2×10^{-6} for the prototype PG 1159 − 035 to values of 1.0×10^{-4} for PG 1707 − 427. The values of WD 1751 + 106 and WD 2134 + 125 lie within this range but below the predictions of Shingles & Karakas (2013) (F mass fractions between 2.0×10^{-5} and 2.7×10^{-4}). The F production in the intershell region is very sensitive on the temperature and therefore on the initial mass (Lugaro et al. 2004). They predict the highest F abundances for stars with initial masses of $2 - 4\,{\rm M_\odot}$ at solar metallicity (F intershell mass fractions of 3–7 $\times\ 10^{-5}$). Again, the values of WD 2134 + 125 and WD 1751 + 106 are about 3–10 times lower than these predictions.

The Ne abundances for the set of mentioned PG 1159 stars are all supersolar and in agreement with evolutionary models. The determined values for the Si, P, and S abundances are at the

Table 3. *Continued.*

	WD 1751 + 106						WD 2134 + 125					
	Literature		This work				Literature		This work			
Abundances	[X]	Mass fraction	[X]	Mass fraction	Number fraction	[X/Fe]	[X]	Mass fraction	[X]	Mass fraction	Number fraction	[X/Fe]
H	− 0.483[g]	2.43×10^{-1}	− 0.5	2.5×10^{-1}	6.4×10^{-1}	− 0.0	− 0.62[h]	1.77×10^{-1}	− 0.7	1.5×10^{-1}	4.9×10^{-1}	0.1
He	0.350[g]	5.59×10^{-1}	0.3	4.6×10^{-1}	3.0×10^{-1}	0.7	0.45[h]	7.03×10^{-1}	0.3	5.2×10^{-1}	4.3×10^{-1}	1.1
C	1.909[g]	1.75×10^{-1}	2.1	2.7×10^{-1}	5.8×10^{-2}	2.5	1.76[h]	1.24×10^{-1}	2.1	3.1×10^{-1}	8.4×10^{-2}	2.9
N	− 0.491[g]	2.00×10^{-4}	0.6	2.6×10^{-3}	4.8×10^{-4}	1.0	− 0.85[h]	8.73×10^{-5}	− 0.3	3.3×10^{-4}	7.7×10^{-5}	0.5
O	− 0.516[g]	1.63×10^{-3}	− 0.1	4.4×10^{-3}	7.2×10^{-4}	0.3	− 1.81[h]	8.20×10^{-5}	− 0.2	3.2×10^{-3}	6.7×10^{-4}	0.6
F	0.694[g]	2.50×10^{-6}	1.0	3.3×10^{-6}	4.5×10^{-7}	1.3	0.34[h]	1.11×10^{-6}	1.5	9.9×10^{-6}	1.7×10^{-6}	2.1
Ne			≤ 1.5	$\leq 3.6 \times 10^{-2}$	$\leq 4.7 \times 10^{-3}$	≤ 1.9	0.00[h]	1.02×10^{-3}	1.2	1.9×10^{-3}	3.1×10^{-3}	2.0
Mg	≤ 0.108[b]	$\leq 7.74 \times 10^{-4}$	≤ 0.8	$\leq 4.7 \times 10^{-3}$	$\leq 5.0 \times 10^{-4}$	≤1.3			≤ 0.5	$\leq 2.2 \times 10^{-3}$	$\leq 3.0 \times 10^{-4}$	≤ 1.3
Al	≤ 0.797[b]	$\leq 2.90 \times 10^{-4}$	≤ 0.6	$\leq 2.3 \times 10^{-4}$	$\leq 2.2 \times 10^{-5}$	≤1.1			0.5	1.7×10^{-4}	2.1×10^{-5}	1.3
Si	− 0.560[g]	1.83×10^{-4}	− 0.6	1.6×10^{-4}	1.5×10^{-5}	− 0.2	− 0.21[h]	4.10×10^{-4}	− 0.7	1.2×10^{-4}	1.4×10^{-5}	0.1
P	− 0.593[g]	1.33×10^{-6}	≤ 0.3	$\leq 1.2 \times 10^{-5}$	$\leq 1.0 \times 10^{-6}$	≤0.8	− 1.15[h]	3.70×10^{-7}	≤ 0.4	$\leq 1.4 \times 10^{-5}$	$\leq 1.5 \times 10^{-6}$	≤ 1.2
S	− 0.378[g]	1.36×10^{-4}	− 0.1	2.4×10^{-4}	1.9×10^{-5}	0.3	0.16[h]	4.69×10^{-4}	≤ − 0.6	$\leq 7.8 \times 10^{-5}$	$\leq 8.0 \times 10^{-6}$	≤ 0.2
Cl			≤ 1.0	$\leq 8.3 \times 10^{-5}$	$\leq 6.1 \times 10^{-6}$	≤ 1.5			≤ 1.0	$\leq 8.1 \times 10^{-5}$	$\leq 7.5 \times 10^{-6}$	≤ 1.8
Ar	≤ 1.307[b]	$\leq 1.04 \times 10^{-3}$	≤ 0.3	$\leq 1.4 \times 10^{-4}$	$\leq 8.8 \times 10^{-6}$	≤0.7	0.00[c]	4.43×10^{-5}	≤ − 0.3	$\leq 3.5 \times 10^{-5}$	$\leq 2.9 \times 10^{-6}$	≤ 0.5
Ca			≤ 0.0	$\leq 6.5 \times 10^{-5}$	$\leq 4.5 \times 10^{-6}$	≤ 0.5						
Cr			≤ 2.0	$\leq 1.7 \times 10^{-3}$	$\leq 8.1 \times 10^{-5}$	≤ 2.5			≤ 2.0	$\leq 1.6 \times 10^{-3}$	$\leq 1.0 \times 10^{-4}$	≤ 2.8
Fe	− 0.691[b]	2.35×10^{-4}	− 0.4	4.5×10^{-4}	2.1×10^{-5}	0.0	≤ − 1.00[h]	$\leq 1.15 \times 10^{-4}$	− 0.8	2.0×10^{-4}	1.2×10^{-5}	0.0
Ni	≤ − 1.000[b]	$\leq 7.30 \times 10^{-6}$					≤ − 1.00[h]	$\leq 7.30 \times 10^{-6}$				
Zn			≤ 1.0	$\leq 1.7 \times 10^{-5}$	$\leq 7.2 \times 10^{-7}$	≤1.5			≤ 1.0	$\leq 1.7 \times 10^{-5}$	$\leq 9.1 \times 10^{-7}$	≤ 1.8
Ga			≤ 2.0	$\leq 5.6 \times 10^{-6}$	$\leq 2.2 \times 10^{-7}$	≤2.5			≤ 2.0	$\leq 5.6 \times 10^{-6}$	$\leq 2.8 \times 10^{-7}$	≤ 2.8
Ge			≤ 2.0	$\leq 2.4 \times 10^{-5}$	$\leq 8.9 \times 10^{-7}$	≤2.5			≤ 2.0	$\leq 2.4 \times 10^{-5}$	$\leq 1.1 \times 10^{-6}$	≤ 2.8
Kr			≤ 3.5	$\leq 3.4 \times 10^{-4}$	$\leq 1.1 \times 10^{-5}$	≤4.0			≤ 3.5	$\leq 3.4 \times 10^{-4}$	$\leq 1.4 \times 10^{-5}$	≤ 4.3
Zr									≤ 3.0	$\leq 2.5 \times 10^{-5}$	$\leq 9.6 \times 10^{-7}$	≤ 3.8
Te			≤ 4.0	$\leq 1.4 \times 10^{-4}$	$\leq 3.8 \times 10^{-6}$	≤4.6			≤ 3.5	$\leq 4.5 \times 10^{-5}$	$\leq 1.2 \times 10^{-6}$	≤ 4.3
I			≤ 4.6	$\leq 1.3 \times 10^{-4}$	$\leq 3.6 \times 10^{-6}$	≤5.2			≤ 5.0	$\leq 3.3 \times 10^{-4}$	$\leq 8.9 \times 10^{-6}$	≤ 5.8
Xe									≤ 4.0	$\leq 1.7 \times 10^{-4}$	$\leq 4.4 \times 10^{-6}$	≤ 4.8

Notes: [X] = log (abundance/solar abundance), [X/Fe] = $\log(n_X/n_{Fe}) - \log(n_{X,\odot}/n_{Fe,\odot})$ with the number fraction n_X for element X, the error of our abundance determination is ±0.3 dex. [a]Löbling (2018), [b]Friederich (2010), [c]Ziegler (2008), [d]Durand et al. (1998), [e]Frew et al. (2016), [f]Napiwotzki (1999), [g]Ringat et al. (2011), [h]Ziegler et al. (2009).

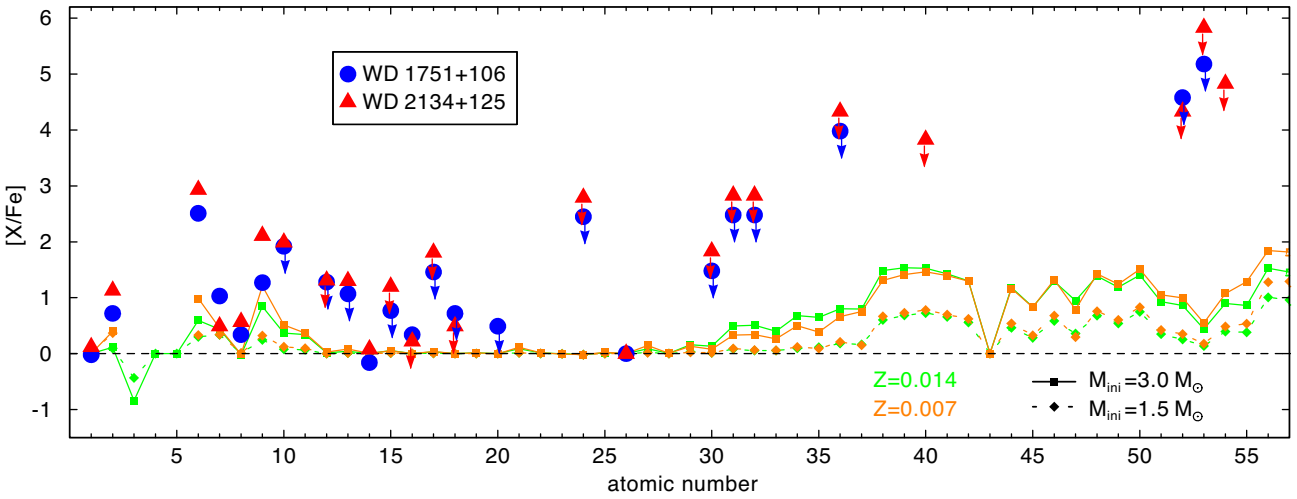

Figure 12. Photospheric abundance ratio [X/Fe] $= \log(n_X/n_{Fe}) - \log(n_{X,\odot}/n_{Fe,\odot})$ with the number fraction n_X for element X of WD 1751 + 106 and WD 2134 + 125 determined from detailed line-profile fits. Upper limits are indicated with arrows. Predictions of Karakas & Lugaro (2016, $M_{ini} = 1.5$ and 3.0 (see legend); metallicity $Z = 0.014$ (green) and 0.007 (cyan)) are shown for comparison.

lower border or slightly below the predictions from evolutionary models. The same holds for the solar upper abundance limit for P in PG 1159 − 035.

The Fe deficiency is not explained by nucleosynthesis calculations like those of Karakas & Lugaro (2016) that predict solar Fe abundances for stars with an initial solar composition, which is due to the fact that iron is not strongly depleted in nuclear processes in AGB stars with masses ranging from 0.8 to 8.0 $M_\odot$ as it is the case for the precursor AGB stars of Abell 43 and NGC 7094. The models of Shingles & Karakas (2013) yield a slightly subsolar Fe abundances but still cannot explain the observed deficiency. For some of the PG 1159 stars of the set used for comparison here, the Fe abundance has been measured and all are found to be solar. The only other star in Fig. 11 which, besides WD 1751 + 106 and WD 2134 + 125 , shows an Fe deficiency is the CSPN of Abell 78 (Section 8.2). The Fe deficiency of 0.4 and 0.8 dex for WD 1751 + 106 and WD 2134 + 125 , respectively, does not include solar values within the error ranges. Löbling (2018) discuss the speculation of Herwig, Lugaro & Werner (2003) that this underabundance can be caused by neutron capture during the former AGB phase leading to a transformation of Fe into Ni and heavier elements. Probably the low Fe abundances determined in WD 1751 + 106 and WD 2134 + 125 are just a consequence of a low initial metal content for these objects. This subsolar metallicity does not rule out a thick or even thin disc membership (Recio-Blanco et al. 2014). Also their location and distance to the Galactic plane support that these are disc objects. The models of Karakas & Lugaro (2016) predict a strong enhancement of the TIEs in the atmospheres of post-AGB stars. Unfortunately, no abundance determination was possible for the TIEs but due to the determined upper abundance limits for Zn, Ga, Ge, Kr, and Te of both stars and Zr for WD 2134 + 125 a strong enhancement can be ruled out. This is consistent with our determination of the wind intensity for which the wind is coupled. Thus, this prevents diffusion and disrupts the equilibrium balance between radiative levitation and gravitational settling. To improve the analysis of TIEs, spectra with much better S/N and the calculation of reliable atomic data are highly desirable.

9 CONCLUSION

Regarding the evolutionary scenario for WD 1751 + 106 and WD 2134 + 125, an AFTP remains the best available candidate. The AFTP models presented here (Fig. 10 and Table 1) are able to reproduce qualitatively the observed trends. Abundances of H, He, C, N, and Ne are reasonably well reproduced by AFTP models. However AFTP models computed from sequences that include convective boundary mixing at the bottom of the pulse driven convective zone (as those presented here) display O abundances much larger than those of our program stars. In fact, the O abundances shown by our stars are in good agreement with those predicted by Lawlor & MacDonald (2006), using AGB models that do not include any type of convective boundary mixing at the bottom of the pulse driven convective zone. These models, however, underestimate the C and Ne abundance, while the H and He abundances reproduce the observed values. Yet, the main argument against the AFTP scenario comes from the expansion ages of the nebulae. According to stellar evolution computations, AFTP models reach the location of our program stars in the HRD less than 2000 yrs after departing from the AGB, while the expansion ages are several times larger than this. This is true regardless the mass-loss prescription adopted in the post-AGB evolution. Unless the masses of the CSPNe are much lower than derived here, the AFTP scenario is unable to reproduce this key observational feature.

It is desirable to determine the iron abundance and the abundances of heavier elements of the ambient PN to investigate on the photospheric composition of Abell 43 and NGC 7094 at the time of the PN's ejection and to analyse the elements produced and ejected during the preceding AGB phase (cf. Lugaro et al. 2017) but this is out of the focus of this paper.

ACKNOWLEDGEMENTS

LL has been supported by the German Research Foundation (DFG, grant WE 1312/49-1). M3B is supported by the PICT 2016-0053 from the Agencia National de Promotión Científica e Tecnológica (ANPCyT), Argentina. This work was partially funded by DA/16/07

grant from the German Academic Exchange Service - Ministerio de Ciencia, Tecnología e Innovación Productiva (DAAD-MinCyT) bilateral cooperation program. This work is based on observations with the NASA/ESA Hubble Space Telescope, obtained at the Space Telescope Science Institute, which is operated by the Association of Universities for Research in Astronomy, Inc., under NASA contract NAS5-26666, and on observations made with the NASA-CNES-CSA Far Ultraviolet Spectroscopic Explorer. Also this is based on data products from observations made with ESO Telescopes at the La Silla Paranal Observatory under programme ID 167.D-0407 . We were supported by the High Performance and Cloud Computing Group at the Zentrum für Datenverarbeitung of the University of Tübingen, the state of Baden-Württemberg through bwHPC, and the DFG (grant INST 37/935-1 FUGG). The GAVO project had been supported by the Federal Ministry of Education and Research (BMBF) at Tübingen (05 AC 6 VTB, 05 AC 11 VTB). We thank the referee Ralf Napiwotzki for his many useful comments that improved this paper. This work used the profile-fitting procedure OWENS developed by M. Lemoine and the FUSE French Team. We thank Falk Herwig, Timothy Lawlor, and James MacDonald for helpful comments and discussion, Ralf Napiwotzki for putting the reduced VLT spectra at our disposal. The TIRO (http://astro-uni-tuebingen.de/ TIRO), TMAD (http://astro-uni-tuebingen.de/ TMAD), and TOSS (http://astro-uni-tuebingen.de/ TOSS) services used for this paper were constructed as part of the activities of the German Astrophysical Virtual Observatory. Some of the data presented in this paper were obtained from the Mikulski Archive for Space Telescopes (MAST). STScI is operated by the Association of Universities for Research in Astronomy, Inc., under NASA contract NAS5-26555. Support for MAST for non-HST data is provided by the NASA Office of Space Science via grant NNX09AF08G and by other grants and contracts. This research has made use of NASA's Astrophysics Data System and the SIMBAD database, operated at CDS, Strasbourg, France. This work has made use of data from the European Space Agency (ESA) mission *Gaia* (https://www.cosmos.esa.int/gaia), processed by the *Gaia* Data Processing and Analysis Consortium (DPAC, https://www.cosmos.esa.int/web/gaia/dpac/consortium). Funding for the DPAC has been provided by national institutions, in particular the institutions participating in the *Gaia* Multilateral Agreement.

REFERENCES

Abell G. O., 1955, PASP, 67, 258
Abell G. O., 1966, ApJ, 144, 259
Acker A., Marcout J., Ochsenbein F., Stenholm B., Tylenda R., Schohn C., 1992, The Strasbourg-ESO Catalogue of Galactic Planetary Nebulae. Parts I, II. European Southern Observatory, Garching, Germany
Althaus L. G., Serenelli A. M., Córsico A. H., Montgomery M. H., 2003, A&A, 404, 593
Althaus L. G., Serenelli A. M., Panei J. A., Córsico A. H., García-Berro E., Scóccola C. G., 2005, A&A, 435, 631
Asplund M., Grevesse N., Sauval A. J., Scott P., 2009, ARA&A, 47, 481
Bailer-Jones C. A. L., Rybizki J., Fouesneau M., Mantelet G., Andrae R., 2018, AJ, 156, 58
Bianchi L., Herald J., Efremova B., Girardi L., Zabot A., Marigo P., Conti A., Shiao B., 2011, Ap&SS, 335, 161
Binnendijk L., 1952, ApJ, 115, 428
Busso M., Gallino R., Wasserburg G. J., 1999, ARA&A, 37, 239
Castor J. I., Abbott D. C., Klein R. I., 1975, ApJ, 195, 157
Cummings J. D., Kalirai J. S., Tremblay P.-E., Ramirez-Ruiz E., Choi J., 2018, ApJ, 866, 21
Cutri R. M. et al., 2003, 2MASS All Sky Catalog of point sources
De Marco O., Long J., Jacoby G. H., Hillwig T., Kronberger M., Howell S. B., Reindl N., Margheim S., 2015, MNRAS, 448, 3587
Dopita M. A. et al., 1996, ApJ, 460, 320
Dreizler S., 1999, in Schielicke R. E., ed., Review in Modern Astronomy 12, Astronomical Instruments and Methods at the turn of the 21st Century. Astronomische Gesellschaft, Hamburg, p. 255
Dreizler S., Werner K., Heber U., 1995, in Koester D., Werner K., Lecture Notes in Physics, Vol. 443. Springer-Verlag, Berlin, p. 160
Dreizler S., Werner K., Heber U., Engels D., 1996, A&A, 309, 820
Durand S., Acker A., Zijlstra A., 1998, A&AS, 132, 13
Fesen R. A., Gull T. R., Heckathorn J. N., 1983, PASP, 95, 614
Fitzpatrick E. L., 1999, PASP, 111, 63
Frew D. J., Parker Q. A., Bojičić I. S., 2016, MNRAS, 455, 1459
Friederich F., 2010, Diploma thesis, Eberhard Karls University Tübingen, Institute for Astronomy and Astrophysics
Gaia Collaboration et al., 2018, A&A, 616, A1
García-Díaz M. T., González-Buitrago D., López J. A., Zharikov S., Tovmassian G., Borisov N., Valyavin G., 2014, AJ, 148, 57
Gesicki K., Zijlstra A. A., 2000, A&A, 358, 1058
Gianninas A., Bergeron P., Dupuis J., Ruiz M. T., 2010, ApJ, 720, 581
Gray D. F., 1975, ApJ, 202, 148
Grevesse N., Scott P., Asplund M., Sauval A. J., 2015, A&A, 573, A27
Groenewegen M. A. T., Lamers H. J. G. L. M., 1989, A&AS, 79, 359
Guerrero M. A., De Marco O., 2013, A&A, 553, A126
Guerrero M. A. et al., 2012, ApJ, 755, 129
Hainich R., Pasemann D., Todt H., Shenar T., Sander A., Hamann W.-R., 2015, A&A, 581, A21
Hainich R. et al., 2014, A&A, 565, A27
Hamann W.-R., Gräfener G., 2004, A&A, 427, 697
Heber U., Hunger K., Jonas G., Kudritzki R. P., 1984, A&A, 130, 119
Herwig F., 2001, Ap&SS, 275, 15
Herwig F., Lugaro M., Werner K., 2003, in Kwok S., Dopita M., Sutherland R., eds, Proc. IAU Symp. 209, Planetary Nebulae: Their Evolution and Role in the Universe. Canberra, Australia, p. 85
Hippelein H., Weinberger R., 1990, A&A, 232, 129
Hubeny I., Hummer D. G., Lanz T., 1994, A&A, 282, 151
Hummer D. G., Mihalas D., 1988, ApJ, 331, 794
Hébrard G., Moos H. W., 2003, ApJ, 599, 297
Hébrard G. et al., 2002, Planet. Space Sci., 50, 1169
Iben I., Jr., Kaler J. B., Truran J. W., Renzini A., 1983, ApJ, 264, 605
Jahn D., Rauch T., Reiff E., Werner K., Kruk J. W., Herwig F., 2007, A&A, 462, 281
Kaler J. B., Feibelman W. A., 1985, ApJ, 297, 724
Karakas A. I., Lugaro M., 2016, ApJ, 825, 26
Koesterke L., Dreizler S., Rauch T., 1998, A&A, 330, 1041
Koesterke L., Hamann W.-R., 1997, in Habing H. J., Lamers H. J. G. L. M., eds, Proc. IAU Symp. 180, Planetary Nebulae, Kluwer, Dordrecht, p. 114
Koesterke L., Werner K., 1998, ApJ, 500, L55
Kohoutek L., 1963, Bull. Astron. Inst. Czech., 14, 70
Kramida A., Ralchenko Yu., Reader J., NIST ASD Team, 2018, NIST Atomic Spectra Database (Ver. 5.6.1). National Institute of Standards and Technonogy, Gaithersburg, Md., Available: https://physics.nist.gov/asd
Kronberger M. et al., 2012, Proc. IAU Symp. 283, Planetary Nebulae: an Eye to the Future. Puerto de la Cruz, Tenerife, Spain, p. 414
Kurucz R. L., 1991, in Crivellari L., Hubeny I., Hummer D. G., eds, Stellar Atmospheres - Beyond Classical Models, D. Reidel Publishing Co. Trieste, Italy, p. 441
Kurucz R. L., 2009, in Hubeny I., Stone J. M., MacGregor K., Werner K., eds, AIP Conf. Proc. Vol. 1171, Recent Directions in Astrophysical Quantitative Spectroscopy and Radiation Hydrodynamics. Am. Inst. Phys., New York, p. 43
Kurucz R. L., 2011, Can. J. Phys., 89, 417
Lawlor T. M., MacDonald J., 2006, MNRAS, 371, 263
Lemoine M. et al., 2002, ApJS, 140, 67

Leuenhagen U., Koesterke L., Hamann W.-R., 1993, Acta Astron., 43, 329
Lugaro M., Karakas A. I., Pignatari M., Doherty C. L., 2017, in Liu X., Stanghellini L., Karakas A., eds, Proc. IAU Symp. 323, Planetary Nebulae: Multi-Wavelength Probes of Stellar and Galactic Evolution. Beijing, China, Nanjing, p. 86
Lugaro M., Ugalde C., Karakas A. I., Görres J., Wiescher M., Lattanzio J. C., Cannon R. C., 2004, ApJ, 615, 934
Löbling L., 2018, Galaxies, 6, 65
McCook G. P., Sion E. M., 1999, ApJS, 121, 1
Miksa S., Deetjen J. L., Dreizler S., Kruk J. W., Rauch T., Werner K., 2002, A&A, 389, 953
Miller Bertolami M. M., 2016, A&A, 588, A25
Miller Bertolami M. M., Althaus L. G., 2006, A&A, 454, 845
Miller Bertolami M. M., Althaus L. G., 2007, A&A, 470, 675
Napiwotzki R., 1999, A&A, 350, 101
Napiwotzki R., Schönberner D., 1991, A&A, 249, L16
Oskinova L. M., Todt H., Ignace R., Brown J. C., Cassinelli J. P., Hamann W.-R., 2011, MNRAS, 416, 1456
Paczyński B., 1970, Acta Astron., 20, 47
Pauldrach A., Puls J., Kudritzki R. P., Mendez R. H., Heap S. R., 1988, A&A, 207, 123
Pereyra M., Richer M. G., López J. A., 2013, ApJ, 771, 114
Ragazzoni R., Cappellaro E., Benetti S., Turatto M., Sabbadin F., 2001, A&A, 369, 1088
Rauch T., 1999, A&AS, 135, 487
Rauch T., Deetjen J. L., 2003, in Hubeny I., Mihalas D., Werner K., eds, ASP Conf. Ser. Vol. 288, Stellar Atmosphere Modeling. Astron. Soc. Pac., San Francisco, p. 103
Rauch T., Gamrath S., Quinet P., Löbling L., Hoyer D., Werner K., Kruk J. W., Demleitner M., 2017a, A&A, 599, A142
Rauch T., Hoyer D., Quinet P., Gallardo M., Raineri M., 2015a, A&A, 577, A88
Rauch T., Köper S., Dreizler S., Werner K., Heber U., Reid I. N., 2004, in Maeder A., Eenens P., eds, Proc. IAU Symp. 215, Stellar Rotation. Cancun, Mexico, p. 573
Rauch T., Quinet P., Hoyer D., Werner K., Demleitner M., Kruk J. W., 2016a, A&A, 587, A39
Rauch T., Quinet P., Hoyer D., Werner K., Richter P., Kruk J. W., Demleitner M., 2016b, A&A, 590, A128
Rauch T., Quinet P., Knörzer M., Hoyer D., Werner K., Kruk J. W., Demleitner M., 2017b, A&A, 606, A105
Rauch T., Werner K., Biémont É., Quinet P., Kruk J. W., 2012, A&A, 546, A55
Rauch T., Werner K., Quinet P., Kruk J. W., 2014a, A&A, 564, A41
Rauch T., Werner K., Quinet P., Kruk J. W., 2014b, A&A, 566, A10
Rauch T., Werner K., Quinet P., Kruk J. W., 2015b, A&A, 577, A6
Recio-Blanco A. et al., 2014, A&A, 567, A5
Reiff E., Rauch T., Werner K., Kruk J. W., Koesterke L., 2008, in Werner A., Rauch T., eds, ASP Conf. Ser. Vol. 391, Hydrogen-Deficient Stars. Astron. Soc. Pac., San Francisco, p. 121
Reindl N., Rauch T., Miller Bertolami M. M., Todt H., Werner K., 2017, MNRAS, 464, L51
Reindl N., Rauch T., Parthasarathy M., Werner K., Kruk J. W., Hamann W.-R., Sander A., Todt H., 2014a, A&A, 565, A40
Reindl N., Rauch T., Werner K., Kruk J. W., Todt H., 2014b, A&A, 566, A116
Ringat E., Friederich F., Rauch T., Werner K., Kruk J. W., 2011, in Zijlstra A., Lykou F., McDonald I., Lagadec E., eds, Asymmetric Planetary Nebulae V Conference, Shaping of Stellar Ejecta. Jodrell Bank Centre for Astrophysics, Manchester, UK
Sander A., Shenar T., Hainich R., Gímenez-García A., Todt H., Hamann W.-R., 2015, A&A, 577, A13
Savitzky A., Golay M. J. E., 1964, Analytical Chemistry, 36, 1627
Schönberner D., 1979, A&A, 79, 108
Schöning T., Butler K., 1989, A&AS, 78, 51
Scott P., Asplund M., Grevesse N., Bergemann M., Sauval A. J., 2015a, A&A, 573, A26
Scott P. et al., 2015b, A&A, 573, A25
Shenar T. et al., 2015, ApJ, 809, 135
Shingles L. J., Karakas A. I., 2013, MNRAS, 431, 2861
Skrutskie M. F. et al., 2006, AJ, 131, 1163
Swift L., 1885, Astron. Nachr., 112, 313
Toalá J. A. et al., 2015, ApJ, 799, 67
Todt H., Hamann W.-R., Gräfener G., 2008, in Hamann W.-R., Feldmeier A., Oskinova L. M., eds, Clumping in Hot-Star Winds. Potsdam, Germany, p. 251
Tremblay P.-E., Bergeron P., 2009, ApJ, 696, 1755
Unglaub K., 2007, in Napiwotzki R., Burleigh M. R., eds, ASP Conf. Ser. Vol. 372, 15th European Workshop on White Dwarfs. Astron. Soc. Pac., San Francisco, p. 201
Unglaub K., 2008, A&A, 486, 923
Vishniac E. T., 1983, ApJ, 274, 152
Werner K., Bagschik K., Rauch T., Napiwotzki R., 1997, A&A, 327, 721
Werner K., Deetjen J. L., Dreizler S., Nagel T., Rauch T., Schuh S. L., 2003, in Hubeny I., Mihalas D., Werner K., eds, ASP Conf. Ser. Vol. 288, Stellar Atmosphere Modeling. Astron. Soc. Pac., San Francisco, p. 31
Werner K., Dreizler S., Rauch T., 2012, Astrophysics Source Code Library, record ascl:1212.015
Werner K., Herwig F., 2006, PASP, 118, 183
Werner K., Koesterke L., 1992, in Heber U., Jeffery C. S., eds, Lecture Notes in Physics, Vol. 401, The Atmospheres of Early-Type Stars. Springer-Verlag, Berlin, p. 288
Werner K., Rauch T., Kepler S. O., 2014, A&A, 564, A53
Werner K., Rauch T., Kruk J. W., 2005, A&A, 433, 641
Werner K., Rauch T., Kruk J. W., 2015, A&A, 582, A94
Werner K., Rauch T., Kruk J. W., 2016, A&A, 593, A104
Ziegler M., 2008, Diploma thesis, Eberhard Karls University Tübingen, Institute for Astronomy and Astrophysics
Ziegler M., Rauch T., Werner K., Koesterke L., Kruk J. W., 2009, J. Phys. Conf. Ser., 172, 012032
Ziegler M., Rauch T., Werner K., Kruk J. W., Oliveira C., 2007, in Napiwotzki R., Burleigh M. R., eds, ASP Conf. Ser. Vol. 372, 15th European Workshop on White Dwarfs. Astron. Soc. Pac., San Francisco, p. 197
Ziegler M., Rauch T., Werner K., Köppen J., Kruk J. W., 2012, A&A, 548, A109

SUPPORTING INFORMATION

Supplementary data are available at *MNRAS* online.

Figure A1. Determination of E_{B-V}.
Figure A2. Synthetic spectra calculated with $T_{\rm eff} = 115\,000$ K and different log g , compared with the UVES SPY observations of He II and H I lines for WD 1751 + 106 (gray).
Figure A3. Synthetic spectra calculated with $T_{\rm eff} = 115\,000$ K and different log g , compared with the UVES SPY observations of He II and H I lines for WD 2134 + 125 (gray). (log g is indicated in panel 6).
Figure A4. Section of the HST/STIS spectrum of WD 2134 + 125 (black) compared with synthetic spectra calculated with $T_{\rm eff} = 115\,000$ K and different log g of 6.1 (green dashed), 5.6 (red solid), and 5.1 (blue dotted).
Figure A5. Synthetic spectra calculated with log $g = 5.6$ for WD 1751 + 106 (top panel) and WD 2134 + 125 (bottom) and different $T_{\rm eff}$ (red: $T_{\rm eff} = 125\,000$ K, purple: $T_{\rm eff} = 115\,000$ K, blue: $T_{\rm eff} = 105\,000$ K), compared with the STIS observation of O V λ 1371.3 Å and the FUSE observation of O VI λλ 1124.7, 1124.9 Å (gray).
Figure A6. FUSE observation (gray) compared with the best static model including ISM line absorption (red).
Figure A7. GHRS and STIS observation (gray) for WD 1751+106 (top) and WD 2134 + 125 (bottom), respectively, compared with the best model (red).

Figure A8. Temperature and density structures and ionization fractions of all ions which are considered in our final model for WD 2134 + 125 .

Figure A9. Synthetic spectra of our best models (red lines) for WD 1751 + 106 (top panel) and WD 2134 + 125 (bottom) around H I Ly α calculated with $n_{\rm HI} = 1.0 \times 10^{21}$ cm^{-2} and 6.5×10^{20} cm^{-2}, respectively, compared with the observations (gray).

Table A1. Statistics of the H – Ar[a] and Ca – Ba[b] model atoms used in our model-atmosphere calculations.

Table A2. Observation log for WD 1751 + 106 and WD 2134 + 125 .

Table A3. Ions with recently calculated oscillator strengths.

Table A4. Abundances used for the calculation of the atmospheric structures.

Please note: Oxford University Press is not responsible for the content or functionality of any supporting materials supplied by the authors. Any queries (other than missing material) should be directed to the corresponding author for the article.

This paper has been typeset from a TEX/LATEX file prepared by the author.

Monthly Notices
of the
ROYAL ASTRONOMICAL SOCIETY

MNRAS **492,** 528–548 (2020)
Advance Access publication 2019 November 20

doi:10.1093/mnras/stz3247

First discovery of trans-iron elements in a DAO-type white dwarf (BD−22°3467)

L. Löbling [1]★ M. A. Maney,[1,2] T. Rauch [1] P. Quinet,[3,4] S. Gamrath,[3] J. W. Kruk[5] and K. Werner [1]

[1]*Institute for Astronomy and Astrophysics, Kepler Center for Astro and Particle Physics, Eberhard Karls University, Sand 1, D-72076 Tübingen, Germany*
[2]*Department of Astronomy and Astrophysics, Eberly College of Science, The Pennsylvania State University, 525 Davey Lab, University Park, PA 16802, USA*
[3]*Physique Atomique et Astrophysique, Université de Mons – UMONS, B-7000 Mons, Belgium*
[4]*IPNAS, Université de Liège, Sart Tilman, B-4000 Liège, Belgium*
[5]*NASA Goddard Space Flight Center, Greenbelt, MD 20771, USA*

Accepted 2019 November 18. Received 2019 November 11; in original form 2019 September 16

ABSTRACT

We have identified 484 lines of the trans-iron elements (TIEs) Zn, Ga, Ge, Se, Br, Kr, Sr, Zr, Mo, In, Te, I, Xe, and Ba, for the first time in the ultraviolet spectrum of a DAO-type white dwarf (WD), namely BD−22°3467, surrounded by the ionized nebula Abell 35. Our TIE abundance determination shows extremely high overabundances of up to 5 dex – a similar effect is already known from hot, H-deficient (DO-type) WDs. In contrast to these where a pulse-driven convection zone has enriched the photosphere with TIEs during a final thermal pulse and radiative levitation has established the extreme TIE overabundances, here the extreme TIE overabundances are exclusively driven by radiative levitation on the initial stellar metallicity. The very low mass ($0.533^{+0.040}_{-0.025}\,M_{\odot}$) of BD−22°3467 implies that a third dredge-up with enrichment of s-process elements in the photosphere did not occur in the asymptotic giant branch (AGB) precursor.

Key words: line: identification – stars: abundances – stars: AGB and post-AGB – stars: atmospheres – stars: individual: BD−22°3467 – planetary nebulae: individual: A66 35.

1 INTRODUCTION

Trans-iron elements (TIEs) are synthesized during the asymptotic giant branch (AGB) phase of a star by the slow neutron-capture (s-)process. Depending on the initial stellar mass, its yields vary strongly (Karakas & Lugaro 2016). To become detectable, TIEs have to be transported from the helium-rich intershell region to the stellar surface. This happens, if the star experiences a third dredge-up (TDU; cf. Herwig 2000). A scenario in which the envelope becomes mixed with the intershell region is known as the late helium-shell flash. Such a late thermal pulse (LTP) was predicted e.g. by Iben et al. (1983). When it occurs after the star's descent from the AGB at already declining luminosity, i.e. close to the end of nuclear burning, the H-burning shell is 'off' and a pulse-driven convection zone (PDCZ) establishes between the He-burning shell and the photosphere. The remaining H is mixed into the stellar interior, becomes diluted or even burned, making the star H-deficient (cf. Fujimoto 1977; Schönberner 1979; Iben et al. 1983; Blöcker 1995). Thus, it was – although surprising – well understandable that lines of 10 TIEs were identified (Werner et al. 2012a) in the ultraviolet (UV) spectrum of the DO-type white dwarf (WD) RE 0503−289 (effective temperature $T_{\rm eff} = 70\,000 \pm 2000$ K, surface gravity $\log(g/{\rm cm\,s^{-2}}) = 7.5 \pm 0.1$; Rauch et al. 2016b), which became an archetype for TIE search in WDs. Presently, 18 of these species are identified in RE 0503−289 (Rauch et al., submitted). Chayer et al. (2005) first succeeded in the detection of TIEs in DO WDs, namely six species in two other objects (HD 149499 B, HZ 21).

In a subsequent investigation, TIE line identification was successfully performed in three related H-deficient objects (two DO-type WDs and one PG 1159-type WD, namely WD 0111+002, PG 0109+111, and PG 1707+427; Hoyer et al. 2018). The commonality of these stars is that they are located close to the so-called PG 1159 wind limit (Unglaub & Bues 2000) that approximately separates the regions of PG 1159-type stars and DO-type WDs in the Hertzsprung–Russell diagram (HRD). Here, the stellar wind is already weak enough and diffusion can establish strong TIE overabundances of up to 5 dex in the photosphere (Rauch et al. 2016a).

The search for TIE lines has not been restricted to He-rich WDs. Vennes, Chayer & Dupuis (2005) discovered the first TIE in WDs at all, namely Ge in three DA WDs. One of them is G191−B2B, an object that is employed as spectrophotometric flux standard for

★ E-mail: loebling@astro.uni-tuebingen.de

the *Hubble Space Telescope* (e.g. Bohlin 2007; Rauch et al. 2013). Recently, the TIEs Cu, Zn, Ga, Ge, As, Sn, and Ba were identified (Rauch et al. 2012, 2013, 2014a,b, 2015, 2016a; Rauch et al., submitted). The TIE abundance pattern is similar to RE 0503−289, but at a lower absolute level probably because of the lower $T_{\rm eff}$ of G191−B2B ($T_{\rm eff}=60\,000$ K; Rauch et al. 2013). TIE line search and abundance analyses are also successfully performed in the field of He-rich, hot subdwarf stars. The first one was LS IV−14°116, for which extreme overabundances of Fe, Sr, Y, and Zr were detected (Naslim et al. 2011). The most recent members of the group of 'heavy metal' subdwarfs are HZ 44, HD 127493, and Feige 46 (e.g. Dorsch, Latour & Heber 2019; Latour, Dorsch & Heber 2019), with TIE enrichment patterns similar to those in Fig. 1.

Abell 35 was discovered by Abell (1955) and characterized as homogeneous disc planetary nebula (PN; Abell 1966). Jacoby (1981) classified the visible nucleus as G8 III−IV. Later, Grewing & Bianchi (1988) classified the hot, ionizing central star as DAO-type white dwarf (WD). Shortwards of 2800 Å, the WD dominates the flux, whereas the cool companion outshines it in the optical. Herald & Bianchi (2002) analysed the binary and found $T_{\rm eff}=80\,000$ K and $\log(g/{\rm cm\,s^{-2}})=7.7$ for the hot and $T_{\rm eff}=5000$ K and $\log g=3.5$ for the cool star. Ziegler et al. (2012) corrected the surface gravity of the WD to $\log g=7.2$ and Frew & Parker (2010) classified the nebula as 'bow shock nebula in a photoionized Strömgren sphere'. Recently, a close reinspection of the UV spectrum of the exciting star of the ionized nebula Abell 35, BD−22°3467 (WD 1250−226; McCook & Sion 1999), led us to the identification of TIE absorption lines. In this work, a systematic TIE line search was performed in order to constrain abundances analogously to Hoyer et al. (2017, for RE 0503−289). It is based on the BD−22°3467 model of Ziegler et al. (2012, atmospheric parameters given in Table A1) that was calculated using the non-local thermodynamic equilibrium (NLTE) model atmosphere code of the Tübingen NLTE Model Atmosphere Package (TMAP;[1] Werner et al. 2003; Werner, Dreizler & Rauch 2012b). In Sections 2 and 3, we briefly describe the available observations and the model atmospheres used for the spectral analysis, respectively. In Section 4, the process of line identification and subsequent abundance measurement is explained. Lastly, we summarize our results and conclude in Section 5.

2 OBSERVATIONS

Our analysis is based on high-resolution *Far Ultraviolet Spectroscopic Explorer* (*FUSE*) and *Hubble Space Telescope*/Space Telescope Imaging Spectrograph (*HST*/STIS) observations. These were obtained from the MAST[2] archive. The *FUSE* spectrum taken with the LWRS aperture has a resolving power of $R=\lambda/\Delta\lambda\approx 20\,000$. Four STIS observations with grating E140M and $R=45\,800$ are available. The observation log is shown in Table B1. We convolved the synthetic spectra with Gaussians to model the respective instrument's resolution. The signal-to-noise ratio of the STIS observations was improved by co-adding the observations. The combined spectra are the same as used by Ziegler et al. (2012). No optical observation of the DAO WD is available, since the G-star companion dominates this spectral range.

3 MODEL ATMOSPHERES AND ATOMIC DATA

The analysis was carried out using TMAP. This code assumes plane-parallel geometry and calculates chemically homogeneous NLTE atmospheres in radiative and hydrostatic equilibrium.

For the TIEs Cu, Zn, Ga, Ge, Se, Br, Kr, Sr, Zr, Mo, In, Te, I, Xe, and Ba, we used the recently calculated data that is available via the Tübingen Oscillator Strengths Service (TOSS). For the elements with $Z\geq 20$, it is necessary to create model atoms using a statistical approach that calculates super levels and super lines (Rauch & Deetjen 2003) to take their complex atomic structure into account for the calculation. The statistics of all elements considered in our model-atmosphere calculations are summarized in Table B2.

We constructed a new classical model ion for Ba VIII from the level and line data of Churilov, Joshi & Gayasov (2001) available via the National Standards and Technology Institute (NIST) Atomic Spectra Database (ASD;[3] Kramida et al. 2018), which was incorporated into the Tübingen Model Atom Database (TMAD).

For all considered elements with an atomic number $Z\leq 28$, we used the same model atoms like Ziegler et al. (2012). For $Z<20$ these were obtained from the TMAD (Rauch & Deetjen 2003) that was constructed as part of the German Astrophysical Virtual Observatory (GAVO). For the iron-group elements (IGEs, atomic number $20\leq Z\leq 28$), Kurucz's line lists[4] (Kurucz 2009, 2011, 2017) were utilized.

For this analysis, we adopted the photospheric parameters of Ziegler et al. (2012) and used their final model ($T_{\rm eff}=80\,000$ K, $\log g=7.2$, see Table A1 for the element abundances) to start our TIE analysis. To identify lines and determine abundances of the 15 TIEs (Cu, Zn, Ga, Ge, Se, Br, Kr, Sr, Zr, Mo, In, Te, I, Xe, and Ba), we performed line-formation calculations by adding each of them individually to the start model from Ziegler et al. (2012), while temperature and density structure of the atmosphere were kept fixed. To verify our method, a final model including all TIEs with their previously determined abundances was then calculated with temperature and density corrections. The deviations in the abundances were marginal.

The observed spectra are affected by reddening due to interstellar material within the line of sight. By comparing the slope of the flux calibrated observations and the *Galaxy Evolution Explorer* (*GALEX*), *Hipparcos*, and Two Micron All-Sky Survey (2MASS) magnitudes (Cutri et al. 2003; Perryman et al. 2009; Bianchi et al. 2011) with the synthetic spectra of the central star, Ziegler et al. (2012) found a colour excess $E(B-V)=0.02\pm0.02$. This value was used to apply interstellar reddening following the law of Fitzpatrick (1999, with the standard $R_V=3.1$) to the model spectra to reproduce the observation. Absorption due to neutral interstellar hydrogen, assuming a column density of $N_{\rm H\,I}=5.0\times10^{20}\,{\rm cm^{-2}}$ (Ziegler et al. 2012), was applied to the synthetic spectra. Furthermore, we applied the interstellar line-absorption model of Ziegler et al. (2012) that was calculated using the program OWENS (Hébrard et al. 2002; Hébrard & Moos 2003) to unambiguously identify lines of stellar and interstellar origin.

4 LINE IDENTIFICATION AND ABUNDANCE DETERMINATION

We calculate synthetic spectra from our line-formation models with each of the 15 elements added individually to the best model of

[1] http://astro.uni-tuebingen.de/ TMAP
[2] http://archive.stsci.edu
[3] https://physics.nist.gov/PhysRefData/ASD
[4] http://kurucz.harvard.edu/atoms.html

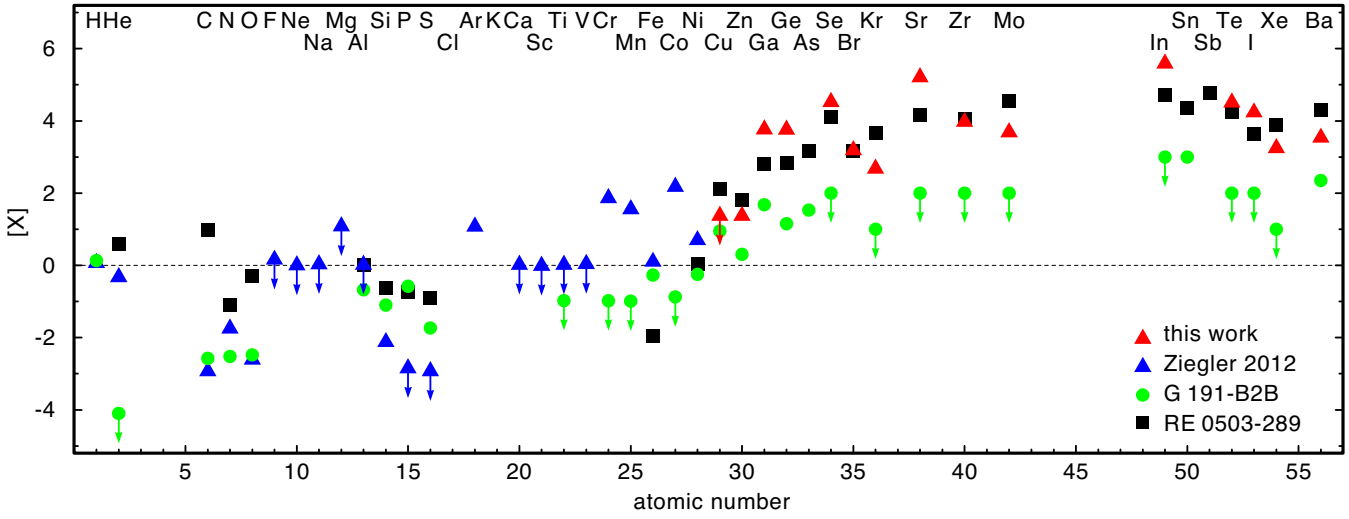

Figure 1. Photospheric abundance ratios [X] = log (mass fraction/solar mass fraction) of BD−22°3467 determined from detailed line profile fits. Solar values are taken from Asplund et al. (2009), Scott et al. (2015a,b), and Grevesse et al. (2015). Upper limits are indicated with arrows. The black, solid line indicates solar abundances. Blue triangles represent the abundances determined by Ziegler et al. (2012), red triangles show the TIE abundances (Table A1). For comparison, the abundances determined for G191−B2B (Rauch et al. 2013, green circles) and RE 0503−289 are shown (Hoyer et al. 2017, black squares).

Ziegler et al. (2012). The spectrum is crowded with a multitude of blended metal lines that hampers their unambiguous identification. To clearly see the contribution of the individual TIE elements, we divided the synthetic spectrum including this species by another model spectrum without it. The individual abundances were varied by small steps of 0.2 dex or smaller to derive the final values from evaluation of line-profile fits by eye. To estimate the influence of the uncertainty in $T_{\rm eff}$ of ±10 000 K and in log g of ±0.3 for the error propagation, we redid the abundance determination for models with $T_{\rm eff}$ = 90 000 K and log g = 6.9 and for $T_{\rm eff}$ = 70 000 K and log g = 7.5. The abundances are affected by typical errors below 0.3 dex.

For Cu, a line identification was not possible with appreciable certainty. Instead, upper limits were determined by reducing the abundance until the strongest computed lines become undetectable. An equivalent width of W_λ = 5 mÅ was set as a detection limit. Tables B3–B17 list all lines of TIEs that appear with an equivalent width above the threshold in the model spectrum. These tables include also those lines that could not be identified in the spectrum of BD−22°3467 due to e.g. blending with other photospheric or interstellar lines to make them a useful tool for the identification of TIE lines in the spectra of other DAO-type WDs. The abundances are given in Table A1 and are illustrated in Fig. 1. The complete *FUSE* and STIS observations compared to our best model are shown online[5] within the Tübingen VISualization (TVIS) tool. The ionization fractions and the temperature structure and electron density in the final atmosphere model are shown in Fig. B1.

The number of identified lines per TIE ion is shown in Table 1. The observation is well reproduced by our final model with the abundances shown in Table A1 as it is illustrated in Figs B2–B16 for prominent lines of each of the TIEs.

5 RESULTS AND CONCLUSIONS

To identify TIE lines, the UV spectrum of BD−22°3467 was closely inspected that led to the discovery of Zn, Ga, Ge, Se, Br, Kr, Sr, Zr, Mo, In, Te, I, Xe, and Ba (Table 1). In total, 484 TIE lines were discovered.

Table 1. Numbers of identified lines in the ionization stages IV–VIII of TIEs in the UV spectrum of BD−22°3467.

Element	Z	IV	V	VI	VII	VIII
Zn	30	2	141			
Ga	31	2	71	52		
Ge	32	2	32	57		
Se	34		14			
Br	35		1	7		
Kr	36			4		
Sr	38		17			
Zr	40		1	28	3	
Mo	42			2		
In	49		28			
Te	52			3		
I	53			4		
Xe	54				4	
Ba	56				3	3

Our spectral analysis has shown that the enrichment of TIEs in BD−22°3467 ($T_{\rm eff}$ = 80 000 ± 10 000 K, log g = 7.2 ± 0.3) and RE 0503−289 ($T_{\rm eff}$ = 70 000 ± 2000 K, log g = 7.5 ± 0.1) is comparably high (≈1.5–5 dex, Fig. 1). The origin of the high enrichment of TIEs is diffusion, i.e. efficient radiative levitation. This was shown already for RE 0503−289 by detailed diffusion calculations (Rauch et al. 2016a). While it was possible to determine abundances for several TIEs with consecutive atomic number in RE 0503−289 and find that the odd–even shape of the solar abundance pattern seems to be reflected also by the enriched TIEs (Fig. 2, cf. Rauch et al., submitted), there is not enough information to confirm this finding based on the results for BD−22°3467.

The evolutionary difference between BD−22°3467 and RE 0503−289 is that the latter most likely experienced an LTP in which it became hydrogen deficient. As a result, a pulse-driven convection zone, established during the flash, enriched the TIEs in the atmosphere. Their abundances were later on amplified to

[5] http://astro.uni-tuebingen.de/ TVIS/objects/Abell35

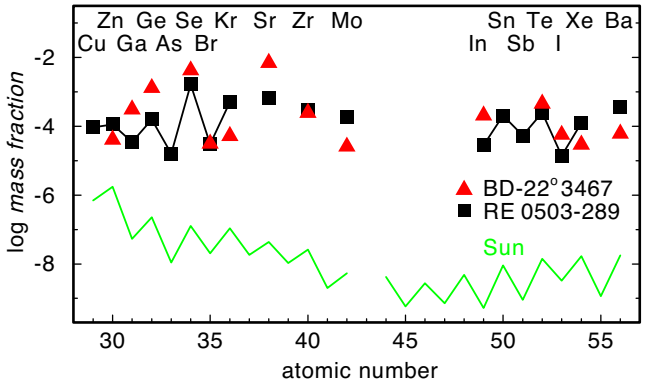

Figure 2. Photospheric TIE abundances in BD−22°3467 (red triangles) compared to RE 0503−289 (black squares; Hoyer et al. 2017; Rauch et al., submitted). Solar values are shown for comparison.

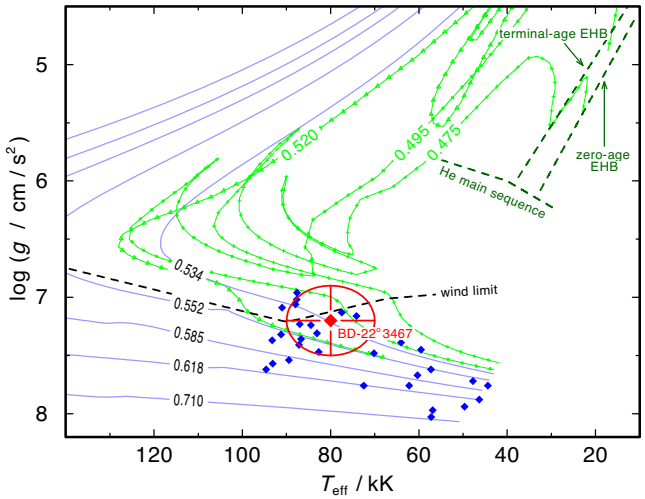

Figure 3. Location of BD−22°3467 (green) with error ellipse in the $T_{\rm eff}$–log g diagram compared to other DAO-type WDs (blue diamonds; Gianninas et al. 2010). Included are post-extended horizontal branch (EHB) evolutionary tracks (green; Dorman, Rood & O'Connell 1993, $Y = 0.288 \approx Y_{\odot}$) and post-AGB tracks for H-burners (blue; Miller Bertolami 2016) labelled with the stellar mass (in $M_{\odot}$). The wind limit for H-rich post-AGB stars is indicated (Unglaub & Bues 2000).

the observed values by radiative levitation. In contrast, the high abundances of TIEs in BD−22°3467 are possibly the result of radiative levitation on the initial stellar metallicity without previous enrichment by s-processed matter. This is because of the very low mass of BD−22°3467 (Fig. 1), which corresponds to an initial mass of below 1.0 $M_{\odot}$ (Cummings et al. 2018), implying that no TDU occurred on the AGB (Karakas & Lugaro 2016). From the position in the $T_{\rm eff}$–log g diagram (Fig. 3) only, a possible evolution without an AGB phase, directly from the extended horizontal branch (EHB) to the WD cooling sequence, cannot be excluded. Conversely, it is then possible that the high amount of TIEs in RE 0503−289 is solely due to diffusion, independent of the occurrence of a previous LTP. This is an interesting conclusion, because a large fraction of DOs is not initiated by an LTP but by a merger event with the so-called O(He) stars as merger products and DO precursors (Reindl et al. 2014). DOs from this evolutionary channel should therefore also go through a phase with an extreme TIE enrichment by diffusion.

We have to keep in mind that diffusion-established abundance patterns do not contain any more information about the previous stellar evolution, i.e. wherever the TIEs (or other elements) stem from, the exhibited surface abundance may be the same. Investigations on yields of the AGB s-process nucleosynthesis elements have to be performed before diffusion dominates the stellar evolution. This is the phase of just declining luminosity when the strength of the stellar wind decreases but is still high enough to maintain the original abundance ratios produced by the s-process. Spectral analyses of stars in that evolutionary phase might help to directly constrain AGB nucleosynthesis.

The formation of Abell 35-like central stars of planetary nebulae (CSPNe), i.e. binary CSPNe with a rapidly rotating late-type (sub)giant and an extremely hot companion (Bond, Ciardullo & Meakes 1993), is discussed controversially in the literature. Thevenin & Jasniewicz (1997) found the companion of BD−22°3467 to be enriched in Ba indicating that this still unevolved star experienced mass transfer from a (post-) AGB star. However, this formation channel is debated since Abell 35 was found to only mimic a PN (Frew & Parker 2010) and the mass of the ionizing star was considered to be too low for a post-AGB star (Ziegler et al. 2012). As explained above, an evolution directly from the EHB to the WD cooling track is possible (Fig. 3). The peculiar ionized nebula around BD−22°3467 is not a real PN but, nevertheless, it also cannot be excluded that the nebula material is in some way connected to the evolution of the central star. Assuming that it ejected a PN as an AGB star, the original PN might have already dispersed. The star has a high proper motion ($\mu_{\alpha} = -54.566 \pm 0.226$ mas yr^{-1} and $\mu_{\delta} = -10.097 \pm 0.187$ mas yr^{-1}; Gaia Collaboration et al. 2018) and, thus, might now be passing through the edges of the ejected former nebula material or another dense interstellar medium (ISM) region while ionizing the surrounding material. The classification of Abell 35 as a bow shock nebula in a photoionized Strömgren sphere in the ambient ISM (Frew & Parker 2010) does not necessarily include a PN but also, does not rule out the post-AGB nature of BD−22°3467. Further detailed abundance analyses of a sample of Abell 35-like CSPNe and their ambient nebulae and companion stars should give us a better handle on their evolution. The nebulae, if ejected from an AGB star, contain signatures of s-process elements (Madonna et al. 2017) and the unevolved companions, if they accreted a fraction of the ejected material. Therefore, a precise knowledge of the companion is mandatory because any accreted material would become diluted in this star's convective envelope.

To better understand the late evolutionary phases of low-mass stars, it is highly desirable to improve the determination of $T_{\rm eff}$ and log g with much narrower error ranges. For this purpose, the analysis of high-resolution optical spectra may be helpful. Although the cool companion dominates this wavelength regime, broad lines of H and He of BD−22°3467 should be detectable like demonstrated by Aller et al. (2015) for the binary central star of NGC 1514. These lines may reduce the error and, thus, allow to better constrain the stellar mass (Fig. 3).

As a remark, we would like to mention that the discrepancy found by Ziegler et al. (2012) between the spectroscopic distance of 361^{+195}_{-137} pc and the distance based on the *Hipparcos* parallax is still present in the era of *Gaia* with a distance of $124.84^{+2.21}_{-2.13}$ pc (Bailer-Jones et al. 2018). Ziegler et al. (2012) demonstrated that the H I lines in the *FUSE* range are poorly reproduced with models with log $g > 7.7$. This phenomenon of too large spectroscopic distances has already been reported in the literature for CSPNe (Schönberner, Balick & Jacob 2018; Schönberner & Steffen 2019).

The argument that missing metal-line blanketing and back warming may result in too high temperatures does not hold in our analysis, because all elements in the model calculation were considered in full NLTE computations. The objects of the mentioned studies are all located before the knee at highest temperatures in the HRD. Thus, the spectroscopic mass derived from fitting of the spectral energy distribution using the parallax distance is systematically too high. In our case, the spectroscopic mass derived from the dereddened *GALEX* FUV flux (Bianchi et al. 2011) using the *Gaia* distance is unreasonably low. With the given $T_{\rm eff}$, at least a $\log g > 8.0$ would be required to reach masses above 0.4 $M_{\odot}$. In conclusion, the discrepancy remains unexplained and needs further investigation.

Following the discovery of TIE lines in BD−22°3467, we have initiated an analogous search in other DAO-type WDs. Since the *FUSE* and *HST* archives provide quite a number of high-quality UV spectra of such stars, which have not been inspected in focus of TIEs, we expect to identify TIE enrichment as a common phenomenon in many hot WDs.

ACKNOWLEDGEMENTS

We thank the referee for the very useful comments that improved this paper. LL has been supported by the German Research Foundation (DFG) under grant WE 1312/49 − 1. MAM had been supported by the DAAD RISE Germany program. The GAVO project at Tübingen had been supported by the Federal Ministry of Education and Research (BMBF) at Tübingen (05 AC 6 VTB, 05 AC 11 VTB). Financial support from the Belgian FRS-FNRS is also acknowledged. PQ is research director of this organization. Some of the data presented in this paper were obtained from the Mikulski Archive for Space Telescopes (MAST). STScI is operated by the Association of Universities for Research in Astronomy, Inc., under NASA contract NAS5-26555. Support for MAST for non-*HST* data is provided by the NASA Office of Space Science via grant NNX09AF08G and by other grants and contracts. The TIRO (http://astro-uni-tuebingen.de/ TIRO), TMAD (http://astro-uni-tuebingen.de/ TMAD), TOSS (http://astro-uni-tuebingen.de/ TOSS), and TVIS (http://astro-uni-tuebingen.de/ TVIS) tools and services used for this paper were constructed as part of the Tübingen project (https://uni-tuebingen.de/de/122430) of the German Astrophysical Virtual Observatory (GAVO, http://www.g-vo.org). This research has made use of NASA's Astrophysics Data System and of the SIMBAD data base, operated at CDS, Strasbourg, France. This work has made use of data from the European Space Agency (ESA) mission *Gaia* (https://www.cosmos.esa.int/gaia), processed by the *Gaia* Data Processing and Analysis Consortium (DPAC, https://www.cosmos.esa.int/web/gaia/dpac/consortium). Funding for the DPAC has been provided by national institutions, in particular the institutions participating in the *Gaia* Multilateral Agreement.

REFERENCES

Abell G. O., 1955, PASP, 67, 258
Abell G. O., 1966, ApJ, 144, 259
Aller A., Miranda L. F., Olguín L., Vázquez R., Guillén P. F., Oreiro R., Ulla A., Solano E., 2015, MNRAS, 446, 317
Asplund M., Grevesse N., Sauval A. J., Scott P., 2009, ARA&A, 47, 481
Bailer-Jones C. A. L., Rybizki J., Fouesneau M., Mantelet G., Andrae R., 2018, AJ, 156, 58
Bianchi L., Herald J., Efremova B., Girardi L., Zabot A., Marigo P., Conti A., Shiao B., 2011, Ap&SS, 335, 161
Blöcker T., 1995, A&A, 299, 755
Bohlin R. C., 2007, in Sterken C., ed., ASP Conf. Ser. Vol. 364, The Future of Photometric, Spectrophotometric and Polarimetric Standardization. Astron. Soc. Pac., San Francisco, p. 315
Bond H. E., Ciardullo R., Meakes M. G., 1993, in Weinberger R., Acker A., eds, Proc. IAU Symp. 155, Planetary Nebulae. Kluwer, Dordrecht, p. 397
Chayer P., Vennes S., Dupuis J., Kruk J. W., 2005, ApJ, 630, L169
Churilov S. S., Joshi Y. N., Gayasov R., 2001, J. Opt. Soc. Am. B, 18, 113
Cummings J. D., Kalirai J. S., Tremblay P.-E., Ramirez-Ruiz E., Choi J., 2018, ApJ, 866, 21
Cutri R. M. et al., 2003, 2MASS All Sky Catalog of Point Sources. NASA/IPAC Infrared Science Archive, http://irsa.ipac.caltech.edu/applications/Gator/
Dorman B., Rood R. T., O'Connell R. W., 1993, ApJ, 419, 596
Dorsch M., Latour M., Heber U., 2019, A&A, 630, A130
Fitzpatrick E. L., 1999, PASP, 111, 63
Frew D. J., Parker Q. A., 2010, Publ. Astron. Soc. Aust., 27, 129
Fujimoto M. Y., 1977, PASJ, 29, 331
Gaia Collaboration et al., 2018, A&A, 616, A1
Gianninas A., Bergeron P., Dupuis J., Ruiz M. T., 2010, ApJ, 720, 581
Grevesse N., Scott P., Asplund M., Sauval A. J., 2015, A&A, 573, A27
Grewing M., Bianchi L., 1988, in Rolfe E. J., ed., A Decade of UV Astronomy with the IUE Satellite, ESA SP-281, Vol. 2. ESA, Noordwijk, p. 177
Hébrard G., Moos H. W., 2003, ApJ, 599, 297
Hébrard G. et al., 2002, Planet. Space Sci., 50, 1169
Herald J. E., Bianchi L., 2002, ApJ, 580, 434
Herwig F., 2000, A&A, 360, 952
Hoyer D., Rauch T., Werner K., Kruk J. W., Quinet P., 2017, A&A, 598, A135
Hoyer D., Rauch T., Werner K., Kruk J. W., 2018, A&A, 612, A62
Iben I.,, Jr, Kaler J. B., Truran J. W., Renzini A., 1983, ApJ, 264, 605
Jacoby G. H., 1981, ApJ, 244, 903
Karakas A. I., Lugaro M., 2016, ApJ, 825, 26
Kramida A., Yu. Ralchenko, Reader J., NIST ASD Team, 2018, NIST Atomic Spectra Database (ver. 5.6.1). National Institute of Standards and Technology, Gaithersburg, MD. Available:https://physics.nist.gov/asd
Kurucz R. L., 2009, in Hubeny I., Stone J. M., MacGregor K., Werner K., eds, AIP Conf. Proc. Vol. 1171, Recent Directions in Astrophysical Quantitative Spectroscopy and Radiation Hydrodynamics. Am. Inst. Phys., New York, p. 43
Kurucz R. L., 2011, Can. J. Phys., 89, 417
Kurucz R. L., 2017, Can. J. Phys., 95, 825
Latour M., Dorsch M., Heber U., 2019, A&A, 629, A148
McCook G. P., Sion E. M., 1999, ApJS, 121, 1
Madonna S., García-Rojas J., Sterling N. C., Delgado-Inglada G., Mesa-Delgado A., Luridiana V., Röderer I. U., Mashburn A. L., 2017, MNRAS, 471, 1341
Miller Bertolami M. M., 2016, A&A, 588, A25
Naslim N., Jeffery C. S., Behara N. T., Hibbert A., 2011, MNRAS, 412, 363
Perryman M. A. C. et al., 2009, A&A, 500, 501 (special issue: reprint of 1997, A&A, 323, L49)
Rauch T., Deetjen J. L., 2003, in Hubeny I., Mihalas D., Werner K., eds, ASP Conf. Ser. Vol. 288, Stellar Atmosphere Modeling. Astron. Soc. Pac., San Francisco, p. 103
Rauch T., Werner K., Biémont É., Quinet P., Kruk J. W., 2012, A&A, 546, A55
Rauch T., Werner K., Bohlin R., Kruk J. W., 2013, A&A, 560, A106
Rauch T., Werner K., Quinet P., Kruk J. W., 2014a, A&A, 564, A41
Rauch T., Werner K., Quinet P., Kruk J. W., 2014b, A&A, 566, A10
Rauch T., Werner K., Quinet P., Kruk J. W., 2015, A&A, 577, A6
Rauch T., Quinet P., Hoyer D., Werner K., Demleitner M., Kruk J. W., 2016a, A&A, 587, A39
Rauch T., Quinet P., Hoyer D., Werner K., Richter P., Kruk J. W., Demleitner M., 2016b, A&A, 590, A128
Reindl N., Rauch T., Werner K., Kepler S. O., Gänsicke B. T., Gentile Fusillo N. P., 2014, A&A, 572, A117
Schönberner D., 1979, A&A, 79, 108

Schönberner D., Steffen M., 2019, A&A, 625, A137
Schönberner D., Balick B., Jacob R., 2018, A&A, 609, A126
Scott P. et al., 2015a, A&A, 573, A25
Scott P., Asplund M., Grevesse N., Bergemann M., Sauval A. J., 2015b, A&A, 573, A26
Thevenin F., Jasniewicz G., 1997, A&A, 320, 913
Unglaub K., Bues I., 2000, A&A, 359, 1042
Vennes S., Chayer P., Dupuis J., 2005, ApJ, 622, L121
Werner K., Deetjen J. L., Dreizler S., Nagel T., Rauch T., Schuh S. L., 2003, in Hubeny I., Mihalas D., Werner K., eds, ASP Conf. Ser. Vol. 288, Stellar Atmosphere Modeling. Astron. Soc. Pac., San Francisco, p. 31
Werner K., Rauch T., Ringat E., Kruk J. W., 2012a, ApJ, 753, L7
Werner K., Dreizler S., Rauch T., 2012b, Astrophysics Source Code Library, record ascl:1212.015
Ziegler M., Rauch T., Werner K., Köppen J., Kruk J. W., 2012, A&A, 548, A109

APPENDIX A: PHOTOSPHERIC PARAMETERS OF BD−22°3467

Table A1. Parameters of BD−22°3467.

$T_{\rm eff}$ / K	$80\,000 \pm 10\,000$ [a]	
$\log(g/{\rm cm\ s^{-2}})$	7.2 ± 0.3 [a]	
$E(B-V)$	0.02 ± 0.02 [a]	
$\log N_{\rm H\,I}/{\rm cm^{-2}}$	20.7 ± 0.1 [a]	
$M/{\rm M_\odot}$	$0.533^{+0.040}_{-0.025}$ [b]	$0.505^{+0.030}_{-0.025}$ [c]
$\log(L/{\rm L_\odot})$	$1.52^{+0.40}_{-0.50}$ [b]	$1.69^{+0.30}_{-0.50}$ [c]

Element	[X]	Mass fraction	Number fraction	ε [d]	[X/Fe]
H[a]	0.07	8.67×10^{-1}	9.67×10^{-1}	12.09	−0.00
He[a]	−0.33	1.17×10^{-1}	3.29×10^{-2}	10.62	−0.40
C[a]	−2.93	2.77×10^{-6}	2.59×10^{-7}	5.51	−3.00
N[a]	−1.75	1.24×10^{-5}	9.99×10^{-7}	6.10	−1.82
O[a]	−2.61	1.42×10^{-5}	9.99×10^{-7}	6.10	−2.68
F[a]	≤0.16	$\leq 5.04 \times 10^{-7}$	$\leq 2.98 \times 10^{-8}$	≤4.57	≤−0.07
Ne[a]	≤−0.00	$\leq 1.26 \times 10^{-3}$	$\leq 6.99 \times 10^{-5}$	≤7.94	≤−0.07
Na[a]	≤0.03	$\leq 2.92 \times 10^{-5}$	$\leq 1.43 \times 10^{-6}$	≤6.25	≤−0.07
Mg[a]	≤1.08	$\leq 8.31 \times 10^{-3}$	$\leq 3.84 \times 10^{-4}$	≤8.68	≤1.00
Al[a]	≤0.02	$\leq 5.56 \times 10^{-5}$	$\leq 2.31 \times 10^{-6}$	≤6.46	≤−0.07
Si[a]	−2.12	5.00×10^{-6}	2.00×10^{-7}	5.40	−2.19
P[a]	≤−2.85	$\leq 8.26 \times 10^{-9}$	$\leq 3.00 \times 10^{-10}$	≤2.58	≤−2.92
S[a]	≤−2.93	$\leq 3.64 \times 10^{-7}$	$\leq 1.27 \times 10^{-8}$	≤4.21	≤−3.00
Ar[a]	1.07	8.65×10^{-4}	2.43×10^{-5}	7.49	1.00
Ca[a]	≤0.02	$\leq 6.41 \times 10^{-5}$	$\leq 1.80 \times 10^{-6}$	≤6.35	≤−0.07
Sc[a]	≤−0.01	$\leq 4.64 \times 10^{-8}$	$\leq 1.16 \times 10^{-9}$	≤3.16	≤−0.07
Ti[a]	≤0.02	$\leq 3.12 \times 10^{-6}$	$\leq 7.31 \times 10^{-8}$	≤4.96	≤−0.07
V[a]	≤0.04	$\leq 3.17 \times 10^{-7}$	$\leq 6.99 \times 10^{-9}$	≤3.94	≤−0.07
Cr[a]	1.86	1.16×10^{-3}	2.50×10^{-5}	7.50	1.77
Mn[a]	1.56	3.81×10^{-4}	7.80×10^{-6}	6.99	1.48
Fe[a]	0.10	1.52×10^{-3}	3.06×10^{-5}	7.58	0.00
Co[a]	2.18	1.57×10^{-4}	3.00×10^{-6}	6.58	1.50
Ni[a]	0.70	3.39×10^{-4}	6.49×10^{-6}	6.91	0.61
Cu	≤1.38	$\leq 1.70 \times 10^{-5}$	$\leq 3.00 \times 10^{-7}$	≤5.58	≤1.30
Zn	1.37	4.08×10^{-5}	7.00×10^{-7}	5.95	1.30
Ga	3.77	3.11×10^{-4}	5.00×10^{-6}	6.80	3.67
Ge	3.76	1.29×10^{-3}	2.00×10^{-5}	7.40	3.67
Se	4.52	4.21×10^{-3}	6.00×10^{-5}	7.88	4.45
Br	3.19	3.13×10^{-5}	4.40×10^{-7}	5.74	3.12
Kr	2.68	5.23×10^{-5}	7.00×10^{-7}	5.95	2.61
Sr	5.21	6.98×10^{-3}	9.00×10^{-5}	8.05	5.10
Zr	3.97	2.44×10^{-4}	3.00×10^{-6}	6.58	3.91
Mo	3.68	2.57×10^{-5}	3.00×10^{-7}	5.58	3.61
In	5.83	3.58×10^{-4}	3.50×10^{-6}	6.64	5.76
Te	4.51	4.55×10^{-4}	4.00×10^{-6}	6.70	4.44
I	4.24	5.66×10^{-5}	5.00×10^{-7}	5.80	4.16
Xe	3.85	1.17×10^{-4}	1.00×10^{-6}	6.10	3.77
Ba	3.54	6.12×10^{-5}	5.00×10^{-7}	5.80	3.53

[a]From Ziegler et al. (2012). [b]Interpolated from post-AGB evolutionary tracks, cf. Fig. 3. [c]Interpolated from post-extended horizontal branch (EHB) evolutionary tracks, cf. Fig. 3. [d]Abundances $\varepsilon_i = \log n_i + c$ with $\Sigma_i a_j n_j = 12.15$ and the atomic weights a_i.

APPENDIX B: ADDITIONAL FIGURES AND TABLES

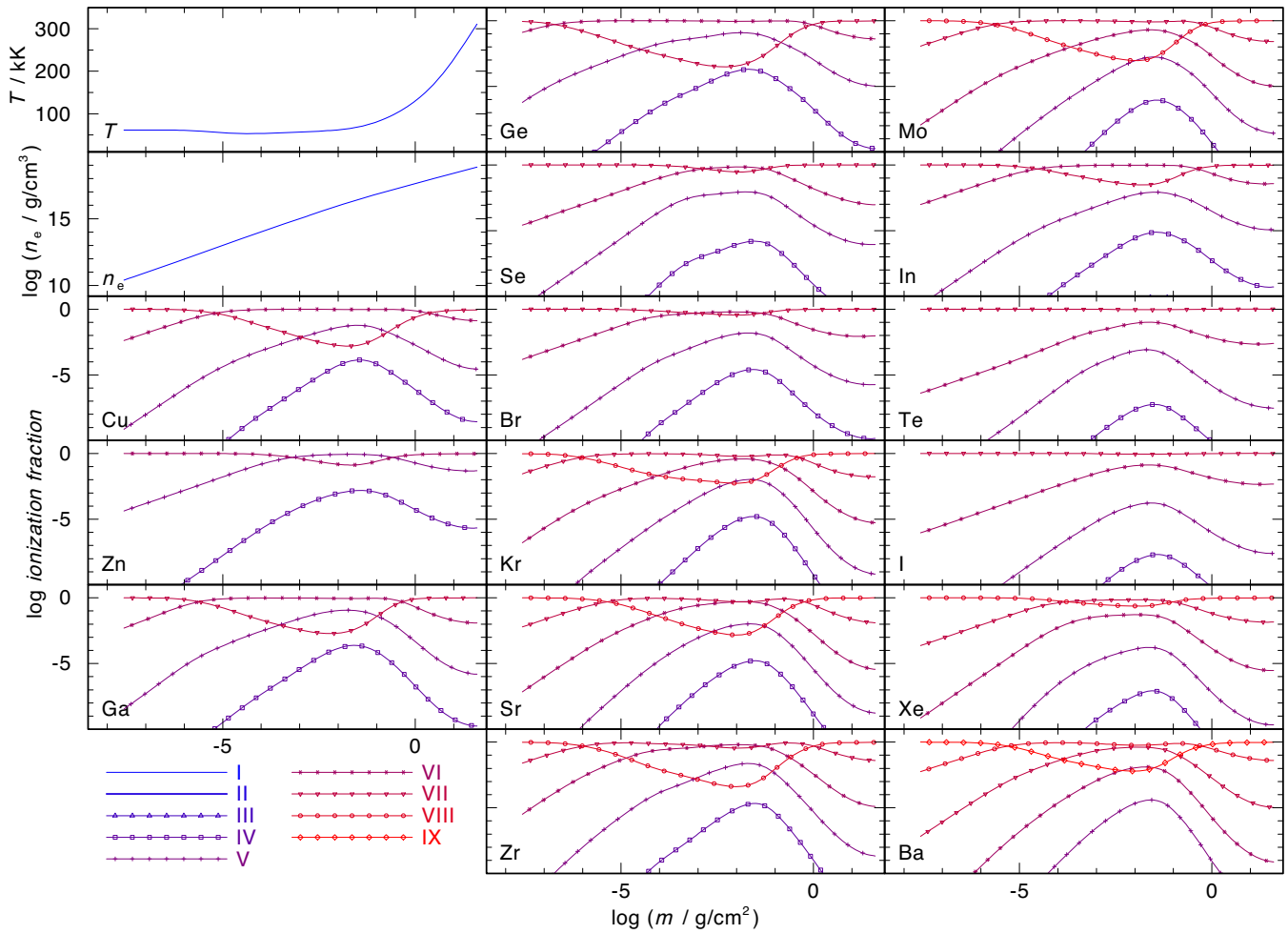

Figure B1. Temperature and electron density structure and ionization fractions of all TIE ions thar are considered in our final model for BD−22°3467.

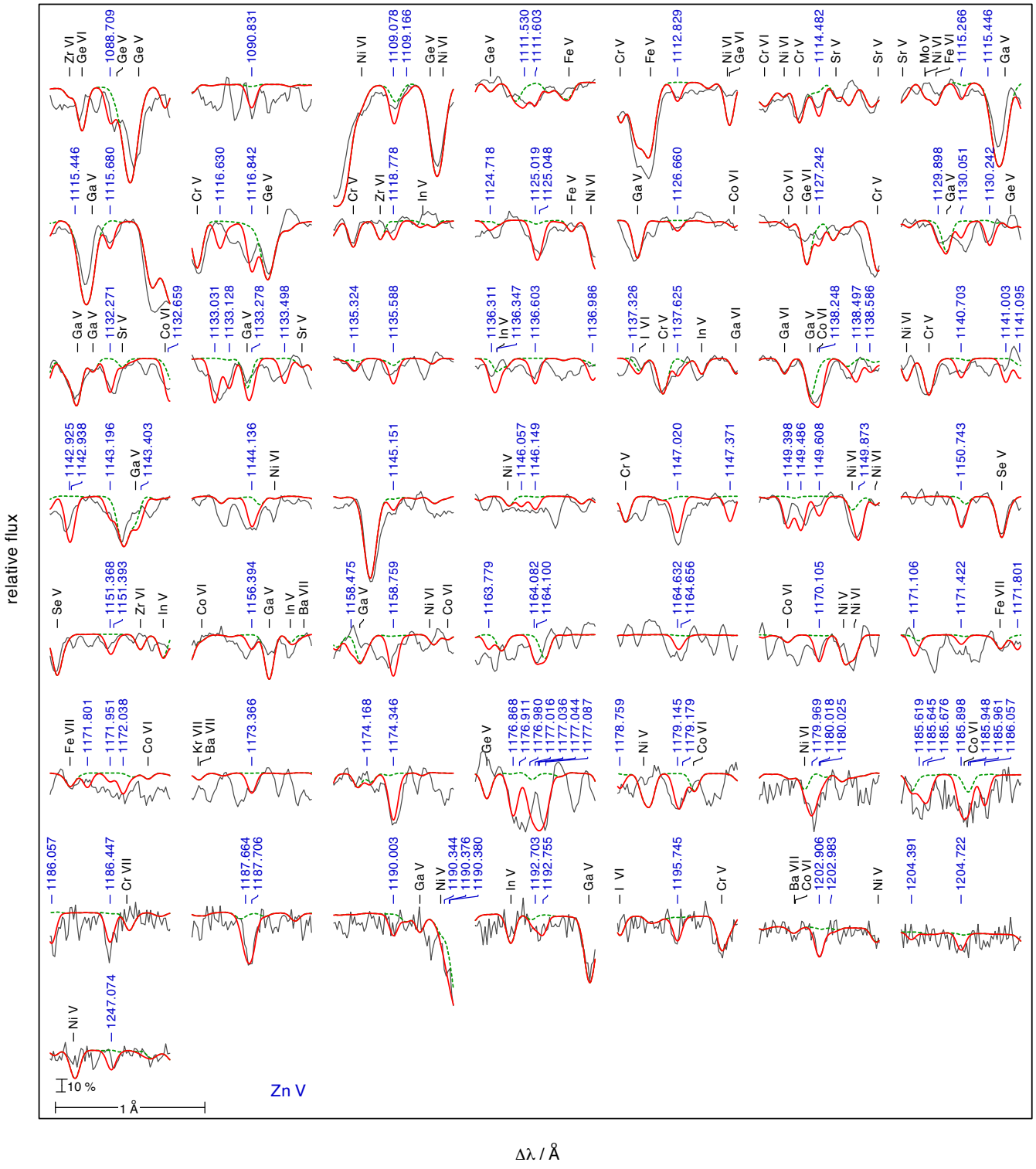

Figure B2. Prominent computed and identified lines of Zn V (blue wavelength labels) in the *FUSE* ($\lambda < 1180$ Å) and STIS observations of BD−22°3467. The model was calculated with the abundances given in Table A1 (red). In addition, a model without Zn (green dashed) is shown.

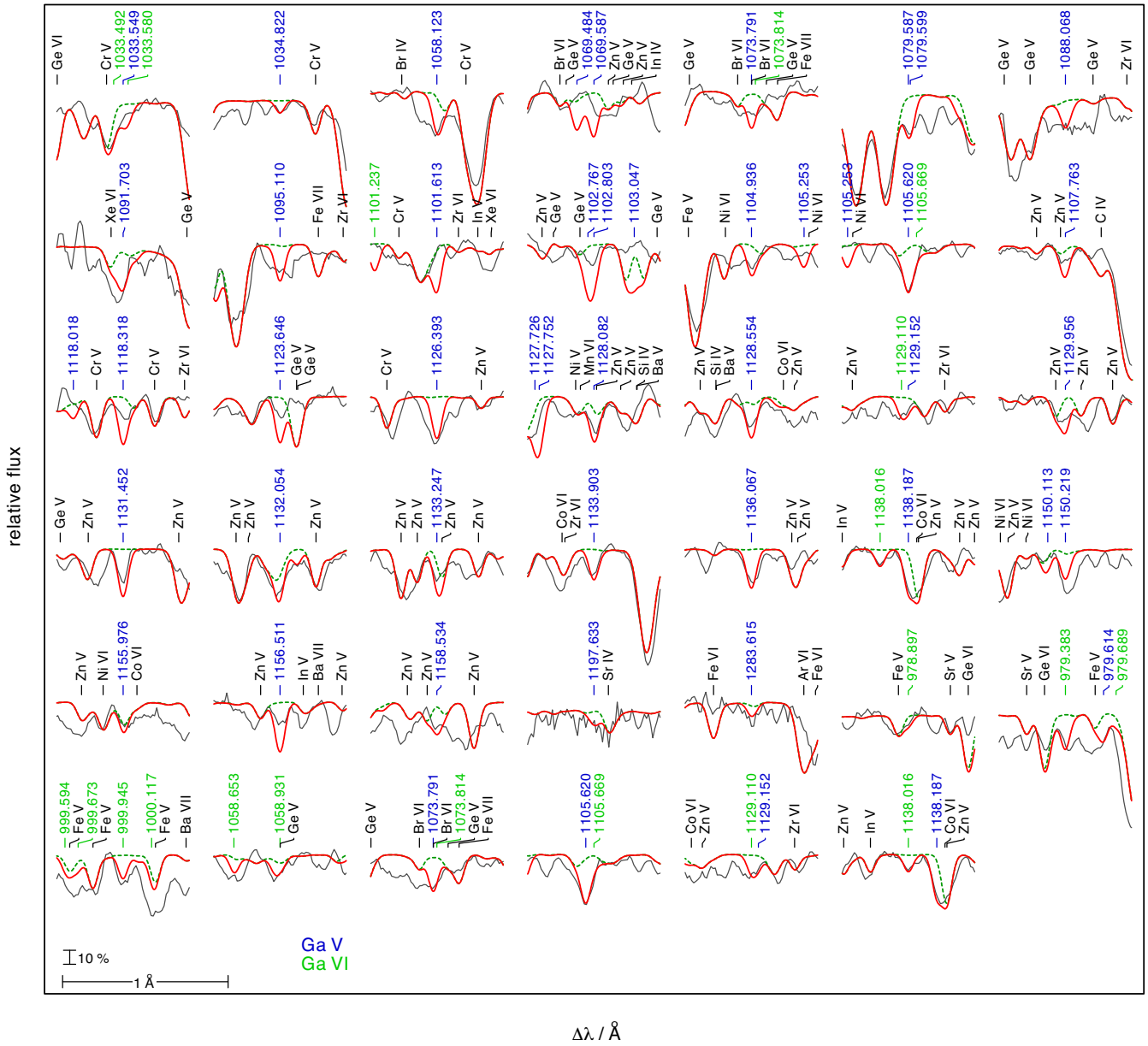

Figure B3. Like Fig. B2, for Ga V (blue) and Ga VI (green).

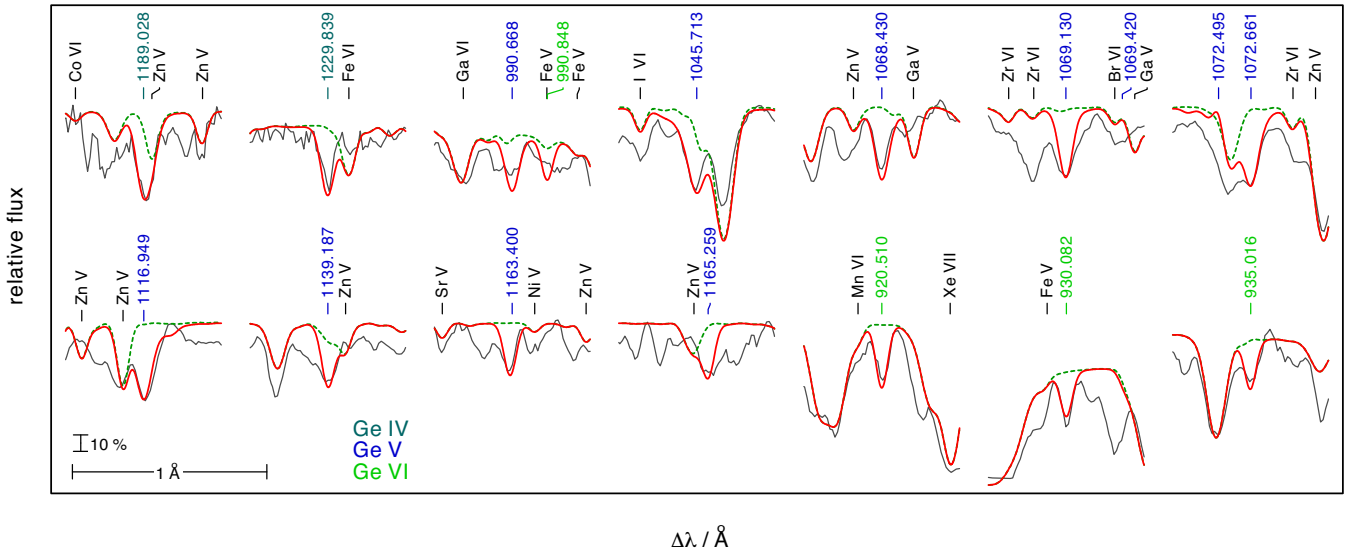

Figure B4. Like Fig. B2, for Ge IV (dark cyan), Ge V (blue), and Ge VI (green).

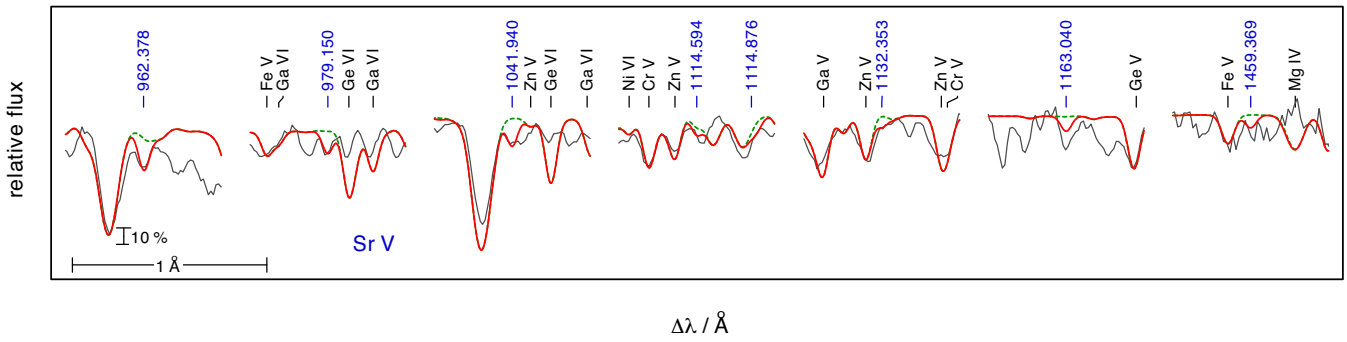

Figure B5. Like Fig. B2, for Sr V (blue).

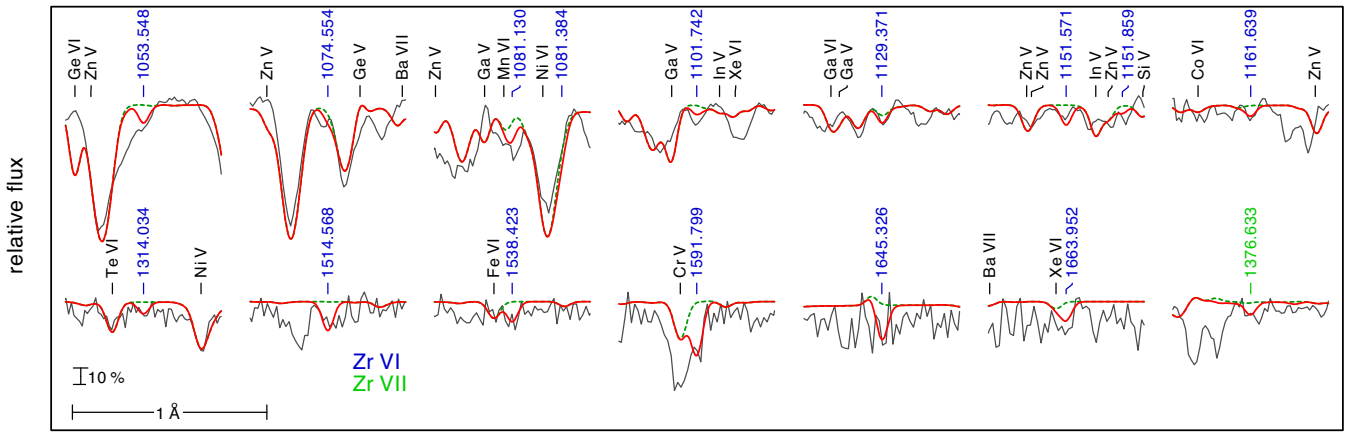

Figure B6. Like Fig. B2, for Zr VI (blue) and Zr VII (green).

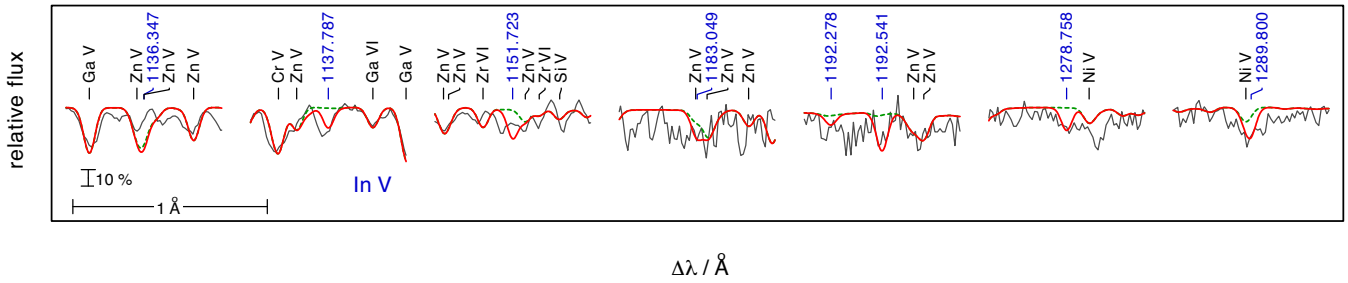

Figure B7. Like Fig. B2, for In V (blue).

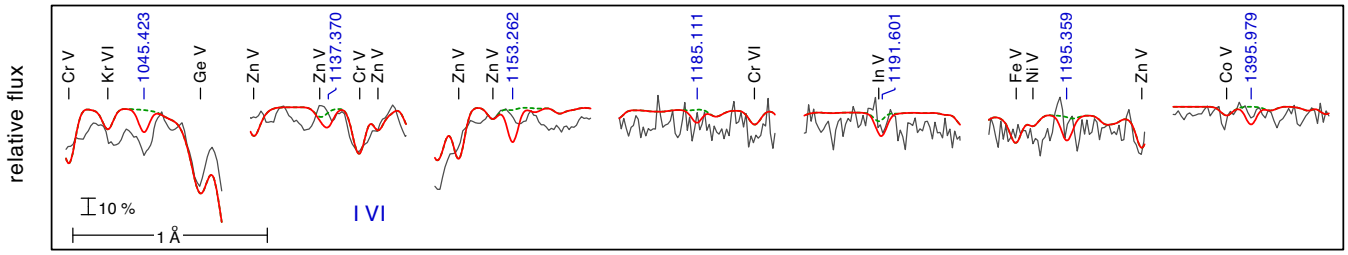

Figure B8. Like Fig. B2, for I VI (blue).

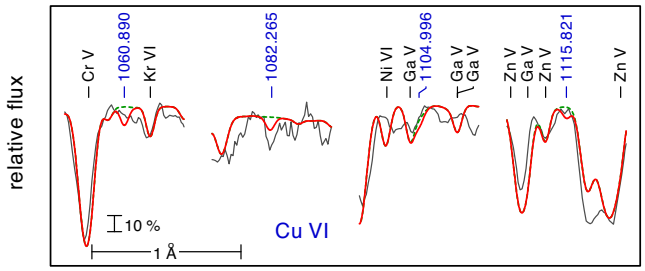

Figure B9. Like Fig. B2, for Cu VI (blue).

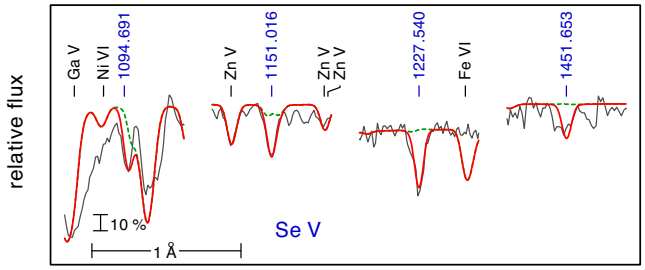

Figure B10. Like Fig. B2, for Se V (blue).

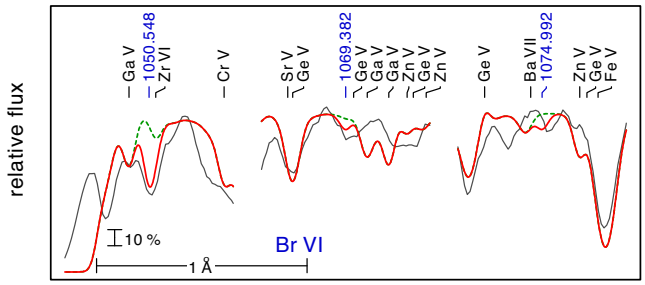

Figure B11. Like Fig. B2, for Br VI (blue).

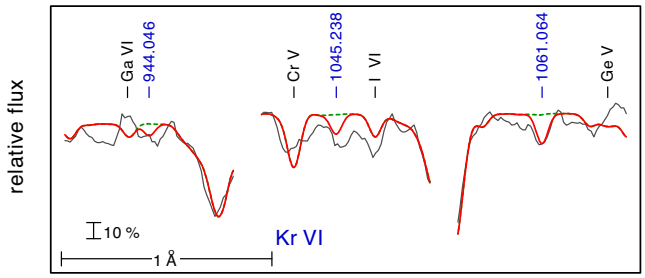

Figure B12. Like Fig. B2, for Kr VI (blue).

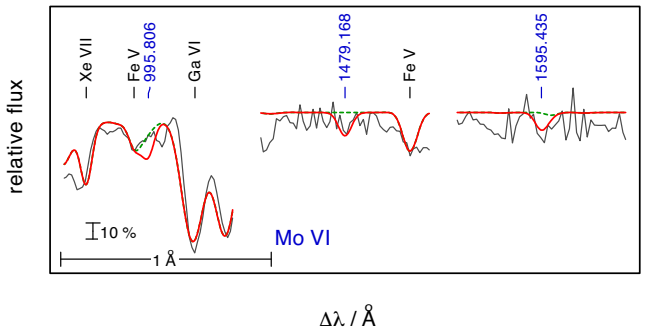

Figure B13. Like Fig. B2, for Mo VI (blue).

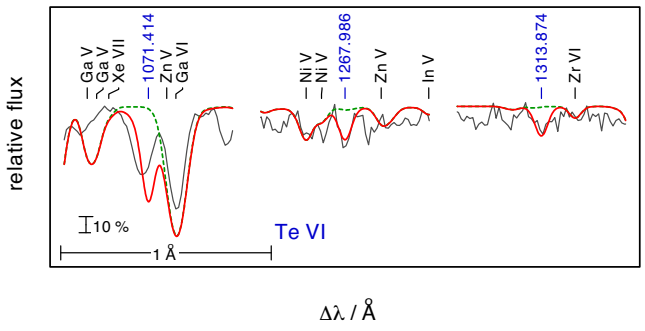

Figure B14. Like Fig. B2, for Te VI (blue).

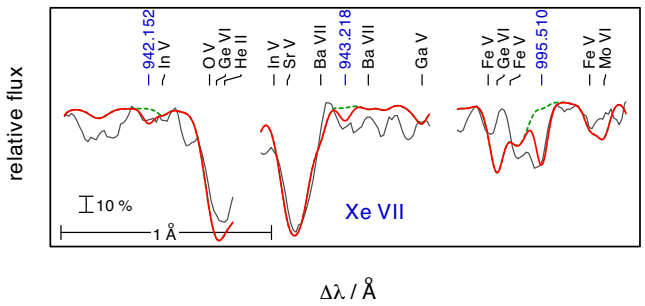

Figure B15. Like Fig. B2, for Xe VII (blue).

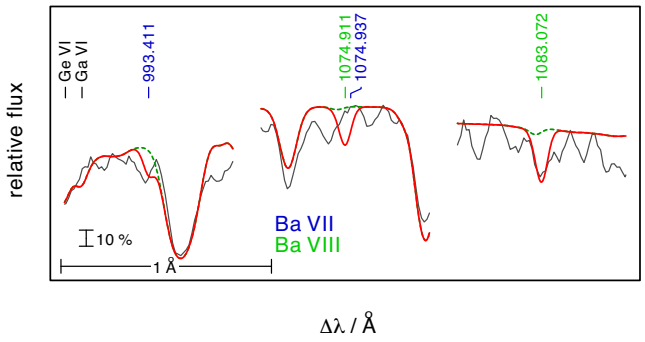

Figure B16. Like Fig. B2, for Ba VII (blue) and Ba VIII (green).

Table B1. Observation log for BD−22°3467.

Instrument	Data set Id	Start time (UT)	Wavelength range (λ)	Aperture/ Grating	Exposure time (s)	Resolving power $R = \lambda / \Delta\lambda$
FUSE[a]	P1330101000	2000-05-20 20:27:37	910−1180	LWRS	4416	20 000
STIS[b]	O4GT02010	1999-04-17 21:14:49	1150−1730	E140M	2050	45 800
STIS	O4GT02020	1999-04-17 22:37:03	1150−1730	E140M	2800	45 800
STIS	O4GT02030	1999-04-18 00:16:10	1150−1730	E140M	2740	45 800
STIS	O4GT02040	1999-04-18 01:52:54	1150−1730	E140M	2740	45 800

[a] *Far Ultraviolet Spectroscopic Explorer*.
[b] Space Telescope Imaging Spectrograph.

Table B2. Statistics of the H–Ar[a] and Ca–Ba[b] model atoms used in our model-atmosphere calculations.

Ion		Levels NLTE	Levels LTE	Lines	Ion		Super levels[c]	Super lines	Individual lines	Ion		Super levels[c]	Super lines	Individual lines
H	I	12	4	66	Ca	IV	6	16	20291	Cu	IV	7	15	8785
	II	1	–	–		V	6	21	141956		V	7	16	5456
He	I	5	98	3		VI	6	19	114545		VI	7	9	3797
	II	16	16	120		VII	6	21	71608		VII	1	0	0
	III	1	–	–		VIII	6	20	9124	Zn	IV	7	11	400
C	III	6	61	12		IX	1	0	0		V	7	15	1879
	IV	54	4	295	Sc	IV	6	20	15024		VI	1	0	0
	V	1	0	0		V	6	21	261235	Ga	IV	7	19	3198
N	III	1	65	0		VI	6	19	237271		V	7	15	517
	IV	16	78	30		VII	6	20	176143		VI	7	13	1914
	V	54	8	297		VIII	6	21	91935		VII	1	0	0
	VI	1	0	0		IX	1	0	0	Ge	IV[d]	8	0	8
O	III	3	69	0	Ti	IV	6	19	1000		V	7	16	2159
	IV	18	76	39		V	6	20	26654		VI	7	12	414
	V	90	36	610		VI	6	19	95448		VII	1	0	0
	VI	54	8	291		VII	6	20	230618	Se	IV	1	0	0
	VII	1	0	0		III	6	21	182699		V	7	19	310
F	III	1	6	0		IX	1	0	0		VI	1	0	0
	IV	1	10	0	V	IV	6	19	37130		VII	1	0	0
	V	15	91	31		V	6	20	2123	Br	III	1	0	0
	VI	12	115	16		VI	6	19	35251		IV	6	12	424
	VII	1	0	0		VII	6	19	112883		V	7	18	394
Ne	II	1	33	0		III	6	20	345089		VI	7	17	158
	III	3	43	0		IX	1	0	0		VII	1	0	0
	IV	3	37	0	Cr	IV	6	20	234170	Kr	IV	7	19	911
	V	20	74	35		V	6	20	43860		V	7	16	553
	VI	1	0	0		VI	6	20	4406		VI	7	19	843
Na	III	1	186	0		VII	6	19	37070		VII	7	21	743
	IV	1	237	0		III	6	20	132221		VIII	1	0	0
	V	8	42	9		IX	1	0	0	Sr	IV	7	21	7578
	VI	43	10	130	Mn	IV	6	20	719387		V	7	19	2022
	VII	1	0	0		V	6	20	285376		VI	7	10	70
Mg	III	1	34	0		VI	6	20	70116		VII	7	10	46
	IV	31	0	93		VII	6	20	8277		VIII	1	0	0
	V	15	37	18		VIII	6	20	37168	Zr	IV	7	20	135
	VI	1	0	0		IX	1	0	0		V	7	22	1449
Al	III	1	6	0	Fe	IV	6	20	3102371		VI	7	12	1098
	IV	15	2	0		V	6	20	3266247		VII	7	15	947
	V	1	16	0		VI	6	20	991935		VIII	1	0	0
	VI	14	24	16		VII	6	20	200455	Mo	IV	7	15	2803
	VII	1	0	0		III	6	18	19587		V	7	22	5829
Si	III	3	31	1		IX	1	0	0		VI	7	23	984
	IV	16	7	44	Co	IV	6	20	552916		VII	7	16	1173
	V	25	0	59		V	6	20	1469717		VIII	1	0	0
	VI	1	0	0		VI	6	18	898484	In	III	1	0	0
P	III	1	9	0		VII	6	19	492913		IV	7	14	564
	IV	15	36	9		VIII	6	20	88548		V	7	10	919
	V	18	7	12		IX	1	0	0		VI	8	10	176
	VI	1	0	0	Ni	IV	6	20	2512561		VII	1	0	0
S	IV	6	94	4		V	6	20	2766664	Te	IV	1	0	0
	V	21	89	37		VI	6	18	7408657		V	1	0	0
	VI	18	19	48		VII	6	18	4195381		VI	7	12	178
	VII	1	0	0		III	6	20	1473122		VII	1	0	0
Ar	IV	1	349	0		IX	1	0	0	I	IV	1	0	0
	V	32	329	38							V	1	0	0
	VI	16	168	21							VI	7	15	197
	VII	40	112	130							VII	1	0	0
	IIII	1	0	0						Xe	IV	7	16	1391
											V	7	15	616
											VI	7	16	243
											VII	7	19	491
											VIII	1	0	0
										Ba	V	7	12	981
											VI	7	6	162
											VII	7	11	493
											VIII[e]	34	0	44
											IX	1	0	0
Total		742	2776	2514			279	884	33219636			359	651	63444

[a]Classical model atoms. [b]Model atoms constructed using a statistical approach (Rauch & Deetjen 2003).
[c]Treated as NLTE levels. [d]Ge IV classical model atom with 8 NLTE levels, 1 LTE level, and 8 transitions.
[e]Ba VIII classical model atom with 34 NLTE levels, 0 LTE level, and 44 transitions.

Table B3. Cu lines with $W_\lambda \geq 5$ mÅ in the model spectrum of BD−22°3467.

Ion	Stage	Wavelength/Å	Comment
Cu	VI	1060.890	Too strong in the model
		1082.265	Too weak in model
		1094.708	Uncertain
		1098.480	Uncertain
		1104.996	Blend Ga V
		1115.821	Uncertain
		1157.930	Uncertain

Table B4. Identified Zn lines with $W_\lambda \geq 5$ mÅ in model spectrum of BD−22°3467.

Ion	Wavelength/Å	Comment
Zn IV	1239.119	
	1281.296	
Zn V	1017.935	Blend ISM
	1023.521	Blend ISM
	1043.353	
	1052.441	Blend ISM
	1053.278	Blend ISM
	1055.878	Blend ISM
	1056.330	Uncertain
	1058.185	Blend Ga V
	1061.472	Uncertain
	1061.656	Blend ISM
	1063.209	Blend ISM
	1063.979	
	1066.547	Uncertain
	1068.284	
	1069.674	Uncertain
	1069.764	Uncertain
	1071.501	Blend ISM
	1072.992	Blend ISM
	1074.241	Uncertain
	1075.171	Too strong in model
	1076.878	
	1085.290	Uncertain
	1086.033	Blend Ge V
	1086.739	Blend ISM
	1088.709	
	1090.831	
	1094.088	Blend ISM
	1095.797	Uncertain
	1095.961	Uncertain
	1098.108	
	1102.490	Uncertain
	1103.598	Too weak in model
	1104.199	Blend ISM
	1106.788	
	1107.318	
	1109.078	
	1109.166	
	1111.530	
	1111.603	
	1112.829	
	1114.482	
	1115.266	
	1115.680	
	1116.630	Too strong in model
	1116.842	
	1117.466	Too weak in the model
	1118.778	
	1119.950	
	1120.101	Uncertain
	1120.325	
	1121.109	Blend Cr V, Fe VI
	1121.524	Uncertain
	1122.502	Blend ISM
	1123.127	Blend Ga V
	1124.718	
	1125.019 1125.048	
	1126.660	
	1127.242	
	1128.098	Blend Ga V
	1128.244	Uncertain
	1128.813	
	1129.898	
	1130.051	
	1130.242	
	1131.242	
	1131.788	
	1132.271	
	1132.659	Blend Co VI
	1133.031	
	1133.128	
	1133.278	
	1133.498	
	1135.324	
	1135.588	
	1136.311	
	1136.603	
	1136.986	
	1137.625	
	1138.248	Blend Co VI
	1138.497	
	1138.586	
	1139.278	Uncertain
	1139.997	Uncertain
	1140.703	
	1141.003	
	1141.095	
	1141.344	Uncertain
	1142.792	
	1142.925	
	1143.196	
	1143.403	Blend Ga V
	1144.136	
	1145.151	
	1146.057	
	1146.149	
	1147.020	
	1147.371	
	1147.648	
	1148.922	
	1149.398	
	1149.486	
	1149.608	
	1149.873	Blend Ni VI
	1150.743	
	1151.368	
	1151.787	Uncertain
	1152.985	
	1153.160	
	1155.027	Blend Fe VII
	1155.725	

Table B4 *– continued*

Ion	Wavelength/Å	Comment
	1156.394	
	1157.725	Uncertain
	1158.475	Blend Ga V
	1158.759	
	1160.221	
	1160.827	Uncertain
	1161.971	
	1162.281	
	1162.401	Uncertain
	1163.779	Uncertain
	1164.090	
	1164.632	
	1165.189	Blend Ge V
	1165.706	
	1165.880	Too strong in model
	1168.302	Uncertain
	1169.200	Uncertain
	1169.301	Uncertain
	1170.105	
	1170.885	Uncertain
	1171.106	Uncertain
	1171.422	
	1171.801	
	1171.951	
	1172.038	
	1173.366	
	1173.823	Uncertain
	1173.892	Too strong in model
	1174.346	
	1174.945	Uncertain
	1176.122	
	1176.527	Too weak in model
	1176.868 1176.911	
	1176.980 1177.016	
	1177.036 1177.087	
	1178.639	
	1178.759	
	1179.145	
	1179.969 1180.018	
	1182.019	Uncertain
	1182.567	
	1183.041 1183.158	
	1183.314	Uncertain
	1185.619 1185.645	
	1185.676	
	1185.898 1185.948	
	1185.961	
	1186.057	
	1186.447	
	1187.706	
	1189.072	
	1189.331	
	1190.003	
	1190.376	
	1192.014	
	1192.703 1192.755	
	1193.846	
	1195.745	
	1198.795	
	1200.639	
	1201.961	
	1202.128	Too strong in model
	1202.906	
	1204.391	

Table B4 *– continued*

Ion	Wavelength/Å	Comment
	1204.722	
	1205.380	Too strong in the model
	1224.788	
	1230.267	
	1238.430	
	1239.108	
	1247.065	
	1262.252	
	1268.158	
	1274.197	
	1281.310	
	1295.850	Too strong in model
	1302.786	
	1318.204	
	1344.241	Too strong in model

Table B5. Like Table B4, for Ga.

Ion	Wavelength / Å	Comment
Ga IV	965.237 965.272	Blend ISM
	981.831	Blend ISM
	1003.780	Blend ISM
	1004.367	
	1005.270	
	1009.849	Blend ISM
	1010.080	Blend ISM
	1014.822	Uncertain
	1074.966	Uncertain
Ga V	943.583	
	962.084	Uncertain
	967.324 967.404	Blend Ge VI
	979.614	
	980.988	
	982.395	Blend ISM
	984.078	
	990.138	Uncertain
	997.855	Blend ISM
	1002.617	Blend ISM
	1009.928	Blend ISM
	1014.456	Blend ISM
	1014.868	Uncertain
	1015.610	Too strong in model
	1019.711	Uncertain
	1032.375	Blend ISM
	1033.492 1033.549 1033.580	
	1034.822	
	1037.334	Blend ISM
	1038.778	Blend ISM
	1040.204	Blend ISM
	1045.850	Blend ISM
	1047.504	
	1050.453	
	1053.930	Blend ISM
	1054.430	Uncertain
	1054.563	Blend Ge V
	1058.123	
	1062.677	
	1063.807	Blend ISM
	1065.371	Uncertain
	1068.593 1068.616	Too strong in model
	1069.484 1069.530	Too strong in model
	1069.587	Too strong in model

Table B5 – *continued*

Ion	Wavelength / Å	Comment
	1071.123 1071.168	
	1073.791	
	1074.911	Uncertain
	1078.225	Blend ISM
	1078.795	
	1079.587 1079.599	
	1079.879 1079.925	
	1080.474	Blend ISM
	1080.988	Uncertain
	1087.358	
	1088.068	
	1091.703	
	1094.355	Blend ISM
	1094.739	
	1095.110	
	1100.401	Uncertain
	1101.613	Uncertain
	1102.767 1102.803	Too strong in model
	1103.047	Too strong in model
	1104.936	
	1105.253	
	1105.620	
	1107.763	
	1109.829	Blend ISM
	1115.561	Blend ISM
	1118.018	
	1118.318	
	1120.260	Blend ISM
	1123.154	
	1123.646	
	1126.393	
	1127.332	
	1127.726	
	1127.752	
	1128.082	Blend Zn V
	1128.554	
	1129.152	
	1129.956	
	1131.452	
	1132.054	
	1132.157	
	1133.247	Blend Zn V
	1133.903	
	1136.067	
	1138.187	
	1143.367	
	1145.974	
	1148.409	Too strong in model
	1150.113	
	1150.219	
	1154.708	Uncertain
	1155.976	
	1156.511	
	1157.729	Uncertain
	1158.534	
	1160.847	Uncertain
	1161.994	Uncertain
	1162.048	Uncertain
	1178.967	Blend Ni V
	1180.958	Uncertain
	1183.110	
	1183.656	
	1189.329	Blend Zn V
	1190.179	Uncertain

Table B5 – *continued*

Ion	Wavelength / Å	Comment
	1191.029	
	1193.061	
	1197.633	
	1265.454	
	1276.911	Blend Fe VI
	1283.615	
	1311.389	
Ga VI	915.720	No observation
	919.117	Blend ISM
	929.964	
	935.522	Blend ISM
	945.329	Blend ISM
	948.171	Blend ISM
	953.738	Blend ISM
	955.510	
	955.616	Blend ISM
	956.648	Blend ISM
	957.642	Blend ISM
	960.172	Blend ISM
	961.262	
	964.264 964.311 964.363	Blend ISM
	964.569 964.647	Blend ISM
	964.831 964.925	Blend ISM
	966.130	Blend ISM
	966.255	Blend ISM
	966.990	
	967.825	Blend ISM
	968.107	
	970.064	
	974.853	
	975.165	
	975.342 975.396	Blend ISM
	976.133	Blend ISM
	977.848	Blend ISM
	978.897	Uncertain
	979.298 979.383	
	979.689	
	980.240	Too strong in model
	980.489	Uncertain
	980.580	Blend ISM
	982.066	Blend ISM
	983.110 983.160	
	983.430 983.485	Uncertain
	983.630	
	984.009	Blend ISM
	985.273	
	985.596	Blend ISM
	985.812	Blend ISM
	986.662	Blend ISM
	987.862	Blend ISM
	988.063	Blend ISM
	989.169	Blend ISM
	989.374	
	990.416	Blend ISM
	990.639	
	992.053	Blend ISM
	992.709	Blend ISM
	993.094	
	993.640 993.654	Blend ISM
	994.051	Blend ISM
	995.305	
	996.027	Blend ISM
	996.309 996.391	Uncertain
	996.556	

Table B5 *– continued*

Ion	Wavelength / Å	Comment
	997.605	Blend ISM
	999.083	Blend ISM
	999.673	
	999.945	
	1000.117	
	1000.531	Too strong in model
	1001.483	
	1001.821	Blend ISM
	1002.376	Blend ISM
	1002.985	Uncertain
	1003.127 1003.147	Uncertain
	1003.390 1003.427	Uncertain
	1003.691	Uncertain
	1004.170	Blend ISM
	1004.355	
	1005.228	Uncertain
	1006.156	Uncertain
	1006.396	Blend ISM
	1006.894 1006.951	Too strong in model
	1007.264	Blend Fe V
	1007.511	Blend Fe V
	1008.086	Blend ISM
	1008.757	Blend ISM
	1008.924 1009.049	Blend ISM
	1009.262	
	1009.512	Blend ISM
	1009.743 1009.796 1009.806	Blend ISM
	1010.102	Blend ISM
	1011.047	Blend ISM
	1011.696 1011.698	Blend ISM
	1012.260	Blend ISM
	1013.620	Blend ISM
	1014.434	Blend ISM
	1015.598	Too strong in model
	1015.782	
	1016.307	Uncertain
	1017.003	
	1017.074	
	1018.785	
	1019.083	Blend ISM
	1019.206	
	1020.741	Blend ISM
	1022.008 1022.098	Uncertain
	1027.809	Uncertain
	1029.168	Uncertain
	1030.457 1030.469	Uncertain
	1037.061	Blend ISM
	1037.419	Blend ISM
	1038.800	Blend ISM
	1042.324	Blend Fe V
	1047.696	Blend ISM
	1051.311	Blend ISM
	1051.589	Blend ISM
	1058.653	
	1058.931	
	1059.854 1058.931	
	1060.387	Uncertain
	1061.790	Blend ISM
	1063.972	Uncertain
	1066.724	Blend ISM
	1071.544	Blend ISM
	1073.814	
	1076.760	
	1077.944	Blend ISM

Table B5 *– continued*

Ion	Wavelength / Å	Comment
	1078.331	Blend ISM
	1089.450	
	1099.109	
	1101.237	
	1105.669	
	1106.251	
	1121.262	Uncertain
	1129.110	
	1138.016	
	1149.078	
	1237.472	
	1259.673	Blend Co VI
	1288.359	

Table B6. Like Table B4, for Ge.

Ion	Wavelength / Å	Comment
Ge IV	936.765	Blend ISM
	1189.028	
	1229.839	
	1494.889	Uncertain
Ge V	942.717	Blend ISM
	958.508	
	965.501	
	971.357	Blend ISM
	977.455	
	984.923	Blend ISM
	986.767	Blend ISM
	988.132	Blend ISM
	990.668	
	992.307	Blend ISM
	1004.380	
	1004.938	Too strong in model
	1008.122	Blend ISM
	1016.667	
	1033.107	Too strong in model
	1035.504	Uncertain
	1038.430	
	1042.127	Too strong in model
	1045.713	
	1048.318 1048.371	Uncertain
	1048.411	
	1050.057	Blend ISM
	1054.590	
	1058.932	
	1068.430	
	1069.132	
	1069.420	Too strong in model
	1069.703	
	1069.857	Uncertain
	1072.495	
	1072.659	
	1080.427 1080.484	Blend ISM
	1080.586	
	1086.653	
	1087.855	
	1089.491 1089.526	
	1092.089	
	1103.185	Uncertain
	1116.947	
	1123.746	Too strong in model
	1125.424	

Table B6 – *continued*

Ion	Wavelength / Å	Comment
	1139.187	
	1163.400	
	1165.259	
	1176.690	Uncertain
	1222.300	
Ge VI	911.098	No observation
	911.114	No observation
	914.143	No observation
	915.041	No observation
	917.352	Blend ISM
	918.280	Blend ISM
	919.278	Blend ISM
	919.731 919.760	Blend ISM
	920.510	
	921.084	Blend ISM
	921.780	Blend ISM
	923.486	Uncertain
	925.476	
	926.822	Too strong in model
	928.136	
	928.907	
	929.428	Blend ISM
	929.631	Blend ISM
	930.081	
	933.766	Blend ISM
	935.016	
	935.912	
	939.152	Blend ISM
	940.427	
	942.474	Blend ISM
	942.567	Blend ISM
	944.851	Blend ISM
	946.589	Blend ISM
	947.937	
	951.739	
	952.415	Blend ISM
	953.132	
	954.504	Blend ISM
	955.708	Blend ISM
	957.548	Blend ISM
	957.886	
	958.100	
	958.310	Uncertain
	960.102	Too strong in model
	964.813	Blend ISM
	965.203	Blend ISM
	965.914	Blend ISM
	967.300	
	968.723	
	969.010	Blend ISM
	969.171	Blend ISM
	969.568	
	970.977	Blend ISM
	971.392	Blend ISM
	973.353	Blend ISM
	975.996	
	979.258	

Table B6 – *continued*

Ion	Wavelength / Å	Comment
	979.905	Blend ISM
	980.431	Blend ISM
	980.697	Too strong in model
	981.946	Blend ISM
	983.648	
	988.180	Too strong in model
	990.049	Blend ISM
	990.848	Blend Fe V
	991.519	Blend ISM
	991.888	Blend ISM
	992.377	Blend He II
	993.015	Blend ISM
	995.289	
	996.771	Too strong in model
	1002.276	Blend ISM
	1004.661	
	1008.410	Blend ISM
	1011.518	
	1013.528	Blend ISM
	1014.766	
	1015.582	Too strong in model
	1016.817	Blend ISM
	1023.527	Blend ISM
	1031.263 1031.324	Blend ISM
	1033.152	Too strong in model
	1034.251	Uncertain
	1039.483	Too strong in model
	1039.890	Too strong in model
	1047.139	Too strong in model
	1047.207	Too strong in model
	1051.515	Blend ISM
	1053.196	Too strong in model
	1061.890	
	1062.394	
	1064.323	
	1080.148	Too strong in model
	1080.510	Blend ISM
	1088.522	
	1102.998	Too strong in model
	1103.103	Too strong in model
	1106.146	Too strong in model
	1113.177	
	1121.431	Uncertain
	1127.159	
	1148.327	Too strong in model
	1227.850	Too strong in model
	1228.870	Too strong in model
	1237.128	
	1237.892	Too strong in model
	1251.447	Too strong in model
	1255.318	
	1257.218	Blend Mo V
	1292.751	Too strong in model
	1300.093	Too strong in model
	1305.406	Too strong in model
	1391.639	Too strong in model
	1500.600	

Table B7. Like Table B4, for Se.

Ion	Wavelength / Å	Comment
Se V	943.957	Blend ISM
	964.515	Blend ISM
	1030.609	
	1047.219	Too strong in model
	1059.951	Uncertain
	1094.691	
	1151.016	
	1184.343	
	1227.540	
	1249.048	Uncertain
	1264.063	Blend Mn VI
	1426.676	
	1433.568	
	1445.567	
	1447.283	
	1447.408	
	1451.653	
	1454.292	
	1473.253	
	1730.014	No observation
	1736.835	No observation
	1740.038	No observation

Table B8. Like Table B4, for Br.

Ion	Wavelength / Å	Comment
Br V	945.815	Blend ISM
	1069.410	
Br VI	955.883	Blend ISM
	966.753	Blend ISM
	969.735	
	981.423	Blend ISM
	1050.548	
	1069.382 1069.432	
	1073.708	
	1074.992	
	1230.318	
	1399.153	Uncertain

Table B9. Like Table B4, for Kr.

Ion	Wavelength / Å	Comment
Kr VI	927.334	Blend ISM
	944.046	Uncertain
	965.093	Blend ISM
	980.411	
	1002.748	
	1045.238	
	1061.064	
Kr VII	918.444	Blend ISM
	960.645	Blend ISM
	1197.166	Uncertain

Table B10. Like Table B4, for Sr.

Ion	Wavelength / Å	Comment
Sr V	917.802	Blend ISM
	927.356	Blend ISM
	928.353	Blend ISM
	935.509	Blend ISM
	936.808	Blend ISM
	942.943	Blend ISM
	946.530	Blend ISM
	951.044	Blend ISM
	951.159	Blend ISM
	955.369	Blend N IV
	957.714	Blend ISM
	962.378	
	969.103	Blend ISM
	979.150	
	985.408	Blend ISM
	1007.201	Uncertain
	1011.422	
	1013.714	Blend ISM
	1020.002	Uncertain
	1020.439	
	1030.445	Too strong in model
	1031.343	Blend ISM
	1038.990	Uncertain
	1041.940	
	1056.104	Uncertain
	1065.215	Uncertain
	1070.578	Uncertain
	1114.594	
	1114.876	Uncertain
	1132.353	Uncertain
	1141.221	Uncertain
	1152.104	Uncertain
	1154.871	
	1163.040	
	1164.173	Blend Zn V
	1175.115	Uncertain
	1200.728	Blend ISM
	1238.652	Blend Ni V
	1280.995	
	1281.911	
	1311.334	
	1311.781	Blend Fe V
	1387.288	
	1415.404	
	1447.665	
	1459.369	
	1472.784	
Sr VI	912.3760	No observation

Table B11. Like Table B4, for Zr.

Ion	Wavelength / Å	Comment
Zr V	1200.802	Blend ISM
	1332.065	
Zr VI	955.500	
	1040.904	
	1040.995	
	1044.483	Uncertain
	1050.580	Blend Br VI
	1053.548	
	1064.818	Blend ISM
	1068.836	
	1072.877	
	1073.197	Uncertain
	1074.554	
	1081.130	
	1081.384	Blend ISM
	1088.439	Uncertain
	1095.491	
	1099.591	
	1101.742	
	1108.491	Blend ISM
	1113.736	Uncertain
	1114.481	
	1118.689	Too strong in model
	1129.371	
	1134.606	Uncertain
	1142.550	
	1143.933	
	1150.774	
	1151.571	
	1158.582	Uncertain
	1161.639	
	1314.034	
	1417.865	
	1514.568	
	1521.699	
	1529.396	
	1536.035	Uncertain
	1538.423	
	1541.255	Uncertain
	1591.799	
	1604.549	Uncertain
	1645.326	
	1663.952	
	1679.018	Uncertain
	1682.241	
	1683.302	Uncertain
	1733.091	No observation
	1733.937	No observation
	1741.948	No observation
	1749.350	No observation
Zr VII	1233.578	
	1234.964	
	1376.633	
	1469.098	Uncertain

Table B12. Like Table B4, for Mo.

Ion	Wavelength / Å	Comment
Mo VI	995.806	Uncertain
	1038.640	Blend ISM
	1047.182	Uncertain
	1479.168	
	1595.435	

Table B13. Like Table B4, for In.

Ion	Wavelength / Å	Comment
In V	933.577	Blend ISM
	940.079	Uncertain
	942.218	Uncertain
	1101.860	Uncertain
	1122.517	Blend ISM
	1135.588	Uncertain
	1136.347	
	1137.787	
	1148.852	
	1151.723	
	1153.836	
	1156.652	
	1160.561	
	1168.056	
	1177.447	
	1181.329	
	1183.049	
	1190.489	Blend ISM
	1191.583	
	1192.278	
	1192.541	
	1196.281	
	1199.170	
	1200.843	Blend ISM
	1210.126	Uncertain
	1228.000	Uncertain
	1228.483	Uncertain
	1238.448	
	1241.025	
	1241.299	
	1242.210	
	1243.632	Blend Ni V
	1252.836	Blend Fe VI
	1256.570	Uncertain
	1276.318	Uncertain
	1278.758	
	1285.468	Uncertain
	1289.800	
	1290.449	
	1292.930	
	1295.035	Uncertain
	1296.427	
	1315.139	
	1317.671	Uncertain
	1320.468	Uncertain
	1334.123	
	1339.599	
	1355.458	Uncertain

Table B14. Like Table B4, for Te.

Ion	Wavelength / Å	Comment
Te VI	951.021	Blend ISM
	1071.414	
	1242.023	Uncertain
	1267.986	
	1313.874	

Table B15. Like Table B4, for I.

Ion	Wavelength / Å	Comment
I VI	911.192	No observation
	919.210	Blend ISM
	970.448	Uncertain
	987.381	Blend ISM
	989.005	Blend ISM
	1000.999	Uncertain
	1045.423	
	1053.389	Blend ISM
	1057.530	
	1120.301	Blend ISM
	1121.218	Uncertain
	1137.370	Uncertain
	1153.262	Too strong in model
	1185.111	Uncertain
	1191.601	
	1195.359	Uncertain
	1395.979	

Table B16. Like Table B4, for Xe.

Ion	Wavelength / Å	Comment
Xe VI	1080.080	Blend Ge VI
	1091.630	Uncertain
	1136.410	Uncertain
Xe VII	912.875	No observation
	920.861	Blend ISM
	942.152	
	943.218	
	970.177	Uncertain
	995.510	
	997.407	Blend Fe V
	1071.226	Uncertain
	1077.110	Blend ISM
	1093.781	Blend ISM
	1243.565	
	1460.856	Uncertain

Table B17. Like Table B4, for Ba.

Ion	Wavelength / Å	Comment
Ba VI	937.595	Blend ISM
Ba VII	924.898	Blend ISM
	943.102	Blend ISM
	993.411	
	1074.937	
	1255.520	Uncertain
	1465.045	
Ba VIII	921.761	Uncertain
	941.168	Uncertain
	952.762	Blend ISM
	961.679	Blend ISM
	1013.130	Blend ISM
	1039.555	
	1048.339	Blend ISM
	1074.911	
	1083.072	
	1113.140	Uncertain

This paper has been typeset from a TEX/LATEX file prepared by the author.

4 Results

4.1 Spectral analysis of the barium central star of the planetary nebula Hen 2−39

This work could confirm the enrichment with C and Ba that was already known (Miszalski et al. 2013). In addition, the abundances or upper limits for 37 elements from N to osmium (Os) could be determined. It was not possible to detect lines of Tc in the observed spectrum. Only an upper limit of $\log \epsilon_{\mathrm{Tc}} < 2.5$[1] could be found. A considerable difficulty in the analysis was the rapid rotation ($v_{\mathrm{rot}} \sin i = 38 \pm 5\,\mathrm{km/s}$) of the subgiant star. This severely broadens the lines so that they overlap. This prohibited abundance analyses based on equivalent width measurements. Hence, observations with an even higher resolution will not help to improve the analysis and narrow down the errors for the abundance determination but only a higher signal-to-noise ratio (S/N) can do that. On the other hand, the fast rotation is a sign for angular momentum transfer onto the companion that should go in hand with mass transfer. By assuming that the companion's enrichment with C and Ba above the initial metallicity of the system is entirely due to mass transfer, we determined the amount of mass for the different TIEs that would need to be accreted by the companion to show the observed abundance pattern. This was done for different masses of the two components while the ratio is determined by the evolutionary status of the more massive one being a CSPN and the less massive one just evolving off the main sequence. Based on the tabulated yields for AGB stars from nucleosynthesis calculations (Karakas & Lattanzio 2014a; Karakas & Lugaro 2016), we found that the primary should have ejected a larger amount of mass of TIEs than the secondary would need to accrete. But still, the ratio of accreted mass needs to be high ($\approx 15\,\%$) so that CE and Bondi-Hoyle accretion can be ruled out. It is desirable to determine the orbital period, since it can also indicate the possible mass transfer mechanism. The fact that it is not known yet (Miszalski et al. 2013) may be a hint that it is not very short (a few days) which would be a clear sign for CE evolution. Wind-RLOF can generate the required accretion fraction (Chen et al. 2017) and is thus considered to be the process responsible for the pollution of the subgiant CS of Hen 2−39. However, the masses derived from this analysis are based on the tabulated, calculated yields and the amount of mass that needs to be accreted. Both values are affected by uncertainties that are not easy to estimate. The yields are affected by the choice of the ^{13}C-pocket, the description for mass loss and

[1] $\log \epsilon = 12 + \log(n_{\mathrm{X}}/n_{\mathrm{H}})$ with number fractions n.

parameterization of convective mixing, the effectiveness of TDU, uncertain atomic neutron capture cross sections, and neutron poisons (c.f., Karakas & Lattanzio 2014a). On the other hand, the calculation of the needed accreted mass is based on assumptions about the surface convection zone of the red giant. The core and envelope mass are derived from approximate equations but depend strongly on metallicity and, thus, opacity of the plasma (Joss et al. 1987). Furthermore, the equations assume, that the star is in equilibrium, which might not be the case for an accreting star.

4.2 Spectral analysis of the hybrid PG 1159-type central stars of the planetary nebulae Abell 43 and NGC 7094

We analyzed observations from UV to optical and redetermined the effective temperature and surface gravity for WD 1751+106 and WD 2134+125. For both stars, the best agreement between the observation and model spectrum was reached for $T_{\rm eff} = 115$ kK and $\log g = 5.6$. We revised and determined abundances for light metals, IGEs and found upper abundance limits for TIEs. The abundances are illustrated in Fig. 4.1. The precise abundances for light metals allowed to compare to other H-deficient CSPNe and (pre-)WDs and evolutionary model predictions. Compared to the CSPNe Abell 30 and Abell 78, and also other H-deficient hot WDs, the He content is high, whereas C, N, and O are lower. We argue, that this indicates different evolution channels, i.e., AFTP for the hybrid PG 1159 stars compared to (V)LTP for the other H-deficient stars. Different masses of the H-rich envelope compared to the He-rich intershell region at the time of the final flash mixing can result in different surface abundances. Especially an N enrichment, as it is seen in the CSs of Abell 30 and Abell 78 is understood as indicator for a VLTP scenario, in which the ingestion of H to the He-rich intershell should produce ^{14}N. We conclude that the AFTP is the most likely explanation for the H-deficiency with remaining H fractions of 25 ± 3 % (WD 1751+106) and 15 ± 3 % (WD 2134+125) by mass. The new evolutionary models for this scenario reproduce the observed abundances for H, He, C, N, and Ne. One unclear aspect is the O abundance. While our new models include boundary mixing at the bottom of the intershell convection zone and predict much higher O abundances, older AFTP calculations (Lawlor & MacDonald 2006) do not take mixing into account and end up with O abundances in the range of WD 1751+106 and WD 2134+125. On the other hand, C and Ne are underestimated by these models, indicating that the convective boundary mixing is still a process that is affected by many uncertainties. Just to note, of the two other known hybrid-PG 1159 stars, SDSS 152116.00+251437.46 also has an O abundance that is significantly lower than the predictions from AFTP evolutionary models of this work. However, the O abundance of WD 2324+397 perfectly agrees with the range seen in the models. We confirmed, that the stars have subsolar Fe abundances of [Fe] = −0.4[2] and [Fe] = −0.8, respectively, although these values are less deficient than previously found (Miksa et al. 2002). The strong deficiency in previous studies might result from not taking additional line broadening due to stellar rotation or macro turbulence into account when analyzing the line profiles. We consider the explanation of a reduced Fe abundance resulting from efficient synthesis of TIEs as unlikely. Although nucleosynthesis calculations predict an

[2] [X] = log (mass fraction/solar mass fraction).

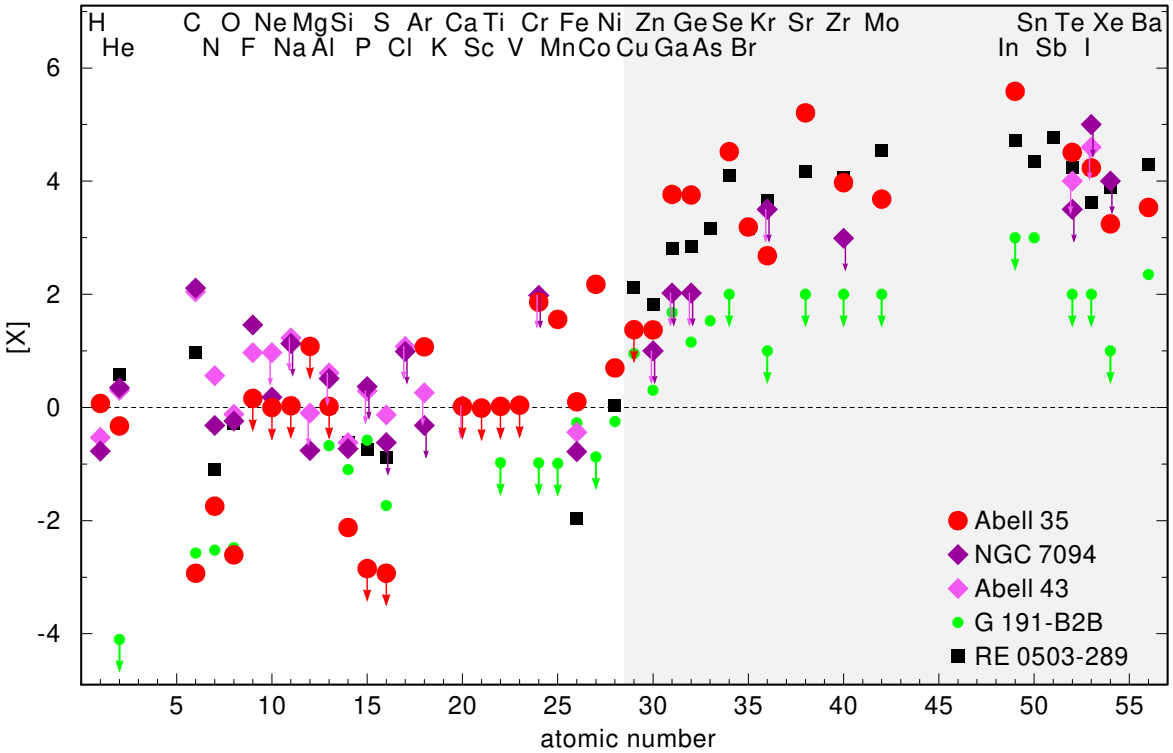

Fig. 4.1: Photospheric abundance ratios [X] = log(mass fraction/solar mass fraction) of the CS of Abell 43, NGC 7094, and Abell 35. Upper limits are indicated with arrows. The black, dashed line indicates solar abundances. Element abundances up to Ni for Abell 35 (red) were taken from Ziegler et al. (2012). For comparison, the abundances determined for RE 0503−289 (Hoyer et al. 2017, black squares) and G191−B2B (Rauch et al. 2012, 2013, 2014a,b, 2015b, 2016a, green dots) are shown.

enhancement of s-process elements, they do not predict a significantly reduced Fe abundance (Karakas & Lugaro 2016). Thus, we argue, that the Fe deficiency more likely reflects the initial metallicity. The assumed low metallicity is not in contradiction to the location of the stars in the Galactic disc, since their metallicity still allows disc membership (Recio-Blanco et al. 2014). The upper abundance limits for the TIEs confirmed the prediction that diffusion is the mechanism enriching heavy elements in the photospheres of hot DO WDs (Rauch et al. 2016a), since such a strong enrichment of the level of RE 0503−289 can be ruled out. In the log $T_{\rm eff}$-log g diagram (Fig. 4.2), both stars are located well before the wind limits for H- and He- dominated WDs (Unglaub & Bues 2000). Pre-WDs before these limits, are predicted to experience mass loss and stellar wind. The wind limits indicate the region where gravitational settling starts to become dominant. The mass loss rate of $\log[\dot{M}\,/\,(M_\odot/\mathrm{yr})] \approx -8.1$ is in hand with this explanation. For this value, the wind is chemically homogeneous (Unglaub 2008) and, thus, cannot enrich any species. Another yet unexplained aspect is, that the evolutionary timescales of the new AFTP models do not agree with expansion ages derived from the nebula. While the models predict these stars to be at the current state within 2 000 yrs after the departure from the AGB, the nebula expansion ages derived from distance,

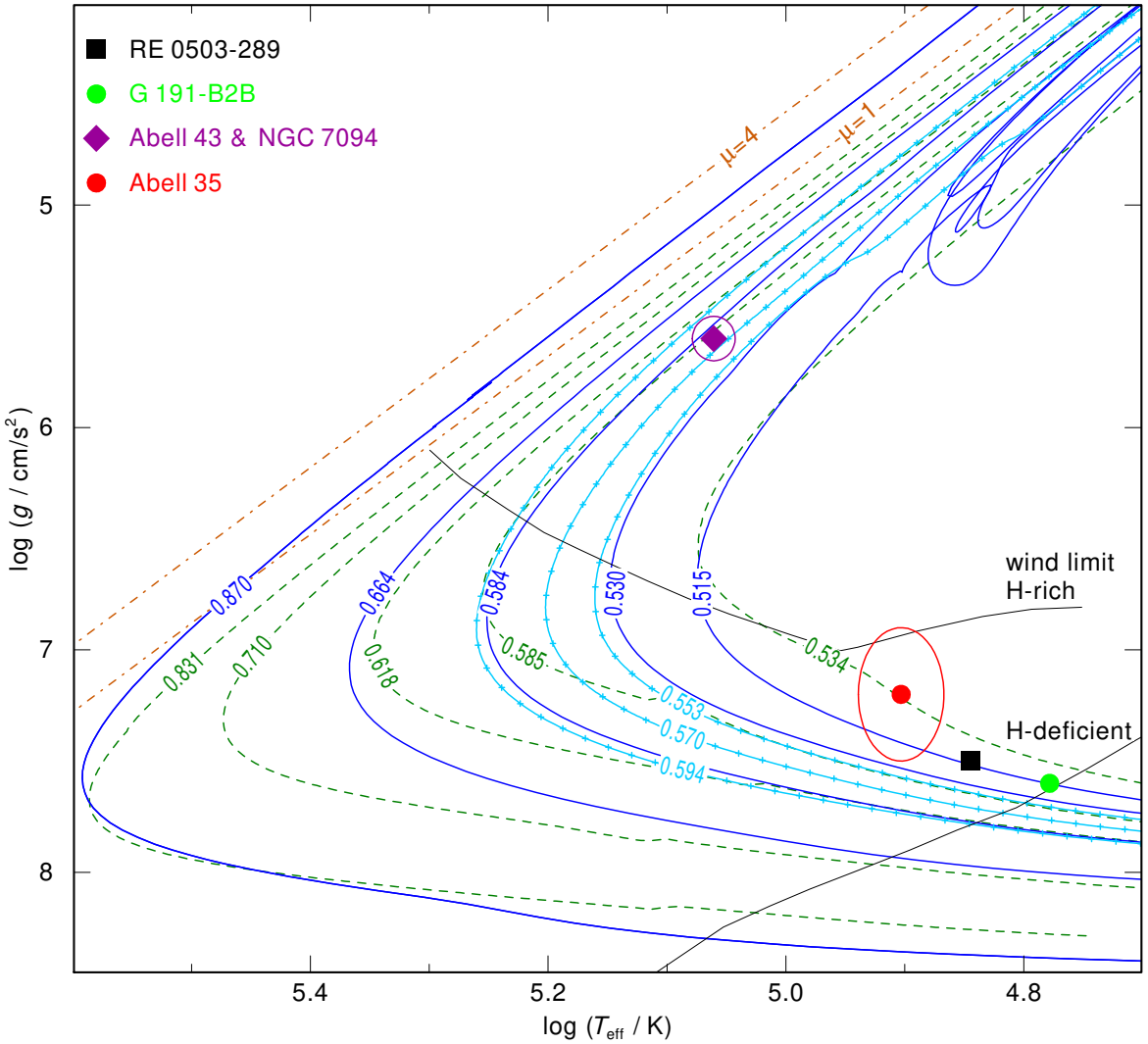

Fig. 4.2: Positions of WD 1751+106 (Abell 43), WD 2134+125 (NGC 7094), and BD−22°3467 (Abell 35) with their error ellipses and related objects in the $\log T_{\rm eff} - \log g$ plane compared with evolutionary tracks (labeled with the respective masses in $M_\odot$) of VLTP stars (Miller Bertolami & Althaus 2006, blue full lines), of H-burning post-AGB stars (Miller Bertolami 2016, calculated with initial solar metallicity, green dashed lines), and of AFTP stars (cyan, thick lines). The orange dashed-dotted $\mu = 1$ and $\mu = 4$ lines indicate the Eddington limits for pure H and He atmospheres, respectively.

apparent size and expansion velocity are about a factor of five to six larger. The expansion ages are already assumed to be lower limits, since they are based on the current expansion velocity and do not take acceleration into account (Gesicki & Zijlstra 2000). The discrepancy between the models and observation based values cannot be solved by assuming less mass loss during the post-AGB evolution but is regardless of that. From inspection of the evolution tracks for AFTP stars it becomes clear, that they coincide with VLTP tracks of the same

mass. This justifies to derive the stellar mass from interpolation between VLTP tracks. The distance from Gaia parallax measurements states a robust test for the spectroscopic distance determination based on the ratio of calculated and observed, dereddened flux, $\log g$, and mass. A systematic difference becomes obvious. Although the distances agree within the error limits, the spectroscopic values are higher than those from precise parallaxes.

4.3 First discovery of trans-iron elements in a DAO-type white dwarf

We analyzed the abundances for 14 TIEs in BD−22°3467 and found an enrichment of a level similar to RE 0503−289. Up to now, several DO WDs were found to be as enriched with TIEs as RE 0503−289 (Hoyer et al. 2018). DO WDs are understood to stem from a (V)LTP scenario in which the envelope became mixed with the intershell region resulting in the H-deficiency and the presence of TIEs at the surface. After the CSPN phase but before crossing the wind limit, these TIE abundances were thought to be amplified due to radiative levitation. This explanation was supported by the fact, that TIEs could also be determined in hot DA-type WDs (e.g., G191−B2B, Vennes et al. 2005; Rauch et al. 2012, 2013, 2014a,b, 2015b, 2016a) but with lower abundances. The strong enrichment found in BD−22°3467 now questions the necessity of a FTP to see a strong enrichment with TIEs in the WD photosphere. BD−22°3467 did not experience a FTP. It even has such a low mass ($0.533^{+0.040}_{-0.025}\,M_\odot$, Ziegler et al. 2012) that its initial mass should be below $1.0\,M_\odot$ (Cummings et al. 2018) which makes it unlikely that traces of nucleosynthesis products were mixed to the surface by TDU (Karakas & Lugaro 2016). The only explanation for the peculiar abundance pattern so far is, that all TIEs are enriched by radiative leitation starting from initial metallicity. This can also be the case for all hot DO WDs with strong enrichment. One explanation, why G191−B2B shows lower TIE abundances is, that it is already cooler and further evolved compared to RE 0503−289 and BD−22°3467 (Fig. 1.3) and thus the heavy elements start to sink.

In contrast to WD 1751+106 and WD 2134+125 (Sect. 4.2), the spectroscopic distance to BD−22°3467 (361^{+195}_{-137} pc, Ziegler et al. 2012) is in disagreement with the value based on the Gaia parallax ($124.84^{+2.21}_{-2.13}$ pc, Bailer-Jones et al. 2018). To end with a reasonable WD mass at the given $T_{\rm eff}$, $\log g \gtrsim 8.0$ would be needed. Models with such high surface gravities do not agree with the fit of broad H I lines in the FUSE spectrum (Ziegler et al. 2012). Missing NLTE line blanketing in the atmosphere calculation, which other studies found to be a possible explanation (Schönberner et al. 2018; Schönberner & Steffen 2019), cannot be the explanation in this case since our models considered opacities of 38 elements from H to Ba. The distance discrepancy remains an unsolved puzzle.

5 Outlook

The presented analysis of the Ba CSPN Hen 2−39 revealed, that a rather conservative mass-transfer mechanism is needed for the formation of Ba stars. However, we could not use the abundance pattern to constrain nucleosynthesis but rather needed to use predicted nucleosynthesis yields to constrain the masses of the binary components. For systems with known masses and orbital parameters, these values can be used when evaluating the agreement between the observed abundances and theoretical predictions. Despite observational evidence, mass-transfer mechanisms and CE evolution are still poorly understood due to the difficulty of modeling the angular momentum evolution (e.g., Paxton et al. 2015). Further analyses of binary CSPNe of different types, i.e., with a pollution of the companion and without, can help to get insights into binary interaction and the effectiveness of mass-transfer mechanisms at different separations.
Up to now, only few attempts have been made to perform spectral analyses of both binary components in parallel (e.g., Aller et al. 2015). This requires multi-wavelength observations (from extreme UV to infrared) to cover the spectral ranges dominated by the hot post-AGB star and by the cooler companion. Having access to the fundamental parameters and abundances of not only one but both components and maybe also of the nebula from an analysis of emission lines in the optical and infrared regime, will also offer the possibility to better constrain the flow of material in the system.

The analyzed hot post-AGB stars in this work are of rather low initial masses, WD 1751+106 and WD 2134+125 should originate from stars with $1.0 - 1.1\,M_{\odot}$ and the progenitor of BD−22°3467 should even be less massive. The initial mass is a parameter, that crucially affects the outcomes of nucleosynthesis. According to theoretical calculations, it does not only determine the effectiveness of nuclear reactions but also convective mixing processes (Karakas & Lugaro 2016). These are still poorly understood processes of AGB evolution and also play an important role already in earlier stages (Henry et al. 2018). The s-process is predicted to be most efficient for stars with initial mass of around $3\,M_{\odot}$ (Karakas & Lugaro 2016), which translates to post-AGB masses of about $0.8\,M_{\odot}$ (Cummings et al. 2018). Detailed spectral analyses CSPNe with the highest known masses in comparison to lower mass stars are necessary to empirically determine the effectiveness of nucleosynthesis depending on the initial mass. Given that the surface abundances of BD−22°3467 are entirely the effect of diffusion acting on initial material, the TIE abundances of hot WDs should not depend on whether the star evolved through an FTP or not. However, during the evolutionary phase as

a CSPN, it should still be necessary to analyze H-deficient stars to see intershell material, because for them it is undisputed that the photosphere became polluted with nucleosynthesis products from the intershell region in the LTP of the He burning shell.
To really be able to perform abundance measurements in the atmospheres of the hottest CSPNe and pre-WDs, it is necessary to include atomic data of higher ionization stages than the ones currently available. Further effort in laboratory measurements and subsequent sophisticated quantum-mechanical calculations are urgently needed.
The origin of line broadening seen in the spectra of WD 1751+106 and WD 2134+125 needs to be further investigated. It may be an effect of rotation or macro turbulence but the line profiles do not allow to constrain the process acting here. The effect was also seen in other PG 1159-type CSPNe (Rauch et al. 2004) while other objects in the same $\log T_{\rm eff} - \log g$ region do not show broadened lines (Werner et al. 2010). Photometric analyses of pulsating objects with broadened lines like WD 1751+106 and WD 2134+125 (Solheim et al. 2007) may help to solve this puzzle by offering an independent determination of the rotational velocity (Kawaler 2004).
The spectroscopic distances of WD 1751+106, WD 2134+125, and BD−22°3467 based on the ratio of observed and calculated flux, surface gravity, and mass were found to be systematically larger than Gaia distances (Löbling et al. 2019b,c). This is also seen in analyses using other NLTE codes (Schönberner et al. 2018; Schönberner & Steffen 2019). No satisfying explanation was found yet and the problem needs further investigation. One possibility are imprecisions in the broadening theory for optical lines of H and He with their gravity sensitive wings that are mainly used to constrain the effective temperature and surface gravity of hot post-AGB stars.

The origin of the s-process elements in the atmosphere of the CS of Abell 35 is unclear. The H abundance rules out a final flash and the extremely low mass also prohibits TDU, another large scale mixing process. It would be necessary to analyze a larger sample of spectra of hot DAO-type WDs and to determine their s-process abundances to dissolve puzzles in their evolution. Precise abundances for more DAO WDs can unravel whether Abell 35 is a unique object or whether other H-rich hot WDs also show similar surface abundances. In the course of this analysis, a detailed reanalysis of the UV spectrum of BD−22°3467 based on the latest atomic data can further constrain $T_{\rm eff}$ and $\log g$ and confirm or correct the extremely low mass of the star. This is a crucial factor since the initial mass determines whether TDU occurs or not. A systematic analysis of a sample of DAO WDs can also be used to test the correlation of the observed abundances with stellar parameters like effective temperature and surface gravity, which are a measure for the evolutionary state and, thus, the strength of the stellar wind. It should allow to empirically probe the location of the wind limit (Unglaub & Bues 2000).

Bibliography

Abate, C., Pols, O. R., Izzard, R. G., Mohamed, S. S., & de Mink, S. E., 2013. *Wind Roche-lobe overflow: Application to carbon-enhanced metal-poor stars.* A&A, 552, A26.

Abbott, B. P., Abbott, R., Abbott, T. D., Acernese, F., Ackley, K., et al., 2017. *Gravitational Waves and Gamma-Rays from a Binary Neutron Star Merger: GW170817 and GRB 170817A. The Astrophysical Journal*, 848(2), L13.

Abell, G. O., 1955. *Globular Clusters and Planetary Nebulae Discovered on the National Geographic Society-Palomar Observatory Sky Survey.* PASP, 67(397), 258.

Abell, G. O., 1966. *Properties of Some Old Planetary Nebulae.* ApJ, 144, 259.

Aller, A., Montesinos, B., Miranda, L. F., Solano, E., & Ulla, A., 2015. *Spectral analysis of BD+30°623, the peculiar binary central star of the planetary nebula NGC 1514*.* MNRAS, 448(3), 2822.

Aller, A., Lillo-Box, J., Vučković, M., Van Winckel, H., Jones, D., Montesinos, B., Zorotovic, M., & Miranda, L. F., 2018. *A new look inside planetary nebula LoTr 5: a long-period binary with hints of a possible third component.* MNRAS, 476, 1140.

Alpher, R. A., Bethe, H., & Gamow, G., 1948. *The Origin of Chemical Elements. Physical Review*, 73(7), 803.

Althaus, L. G., Panei, J. A., Miller Bertolami, M. M., García-Berro, E., Córsico, A. H., Romero, A. D., Kepler, S. O., & Rohrmann, R. D., 2009. *New Evolutionary Sequences for Hot H-Deficient White Dwarfs on the Basis of a Full Account of Progenitor Evolution.* ApJ, 704(2), 1605.

Asplund, M., Grevesse, N., Sauval, A. J., & Scott, P., 2009. *The Chemical Composition of the Sun.* ARA&A, 47, 481.

Bailer-Jones, C. A. L., Rybizki, J., Fouesneau, M., Mantelet, G., & Andrae, R., 2018. *Estimating Distance from Parallaxes. IV. Distances to 1.33 Billion Stars in Gaia Data Release 2.* AJ, 156, 58.

Bidelman, W. P. & Keenan, P. C., 1951. *The Ba II Stars.* ApJ, 114, 473.

Bidelman, W. P., 1962. *Line Identifications in Peculiar Stars.* AJ, 67, 111.

Bischoff-Kim, A., Provencal, J. L., Bradley, P. A., Montgomery, M. H., Shipman, H. L., Harrold, S. T., Howard, B., Strickland, W., Chandler, D., Campbell, D., Arredondo, A., Linn, R., Russell, D. P., Doyle, D., Brickhouse, A., Peters, D., Kim, S. L., Jiang, X. J., Mao, Y. N., Kusakin, A. V., Sergeev, A. V., Andreev, M., Velichko, S., Janulis, R., Pakstiene, E., Aliçavuș, F., Horoz, N., Zola, S., Ogłoza, W., Koziel-Wierzbowska, D., Kundera, T., Jableka, D., Debski, B., Baran, A., Meingast, S., Nagel, T., Löbling, L., Heinitz, C., Hoyer, D., Bognár, Z., Castanheira, B. G., & Erdem, A., 2019. *GD358: Three Decades of Observations for the In-depth Asteroseismology of a DBV Star.* ApJ, 871(1), 13.

Böhm-Vitense, E., 1958. *Über die Wasserstoffkonvektionszone in Sternen verschiedener Effektivtemperaturen und Leuchtkräfte. Mit 5 Textabbildungen.* ZAp, 46, 108.

Bohr, N., 1913. *The Spectra of Helium and Hydrogen.* Nature, 92(2295), 231.

Boltzmann, L., 1866. *Über die mechanische Bedeutung des zweiten Hauptsatzes der Wärmetheorie: (vorgelegt in der Sitzung am 8. Februar 1866).* Staatsdruckerei.

Bond, H. E., Ciardullo, R., & Meakes, M. G., 1993. *The Abell 35-Type Planetary Nuclei.* In *Planetary Nebulae*, editors Weinberger, R. & Acker, A., IAU Symposium, 155, 397.

Bond, H. E., Pollacco, D. L., & Webbink, R. F., 2003. *WeBo 1: A Young Barium Star Surrounded by a Ringlike Planetary Nebula.* AJ, 125, 260.

Bondi, H. & Hoyle, F., 1944. *On the mechanism of accretion by stars.* MNRAS, 104, 273.

Burbidge, E. M., Burbidge, G. R., Fowler, W. A., & Hoyle, F., 1957. *Synthesis of the Elements in Stars. Reviews of Modern Physics*, 29(4), 547.

Busso, M., Gallino, R., & Wasserburg, G. J., 1999. *Nucleosynthesis in Asymptotic Giant Branch Stars: Relevance for Galactic Enrichment and Solar System Formation.* ARA&A, 37, 239.

Carbon, D. F., 1984. *Line blanketing.* Methods in radiative transfer, 395.

Castelli, F., 2005. *ATLAS12: how to use it. Memorie della Societa Astronomica Italiana Supplementi*, 8, 25.

Chayer, P., Vennes, S., Dupuis, J., & Kruk, J. W., 2005. *Abundance of Elements beyond the Iron Group in Cool DO White Dwarfs.* ApJ, 630(2), L169.

Chen, Z., Frank, A., Blackman, E. G., Nordhaus, J., & Carroll-Nellenback, J., 2017. *Mass transfer and disc formation in AGB binary systems.* MNRAS, 468, 4465.

Chornock, R., Berger, E., Kasen, D., Cowperthwaite, P. S., Nicholl, M., Villar, V. A., Alexander, K. D., Blanchard, P. K., Eftekhari, T., Fong, W., Margutti, R., Williams, P. K. G., Annis, J., Brout, D., Brown, D. A., Chen, H. Y., Drout, M. R., Farr, B., Foley, R. J., Frieman, J. A., Fryer, C. L., Herner, K., Holz, D. E., Kessler, R., Matheson, T., Metzger, B. D., Quataert, E., Rest, A., Sako, M., Scolnic, D. M., Smith, N., & Soares-Santos, M.,

2017. *The Electromagnetic Counterpart of the Binary Neutron Star Merger LIGO/Virgo GW170817. IV. Detection of Near-infrared Signatures of r-process Nucleosynthesis with Gemini-South.* ApJ, 848(2), L19.

Coc, A. & Vangioni, E., 2017. *Primordial nucleosynthesis. International Journal of Modern Physics E*, 26(8), 1741002.

Cowan, R. D., 1981. *The theory of atomic structure and spectra.* Los Alamos Series in Basic and Applied Sciences. University of California Press.

Cummings, J. D., Kalirai, J. S., Tremblay, P.-E., Ramirez-Ruiz, E., & Choi, J., 2018. *The White Dwarf Initial-Final Mass Relation for Progenitor Stars from 0.85 to 7.5 $M_{\odot}$.* ApJ, 866, 21.

Dreizler, S., Werner, K., & Heber, U., 1995. *PG 1159 Stars and Their Evolutionary Link to DO White Dwarfs.* In *White Dwarfs*, editors Koester, D. & Werner, K., Lecture Notes in Physics, Berlin Springer Verlag, 443, 160.

Eddington, A. S., 1920. *The Internal Constitution of the Stars. The Scientific Monthly*, 11 (4), 297.

Eggleton, P., 2006. *Evolutionary Processes in Binary and Multiple Stars.* Cambridge University Press.

Einstein, A., 1916. *Die Grundlage der allgemeinen Relativitätstheorie. Annalen der Physik*, 354(7), 769.

Fontaine, G., Brassard, P., & Bergeron, P., 2001. *The Potential of White Dwarf Cosmochronology.* PASP, 113(782), 409.

Fowler, R. H. & Milne, E. A., 1923. *The intensities of absorption lines in stellar spectra, and the temperatures and pressures in the reversing layers of stars.* MNRAS, 83, 403.

Fraunhofer, J., 1817. *Bestimmung des Brechungs- und des Farbenzerstreungs-Vermögens verschiedener Glasarten, in Bezug auf die Vervollkommnung achromatischer Fernrohre. Annalen der Physik*, 56(7), 264.

Frew, D. J. & Parker, Q. A., 2010. *Planetary Nebulae: Observational Properties, Mimics and Diagnostics.* PASA, 27(2), 129.

Fujimoto, M. Y., 1977. *On the Origin of R-Type Carbon Stars: Possibility of Hydrogen Mixing during Helium Flicker.* PASJ, 29, 331.

Gaia Collaboration, Brown, A. G. A., Vallenari, A., Prusti, T., de Bruijne, J. H. J., et al., 2018. *Gaia Data Release 2. Summary of the contents and survey properties.* A&A, 616, A1.

Gesicki, K. & Zijlstra, A. A., 2000. *Expansion velocities and dynamical ages of planetary nebulae.* A&A, 358, 1058.

Green, R. F., Schmidt, M., & Liebert, J., 1986. *The Palomar-Green Catalog of Ultraviolet-Excess Stellar Objects.* ApJS, 61, 305.

Grevesse, N., Scott, P., Asplund, M., & Sauval, A. J., 2015. *The elemental composition of the Sun. III. The heavy elements Cu to Th.* A&A, 573, A27.

Grewing, M. & Bianchi, L., 1988. *The nucleus of Abell 35: a hot companion to SAO 181201.* In *ESA Special Publication*, 177.

Han, Z., Eggleton, P. P., Podsiadlowski, P., & Tout, C. A., 1995. *The formation of barium and CH stars and related objects.* MNRAS, 277, 1443.

Heap, S. R., 1975. *Spectroscopic studies of very old hot stars. I. NGC 246 and its exciting star.* ApJ, 196, 195.

Henry, R. B. C., Stephenson, B. G., Miller Bertolami, M. M., Kwitter, K. B., & Balick, B., 2018. *On the production of He, C, and N by low- and intermediate-mass stars: a comparison of observed and model-predicted planetary nebula abundances.* MNRAS, 473(1), 241.

Herald, J. E. & Bianchi, L., 2002. *The Binary Central Star of the Planetary Nebula A35.* ApJ, 580(1), 434.

Herwig, F., 2001. *Internal mixing and surface abundance of [WC]-CSPN.* Ap&SS, 275, 15.

Herwig, F., Blöcker, T., Langer, N., & Driebe, T., 1999. *On the formation of hydrogen-deficient post-AGB stars.* A&A, 349, L5.

Herwig, F., 2005. *Evolution of Asymptotic Giant Branch Stars.* ARA&A, 43(1), 435.

Hoyer, D., Rauch, T., Werner, K., Kruk, J. W., & Quinet, P., 2017. *Complete spectral energy distribution of the hot, helium-rich white dwarf RX J0503.9-2854.* A&A, 598, A135.

Hoyer, D., Rauch, T., Werner, K., & Kruk, J. W., 2018. *Search for trans-iron elements in hot, helium-rich white dwarfs with the HST Cosmic Origins Spectrograph.* A&A, 612, A62.

Hoyle, F., 1946. *The synthesis of the elements from hydrogen.* MNRAS, 106, 343.

Hubeny, I. & Mihalas, D., 2014. *Theory of Stellar Atmospheres.* Princeton University Press.

Jacoby, G. H., 1981. *The peculiar planetary nebula Abell 35.* ApJ, 244, 903.

Jones, D. & Boffin, H., 2017. *Binary stars as the key to understanding planetary nebulae. Nature Astronomy*, 1, 0117.

Jorissen, A. & Mayor, M., 1988. *Radial velocity monitoring of a sample of barium and S stars using CORAVEL - Towards an evolutionary link between barium and S stars?* A&A, 198, 187.

Jorissen, A., Van Eck, S., Mayor, M., & Udry, S., 1998. *Insights into the formation of barium and Tc-poor S stars from an extended sample of orbital elements.* A&A, 332, 877.

Joss, P. C., Rappaport, S., & Lewis, W., 1987. *The core mass-radius relation for giants - A new test of stellar evolution theory.* ApJ, 319, 180.

Karakas, A. I. & Lattanzio, J. C., 2014a. *The Dawes Review 2: Nucleosynthesis and Stellar Yields of Low- and Intermediate-Mass Single Stars.* PASA, 31, e030.

Karakas, A. I. & Lugaro, M., 2016. *Stellar Yields from Metal-rich Asymptotic Giant Branch Models.* ApJ, 825, 26.

Karakas, A. I. & Lattanzio, J. C., 2014b. *The Dawes Review 2: Nucleosynthesis and Stellar Yields of Low- and Intermediate-Mass Single Stars.* PASA, 31, e030.

Kasen, D., Metzger, B., Barnes, J., Quataert, E., & Ramirez-Ruiz, E., 2017. *Origin of the heavy elements in binary neutron-star mergers from a gravitational-wave event.* Nature, 551(7678), 80.

Kawaler, S. D., 2004. *White Dwarf Rotation: Observations and Theory (Invited Review).* In *Stellar Rotation*, editors Maeder, A. & Eenens, P., IAU Symposium, 215, 561.

Kippenhahn, R. & Meyer-Hofmeister, E., 1977. *On the radii of accreting main sequence stars.* A&A, 54, 539.

Kirchhoff, G. & Bunsen, R., 1861. *Chemische Analyse durch Spectralbeobachtungen. Annalen der Physik*, 189(7), 337.

Knigge, C., 2011. *The Evolution of Cataclysmic Variables.* Astronomical Society of the Pacific Conference Series, 447, 3.

Kopal, Z., 1959. *Close binary systems.* The International Astrophysics Series. Chapman & Hall.

Kurucz, R. L., 1970. *Atlas: a Computer Program for Calculating Model Stellar Atmospheres. SAO Special Report*, 309.

Kurucz, R. L., 2014. *Model Atmosphere Codes: ATLAS12 and ATLAS9.* GeoPlanet: Earth and Planetary Sciences, 39.

Lawlor, T. M. & MacDonald, J., 2006. *The mass of helium in white dwarf stars and the formation and evolution of hydrogen-deficient post-AGB stars.* MNRAS, 371, 263.

Leibundgut, B., 2000. *Type Ia Supernovae.* A&A Rev., 10(3), 179.

Lester, J. B. & Neilson, H. R., 2008. *satlas: spherical versions of the atlas stellar atmosphere program.* A&A, 491(2), 633.

Löbling, L., 2017. *The Tübingen Model-Atom Database: A Revised Aluminum Model Atom and its Application for the Spectral Analysis of White Dwarfs.* In *20th European White Dwarf Workshop*, editors Tremblay, P. E., Gaensicke, B., & Marsh, T., ASPCS, 509, 235.

Löbling, L., 2020. *NLTE Spectral analysis of the intermediate helium-rich sdB star CPD-20° 1123. Submitted to* MNRAS.

Löbling, L., Boffin, H. M. J., & Jones, D., 2019a. *Spectral analysis of the barium central star of the planetary nebula Hen 2-39.* A&A, 624, A1.

Löbling, L., Maney, M. A., Rauch, T., Quinet, P., Gamrath, S., Kruk, J. W., & Werner, K., 2019b. *First discovery of trans-iron elements in a DAO-type white dwarf (BD−22°3467).* *Monthly Notices of the Royal Astronomical Society*, 492(1), 528.

Löbling, L., Rauch, T., Miller Bertolami, M. M., Todt, H., Friederich, F., Ziegler, M., Werner, K., & Kruk, J. W., 2019c. *Spectral analysis of the hybrid PG 1159-type central stars of the planetary nebulae Abell 43 and NGC 7094.* MNRAS, 489(1), 1054.

Löbling, L., 2018. *Sliding along the Eddington Limit—Heavy-Weight Central Stars of Planetary Nebulae.* *Galaxies*, 6(2), 65.

McClure, R. D., 1983. *The binary nature of the barium stars. II - Velocities, binary frequency, and preliminary orbits.* ApJ, 268, 264.

McClure, R. D. & Woodsworth, A. W., 1990. *The binary nature of the barium and CH stars. III - Orbital parameters.* ApJ, 352, 709.

McClure, R. D., Fletcher, J. M., & Nemec, J. M., 1980. *The binary nature of the barium stars.* ApJ, 238, L35.

McCook, G. P. & Sion, E. M., 1999. *A Catalog of Spectroscopically Identified White Dwarfs.* ApJS, 121, 1.

Mendeleev, D., 1869. *Über die Beziehungen der Eigenschaften zu den Atomgewichten der Elemente.* *Zeitschrift für Chemie*, 405.

Merrill, P. W., 1952. *Spectroscopic Observations of Stars of Class S.* ApJ, 116, 21.

Merrill, P. W. & Greenstein, J. L., 1956. *Revised List of Absorption Lines in the Spectrum of R Andromedae.* ApJS, 2, 225.

Merrill, P. W. & Lowen, A. L., 1954. *Strontium Lines in Late-type Spectra.* PASP, 66(391), 180.

Merrill, P. W. & Lowen, L., 1953. *The Gallium Line Lambda 4172 in Spectra of Long-Period Variable Stars.* PASP, 65(385), 221.

Meyer, L., 1870. *Die Natur der chemischen Elemente als Funktion ihrer Atomgewichte.* *Annalen der Chemie und Pharmacie: Supplementband VII*, 354.

Mihalas, D., 1978. *Stellar Atmospheres.* Astronomy and Astrophysics Series. W. H. Freeman.

Miksa, S., Deetjen, J. L., Dreizler, S., Kruk, J. W., Rauch, T., & Werner, K., 2002. *Iron abundance in hot hydrogen-deficient central stars and white dwarfs from FUSE, HST, and IUE spectroscopy.* A&A, 389, 953.

Miller Bertolami, M. M., 2016. *New models for the evolution of post-asymptotic giant branch stars and central stars of planetary nebulae.* A&A, 588, A25.

Miller Bertolami, M. M. & Althaus, L. G., 2006. *Full evolutionary models for PG 1159 stars. Implications for the helium-rich O(He) stars.* A&A, 454, 845.

Miszalski, B., Boffin, H. M. J., Frew, D. J., Acker, A., Köppen, J., Moffat, A. F. J., & Parker, Q. A., 2012. *A barium central star binary in the Type I diamond ring planetary nebula Abell 70.* MNRAS, 419, 39.

Miszalski, B., Boffin, H. M. J., Jones, D., Karakas, A. I., Köppen, J., Tyndall, A. A., Mohamed, S. S., Rodríguez-Gil, P., & Santander-García, M., 2013. *SALT reveals the barium central star of the planetary nebula Hen 2-39.* MNRAS, 436, 3068.

Mohamed, S. & Podsiadlowski, P., 2007. *Wind Roche-Lobe Overflow: a New Mass-Transfer Mode for Wide Binaries.* In *15th European Workshop on White Dwarfs*, editors Napiwotzki, R. & Burleigh, M. R., Astronomical Society of the Pacific Conference Series, 372, 397.

Morton, D. C., 2000. *Atomic Data for Resonance Absorption Lines. II. Wavelengths Longward of the Lyman Limit for Heavy Elements.* ApJS, 130(2), 403.

Morton, D. C., 2003. *Atomic Data for Resonance Absorption Lines. III. Wavelengths Longward of the Lyman Limit for the Elements Hydrogen to Gallium.* ApJS, 149(1), 205.

Nagae, T., Oka, K., Matsuda, T., Fujiwara, H., Hachisu, I., & Boffin, H. M. J., 2004. *Wind accretion in binary stars. I. Mass accretion ratio.* A&A, 419, 335.

Napiwotzki, R., 1999. *Spectroscopic investigation of old planetaries. IV. Model atmosphere analysis.* A&A, 350, 101.

Nesvacil, N., Stütz, C., & Weiss, W. W., 2003. *ATLAS model atmospheres.* Astronomical Society of the Pacific Conference Series, 298, 173.

Oganessian, Y. T., Utyonkov, V. K., Lobanov, Y. V., Abdullin, F. S., Polyakov, A. N., Sagaidak, R. N., Shirokovsky, I. V., Tsyganov, Y. S., Voinov, A. A., Gulbekian, G. G., Bogomolov, S. L., Gikal, B. N., Mezentsev, A. N., Iliev, S., Subbotin, V. G., Sukhov, A. M., Subotic, K., Zagrebaev, V. I., Vostokin, G. K., Itkis, M. G., Moody, K. J., Patin, J. B., Shaughnessy, D. A., Stoyer, M. A., Stoyer, N. J., Wilk, P. A., Kenneally, J. M., Landrum, J. H., Wild, J. F., & Lougheed, R. W., 2006. *Synthesis of the isotopes of elements 118 and 116 in the* ^{249}Cf *and* ^{245}Cm $+^{48}$ Ca *fusion reactions. Phys. Rev. C*, 74, 044602.

O'Toole, S. J., 2004. *Beyond the iron group: Heavy metals in hot subdwarfs.* A&A, 423, L25.

O'Toole, S. J. & Heber, U., 2006. *Abundance studies of sdB stars using UV echelle HST/STIS spectroscopy.* A&A, 452(2), 579.

Paxton, B., Marchant, P., Schwab, J., Bauer, E. B., Bildsten, L., Cantiello, M., Dessart, L., Farmer, R., Hu, H., Langer, N., Townsend, R. H. D., Townsley, D. M., & Timmes, F. X., 2015. *Modules for Experiments in Stellar Astrophysics (MESA): Binaries, Pulsations, and Explosions.* ApJS, 220(1), 15.

Payne, C. H., 1925. *Stellar Atmospheres; a Contribution to the Observational Study of High Temperature in the Reversing Layers of Stars.* PhD thesis, RADCLIFFE COLLEGE.

Rauch, T., 1999. *Narrow-band imaging and a search for planetary nebulae.* A&AS, 135, 487.

Rauch, T., 2012. *Recent Investigations on AA Doradus.* Astronomical Society of the Pacific Conference Series, 452, 111.

Rauch, T. & Deetjen, J. L., 2003. *Handling of Atomic Data.* In *Stellar Atmosphere Modeling*, editors Hubeny, I., Mihalas, D., & Werner, K., ASPCS, 288, 103.

Rauch, T., Köper, S., Dreizler, S., Werner, K., Heber, U., & Reid, I. N., 2004. *The Rotational Velocity of Helium-rich Pre-White Dwarfs.* In *Stellar Rotation*, editors Maeder, A. & Eenens, P., IAU Symposium, 215, 573.

Rauch, T., Werner, K., Biémont, É., Quinet, P., & Kruk, J. W., 2012. *Stellar laboratories: new Ge V and Ge VI oscillator strengths and their validation in the hot white dwarf RE 0503-289.* A&A, 546, A55.

Rauch, T., Werner, K., Bohlin, R., & Kruk, J. W., 2013. *The virtual observatory service TheoSSA: Establishing a database of synthetic stellar flux standards. I. NLTE spectral analysis of the DA-type white dwarf G191-B2B.* A&A, 560, A106.

Rauch, T., Werner, K., Quinet, P., & Kruk, J. W., 2014a. *Stellar laboratories. III. New Ba V, Ba VI, and Ba VII oscillator strengths and the barium abundance in the hot white dwarfs G191-B2B and RE 0503-289.* A&A, 566, A10.

Rauch, T., Werner, K., Quinet, P., & Kruk, J. W., 2014b. *Stellar laboratories. II. New Zn IV and Zn V oscillator strengths and their validation in the hot white dwarfs G191-B2B and RE 0503-289.* A&A, 564, A41.

Rauch, T., Hoyer, D., Quinet, P., Gallardo, M., & Raineri, M., 2015a. *Stellar laboratories. V. The Xe VI ultraviolet spectrum and the xenon abundance in the hot DO-type white dwarf RE 0503-289.* A&A, 577, A88.

Rauch, T., Werner, K., Quinet, P., & Kruk, J. W., 2015b. *Stellar laboratories. IV. New Ga IV, Ga V, and Ga VI oscillator strengths and the gallium abundance in the hot white dwarfs G191-B2B and RE 0503-289.* A&A, 577, A6.

Rauch, T., Quinet, P., Hoyer, D., Werner, K., Demleitner, M., & Kruk, J. W., 2016a. *Stellar laboratories. VI. New Mo IV-VII oscillator strengths and the molybdenum abundance in the hot white dwarfs G191-B2B and RE 0503-289.* A&A, 587, A39.

Rauch, T., Quinet, P., Hoyer, D., Werner, K., Richter, P., Kruk, J. W., & Demleitner, M., 2016b. *Stellar laboratories. VII. New Kr IV - VII oscillator strengths and an improved spectral analysis of the hot, hydrogen-deficient DO-type white dwarf RE 0503-289.* A&A, 590, A128.

Rauch, T., Gamrath, S., Quinet, P., Löbling, L., Hoyer, D., Werner, K., Kruk, J. W., & Demleitner, M., 2017a. *Stellar laboratories . VIII. New Zr IV-VII, Xe IV-V, and Xe VII oscillator strengths and the Al, Zr, and Xe abundances in the hot white dwarfs G191-B2B and RE 0503-289.* A&A, 599, A142.

Rauch, T., Quinet, P., Knörzer, M., Hoyer, D., Werner, K., Kruk, J. W., & Demleitner, M., 2017b. *Stellar laboratories . IX. New Se V, Sr IV-VII, Te VI, and I VI oscillator strengths and the Se, Sr, Te, and I abundances in the hot white dwarfs G191-B2B and RE 0503-289.* A&A, 606, A105.

Rauch, T., Gamrath, S., Quinet, P., Demleitner, M., Knörzer, M., Werner, K., & Kruk, J. W., 2020. *Stellar laboratories. X. New Cu IV-VII oscillator strengths and the first detection of copper and indium in hot white dwarfs.* A&A, 637, A4.

Recio-Blanco, A., de Laverny, P., Kordopatis, G., Helmi, A., Hill, V., Gilmore, G., Wyse, R., Adibekyan, V., Randich, S., & Asplund, M., 2014. *The Gaia-ESO Survey: the Galactic thick to thin disc transition.* A&A, 567, A5.

Reindl, N., Rauch, T., Werner, K., Kruk, J. W., & Todt, H., 2014. *On helium-dominated stellar evolution: the mysterious role of the O(He)-type stars.* A&A, 566, A116.

Saha, M. N., 1921. *On a Physical Theory of Stellar Spectra. Proceedings of the Royal Society of London Series A*, 99(697), 135.

Schönberner, D., 1979. *Asymptotic giant branch evolution with steady mass loss.* A&A, 79, 108.

Schönberner, D. & Steffen, M., 2019. *Confronting expansion distances of planetary nebulae with Gaia DR2 measurements.* A&A, 625, A137.

Schönberner, D., Balick, B., & Jacob, R., 2018. *Expansion patterns and parallaxes for planetary nebulae.* A&A, 609, A126.

Scott, P., Asplund, M., Grevesse, N., Bergemann, M., & Sauval, A. J., 2015a. *The elemental composition of the Sun. II. The iron group elements Sc to Ni.* A&A, 573, A26.

Scott, P., Grevesse, N., Asplund, M., Sauval, A. J., Lind, K., Takeda, Y., Collet, R., Trampedach, R., & Hayek, W., 2015b. *The elemental composition of the Sun. I. The intermediate mass elements Na to Ca.* A&A, 573, A25.

Solheim, J. E., Vauclair, G., Mukadam, A. S., Janulis, R., & Dobrovolskas, V., 2007. *Abell 43: longest period planetary nebula nucleus variable.* A&A, 468(3), 1057.

Sommerfeld, A., 1916. *Zur Quantentheorie der Spektrallinien. Annalen der Physik*, 356(17), 1.

Taam, R. E., 1994. *The Common Envelope Phase of Binary Evolution.* Astronomical Society of the Pacific Conference Series, 56, 208.

Thevenin, F. & Jasniewicz, G., 1997. *Barium-rich G stars in the nuclei of the planetary nebulae Abell 35 and LoTr5.* A&A, 320, 913.

Tokovinin, A., 2014. *From Binaries to Multiples. I. Data on F and G Dwarfs within 67 pc of the Sun.* AJ, 147(4), 86.

Tyndall, A. A., Jones, D., Boffin, H. M. J., Miszalski, B., Faedi, F., Lloyd, M., Boumis, P., López, J. A., Martell, S., Pollacco, D., & Santander-García, M., 2013. *Two rings but no fellowship: LoTr 1 and its relation to planetary nebulae possessing barium central stars.* MNRAS, 436, 2082.

Unglaub, K., 2008. *Mass-loss and diffusion in subdwarf B stars and hot white dwarfs: do weak winds exist?* A&A, 486(3), 923.

Unglaub, K. & Bues, I., 2000. *The chemical evolution of hot white dwarfs in the presence of diffusion and mass loss.* A&A, 359, 1042.

Unglaub, K. & Bues, I., 2001. *The influence of diffusion and mass loss on the chemical composition of subdwarf B stars.* A&A, 374, 570.

Unsöld, A., 1928. *Über die Struktur der Fraunhoferschen Linien und die quantitative Spektralanalyse der Sonnenatmosphäre. Zeitschrift für Physik*, 46(11), 765.

Vennes, S., Chayer, P., & Dupuis, J., 2005. *Discovery of Photospheric Germanium in Hot DA White Dwarfs.* ApJ, 622(2), L121.

Werner, K., 1986. *Construction of non-LTE model atmospheres using approximate lambda operators.* A&A, 161, 177.

Werner, K., 1989. *Non-LTE model atmosphere calculations with approximate lambda operators - Application of tridiagonal operators.* A&A, 226(1), 265.

Werner, K. & Herwig, F., 2006. *The Elemental Abundances in Bare Planetary Nebula Central Stars and the Shell Burning in AGB Stars.* PASP, 118, 183.

Werner, K., Deetjen, J. L., Dreizler, S., Nagel, T., Rauch, T., & Schuh, S. L., 2003. *Model Photospheres with Accelerated Lambda Iteration.* In *Stellar Atmosphere Modeling*, editors Hubeny, I., Mihalas, D., & Werner, K., ASPCS, 288, 31.

Werner, K., Rauch, T., Ringat, E., & Kruk, J. W., 2012. *First Detection of Krypton and Xenon in a White Dwarf.* ApJ, 753, L7.

Werner, K., Rauch, T., & Kruk, J. W., 2010. *Detection of Iron in PG1159 Stars.* ApJ, 719 (1), L32.

Wesemael, F., Green, R. F., & Liebert, J., 1985. *Spectrophotometric and model-atmosphere analyses of the hot DO and DAO white dwarfs from the Palomar-Green survey.* ApJS, 58, 379.

Wollaston, W. H., 1802. *XII. A method of examining refractive and dispersive powers, by prismatic reflection. Philosophical Transactions of the Royal Society of London*, 92, 365.

Ziegler, M., Rauch, T., Werner, K., Köppen, J., & Kruk, J. W., 2012. *BD-22°3467, a DAO-type star exciting the nebula Abell 35.* A&A, 548, A109.